Dissertation in Astronomy

submitted to the
Combined Faculties of the Natural Sciences and Mathematics
of the
Ruperto-Carola-University of Heidelberg
Germany

for the degree of
Doctor of Natural Sciences

put forward by

Fabrizio Arrigoni Battaia, M.Sc.
born in Milan, Italy

oral examination: 22 July 2015

CHARACTERIZING THE CIRCUMGALACTIC MEDIUM IN EMISSION

Fabrizio Arrigoni Battaia

Max-Planck-Institut für Astronomie

Referees: Dr. Joseph F. Hennawi
Prof. Dr. Ralf S. Klessen

ABSTRACT

In this thesis I focus on understanding the physical properties of extended Lyα emitting gas at high redshift ($z \sim 2-3$), from the circumgalactic medium (CGM) and intergalactic medium (IGM). First, I investigate the physics of giant ($\sim$ 100 kpc), luminous ($\sim 10^{44}$ erg s^{-1}) Lyα nebulae known as Lyman alpha blobs (LABs). The mechanism powering the emission of LABs is poorly understood, although they are now often associated with active galactic nuclei (AGN). Our poor understanding results primarily from the lack of information beyond the Lyα line. Targeting 13 LABs, I thus conduct a deep search for the He II λ1640 and C IV λ1549 lines, which probe the volume density, the metallicity, and the ionization level within the nebulae. Although I did not detect any emission down to unprecedented surface brightness levels, I show that LABs could be still consistent with photoionization from an obscured AGN. Second, I led a narrow-band imaging survey (FLASHLIGHT) targeting the Lyα line around 25 $z \sim 2$ quasars. FLASHLIGHT is the deepest line imaging study ever undertaken around quasars, and aims to uncover the emission from their CGM. During this campaign, I took part in the discovery of the largest ($\sim$ 500 kpc) Lyα nebula known at high redshift: UM 287. Its bright large scale emission is in tension with our current understanding of the physical state of gas in massive dark matter halos. As for the LABs, I obtained even deeper He II and C IV spectroscopy of UM 287, and again failed to detect emission. Using photoionization modeling I show that the extended Lyα emission is likely arising from remarkably dense and compact clouds, which are clearly unresolved in current cosmological simulations. Lastly, by stacking the FLASHLIGHT data, I obtain the first measurement of the average Lyα emission from the typical quasar CGM, i.e. $\sim 10^{-20}$ erg s^{-1} cm^{-2} arcsec^{-2}. Combined with absorption line measurements on the total CGM gas mass, this provides the first measurement of the gas density in the quasar CGM. Given this low surface brightness, the next generation of telescopes is probably needed to routinely detect CGM emission around individual quasars. Nevertheless, this thesis paves the way for the understanding of the CGM in emission, which is timely given the upcoming instruments.

ZUSAMMENFASSUNG

In dieser Doktorarbeit konzentriere ich mich auf das Verständnis der physikalischen Eigenschaften ausgedehnten Lyα-emittierenden Gases bei hoher Rotverschiebung ($z \sim 2-3$) des zirkumgalaktischen Mediums [circumgalactic medium, CGM] und des intergalaktischen Mediums (IGM). Erstens untersuche ich die Physik riesiger ($\sim$ 100 kpc), leuchtkräftiger ($\sim 10^{44}$ erg s^{-1}) Lyα-Nebel, bekannt als Lyα-Blobs (LABs). Die Quelle der Emission von LABs ist bisher wenig verstanden, obwohl sie neuerdings oft mit aktiven Galaxienkernen [active galactic nuclei, AGN] assoziiert werden. Unser geringes Verständnis resultiert hauptsächlich aus dem Fehlen von Information über die Lyα-Linie hinaus. Daher führte ich bei 13 LABs eine tiefe Suche nach der He II λ1640 und der C IV λ1549 Linie durch, welche die Volumendichte, Metallizität und den Ionisationsgrad innerhalb der Nebel ergründen. Obwohl ich trotz zuvor unerreichter tiefer Flächenhelligkeit keine Emission nachweisen konnte, zeige ich, dass LABs noch im Einklang mit Photoionisation durch einen AGN sein können. Zweitens leitete ich eine Schmalbandbild-Untersuchung (FLASHLIGHT) um die Lyα-Linie von 25 $z \sim 2$ Quasaren. FLASHLIGHT ist die tiefste bisher unternommene Linienabbildungsstudie um Quasare, und zielt darauf ab, die Emission ihres CGMs aufzudecken. Während dieser Kampagne nahm ich teil an der Entdeckung des größten ($\sim$ 500 kpc) bekannten Lyα-Nebels bei hoher Rotverschiebung: UM 287. Seine helle großskalige Emission ist schwer vereinbar mit unserem jetzigen Verständnis des physikalischen Zustands von Gas in massiven Halos dunkler Materie. Ebenso wie für die LABs erlangte ich sogar tiefere He II und C IV-Spektroskopie von UM 287, und detektierte wiederum keine Emission. Mittels Photoionisationsmodellen zeige ich, dass die ausgedehnte Lyα-Emission wahrscheinlich von außerordentlich dichten und kompakten Gaswolken herrührt, die in derzeitigen kosmologischen Simulationen nicht aufgelöst werden können. Schließlich erhalte ich durch Mittelung der FLASHLIGHT-Daten die erste Messung der mittleren Lyα-Emission des typischen CGMs eines Quasars als $\sim 10^{-20}$ erg s^{-1} cm^{-2} arcsec^{-2}. Kombiniert mit Absorptionslinienmessungen der Gesamtmasse des CGMs liefert dies die erste Messung der Gasdichte im CGM von Quasaren. Bei dieser geringen Flächenhelligkeit wird wahrscheinlich die nächste Generation von Teleskopen benötigt, um die Emission des CGMs um einzelne Quasare regelmäßig zu detektieren. Gleichwohl ebnet diese Doktorarbeit den Weg für das Verständnis des CGMs in Emission, zeitgerecht zu den bevorstehenden Instrumenten.

To my friends:
wherever they are,
wherever they will go.

Twenty years from now
you will be more disappointed by the things that you didn't do
than by the ones you did so.
So throw off the bowlines.
Sail away from the safe harbor.
Catch the trade winds in your sails.
Explore. Dream. Discover.

Mark Twain

CONTENTS

1 INTRODUCTION 1
1.1 THE LYα LINE 5
1.2 ABSORPTION LINE STUDIES 7
1.2.1 IGM 7
1.2.2 CGM 9
1.3 EMISSION LINE STUDIES 10
1.3.1 CHRONICLE OF LYα SURVEYS 11
1.3.1.1 Giant Lyα Nebulae 11
1.3.1.2 Extended Lyα Emission around QSOs 16
1.3.1.3 High-Redshift Radio Galaxies 19
1.3.1.4 Lyman α Blobs - LABs 20
1.3.2 THE NEED OF ADDITIONAL LINE DIAGNOSTICS 22
1.4 THESIS OUTLINE 24

2 A SIMPLE MODEL FOR COOL HALO GAS 27
2.1 FLUORESCENT LYα EMISSION 29
2.1.1 OPTICALLY THIN REGIME 31

2.1.2 Optically Thick Regime 32
2.2 The Impact of Resonant Scattering 33
2.3 Caveats 34

3 A Deep Narrowband Imaging Search for C iv and He ii Emission from Lyα Blobs **37**
3.1 Observations and data reduction 38
3.1.1 VLT/FORS2 observations and data reduction 38
3.1.2 Subaru Suprime-Cam Data 41
3.1.3 Continuum subtraction 42
3.1.4 Surface Brightness Limits 43
3.2 Observational Results 50
3.3 Previous Observations of He ii and C iv 54
3.4 Discussion 57
3.4.1 Comparison with Photoionization Models 57
3.4.2 Comparison with Shock Models 64
3.4.3 Comparison to Previous Modeling of Extended Lyα Emission Nebulae . 67
3.5 Summary and Conclusions 68

4 **FLASHLIGHT** **71**
4.1 The FLASHLIGHT idea: using QSOs as Searchlights 72
4.2 Observations 72
4.3 Data Reduction of the Gemini data 75
4.4 Overview of the Current Results of the Survey 78

5 Discovery and Analysis of the largest Lyα Nebula ever Observed **81**
5.1 The Discovery 82

5.2 OBSERVATIONS AND DATA REDUCTION 88

5.2.1 CONTINUUM SUBTRACTION 90

5.2.2 DATA REDUCTION AND ANALYSIS FOR THE COMPANION QUASAR 91

5.3 ANALYSIS OF THE NEBULA'S ENVIRONMENT AND EMISSION 92

5.3.1 GALAXY OVERDENSITY ANALYSIS 92

5.3.2 CONVERTING THE OBSERVED LYα EMISSION TO GAS COLUMN DENSITIES 93

5.4 DEEP HE II AND C IV SPECTROSCOPY: DENSE COMPACT GAS CLUMPS 95

5.4.1 OBSERVATIONS AND DATA REDUCTION 96

5.4.2 OBSERVATIONAL RESULTS 99

5.4.2.1 Kinematics of the Nebula 104

5.4.3 MODELING THE LYα, C IV AND HE II EMISSION AROUND UM 287 105

5.4.3.1 Brief Reminder of the Photoionization Modeling 105

5.4.3.2 The Impact of Resonant Scattering 107

5.4.3.3 Modeling the UM 287 Quasar SED 108

5.4.3.4 Input Parameters to Cloudy 109

5.4.4 MODELS VS OBSERVATIONS 111

5.4.4.1 Constraints from Absorption Lines 116

5.4.4.2 Comparison to Absorption Line Studies 119

5.4.5 MODEL SPECTRA VS CURRENT OBSERVATIONAL LIMITS 120

5.4.6 CAVEATS 123

5.4.7 SUMMARY AND CONCLUSIONS 127

6 THE FIRST RADIAL EMISSION PROFILE OF THE CIRCUMGALACTIC MEDIUM OF QUASARS 131

6.1 IMAGE PREPARATION FOR THE PROFILE EXTRACTION 131

6.2 TESTING OUR NARROW-BAND IMAGES 134

6.2.1 The 'Zero' Level . . . 134
6.2.2 Constraining the PSF of the NB Images . . . 136
6.3 Results . . . 139
6.3.1 Quantifying the Significance of our Results . . . 143
6.4 Discussion . . . 147
6.5 Summary and Conclusions . . . 150

7 Summary and Future Perspective **153**
7.1 The Scientific Framework . . . 153
7.2 This Work . . . 155
7.3 Future Work . . . 158
7.3.1 Observational Game Changers . . . 159

Bibliography **163**

Acknowledgements **179**

LIST OF FIGURES

1.1 The Cosmic Web in the Bolshoi cosmological simulation. 2

1.2 ‘Hot mode’ and ‘cold mode’ accretion 4

1.3 The largest Lyα nebula known around a radio-quiet QSO, before this work. . . 18

1.4 An example of high redshift radio galaxy, with its Lyα nebula. 20

2.1 Toy-model of the cool halo gas of a QSO (Hennawi & Prochaska 2013). 28

3.1 Filter profiles for our study on LABs: NB497, SII+62, OI/2500+57,V,R, and i. 38

3.2 The SSA22 protocluster: LAEs and LABs spatial distribution. 39

3.3 Distribution of seeings in our NB observations. 40

3.4 Analysis of the systematics in the He II line image. 44

3.5 Analysis of the systematics in the C IV line image. 45

3.6 Detection significance of simulated sources as a function of sizes in He II 48

3.7 Detection significance of simulated sources as a function of sizes in C IV 49

3.8 Postage-stamp images in all the available filters of the LABs in our study. . . . 51

3.9 Postage-stamp images in all the available filters of the LABs in our study (cont’d). 52

3.10 Postage-stamp χ images in the He II and C IV filters of the LABs in our study. . 53

3.11 Constraints from our LABs observations on a HeII/Lyα vs CIV/Lyα log-log plot. 57

3.12 Comparison between photoionization models and our observations. 62

3.13 Comparison between shock models and our observations. 66

4.1 Selection method used for our custom-built NB filters. 73

4.2 $\mathrm{SB}_{\mathrm{Ly}\alpha}$ map of a newly discovered LAB (FLASHLIGHT survey). 79

5.1 Processed and combined images of the field surrounding the quasar UM 287. . 82

5.2 Lyα image of the UM 287 nebula (also known as Slug Nebula). 83

5.3 Luminosity-size plot for previously detected, bright Lyα nebulae and UM 287. 84

5.4 Inferred hydrogen column densities associated with the UM 287 nebula. 87

5.5 Transmission curves of the filters used in the discovery of the UM 287 nebula. . 89

5.6 Spectrum of the quasar UM 287 and of the faint companion quasar. 91

5.7 Pixel-to-pixel correlations for $\mathrm{SB}_{\mathrm{Ly}\alpha}$ for scenarios (1) and (2). 94

5.8 Slit setup for the deep He II and C IV spectroscopy of the UM 287 nebula. . . . 97

5.9 Two-dimensional spectra for the red slit shown in Figure 5.8. 100

5.10 Two-dimensional spectra for the blue slit shown in Figure 5.8. 101

5.11 Detection significance of extended emission in our deep spectra. 103

5.12 SED of the quasar UM 287, used as incident radiation field in our modeling. . . 109

5.13 Constraints of the UM 287 nebula on the HeII/Lyα versus CIV/Lyα log-log plot. 112

5.14 Constraints on n_{H}, N_{H}, R, Z for gas clouds within the UM 287 nebula. 115

5.15 Constraints on N_{CIV} and N_{NV} from our modeling and observations. 117

5.16 Predicted median spectra of the UM 287 nebula at $\sim$ 160 kpc. 121

5.17 Effect of using different slopes: $\alpha_{\mathrm{EUV}} = -1.1, -1.7, -2.3$. 125

5.18 Schematic representation on the effects of slope variation on the $n_{\mathrm{H}} - Z$ plane. . 126

6.1 Example of GMOS/Gemini-South data (FLASHLIGHT survey). 132

6.2 Example of a NB image after masking all the sources. 133
6.3 Average radial surface brightness profile of the ‘zero’ level in our images. . . . 134
6.4 Issues in stacking a large number of images. 135
6.5 PSF determination: average radial profile of 115 stars in our NB images. 136
6.6 Comparison of the 2D stack images: QSOs, Stars, ‘CGM’, and ‘zero’ level. . . 138
6.7 Comparison between the stacked QSO profile and the PSF of the NB images. . 140
6.8 Comparison between QSO, stars and CGM profiles. 141
6.9 Dependence of the CGM profile on each individual QSO. 142
6.10 χ histograms of 1000 realizations of our same experiment (bootstrap analysis). . 144
6.11 Statistical significance of the CGM radial profile. 145
6.12 Bootstrap analysis around the ‘zero’ flux level for the Lyα profile. 146
6.13 Statistical significance of our detection within 50 kpc and 500 kpc. 146

7.1 A newly discovered giant Lyα nebula around a radio-quiet $z \sim 3$ quasar. 160

List of Tables

1.1 Summary of absorption line system properties (adapted from Meiksin 2009). . . . 8

1.2 List of the largest and brightest Lyα nebulae in the literature. The data are homogenized to the same cosmology, i.e the standard ΛCDM cosmology ($\Omega_{\rm M}$ = 0.3, Ω_{Λ} = 0.7, h = 0.7). Nebulae discovered in this work are not listed here. 13

1.2 List of the largest and brightest Lyα nebulae in the literature. The data are homogenized to the same cosmology, i.e the standard ΛCDM cosmology ($\Omega_{\rm M}$ = 0.3, Ω_{Λ} = 0.7, h = 0.7). Nebulae discovered in this work are not listed here. 14

1.2 List of the largest and brightest Lyα nebulae in the literature. The data are homogenized to the same cosmology, i.e the standard ΛCDM cosmology ($\Omega_{\rm M}$ = 0.3, Ω_{Λ} = 0.7, h = 0.7). Nebulae discovered in this work are not listed here. 15

1.2 List of the largest and brightest Lyα nebulae in the literature. The data are homogenized to the same cosmology, i.e the standard ΛCDM cosmology ($\Omega_{\rm M}$ = 0.3, Ω_{Λ} = 0.7, h = 0.7). Nebulae discovered in this work are not listed here. 16

3.1 VLT FORS2 Observations and Subaru Data 41

3.2 Properties of the 13 LABs in our sample. 42

3.3 Extracted fluxes and significance for the 13 LABs in our sample. 46

3.4 Properties of He ii and C iv emission from LABs in the literature. 55

4.1 Summary of the GMOS/Gemini-South Observations used in this work. 76

> *"In your life, I wish you at least a blackout in a clear night."*
>
> Mario Rigoni Stern

Chapter 1

INTRODUCTION

In the current ΛCDM paradigm of structure formation, small primordial energy-density perturbations ($10^{-5} - 10^{-4}$, depending on the angular scale) evolved, due to gravitational instabilities, in today's Universe (e.g., Dodelson 2003; Padmanabhan 2006; Fukugita et al. 1998 and references therein). This growth of structures has thus rearranged baryons[1] from the almost homogeneous primordial plasma to a mixture of physical states (plasma; condensed, atomic, and molecular gas; dust), which are visible in the wide assortment of known astrophysical systems, e.g. planets, stars, stellar remnants, galaxies, and clusters of galaxies. However, at early epochs ($z \gtrsim 1.5$) [2], $> 80\%$ of the baryons (Prochaska & Tumlinson 2009; Meiksin 2009, and references therein) were contained in the so-called cosmic web (Bond et al. 1996; see Figure 1.1), a gaseous network developed during the structure formation process, which is organized in filaments, sheets,

---

[1] In the ΛCDM paradigm, the Universe is composed by three components: dark energy (present as a cosmological constant), dark matter (collisionless particles,interacting only gravitationally), and baryons (i.e., ordinary matter). At the moment of writing, the most recent estimates (Planck Collaboration et al. 2015) of the relative amount of these constituents are that ordinary matter accounts for only $\sim 4.9\%$ of the mass-energy of the Universe, while dark matter and dark energy account for $\sim 26\%$ and $\sim 69.1\%$, respectively.

[2] The redshift z of an object is defined as

$$z \equiv \frac{\lambda_{\rm obs}}{\lambda_{\rm em}} - 1$$

where $\lambda_{\rm obs}$ and $\lambda_{\rm em}$ are the observed wavelength and the emitted wavelength of its radiation, respectively. In cosmology, the redshift can be directly related to the scale factor $a(t)$ of the Robertson-Walker metric, and thus to a look back time. The cosmological redshift can be shown to be

$$z = \frac{a(t_{\rm obs})}{a(t_{\rm em})} - 1 = \frac{1}{a(t_{\rm em})} - 1$$

where, by convention, the scale factor at the present time is set to be $a(t_{\rm obs}) = 1$. The redshift thus takes into account the increase in wavelength of radiation, which happens while it traverses the expanding Universe from its emission point to its detection point.

and knots. This diffuse medium, which traces the large-scale structure of the Universe, is also called intergalactic medium (IGM).

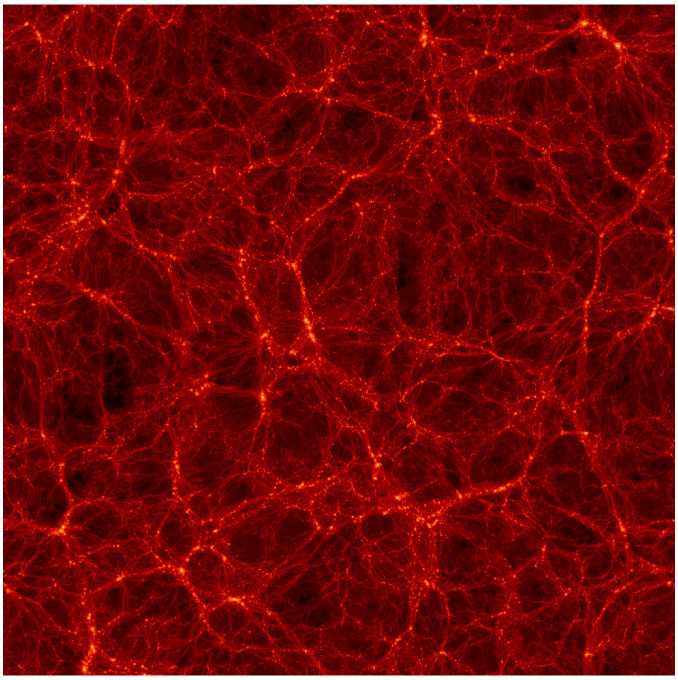

Figure 1.1: The large-scale structure of the Universe as traced by the dark matter in the framework of the Bolshoi cosmological simulation (e.g., Klypin et al. 2011). The characteristic filaments and knots of the cosmic web are well visible. This snapshot is taken at $z = 0$. Image credit: http://hipacc.ucsc.edu/Bolshoi/index.html .

In this framework, the accepted model for galaxy formation was that baryons collapsed from the IGM onto the potential wells of dark matter halos, were shock-heated to the virial temperature[3]

$$T_{\rm vir} = \frac{GMm_{\rm p}}{3k_{\rm B}R} = 3.5\times10^{6}\left(\frac{M}{10^{12.5}\,{\rm M}_{\odot}}\right)\left(\frac{R}{160\,{\rm kpc}}\right)^{-1}\,{\rm K}, \tag{1.1}$$

---

[3] If a system of particles is in steady state, i.e. its overall description does not change with time (or in other words, its macroscopic parameters remain fixed within a finite range), it can be shown that its total kinetic energy, KE, and its total potential energy, W, satisfy the relation (virial theorem; e.g., Binney & Tremaine 2008)

$$2KE + W = 0$$

In the case of a dark matter halo with mass M within a radius R (and ignoring the self-gravitation of the gas, i.e. its mass is $< M$), the total potential energy can be written as

$$W = -\frac{GMNm_{\rm p}}{R},$$

where G is the gravitational constant, $m_{\rm p}$ is the proton's mass, and N is the number of particles. The total average kinetic energy, in turn, can be written as

$$KE = \frac{3}{2}Nk_{\rm B}T,$$

where $k_{\rm B}$ is the Boltzmann constant. Note that this formula is valid only for atomic gas, i.e. the particles are assumed to be point masses, and thus, it does not take into account internal degrees of freedom, such as molecular rotation and vibration. Based on these assumptions, the virial temperature is defined as in the main text (White & Rees 1978).

and subsequently cooled down to form stars (White & Rees 1978). Specifically, the accretion shock is a generic prediction if $T_{\rm vir}$ is larger than the temperature of the accreting gas (Binney 1977), i.e. the cold gas accretes supersonically (the sound speed scales as $v_{\rm s} \propto T^{-1/2}$), and a shock front develops between the lower density, supersonic flow and the higher density, subsonic flow. Thus, during the halo formation, the accreting gas is expected to be heated to $\sim T_{\rm vir}$ through one strong shock or in a series of weak ones (White & Rees 1978).

The fate of the shock-heated gas, which is indeed ionized given the high temperatures, would then depend on the ability of the gas pressure to counteract gravitational collapse. The outcome is regulated by two-body radiative processes, that enable gas cooling, and by the overall mass of the system. At the typical densities expected for this gas ($n_{\rm H} \sim 10^{-4} - 10$ cm^{-3}, Meiksin 2009), the gas cooling is achieved through free-free emission (or bremsstrahlung), radiative recombination, collisional ionization, and collisional excitation. The net cooling rate $\Lambda(T,n,Z)$ [erg s^{-1} cm^{-3}] depends on the gas temperature T, number density n , and metallicity Z, as well as on the radiation field (photoionization and photo-heating; e.g., Cantalupo 2010; Gnedin & Hollon 2012; Kannan et al. 2014b). To understand the possible gas cooling regimes in structure formation, it is important to define the involved characteristic time scales: the cooling time $t_{\rm cool}$ and the gravitational free fall time $t_{\rm ff}$. The cooling time can be written as (Draine 2011)

$$t_{\rm cool} = \frac{3k_{\rm B}T}{2\Lambda/n}, \tag{1.2}$$

while the gravitational free fall time is given by (Binney & Tremaine 2008)

$$t_{\rm ff} \sim \frac{1}{\sqrt{G\rho}}. \tag{1.3}$$

Therefore, two different cases can be established (Rees & Ostriker 1977; White & Rees 1978; White & Frenk 1991)

1) $t_{\rm cool} > t_{\rm ff}$ A quasi-hydrostatic equilibrium configuration. The gas is pressure-supported and will contract very slowly, being able to eventually fragment[4].

2) $t_{\rm cool} < t_{\rm ff}$ The gas cooling is fast and the pressure is not able to counteract the collapse, which occurs on a free-fall time scale. The gas thus easily contracts and forms stars efficiently.

The first case is typical for massive halos ($M \gtrsim 10^{12}$ M$_\odot$), where a shock is developed at the virial radius $R_{\rm vir} = \frac{GM}{\sigma^2}$ (with σ the velocity dispersion of the system) or at slightly larger radii (Voit et al. 2003; Nelson et al. 2015). The second case applies to less massive halos, for which the shock forms at smaller radii (Rees & Ostriker 1977; White & Frenk 1991). Through this cooling process, the gas is eventually able to radiate away its gravitational energy, settle down into a galactic disk, and be able to form stars. A disk structure is formed because radiative cooling conserves angular momentum, which in turn has been produced at early epochs by tidal torques from large scale structures (Fall & Efstathiou 1980; Mo et al. 1998).

---

[4] To have an appreciable contraction, $t_{\rm cool}$ has to be smaller than the Hubble time $\frac{1}{H_0}$, i.e. approximately the present age of the Universe.

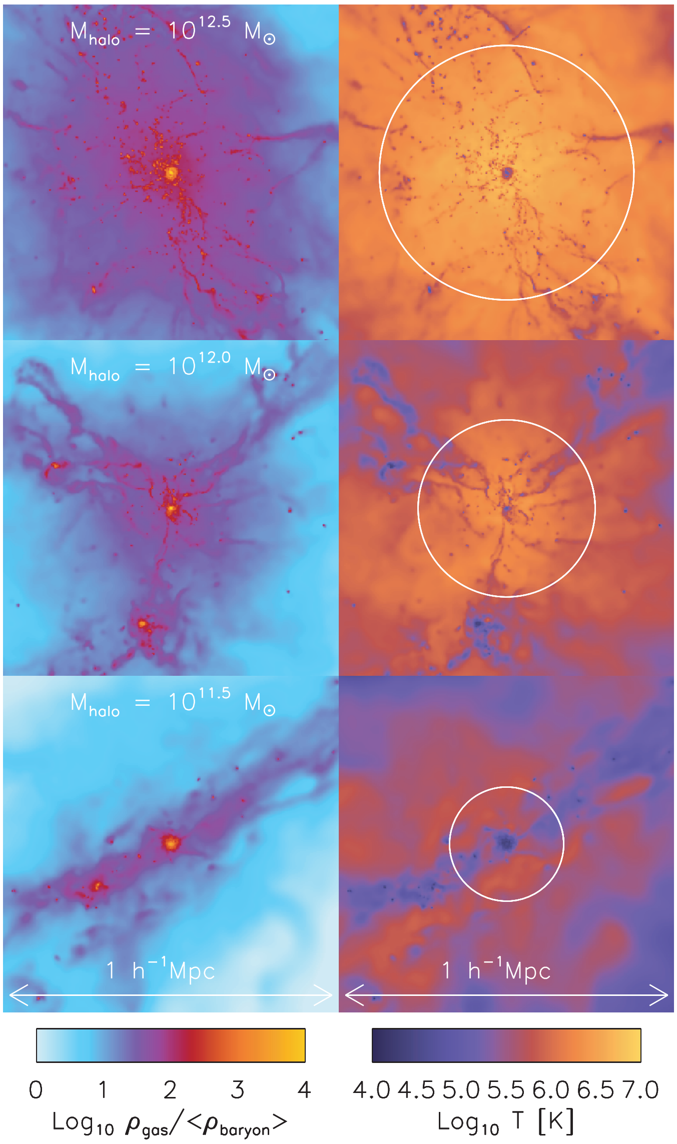

Figure 1.2: Gas overdensity (first column) and temperature (second column) in a cubic region of 1 h^{-1} comoving Mpc centered on halos of $M_{DM} \approx 10^{12.5}, 10^{12}$ and $10^{11.5}$ $M_\odot$ (from top to bottom) at $z = 2$. The white circles indicate the virial radii of the halos. Hot accretion dominates for high-mass halos and cold accretion for low-mass halos (see text for details). The galaxies in the centers of these halos are discs, surrounded by cold gas. Figure adapted from van de Voort et al. (2011).

However, it has now being shown that this process of cooling from a hot virialized halo accounts for only a small fraction of the fuel for star formation. In particular, cosmological hydrodynamical simulations indicate that a "cold mode" ($T < 10^5$ K) of accretion onto galaxies occurs along filaments (Kereš et al. 2005; Ocvirk et al. 2008), and dominates for low mass halos ($M < 10^{12}$ $M_\odot$; see Figure 1.2). The most attractive feature of this now ubiquitous picture, is the efficient transport of cold gas to the center of star-forming galaxies (Dekel et al. 2009), which provides a natural mechanism to sustain the large star formation rates observed at high-redshift (Solomon & Vanden Bout 2005; Erb 2008; Swinbank et al. 2010).

In any case, whether the gas shock-heats to the halo virial temperature and cools slowly ("hot mode"), or flows preferentially along cold filamentary streams ("cold mode"), the cold gas will eventually collapse and fragment due to gravitational instabilities, and form stars (e.g., Larson 1978; Klessen et al. 1998; Clark et al. 2011). This star formation results in the growth of galactic bulges, and in the innermost regions, the gas could also be accreted onto a super-massive black hole (SMBH), powering an active galactic nucleus (AGN). Many theories suggest that star-formation and/or black hole accretion could be self-regulating (e.g., Silk & Rees 1998; Fabian 1999; King 2003). In this case, "feedback" processes from stars and AGNs themselves would inject energy back into the interstellar medium (ISM), heating the gas, and preventing further star-formation or accretion to take place. In particular, stars interact with the surrounding gas through photo-heating, stellar winds, radiation pressure, and supernova explosions (e.g., Larson 1974; Dekel & Silk 1986). AGN feedback involves higher energies, and it could be strong enough to be able to remove the reservoir of cold gas needed for later star formation or accretion (e.g., Somerville et al. 2008). These feedback processes could result in a galactic wind (Veilleux et al. 2005 and references therein), now ubiquitously observed at low and high redshifts (e.g., Heckman et al. 1990; Martin et al. 2012; Rubin et al. 2014).

The complex interplay between gas accreted from the IGM and galactic outflows, which may be signatures of mechanical/radiative feedback, are poorly understood. This happens particularly at high-redshift, where the feedback processes are often considered to be more intense. These processes conspire to determine the structure of the so-called circumgalactic medium (CGM), which comprises the interface between galaxies and the IGM.

In the following Section (§1.1) I will introduce the main characteristics of the Lyα line. In Sections §1.2 and §1.3, I briefly summarize the main results from previous extensive research that has been carried out on the IGM and CGM at $z \sim 2-3$. This epoch is of particular interest since, as said previously, baryons mostly reside in these media, and star formation and AGN activity are at their peak (e.g., Schmidt et al. 1995; Hopkins & Beacom 2006; Madau & Dickinson 2014).

1.1 THE LYα LINE

The Lyα line (λ = 1215.67 Å) plays a fundamental role in the observations and study of several astrophysical phenomena, particularly at high redshift. As the Lyα line is in the far-ultraviolet, its emission is visible from the ground only for $z \gtrsim 1.6$. A Lyα photon ($h\nu_{\mathrm{Ly}\alpha}$ = 10.2 eV) is emitted by a hydrogen atom in the resonant transition $2p \rightarrow 1s$. It is the strongest H I line, characterized by an Einstein coefficient $A_{2p\rightarrow 1s} = 6.265\times 10^{8}\ \mathrm{s}^{-1}$, i.e. the transition occurs almost instantaneously (radiative lifetime of $1/A_{2p\rightarrow 1s} = 1.59$ ns). The Lyα photons should be subject to substantial resonant scattering under most astrophysical conditions (e.g., Gould & Weinberg 1996). Indeed, the Lyα optical depth at the line center, which gives a rough estimate of the number of scatterings experienced by a photon, can be written as (e.g., Draine 2011)

$$\tau_0(\mathrm{Ly}\alpha) = 8.02\times 10^{4}\left(\frac{15\ \mathrm{km\,s^{-1}}}{b}\right)\tau(\lambda) \tag{1.4}$$

where b is the Doppler broadening parameter, which includes both thermal and turbulent gas motions ($b = \sqrt{v^2_{\mathrm{thermal}} + v^2_{\mathrm{turb}}}$), and $\tau(\lambda)$ is the optical depth for ionizing photons for $\lambda \leq \lambda_{\mathrm{LL}}$. The optical depth is given by

$$\tau(\lambda) \;=\; N_{\mathrm{HI}}\sigma_{\mathrm{pi}} \approx N_{\mathrm{HI}}\,\sigma_0\left(\frac{h\nu}{I_{\mathrm{H}}}\right)^{-3} = \left(\frac{N_{\mathrm{HI}}}{10^{17.2}\ \mathrm{cm^{-2}}}\right)\left(\frac{\lambda}{912\text{Å}}\right)^{3} \tag{1.5}$$

where $\sigma_{\mathrm{pi}} \approx \sigma_0\left(\frac{h\nu}{I_{\mathrm{H}}}\right)^{-3}$ is the photoionization cross section, $\sigma_0 = 6.304\times 10^{-18}\ \mathrm{cm}^2$ is the cross section at 912 Å, and $I_{\mathrm{H}} = 13.6$ eV is the ionization potential of hydrogen. The quoted value $N_{\mathrm{HI}} = 10^{17.2}\ \mathrm{cm}^{-2}$ corresponds to $\tau = 1$, and thus defines two regimes: an optically thin regime ($N_{\mathrm{HI}} \ll 10^{17.2}\ \mathrm{cm}^{-2}$) and an optically thick regime ($N_{\mathrm{HI}} \gg 10^{17.2}\ \mathrm{cm}^{-2}$) to the ionizing continuum.

From eqn. (1.4) and (1.5), it is clear that the Lyα optical depth is large. A cloud would be optically thin to Lyα photons ($\tau_0(\mathrm{Ly}\alpha) < 1$), i.e. transparent to Lyα photons, only for low neutral hydrogen column densities ($N_{\mathrm{HI}} \lesssim 10^{14}\ \mathrm{cm}^{-2}$). Therefore, a Ly$\alpha$ photon typically experiences a large amount of scattering (i.e. it is reabsorbed and reemitted in a different direction) before escaping the system.

This process makes the study of the Lyα line very complex for different reasons[5]. First, resonant scattering leads to double-peaked emission line profiles, as Lyα photons must diffuse in velocity space far from the line center to be able to escape the system (e.g. Neufeld 1990; Gould & Weinberg 1996; Cantalupo et al. 2005; Dijkstra et al. 2006a,b; Verhamme et al. 2006). In particular, after a scattering event, the photon's frequency remains unchanged in the center-of-mass frame of the interacting hydrogen atom and photon. Nevertheless, as the hydrogen atoms have velocities, each Lyα photon experiences a random walk in frequency. This results in the photon being moved towards the line wings, where the optical depth is smaller, and thus the probability of escaping the nebula is higher (Draine 2011). Further, when combined with kinematic effects, the shape of the Lyα line can be even more altered (e.g., Verhamme et al. 2006). Resonant scattering could also lead to an increase of the observed size on the plane of the sky for both point sources and extended sources (e.g., Steidel et al. 2011), and thus modify significantly the morphology of a system depending on its geometry. Another problem, given this large number of scattering, is that the Lyα line is highly subject to absorption by dust, if present. However, dust absorption has been shown to be highly dependent on the geometry of the system. For example, a clumpy dust distribution could result in a boost of the Lyα equivalent width (EW), since continuum photons would be absorbed by dust, while the Lyα photons would eventually escape the system after having resonantly scattered (e.g., Neufeld 1991; Hansen & Oh 2006; Finkelstein et al. 2007, 2008). Thus, a complete understanding and analysis of the Lyα line requires careful radiative transfer calculations for most of the astrophysical systems. However, if a non-resonant tracer (e.g. the Hα line) is available, a comparison with the Lyα line could rule out the presence of strong contributions from resonant scattering, enabling a better characterization of the system.

---

[5] This is even more accentuated in systems where the Lyα line is the only tracer available.

1.2 ABSORPTION LINE STUDIES

As is clear from the foregoing introduction, to understand the global picture of galaxy formation, the complex interactions between galaxies and AGNs with the IGM/CGM, which are feeding them, should be treated simultaneously. For decades, the preferred technique for characterizing the IGM and the CGM has been the analysis of absorption features along background sight lines (e.g., Meiksin 2009; Hennawi & Prochaska 2013, and references therein).

1.2.1 IGM

A detailed review on the IGM studies is given by Meiksin (2009, and references therein). Here, I will briefly summarize only the physical properties needed for a better understanding of the subsequent Chapters, and I will not attempt to describe the large amount of detailed studies aimed at constraining cosmological parameters (e.g., Schaye et al. 2000; Weinberg et al. 2003; White et al. 2010; Rorai et al. 2013; Font-Ribera et al. 2014; Lee et al. 2015).

It was realized very early that the presence of the IGM would lead to absorption features in the spectra of bright background sources (Bahcall & Salpeter 1965; Lynds 1971; Sargent 1980), e.g. QSOs. The distinct pattern of a wealth of absorption lines short-ward of the Lyα emission of a QSO[6] is known as Lyα forest. It originates from the intervening neutral hydrogen atoms, which scatter out of the line-of-sight the Lyα line photons (Meiksin 2009). The absorption features visible within the Lyα forest are usually divided into three categories, based on the 'strength' of the absorption, i.e. on the amount of neutral hydrogen, and hence on their physical origin. Firstly,

---

[6] Or any other bright high-redshift object, e.g. also afterglow of γ-ray bursts can show this absorption features (e.g., Vreeswijk et al. 2004).

Table 1.1. Summary of absorption line system properties (adapted from Meiksin 2009).

	$N_{\rm HI}$ (cm^{-2})	b (km s^{-1})	$n_{\rm H}^*$ (cm^{-3})	T^* (K)	Z^{*a}
Lyα forest	$\lesssim 10^{17.2}$	15 – 60	10^{-8} – 10^{-3}	5000 – 50000	-4 to -2
LLS	$10^{17.2}$ – 10^{19}	~ 15*	~ 10^{-3} – 10^{-2}	~ 30000	-4 to -2
SLLS	10^{19} – $10^{20.3}$	~ 15*	~ 10^{-2}	~ 10000	-1 to +0.6
DLA	$> 10^{20.3}$	~ 15	~ 10^{-2} – 10	10000 – 100	-1.5 to -0.8

[*] Values not well constrained by the observations. The ranges shown are approximate.

[a] Metallicity quoted as the logarithmic fraction of the solar metallicity $Z_\odot$.

the properly called Lyα forest systems are optically thin absorbers ($N_{\rm HI} \lesssim 10^{17.2}$ cm^{-2}), which are currently estimated to arise from gas clouds in the filamentary IGM (e.g., Cen et al. 1994; Lukić et al. 2015). Secondly, Lyman limit systems (LLS) are stronger absorption systems. They are characterized by $N_{\rm HI} \gtrsim 10^{17.2}$ cm^{-2}, and are thus optically thick to the ionizing radiation. Indeed, LLSs are recognized by the abrupt absorption short-ward of their Lyman break, and by the shape of the flux recovery at shorter wavelengths. It has been suggested that they probe the optically thick part of the accreting IGM, or, given the presence of associated metal absorptions, also the reprocessed CGM of galaxies (e.g., Lehner et al. 2013). Finally, the so-called damped Lyα systems (DLAs; Wolfe et al. 1986; Prochaska & Wolfe 2009) have very high neutral column densities, i.e. $N_{\rm HI} > 10^{20.3}$ cm^{-2}, and are thus easily recognized by the distinctive strong absorption features with Lorentzian damping wings. DLAs are considered to be the footprints of galaxies along the line-of-sight (e.g., Wolfe et al. 1986), but the direct observation of their emitting counterparts turned out to be challenging (e.g., Moller & Warren 1993; Wolfe et al. 2005; Krogager et al. 2012; Fumagalli et al. 2015 and references therein). Sometimes, absorbers with 10^{19} cm^{-2} $< N_{\rm HI} < 10^{20.3}$ cm^{-2} are referred to as super Lyman limit systems (SLLSs) or sub-damped systems, because they start to show the damping wings, and thus their column densities can be more firmly estimated (Wolfe et al. 2005).

The observed and derived physical properties of these systems are summarized in Table 1.1, adapted from Meiksin (2009). With the exception of DLAs, where gas is mainly neutral, in the rest of QSO absorbers, hydrogen is ionized. Note that some of the quantities in this table are poorly constrained (for further details, see Meiksin 2009, and references therein).

1.2.2 CGM

As discussed earlier, the CGM is the complex interface between the IGM and the galaxies themselves. A significant amount of effort has been devoted to the study of this phase for galaxies close to QSO sightlines at $z \sim 2-3$. The absorption features arising in the QSO spectra due to the intervening CGM (Bahcall & Salpeter 1965) can be used to study the interplay between outflows and accretion.

As mentioned in the previous Section, a first approach is to search for galaxy counterparts to strong DLA (e.g., Djorgovski et al. 1996), resulting, by construction, in a biased sample towards high metallicities. This method seems to be able to distinguish both the accreting gas (Bouché et al. 2013), and the outflowing gas (e.g., Noterdaeme et al. 2012; Péroux et al. 2013), yet with some uncertainties. Another approach is to look for galaxies close to QSO sightlines, but without any absorption pre-selection. A precise redshift measurement is essential to link an absorption feature in the QSO spectra to a galaxy close by. For this reason, high redshift studies have mostly focused on the brightest galaxies, for which z can be better constrained. Specifically, several works targeted the so-called Lyman break galaxies (LBGs), star-forming galaxies selected by a drop-out technique (e.g., Steidel & Hamilton 1993). Regarding the hydrogen spatial distribution, Adelberger et al. (2003, 2005) have shown that the H I Lyα absorption at $z \sim 3$ is in excess (in comparison to the mean absorption level) out to $5\,h^{-1}$ Mpc of galaxies, while it decreases significantly within $1\,h^{-1}$ Mpc. Although these results need to be verified (e.g., Kawata & Rauch 2007; Crighton et al. 2011), they suggest clustering of H I gas around high-redshift galaxies, which is then ionized (heated) at smaller scales. After this work, expensive spectroscopic and imaging surveys of LBGs have been conducted (Steidel et al. 2010; Crighton et al. 2011; Rakic et al. 2012; Rudie et al. 2012) in order to characterize the gas present in the CGM of these galaxies. These studies have found that typical star-forming galaxies exhibit a modest $\sim 20\%$ covering factor of optically thick neutral hydrogen (Rudie et al. 2012), while regarding the metal distribution, enrichment levels ranging from extremely metal-poor ($\sim 10^{-2}\,Z_{\odot}$, Crighton et al. 2013) to nearly solar ($0.1-0.6\,Z_{\odot}$, Crighton et al. 2015) have been found. Moreover, metal-enriched gas can be track down to large distances from the galaxies studied. In particular, a C IV-galaxy cross correlation study has shown evidence for the presence of metals out to 300 kpc (Adelberger et al. 2003, 2005), while Steidel et al. (2010) used galaxy pairs to demonstrate that $z \sim 2-3$ galaxies show metal-enriched gas out to $\sim$ 125 kpc. Finally, Turner et al. (2014) confirm the presence of metals out to at least 180 kpc, with high ionization species (e.g. C IV) possibly extending out to even larger distances ($\sim$ Mpc).

On the other hand, using projected QSO pairs, Hennawi et al. (2006) launched the innovative technique of studying a foreground quasar CGM by analyzing the spectrum of a background quasar, initiating the Quasars Probing Quasars survey(Hennawi & Prochaska 2007; Prochaska

& Hennawi 2009; Hennawi & Prochaska 2013; Prochaska et al. 2013a,b, 2014). In this way, it is possible to study the gas properties on scales of a few 10 kpc to several Mpc of the much more massive dark matter halos ($\sim 10^{12.5}$ $M_{\odot}$, White et al. 2012) traced by quasars. These studies have revealed a massive ($\gtrsim 10^{10}$ $M_{\odot}$) reservoir of cool ($T \simeq 10^4$ K) gas in the CGM of massive halos (see also Bowen et al. 2006; Farina et al. 2013). This result appears to be in conflict with predictions from hydrodynamical zoom-in simulations of galaxy formation (e.g., Fumagalli et al. 2014), in which the gas present in these massive halos is preferentially shock heated. This gas, traced by optically thick absorbers, shows high covering factors $f_C > 0.6$, and appears to be metal enriched, with absorption in the C II and C IV lines out to ≈ 200 kpc. Furthermore, Hennawi & Prochaska (2007) interpreted the lack of optically thick absorption along the line-of-sight, as compared to the absorption in the transverse direction, as evidence for the anisotropic illumination by the quasar: the gas clouds along the line-of-sight are probably highly ionized, being illuminated by the QSO. Finally, Prochaska & Hennawi (2009) carried out a detailed photoionization modeling of an optically thick system ($N_{\rm HI} \approx 10^{19.7}$) coincident with the foreground quasar redshift to estimate the physical properties of the CGM. They found that this system has nearly solar metallicity, its gas is predominantly ionized ($T \lesssim 20000$ K), and with a volume density $n_{\rm H} \simeq 1\,{\rm cm}^{-3}$ at an impact parameter of $R_{\perp} = 108$ kpc. Using the column density and volume density values, it is trivial to see that this system shows small characteristic sizes $\sim 10 - 100$ pc for the absorbing clouds. However, this was the analysis of one particular system. Photoionization modeling of a large sample of absorbers in the quasar's CGM seems to indicate that typical gas densities are much lower $n_{\rm H} \sim 0.01 \ll 1\,{\rm cm}^{-3}$ (Lau et al. 2015), although with large uncertainties due to the unknown radiation field.

1.3 EMISSION LINE STUDIES

As mentioned previously, the IGM and CGM have been preferentially studied through absorption features along background sight lines. However, absorption studies are limited both by the rarity of suitably bright background sources, and by the one-dimensional information that they provide[7]. Therefore, these studies need to be complemented by direct observations of the medium in emission. In particular, it has been shown that UV background radiation could be reprocessed by these media, and be detectable as fluorescent Lyα emission, i.e. recombinations that result in Lyα photons (Hogan & Weymann 1987; Binette et al. 1993; Gould & Weinberg 1996; Cantalupo et al. 2005). However, current facilities are still not capable of revealing such low radiation levels, e.g. an expected surface brightness (SB) of the order of ${\rm SB}_{{\rm Ly}\alpha} \sim 10^{-20}$ erg s^{-1} cm^{-2} arcsec^{-2} (see e.g. Rauch et al. 2008). Nonetheless, this signal can be boosted by orders of magnitude, and thus reach observable levels ($\mathrm{SB}_{\mathrm{Ly}\alpha} \sim 10^{-19} - 10^{-18}\,\mathrm{erg\,s^{-1}\,cm^{-2}\,arcsec^{-2}}$), by the intense ionizing flux of a nearby quasar, which, like a flashlight, illuminates the gas in its surroundings (Rees 1988; Haiman & Rees 2001; Alam & Miralda-Escudé 2002; Cantalupo et al. 2012). Thus, notwithstanding the well understood difficulties implied by the use of the Lyα line (see §1.1 and references therein), several studies have tried to confirm this picture, and study the CGM and IGM in emission.

---

[7] However Lee et al. 2014 used the information enclosed in the Lyα forest of bright high-redshift galaxies to reconstruct the three-dimensional absorption field at $z \sim 2.3$.

1.3.1 CHRONICLE OF LYα SURVEYS

Before being able to detect the faint signal from the diffuse IGM and CGM gas, we had to become experts in detecting the galaxies themselves at high-redshift. Everything started with the prediction by Partridge & Peebles (1967a,b) that star-forming galaxies should be easily identified by the Lyα emission and the Lyman break. However, early attempts using photometric plates and photoelectric photometry were unsuccessful, given their low sensitivity (Partridge 1974; Davis & Wilkinson 1974). One of the first successful Lyα line results was the redshift spectroscopic determination of high-redshift radio galaxies (HzRGs), initially discovered because of their strong radio emission (e.g., Spinrad et al. 1985; McCarthy 1993 and references therein). Objects at $z \gtrsim 5$ were discovered using this method (van Breugel et al. 1999), and also serendipitously (Dey et al. 1998; Stern & Spinrad 1999 and references therein).

The first Lyα imaging surveys using narrow-band filters resulting in small samples of Lyα emitting galaxies were conducted with 4m class telescopes in fields with known QSOs or to identify known QSO absorption systems (e.g., Djorgovski et al. 1985; Schneider et al. 1986; Hu & Cowie 1987; Steidel et al. 1991; Lowenthal et al. 1991). However, in this same period, some studies reported null detections due to still low sensitivity for the used technique (e.g., Hu & Cowie 1987; Lowenthal et al. 1990). The 1990s and the early 2000s were the benchmark to new observations and possibilities. The game changer was the advent of large CCDs and the 8-10m class telescopes. Lyα surveys were not only able to uncover larger samples of galaxies (e.g., Hu & McMahon 1996; Cowie & Hu 1998; Thommes et al. 1998; Hu et al. 1998; Kudritzki et al. 2000; Kurk et al. 2000; Malhotra & Rhoads 2002), but with the higher sensitivity achieved, large-scale ($\sim$ hundreds of kpc) Lyα emitting objects or regions were discovered. This marked the starting point for the study of the CGM and IGM in emission.

1.3.1.1 GIANT LYα NEBULAE

The new high performing facilities and instruments available since the late 1990s have encouraged several studies which specifically search for the fluorescence signal from the IGM, in particular in proximity to a quasar (e.g., Fynbo et al. 1999; Francis & Bland-Hawthorn 2004; Cantalupo et al. 2007; Rauch et al. 2008; Hennawi & Prochaska 2013). So far, the interpretation of these studies, resulting most of the time in non-detections or in questionable detections, is not straightforward. However, recently Cantalupo et al. (2012) identified a population of compact Lyα emitters with rest-frame equivalent widths exceeding the maximum value expected from star-formation, $EW_0^{\mathrm{Ly}\alpha} > 240$ Å (e.g., Charlot & Fall 1993). These are, up to date, the best candidates for fluorescent emission powered by a nearby quasar. Besides illuminating nearby clouds in the IGM, a quasar, or any other AGN, can irradiate gas in its own host galaxy or CGM, making the detection and characterization of this diffuse and elusive component possible.

In table 1.2, I list the largest and brightest Lyα nebulae known at high-z, with the exception of the new discoveries studied in this work[8]. The size and total luminosity quoted have been homogenized to the same standard ΛCDM cosmology ($\Omega_{\mathrm{M}} = 0.3$, $\Omega_\Lambda = 0.7$, $h = 0.7$). Note that these quantities are highly dependent on the corresponding survey's sensitivity, e.g. the size of a Lyα nebula is frequently reported as the maximum extent of the 2σ isophote. In the following Sections, I briefly review the extended Lyα emission around QSOs, around high-redshift radio galaxies (HzRGs), and in Lyα blobs (LABs).

---

[8] I tried to be as exhaustive as possible in the literature search, however I cannot claim the list is complete, especially regarding the largest sample of HzRGs.

Table 1.2. List of the largest and brightest Lyα nebulae in the literature. The data are homogenized to the same cosmology, i.e the standard ΛCDM cosmology ($\Omega_M = 0.3$, $\Omega_\Lambda = 0.7$, $h = 0.7$). Nebulae discovered in this work are not listed here.

Name	Type[a]	z	$d^{b}_{\mathrm{Ly}\alpha}$ (kpc)	$L_{\mathrm{Ly}\alpha}$ (10^{43} erg s^{-1})	References
MRC1138-262	HzRG	2.16	263	275.4	Kurk et al. (2002); Venemans et al. (2007)
4C41.17	HzRG	3.798	190	139.7	Reuland et al. (2003, 2007)
4C03.24 (or 1243+036)	HzRG	3.6	155	41.8	van Ojik et al. (1996, 1997)
TNJ1338-1942	HzRG	4.11	140	51.4	De Breuck et al. (1999); Venemans et al. (2007); Swinbank et al. (2015)
1707+105	HzRG	2.357	139	3.9	Roettgering et al. (1997); van Ojik et al. (1997)
B3J2330+3927	HzRG	3.087	139	28.6	Matsuda et al. (2009)
0828+193	HzRG	2.572	136	9.9	Villar-Martín et al. (2002, 2003a)
MRC2104-242	HzRG	2.491	129	0.9	Villar-Martín et al. (2003a, 2006)
1558-003	HzRG	2.527	120	13.1	Villar-Martín et al. (2003a, 2007a)
4C48.48 (or 1931+480)	HzRG	2.343	117	23.8	Chambers et al. (1996); Villar-Martín et al. (2003a); Sánchez & Humphrey (2009)
TXS0211-122	HzRG	2.333	113	1.4	van Ojik et al. (1997); Villar-Martín et al. (2003a); Humphrey et al. (2013)
0355-037	HzRG	2.156	108	1.5	Roettgering et al. (1997); van Ojik et al. (1997)
0828+193	HzRG	2.577	107	6.3	Roettgering et al. (1997); van Ojik et al. (1997)
3C294	HzRG	1.786	106	37.6	McCarthy et al. (1990)
1410-001	HzRG	2.36	104	10.2	Villar-Martín et al. (2003a)
BRL1602-174	HzRG	2.04	97	84.9	Venemans et al. (2007)
0731+438	HzRG	2.429	95	11.2	Villar-Martín et al. (2003a)
6C1232+39	HzRG	3.22	90	10.4	Eales et al. (1993)
4C23.56 (or 2105+236)	HzRG	2.479	86	7.2	Knopp & Chambers (1997); Villar-Martín et al. (2003a)
MG2141+192(B1950)	HzRG	3.594	85	14.9	Maxfield et al. (2002)
1410-001	HzRG	2.366	82	12.2	Roettgering et al. (1997); van Ojik et al. (1997)
1558-003	HzRG	2.531	80	6.5	Roettgering et al. (1997); van Ojik et al. (1997)
B20902+34	HzRG	3.395	79	58.0	Reuland et al. (2003, 2007)
4C40.36 (or 1809+407)	HzRG	2.265	78	1.5	Chambers et al. (1996); Villar-Martín et al. (2003a); Sánchez & Humphrey (2009)
0140-257	HzRG	2.64	76	2.4	Villar-Martín et al. (2007a)
0200+015	HzRG	2.231	74	5.0	Roettgering et al. (1997); van Ojik et al. (1997)
MRC2048-272	HzRG	2.06	71	7.2	Venemans et al. (2007)
4C60.07	HzRG	3.791	68	136.4	Reuland et al. (2003, 2007)
0943-242	HzRG	2.922	66	1.2	Villar-Martín et al. (2003a)
0748+134	HzRG	2.424	62	2.9	Roettgering et al. (1997); van Ojik et al. (1997)
2025-218	HzRG	2.63	51	14.2	Villar-Martín et al. (2007a)
MRC0943-242	HzRG	2.92	49	27.9	Venemans et al. (2007)
0214+183	HzRG	2.133	49	0.6	Roettgering et al. (1997); van Ojik et al. (1997)
1545-234	HzRG	2.754	47	3.3	Roettgering et al. (1997); van Ojik et al. (1997)
1357+007	HzRG	2.678	47	3.6	Roettgering et al. (1997); van Ojik et al. (1997)
0529-549	HzRG	2.575	47	2.5	Roettgering et al. (1997); van Ojik et al. (1997)
0417-181	HzRG	2.775	44	1.5	Roettgering et al. (1997); van Ojik et al. (1997)
MRC0316-257	HzRG	3.13	40	8.1	Venemans et al. (2007)
TNJ2009-3040	HzRG	3.16	40	34.4	Venemans et al. (2007)
2202+128	HzRG	2.708	38	4.2	Roettgering et al. (1997); van Ojik et al. (1997)
MRC0052-241	HzRG	2.86	33	8.6	Venemans et al. (2007)
TNJ0924-2201	HzRG	5.20	13	1.8	Venemans et al. (2007)
Q0805+046	QSO-R	2.877	116	62.8	Heckman et al. (1991a,b)
Q0758+097	QSO-R	2.683	110	10.5	Heckman et al. (1991a,b)
Q0445+097	QSO-R	2.113	106	7.3	Heckman et al. (1991a,b)
Q2222+051	QSO-R	2.328	104	7.4	Heckman et al. (1991b)
Q0941+261	QSO-R	2.913	99	6.4	Heckman et al. (1991a,b)
Q0017+154	QSO-R	2.012	97	12.9	Heckman et al. (1991b)
Q1318+113	QSO-R	2.176	96	25.0	Heckman et al. (1991a,b)

Table 1.2 (cont'd)

Name	Type^{a}	z	$d^{b}_{\mathrm{Ly}\alpha}$ (kpc)	$L_{\mathrm{Ly}\alpha}$ (10^{43} erg s^{-1})	References
Q2338+042	QSO-R	2.594	94	15.4	Heckman et al. (1991b); Lehnert & Becker (1998)
Q0730+257	QSO-R	2.686	93	5.3	Heckman et al. (1991b)
TXS1436+157	QSO-R	2.537	92	4.6	Roettgering et al. (1997); van Ojik et al. (1997); Humphrey et al. (2013)
Q1658+575	QSO-R	1.979	89	9.9	Heckman et al. (1991b)
Q1354+258	QSO-R	2.032	88	21.1	Heckman et al. (1991b)
Q2150+053	QSO-R	2.323	87	7.4	Heckman et al. (1991b)
Q1345+258	QSO-R	2.039	79	26.8	Heckman et al. (1991b)
Q0225-014	QSO-R	2.037	44	5.3	Heckman et al. (1991b)
Q0109+176	QSO-R	2.157	26	1.5	Heckman et al. (1991b)
Jackpot	4 QSOs	2.04	310	21.0	Hennawi et al. (2015)
J2233-606	QSO	2.238	105	13.6	Bergeron et al. (1999)
J0049+3510	QSO	2.48	85	35.4	Barrio et al. (2008)
NDFWSJ143725.0+351048	QSO	2.332	80*	5.3	Yang et al. (2009)
BR1033-0327	QSO	4.510	70	2.4	North et al. (2012); Courbin et al. (2008)
AMS05	QSO	2.85	66	2.7	Smith et al. (2009)
Q1759+7539	QSO	3.049	65	9.0	Christensen et al. (2006)
SDSSJ21474-0838	QSO	4.510	56	23.2	North et al. (2012)
SDSSJ14472+0401	QSO	4.510	42	0.2	North et al. (2012)
Q1205-30	QSO	3.04	40	6.3	Weidinger et al. (2004, 2005); Fynbo et al. (2000)
SDSSJ1240+1455	QSO	3.113	40	4.2	Matsuda et al. (2011)
PKS1614+051	QSO	3.21	40	10.3	Matsuda et al. (2011)
0054-284	QSO	3.616	38	0.8	Bremer et al. (1992)
Q1425+606	QSO	3.204	37	10.1	Christensen et al. (2006)
0055-264	QSO	3.656	30	1.1	Bremer et al. (1992)
Q1451+122	QSO	3.253	16	1.9	Christensen et al. (2006)
CFHQSJ2329-0301^{c}	QSO	6.417	16	4.3	Goto et al. (2009); Willott et al. (2011); Goto et al. (2012)
Q0953+4749	QSO	4.489	14	0.8	Christensen et al. (2006); Bunker et al. (2003)
Q2233+131	QSO	3.301	11	1.2	Christensen et al. (2006)
SDSSJ2228+0110^{c}	QSO	5.95	9	1.2	Roche et al. (2014)
Himiko	LAE	6.595	18	4.6	Ouchi et al. (2009)
K-LAE	LAE	6.538	15	1.3	Kashikawa et al. (2012)
SSA22-Sb1-LAB1	LAB	3.099	187	9.2	Steidel et al. (2000); Matsuda et al. (2004, 2011)
SSA22-Sb6-LAB1	LAB	3.094	178	6.6	Matsuda et al. (2011)
LABd05	LAB	2.7	169	19.2	Dey et al. (2005)
SSA22-Sb1-LAB2	LAB	3.091	168	7.7	Steidel et al. (2000); Matsuda et al. (2004, 2011); Martin et al. (2014c)
SSA22-Sb5-LAB1	LAB	3.1	157	4.3	Matsuda et al. (2011)
SSA22-Sb3-LAB1	LAB	3.099	135	23.2	Matsuda et al. (2011)
GOODS-N-LAB1	LAB	3.075	133	6.1	Matsuda et al. (2011)
SSA22-Sb2-LAB1	LAB	3.1	130	2.8	Matsuda et al. (2011)
SSA22-Sb2-LAB2	LAB	3.1	123	1.6	Matsuda et al. (2011)
SSA22-Sb1-LAB5	LAB	3.1	118	1.5	Matsuda et al. (2011)
SSA22-Sb5-LAB2	LAB	3.1	115	2.4	Matsuda et al. (2011)
SSA22-Sb6-LAB4	LAB	3.116	114	2.3	Matsuda et al. (2011)
SSA22-Sb1-LAB3	LAB	3.096	110	5.9	Matsuda et al. (2011)
SXDS-N-LAB1	LAB	3.1	108	3.8	Matsuda et al. (2011)
SSA22-Sb1-LAB16	LAB	3.104	108	0.9	Matsuda et al. (2011)
LAB2330+3922	LAB	3.087	106	4.5	Matsuda et al. (2009)
J2143-4423-B1	LAB	2.38	100	3.5	Francis et al. (1996, 2001); Palunas et al. (2004)
PRG2	LAB	2.267	99	1.9	Prescott et al. (2013)

Table 1.2 (cont'd)

Name	Type[a]	z	$d_{\mathrm{Ly}\alpha}$[b] (kpc)	$L_{\mathrm{Ly}\alpha}$ (10^{43} erg s^{-1})	References
SJ-LAB	LAB	2.83	92	22.3	Smith & Jarvis (2007)
NDFWSJ143059.0+353324	LAB	2.319	80*	2.7	Yang et al. (2009)
PRG1	LAB	1.673	78	0.8	Prescott et al. (2013, 2009)
PRG3	LAB	2.137	74	0.4	Prescott et al. (2013)
CDFS-LAB01	LAB	2.3	73*	7.8	Yang et al. (2010)
P96-19	LAB[d]	2.39	69	2.3	Keel et al. (1999)
P96-18	LAB[d]	2.39	69	5.5	Keel et al. (1999)
J2143-4423-B6	LAB	2.38	65	0.7	Palunas et al. (2004)
J2143-4423-B5	LAB	2.38	65	0.8	Palunas et al. (2004)
SSA22-Sb1-LAB4	LAB	3.1	65*	3.8	Matsuda et al. (2004)
J2143-4423-B7	LAB	2.38	61	0.4	Palunas et al. (2004)
CDFS-LAB03	LAB	2.3	61*	3.2	Yang et al. (2010)
NDFWSJ143057.8+353431	LAB	2.318	60*	1.6	Yang et al. (2009)
GOODS-S-LAB	LAB	3.16	60	1.0	Nilsson et al. (2006); Prescott et al. (2015b)
CDFS-LAB02	LAB	2.3	57*	3.3	Yang et al. (2010)
SSA22-Sb1-LAB6	LAB	3.1	56*	1.6	Matsuda et al. (2004)
SSA22-Sb1-LAB7	LAB	3.1	54*	1.5	Matsuda et al. (2004)
SSA22-Sb1-LAB8	LAB	3.1	54*	1.7	Matsuda et al. (2004)
SSA22-Sb1-LAB9	LAB	3.1	53*	1.3	Matsuda et al. (2004)
CDFS-LAB04	LAB	2.3	51*	2.6	Yang et al. (2010)
SSA22-Sb1-LAB10	LAB	3.1	50*	2.2	Matsuda et al. (2004)
NDFWSJ142503.4+345854	LAB	2.321	50*	2.3	Yang et al. (2009)
SSA22-Sb1-LAB11	LAB	3.1	47*	0.9	Matsuda et al. (2004)
SSA22-Sb1-LAB12	LAB	3.1	46*	0.9	Matsuda et al. (2004)
SSA22-Sb1-LAB13	LAB	3.1	45*	1.0	Matsuda et al. (2004)
SSA22-Sb1-LAB14	LAB	3.1	44*	1.2	Matsuda et al. (2004)
SSA22-Sb1-LAB15	LAB	3.1	43*	2.2	Matsuda et al. (2004)
SSA22-Sb1-LAB16	LAB	3.1	43*	9.9	Matsuda et al. (2004)
CDFS-LAB05	LAB	2.3	43*	1.7	Yang et al. (2010)
SSA22-Sb1-LAB17	LAB	3.1	42*	1.4	Matsuda et al. (2004)
CDFS-LAB08	LAB	2.3	41*	1.2	Yang et al. (2010)
SSA22-Sb1-LAB18	LAB	3.1	40*	0.6	Matsuda et al. (2004)
CDFS-LAB07	LAB	2.3	40*	1.5	Yang et al. (2010)
SSA22-Sb1-LAB20	LAB	3.1	39*	0.6	Matsuda et al. (2004)
SSA22-Sb1-LAB19	LAB	3.1	39*	1.3	Matsuda et al. (2004)
SSA22-Sb1-LAB22	LAB	3.1	38*	0.8	Matsuda et al. (2004)
SSA22-Sb1-LAB21	LAB	3.1	38*	0.8	Matsuda et al. (2004)
CDFS-LAB06	LAB	2.3	38*	1.5	Yang et al. (2010)
SSA22-Sb1-LAB25	LAB	3.1	37*	0.6	Matsuda et al. (2004)
SSA22-Sb1-LAB24	LAB	3.1	37*	0.7	Matsuda et al. (2004)
SSA22-Sb1-LAB23	LAB	3.1	37*	0.9	Matsuda et al. (2004)
SSA22-Sb1-LAB28	LAB	3.1	36*	2.2	Matsuda et al. (2004)
SSA22-Sb1-LAB27	LAB	3.1	36*	0.7	Matsuda et al. (2004)
SSA22-Sb1-LAB26	LAB	3.1	36*	0.6	Matsuda et al. (2004)
SSA22-Sb1-LAB32	LAB	3.1	35*	0.6	Matsuda et al. (2004)
SSA22-Sb1-LAB31	LAB	3.1	35*	1.1	Matsuda et al. (2004)
SSA22-Sb1-LAB30	LAB	3.1	35*	0.9	Matsuda et al. (2004)
SSA22-Sb1-LAB29	LAB	3.1	35*	0.7	Matsuda et al. (2004)
COSMOS-LAB01	LAB	2.3	35*	1.2	Yang et al. (2010)

Table 1.2 (cont'd)

Name	Type[a]	z	$d^{b}_{\mathrm{Ly}\alpha}$ (kpc)	$L_{\mathrm{Ly}\alpha}$ (10^{43} erg s^{-1})	References
CDFS-LAB09	LAB	2.3	35^{*}	1.2	Yang et al. (2010)
SSA22-Sb1-LAB35	LAB	3.1	34^{*}	0.9	Matsuda et al. (2004)
SSA22-Sb1-LAB34	LAB	3.1	34^{*}	0.7	Matsuda et al. (2004)
SSA22-Sb1-LAB33	LAB	3.1	34^{*}	0.9	Matsuda et al. (2004)
CDFS-LAB12	LAB	2.3	34^{*}	1.0	Yang et al. (2010)
CDFN-LAB01	LAB	2.3	34^{*}	1.3	Yang et al. (2010)
PRG4	LAB	1.888	33	0.3	Prescott et al. (2013)
COSMOS-LAB03	LAB	2.3	33^{*}	0.8	Yang et al. (2010)
CDFS-LAB14	LAB	2.3	33^{*}	0.9	Yang et al. (2010)
CDFS-LAB10	LAB	2.3	33^{*}	1.1	Yang et al. (2010)
CDFN-LAB04	LAB	2.3	33^{*}	0.9	Yang et al. (2010)
COSMOS-LAB04	LAB	2.3	32^{*}	1.0	Yang et al. (2010)
COSMOS-LAB02	LAB	2.3	32^{*}	0.9	Yang et al. (2010)
CDFS-LAB15	LAB	2.3	32^{*}	0.9	Yang et al. (2010)
CDFS-LAB13	LAB	2.3	32^{*}	1.0	Yang et al. (2010)
CDFN-LAB03	LAB	2.3	32^{*}	1.0	Yang et al. (2010)
CDFN-LAB02	LAB	2.3	32^{*}	1.2	Yang et al. (2010)
CDFS-LAB11	LAB	2.3	31^{*}	1.1	Yang et al. (2010)
CDFN-LAB05	LAB	2.3	31^{*}	0.7	Yang et al. (2010)
CDFS-LAB16	LAB	2.3	30^{*}	0.7	Yang et al. (2010)

[a] The type indicates if the Lyα nebula is found around a high redshift radio galaxies (HzRGs), radio-loud quasar (QSO-R), and radio-quiet quasar (QSO). Lyα blobs (LABs) do not show a clear association with a central source, while the Lyα emitters (LAE) here reported are extended sources at high redshift whose powering source is not well constrained.

[b] Maximum diameter distance of the Lyα emission. The values with a $*$ are calculated assuming circular sources, i.e. these are diameters of a circle with area equal to the area of the source.

[c] These sources need confirmation.

[d] These LABs can be associated with a QSO.

1.3.1.2 EXTENDED LYα EMISSION AROUND QSOS

QSOs[9] are currently interpreted as the most luminous class of the so-called active galactic nuclei (AGN): accreting super massive black holes (SMBHs), now believed to be present in the center of most galaxies (e.g., Rees 1984; Magorrian et al. 1998; Ferrarese & Merritt 2000; Gültekin et al. 2009). A substantial fraction of the energy emitted by an AGN comes from very small scales (< pc). As matter falls towards the SMBH, it settles into an accretion disk ($\lesssim$ 0.1 pc) and releases, due to viscous processes, its gravitational and kinetic energy in the form of thermal emission. This emission ranges from soft X-rays to the optical (Shakura & Sunyaev 1973; Page & Thorne 1974), and is recognizable in the spectral energy distribution (SED) as the so-called "Big Blue Bump" (BBB) (Shields 1978; Malkan & Sargent 1982; Czerny & Elvis 1987; Risaliti

---

[9] In this Thesis I will use the term 'QSO' (quasi-stellar object) and 'quasar' interchangeably.

& Elvis 2004 and references therein). The accretion disk is believed to be surrounded by dust (or more generally by an obscuring medium) on larger scales ($\sim$ pc, e.g., Jaffe et al. 2004), yielding differences in the observed properties of AGNs due to orientation effects with respect to the line of sight to the observer (Antonucci 1993). Specifically, the obscuring medium has a geometry able to block the emission from the innermost regions ($\sim$ pc) usually detected as broad lines (FWHM $>$ 1000 km s^{-1}) in the spectrum of AGNs (e.g., Peterson 1993; Bianchi et al. 2012 and references therein), the so-called broad line regions (BLRs, Antonucci & Miller 1985), but does not affect the emission coming from larger scales (10 – 100 pc), the so-called narrow line regions (NLRs, FWHM $<$ 1000 km s^{-1}). In this paradigm of AGN unification (Antonucci 1993; Urry & Padovani 1995), QSOs are the class of AGN that direct their ionizing radiation towards the observer, and thus show broad emission lines. However, as the geometry and composition of the obscuring medium is still debated (Bianchi et al. 2012 and references therein), it is unclear how the radiation of a QSO is seen at large scales, e.g. the opening angle of the ionization cones is far from being well constrained (Pogge 1988; Tadhunter & Tsvetanov 1989; Evans et al. 1991; Kreimeyer & Veilleux 2013). Furthermore, the SED of a QSO is difficult to be completely characterized in the ultraviolet (UV), due to the absorption of the intervening IGM, with consequent uncertainties in estimating the properties of the BBB (Lusso et al. 2015 and references therein). Our ignorance on this part of the ionizing spectrum of a QSO has to be taken into account when considering the effect of photoionization (and photoheating) from these sources.

Despite these open issues, as anticipated in §1.3.1, several studies have tried to detect the reprocessed emission of the CGM, assuming that the gas is illuminated by the intense radiation of a QSO[10]. Different techniques have been used: narrow-band imaging (e.g., Hu & Cowie 1987; Heckman et al. 1991b; Yang et al. 2010), integral field spectroscopy (e.g., Christensen et al. 2006), and long slit spectra (e.g., Heckman et al. 1991a; North et al. 2012). In particular, these studies targeted Lyα emission in the vicinity of $z \sim 2-4$ quasars, expected to inhabit a dark matter halo of $M_{\rm DM} \sim 10^{12.5}$ M$_\odot$ with a virial radius of $R_{\rm vir} \sim 160$ kpc (White et al. 2012). However, precisely because of the different methodologies, different sensitivities, and redshifts probed, a detailed comparison and understanding of the phenomenon is hampered, and this research can be basically seen only as a statistical test of our ability to detect this low surface brightness signal. Approximately 10% of quasars are radio-loud (e.g., Ivezić et al. 2002), e.g. $R = f_{\nu,5\rm GHz}/f_{\nu,4400\text{Å}} > 10$ (Kellermann et al. 1989; Hao et al. 2014 and references therein). It seems that there is a higher detection frequency of radio-loud quasars that are associated with brighter Lyα emission on scales of $\sim 10-50$ kpc, as compared to radio-quiet QSOs (Heckman et al. 1991b). This may be in agreement with the expectation that radio-loud objects inhabit more

---

[10] The bolometric luminosity in play for AGN spans 8 order of magnitudes, ranging from 10^{39} erg s^{-1} (e.g., NGC4395, Kraemer et al. 1999) to 10^{47} erg s^{-1} (most luminous QSOs, e.g., Dietrich et al. 2002).

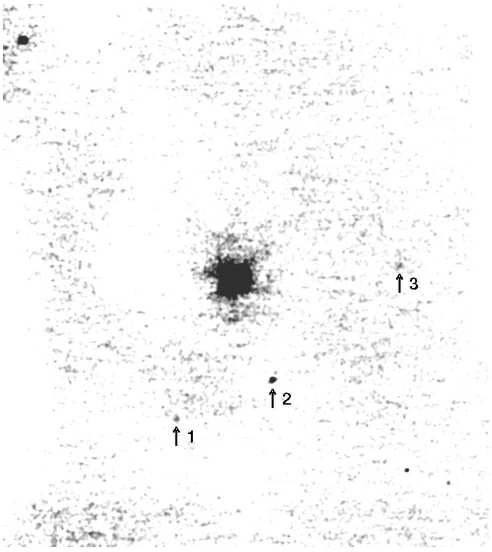

Figure 1.3: The image shows the Lyα map of a 66.3″×74.5″ field around the quasar J2233-606 (Bergeron et al. 1999). The maximum size of the nebula reported around this quasar is 105 kpc (the quoted surface brightness limit for this image is $\mathrm{SB}_{\mathrm{Ly}\alpha} = 1.5 \times 10^{-17}$ erg s^{-1} cm^{-2} arcsec^{-2}), representing the most extended Lyα emission detected around a QSO before this work. Three galaxies detected in the Lyα line are also labelled. Figure adapted from Bergeron et al. (1999).

massive, and thus richer environments (Venemans et al. 2007; Fanidakis et al. 2013)[11]. However, this so-called Lyα 'fuzz' has now also been reported with high frequency around radio-quiet quasars (Christensen et al. 2006; Hennawi & Prochaska 2013), and may be powered by the same mechanism giving rise to the extended narrow emission line regions (EELRs), which are detected using the [O III] and Balmer lines around low-z ($z < 0.5$) AGNs on scales of tens of kpc (e.g., Greene et al. 2011).

The emission targeted in this work, on scales of hundreds of kpc, is distinct from this Lyα 'fuzz'. At the beginning of this work (October 2011), Bergeron et al. (1999) reported the largest Lyα nebulosity observed around a radio-quiet QSO (105 kpc; see Figure 1.3), while Heckman et al. (1991b) had reported the largest one around a radio-loud QSO (116 kpc). However, given their sensitivities, these observations did not probe larger scales, typical of the CGM and the IGM. Nevertheless, deeper surface brightness limits and photoionization modeling lead to the first attempts in the characterization of the properties of the emitting gas only using the Lyα line (Hennawi et al. 2009). The results suggest the presence of dense ($n_{\mathrm{H}} \sim 100$ cm^{-3}), compact (~ 10 pc), Lyα emitting clouds within the diffuse CGM. New instruments, such as the Palomar Cosmic Web Imager (PCWI, Matuszewski et al. 2010), started (at the end of this work) to probably uncover the gas on scales of hundreds of kpc, at the interface between the QSOs and the IGM (Martin et al. 2014a). However, a confirmation of these results and a stronger analysis are still required. Indeed, at the moment, direct observational evidence for the presence of the cold flows explained in the foregoing introduction has remained dubious (e.g., Rauch et al. 2011; Cantalupo et al. 2014; Martin et al. 2014b).

---

[11] However, the interpretation of the extended Lyα line associated with a strong (and probably extended) central radio source is more complicated because one has to take into account the interactions between the radio emission and the ambient medium (see §1.3.1.3).

1.3.1.3 HIGH-REDSHIFT RADIO GALAXIES

Extended Lyα nebulae have also been frequently observed around high-redshift ($z \geq 2$) radio galaxies (HzRGs; e.g., McCarthy 1993; van Ojik et al. 1997; Nesvadba et al. 2006; Villar-Martín et al. 2007a; Reuland et al. 2007). With an average Lyα luminosity of $L_{\mathrm{Ly}\alpha} \sim 10^{44.5}$ erg s^{-1} and a diameter $\gtrsim$ 100 kpc, these nebulae tend to be brighter and larger than those around QSOs (see Figure 1.4), although current surveys are very inhomogeneous. An important difference between these two types of nebulae, however, is that in the case of quasars, a strong source of ionizing photons is directly identified, whereas for HzRGs the AGN is obscured from our view point (see e.g. Miley & De Breuck 2008a), in accord with unified models of AGN (e.g., Antonucci 1993; Urry & Padovani 1995; Elvis 2000).

HzRGs are believed to be massive galaxies hosting an obscured AGN. They could be the progenitors of the most massive galaxies we see in the local Universe, i.e. massive elliptical galaxies. This scenario is corroborated by clustering analysis of Lyα emitter galaxies around these objects, which have shown dense environments around HzRGs (Venemans et al. 2007; Kurk et al. 2000). Furthermore, these sources produce powerful radio jets and X-ray emission (e.g., Cielo et al. 2014; Krawczynski & Treister 2013 and references therein), whose impact has to be taken into account to correctly study the properties of the gas on large scales, especially given the fact that the Lyα nebulae can be more extended than the radio structure (e.g., Eales et al. 1993; Kurk et al. 2002), and often polarized and aligned with the radio axis (McCarthy et al. 1995). Specifically, the extreme central kinematics (FWHM$\gtrsim$ 1000 km s^{-1}, Villar-Martín et al. 2003b) of the gas detected in Lyα suggest the presence of starburst superwinds triggered by the jet-gas interaction (e.g., McCarthy 1993; Zirm et al. 2005; Villar-Martín et al. 2007a). On larger scales ($\sim$ 100 kpc), instead, it has been shown that Lyα nebulae have quiescent kinematics (FWHM$<$ 700 km s^{-1}), maybe tracing the in-falling material at the halo periphery, and not being perturbed by interactions with the radio structures (Villar-Martín et al. 2007b; Humphrey et al. 2007). Some of these giant Lyα nebulae show strong optically thick H I absorption features across the full spatial extent of the Lyα emission (e.g, van Ojik et al. 1997). Being usually blue-shifted from the center of the Lyα emission, these absorption features are interpreted as expanding shells surrounding the HzRG (e.g., Binette et al. 2000).

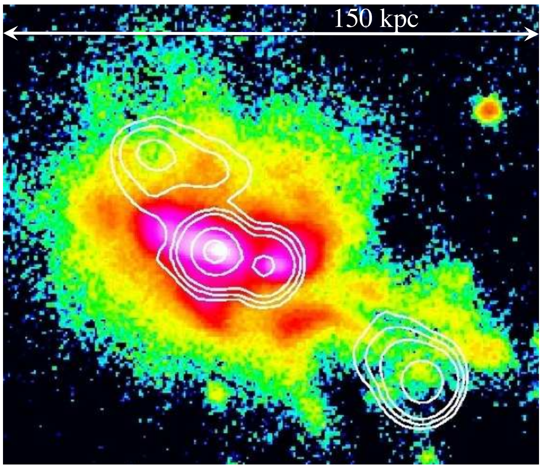

Figure 1.4: Structure of the high redshift radio galaxy 4C41.17 at $z = 3.8$. Contours (white) obtained at 1.4 GHz with the Very Large Array (VLA) are superimposed on a Keck narrow-band image (color map) targeting the Lyα line at the redshift of the source. The radio angular size of ~ 90 kpc is smaller in comparison to the extended Lyα halo. Figure adapted from Miley & De Breuck (2008b), and Reuland et al. (2003).

HzRGs emit a rich emission-line spectrum, dominated in the UV rest-frame by Lyα , He II λ1640, C IV λ1549, and C III λ1909, also on large scales (up to ~ 100 kpc). Such emission lines are explained via a combination of photoionization from the central AGN and jet-induced star-formation (e.g., Vernet et al. 2001; Humphrey et al. 2008). The studies of these emission lines reveal high levels of metal enrichment on large scales (up to solar), and densities as high as ($n_{\rm H} \sim 100$ cm^{-3}). However, single density (or more generally single cloud population) models are not able to simultaneously reproduce both the high and low ionization lines, implying ranges in $n_{\rm H}$ or distinct cloud populations (Binette et al. 1996), or suggesting the importance of the effects of radiation pressure (Dopita et al. 2002; Stern et al. 2014).

1.3.1.4 LYMAN α BLOBS - LABS

Intriguingly, the so-called Lyα blobs (LABs), large (50–100 kpc) luminous ($L_{\rm Ly\alpha} \sim 10^{43-44}$ erg s^{-1}), radio-quiet Lyα nebulae at $z \sim 2-6$, exhibit properties similar to Lyα nebulae around QSOs and HzRGs, but without obvious evidence for the presence of an AGN (e.g., Keel et al. 1999; Steidel et al. 2000; Francis et al. 2001; Matsuda et al. 2004, 2011; Dey et al. 2005; Saito et al. 2006; Smith & Jarvis 2007; Ouchi et al. 2009; Prescott et al. 2009, 2012; Yang et al. 2009, 2010). LABs are believed to be the sites of massive galaxy formation, where strong feedback processes may be expected to occur, and seem to reside preferentially in overdense environments (Yang et al. 2009, 2010). However, despite intense interest and multi-wavelength studies, the physical mechanism powering the Lyα emission in the LABs is still poorly understood.

LABs were serendipitously discovered in narrow-band Lyα surveys targeting the vicinity of quasars (Francis et al. 1996) or known galaxy overdensities (e.g., the two famous LAB1 and LAB2, Steidel et al. 2000). They triggered great interest because of the lack of clear sign of AGN activity. Thus, a lot of theoretical studies were conducted, proposing several scenarios, including photo-ionization by AGNs (Geach et al. 2009), shock-heated gas by galactic superwinds (Taniguchi & Shioya 2000), cooling radiation from cold-mode accretion (Fardal et al. 2001; Haiman et al. 2000; Dijkstra & Loeb 2009a; Goerdt et al. 2010; Faucher-Giguère et al. 2010), and resonant scattering of Lyα from star-forming galaxies (Steidel et al. 2011; Hayes et al. 2011).

Observational follow-up studies have produced an even more complicated picture, leading sometimes to the discovery of embedded galaxies or AGNs within the LABs. For example, LAB1 and LAB2 (Steidel et al. 2000) were observed in submillimeter, near infrared (NIR) and X-ray. The results show the probable presence of an obscured AGN in LAB2, supported by a hard X-ray detection with 2μm emission. LAB1, on the other hand, seems to be powered by extended star-formation, given its NIR colors and the strong submillimeter counterparts observed only in low resolution observations (Matsuda et al. 2007). However, none of the above observations has firmly constrained the nature of these sources, and this example can be taken as being representative of the whole effort in the determination of the powering mechanism of these large scale nebulosities. It frequently happens that a LAB is considered a ‘prototype’ for a particular powering scenario, and subsequent observations or simulations overturn the interpretation. The latest example is the case of a LAB which was explained by Nilsson et al. (2006) as being originated by cooling radiation, and recently re-interpreted by Prescott et al. (2015b) as being powered by an AGN.

The polarization of the resonant Lyα line could give us new information on the properties of the gas. It is expected that Lyα photons that scatter in the wings of the line profile, and thus those that escape the nebula, should have three times higher polarization than photons scattering in the line core (Stenflo 1980). However, this is highly dependent on the geometry of the system and on the amount of scattering that a photon undergoes. Specifically, a general expectation is that more scattering leads to less polarized emission (Prescott et al. 2011). Thus, polarimetry is a promising way to corroborate if Lyα is produced in situ or if it has been scattered (e.g., Dijkstra & Loeb 2008). However, due to difficulties in the observational technique, until now, only two LABs have been observed with imaging polarimetry[12]. Prescott et al. (2011) show a non-detection in the source discovered by Dey et al. (2005), while Hayes et al. (2011) measured a signal of $P = 11.9\% \pm 2\%$ within a radius of $7''$ in LAB1, with a trend of increasing polarization at larger radii, consistent with illumination by a central source. Once again, this is in obvious conflict with the above-mentioned interpretation of the origin of this source by Matsuda et al. (2007), i.e. extended star formation. A clear picture of the polarization signal in these large Lyα nebulae is far from being achieved, and new studies are currently ongoing (Yujin Yang private communication).

---

[12] Regarding all the other Lyα nebulae, only another object has been studied with imaging polarimetry, i.e. the $z = 2.34$ radio galaxy TXS0211-122 (Humphrey et al. 2013). This work quoted a signal of $P = 16.4\% \pm 4.6\%$, indicating that the nebula is at least partly powered by scattering of Lyα photons.

Thus, the overall message is that the ignorance on the physical processes powering LAB emission likely results from the lack of other emission-line diagnostics besides the strong Lyα line (e.g., Matsuda et al. 2006), and our inability in disentangling the different contributions arising from each of the powering mechanisms.

1.3.2 THE NEED OF ADDITIONAL LINE DIAGNOSTICS

The four mechanisms mentioned above, which have been proposed to power the Lyα blobs, could also act together, and could be in play in any other large scale Lyα nebula. To understand their importance, other tracers different to Lyα are thus needed. Roughly speaking, it is needed a non-resonant line to constrain the importance of the resonant scattering of the Lyα photons, and at least a metal line to constrain the metallicity and the hardness of a possible ionizing source. Specifically, the He II recombination line[13], and the C IV line[14] could be good choices, as has already been shown in the case of HzRGs. In the following, the four mechanisms are reviewed, particularly discussing how they might generate C IV and He II line emission. The search of emission from these lines in LABs and in a nebula around a QSO will be treated in Chapter 3 and §5.4.

1. **Photoionization by a central AGN**: as stressed above, it is well established that the ionizing radiation from a central AGN can power giant Lyα nebulae, with sizes up to ~200 kpc, around high-z radio galaxies (e.g., Villar-Martín et al. 2003b; Reuland et al. 2003; Venemans et al. 2007) and quasars (e.g., Heckman et al. 1991b; Christensen et al. 2006; Smith et al. 2009; Cantalupo et al. 2014). If the halo gas is already polluted with heavier elements (e.g., C, O) by outflows from the central source, one expects to detect both C IV and He II emission from the extended Lyα-emitting gas. If not, only extended He II emission is expected. Indeed, extended C IV and He II emission have been clearly detected in HzRGs (Villar-Martín et al. 2003a; Humphrey et al. 2006; Villar-Martín et al. 2007a)

---

[13] The He II λ1640Å is the first line of the Balmer series emitted by the Hydrogen-like atom He^+, i.e. corresponding to the Hα line.

[14] Throughout this work, C IV λ1549 represents the resonant doublet emission line, C IV $\lambda\lambda$ 1548,1550, which arises from the transition between the first excited level of the C^{3+} ion to its ground state, i.e $1s^2 2p \rightarrow 1s^2 2s$.

and tentatively detected around QSOs (Heckman et al. 1991b,a; Humphrey et al. 2013) on scales of 10-100 kpc. The photoionization scenario gains credence from a number of studies suggesting that LABs host an AGN which is obscured from our perspective (Geach et al. 2009; Overzier et al. 2013; Yang et al. 2014a; Prescott et al. 2015b, but see Nilsson et al. 2006; Smith & Jarvis 2007).

2. **Shocks powered by galactic-scale outflows**: Several studies have argued that shell-like or filamentary morphologies, large Lyα line widths ($\sim$1000 km s^{-1}), and enormous Lyα sizes ($\sim$100 kpc) imply that extreme galactic-scale outflows, and specifically the ionizing photons produced by strong shocks, power the LABs (Taniguchi & Shioya 2000; Taniguchi et al. 2001; Ohyama et al. 2003; Wilman et al. 2005; Mori & Umemura 2006). If violent star-formation feedback powers a large-scale superwind, the halo should be highly enriched, and with a significant amount of gas at $T \sim 10^5$ K. One would therefore also expect to detect extended He II and C IV emission, but with potentially different line ratios than in the simple photoionization case. Note that collisional excitation of singly ionized helium peaks at $T \sim 10^5$ K, making the He II line one of the dominant observable coolants at this temperature (Yang et al. 2006). Note however, that the relatively quiescent ISM kinematics of star-forming galaxies embedded within LABs appear to be at odds with this scenario (McLinden et al. 2013; Yang et al. 2011, 2014b).

3. **Gravitational cooling radiation**: A large body of theoretical work has suggested that Lyα emission nebulae could result from Lyα cooling radiation powered by gravitational collapse (Haiman et al. 2000; Furlanetto et al. 2005; Dijkstra et al. 2006b; Faucher-Giguère et al. 2010; Rosdahl & Blaizot 2012). In the absence of significant metal-enrichment, collisionally excited Lyα is the primary coolant of $T \sim 10^4$ K gas; hence cool gas steadily accreting onto halos hosting Lyα nebulae may radiate away their gravitational potential energy in the Lyα line. However, the predictions of the Lyα emission from these studies are uncertain by orders of magnitude (e.g. Furlanetto et al. 2005; Faucher-Giguère et al. 2010; Rosdahl & Blaizot 2012) because the emissivity of collisionally excited Lyα is exponentially sensitive to gas temperature. Accurate prediction of the temperature requires solving a coupled radiative transfer and hydrodynamics problem which is not currently computational feasible (but see Rosdahl & Blaizot 2012). While Yang et al. (2006) suggest that the He II cooling emission could be as high as 10% of Lyα near the embedded galaxies (i.e. point-source emission) where the density of IGM/CGM is highest, the extended ($\gtrsim$ 20 kpc) He II emission may be challenging to detect with current facilities (HeII/Lyα < 0.1). Note that if Lyα emission arises from cooling radiation of pristine gas, no *extended* C IV emission is expected.

4. **Resonant scattering of Lyα from embedded sources**: In this scenario, Lyα photons are produced in star-forming galaxies or AGNs embedded in the Lyα nebula, but the extended

> sizes of the Lyα halos result from resonant scattering of Lyα photons as they propagate outwards (Dijkstra & Loeb 2008; Hayes et al. 2011; Cen & Zheng 2013; Cantalupo et al. 2014). In this picture, non-resonant He II emission (*if* produced in the galaxies or AGN) should be compact, in contrast with the extended Lyα halos. In other words, if extended He II is detected on the same scale as the extended Lyα emission, this implies that resonant scattering does not play a significant role in determining the extent of the Lyα nebulae. Conversely, as the C IV line is a resonant line, it is conceivable that a contribution to its extended emission, if present, could arise due to scattering by the same medium scattering Lyα, provided that the halo gas is optically thick to C IV , which in turn depends on the metallicity and ionization state of the halo gas. In this context, it is interesting to note that Prochaska et al. (2014) find a high covering factor of optically thick C II and C IV absorption line systems out to > 200 kpc around $z \sim 2$ QSOs, implying that the CGM of massive halos is significantly enriched.

In summary, a detection of extended emission in the C IV line will provide us information on the intensity and hardness of an ionizing source or the speed of shocks in a superwind (e.g., Ferland et al. 1984; Nagao et al. 2006; Allen et al. 2008), the metallicity of gas in the CGM, and the sizes of metal-enriched halos. A detection of extended (non-resonant) He II emission similarly constrains the ionizing spectrum or the speed of shocks, and can be used to test whether Lyα photons are resonantly scattered, as well as constrain the amount of material in a warm $T \sim 10^5$ K phase. To date, there are five detections of extended C IV and He II emission from LABs reported in the literature (Dey et al. 2005 and Prescott et al. 2009, 2013). The extended C IV and He II emission from these Lyα nebulae has fluxes up to $F_{\rm C\,IV} \sim 4 \times 10^{-17}\,{\rm erg\,s^{-1}\,cm^{-2}}$ and $F_{\rm He\,II} \sim 6 \times 10^{-17}\,{\rm erg\,s^{-1}\,cm^{-2}}$, implying C IV/Ly$\alpha \lesssim 0.13$ and He II/Ly$\alpha \lesssim 0.13$. On the other hand, as said previously (§1.3.1.3), HzRGs show these line emissions on large scales ($\sim$ 100 kpc). However, it is missing in the literature a detailed modeling of the emission on these large scales to reproduce both the observed Lyα emission and the He II and C IV constraints, particularly for the case of LABs.

1.4 THESIS OUTLINE

In this manuscript, I present the work I have conducted during my PhD under the supervision of Joseph F. Hennawi at the Max-Planck-Institut für Astronomie.

This work is based on fundamental questions explicitly stated in the above introduction: is it possible to detect other emission lines from LABs, and thus disentangle the different powering mechanisms that have so far been proposed? Are we able to detect large scale Lyα nebulae around high-z quasar? What is the luminosity, frequency, morphology, covering factor of these Lyα nebulae? Can we study the properties of the CGM and IGM in emission? What constraints can we place on the physical parameters (volume density, column density, metallicity, ionization) of this media?

I start addressing these questions by mainly resolving evident deficiencies in the observational strategies. Before my work, there was no structured effort in the literature to detect additional emission lines from LABs. Regarding extended emission around QSOs, previous studies were not sensitive enough to detect large-scale $\sim 100-500$ kpc Lyα nebulae mainly because of two reasons: 1) almost all previous (before 2011) observed QSOs are at $z \sim 3$, where the $(1+z)^4$ cosmological surface brightness dimming dictates that one must integrate ~ 10 times longer than at $z \sim 2$; and 2) previous narrow-band studies used wide low throughput filters FWHM$= 70-100$ Å, which included too much sky background. Thus, the combination of these two facts inhibit the study of the emission from the CGM[15].

Chapter 2 presents an overview of the model for cool halo gas in the halo of a QSO introduced by Hennawi & Prochaska (2013, Section 2). This model is extensively used in this thesis. Chapter 3 presents the narrow-band observations of a sample of 13 LABs in the He II and C IV lines, with the respective modeling and analysis. In Chapter 4, I briefly introduce the FLASHLIGHT survey that I conducted to characterize the Lyα emission around QSOs at $z \sim 2$ with the Keck and Gemini-South telescopes. In Chapter 5, I describe the discovery (made in the context of the FLASHLIGHT survey) of the largest Lyα nebulosity known to date, together with its detailed modeling and current interpretation. Further, in Chapter 6, I show the first radial emission profile of the CGM of quasars, computed using the data from the FLASHLIGHT survey, which I collected at the Gemini-South telescope. Finally, Chapter 7 summarizes the main conclusions of this thesis, and discusses the preliminary results from a new survey and future directions.

Throughout this work, I adopt the cosmological parameters $H_0 = 70$ km s^{-1} Mpc^{-1}, $\Omega_M = 0.3$ and $\Omega_\Lambda = 0.7$. In this standard cosmology, $1''$ corresponds to 7.6 physical kpc at $z = 3.1$ (useful in Chapter 3), 8.2 physical kpc at z=2.279 (useful in Chapter 5), or 8.4 physical kpc at z=2.253 (useful in Chapter 6)[16]. All magnitudes are in the AB system (Oke 1974).

---

[15] Note that $z \sim 3$, and thus $\lambda \sim 5000$ Å was selected because CCDs were more sensitive at these wavelengths. Moreover, FWHM$= 70-100$ Å narrow-band filters can be found already available at telescopes (e.g., [O III] filters) at these wavelengths, while narrower filters need to be custom designed and purchased, resulting of course in higher costs.

[16] I assume this cosmology throughout this work. However I am aware of the effort in trying to better reconcile observations with the current cosmological paradigm, also with modification to the dark energy component (e.g., Penzo et al. 2014).

“The ability to simplify means to eliminate the unnecessary so that the necessary may speak.”

Hans Hofmann

Chapter 2

A SIMPLE MODEL FOR COOL HALO GAS

In this Chapter, I describe extensively the simple model for cool halo gas ($T \sim 10^4$ K) presented in Hennawi & Prochaska (2013). This description is fundamental for the understanding of the photoionization modeling in Chapters 3 and 5, and in particular to comprehend the analytical expectations for the surface brightness of the Lyα line. Although extremely simple, this model results to be a good zeroth-order approximation to the more complicated problem (see §2.3 for its caveats). If the Reader is already familiar with this work, He/She can skip this chapter and start directly from Chapter 3.

As shown in Figure 2.1, Hennawi & Prochaska (2013) assume a simple configuration in which a QSO inhabits a spherical halo of radius R. The cool gas in this halo is spatially uniformly distributed as a population of clouds with a single uniform hydrogen volume density $n_{\rm H}$.

The spatial distribution of the gas is then fully described if the hydrogen column density $N_{\rm H}$, and the cloud covering factor $f_{\rm C}$ are specified. In particular, the covering factor is defined as

$$f_{\rm C} \equiv \langle \int \frac{df_{\rm C}}{ds} ds \rangle, \tag{2.1}$$

where the angle brackets denote an average over the projected area of the spherical halo on the sky, and $\frac{df_{\rm C}}{ds} = n_{\rm c}\sigma_{\rm c}$ ($n_{\rm c}$ is the number density of clouds, and $\sigma_{\rm c}$ is the cloud cross-sectional area). In the case of uniformly distributed clouds, this gives

$$f_{\rm C} = \frac{4}{3} R n_{\rm c} \sigma_{\rm c}. \tag{2.2}$$

---

[*] This chapter is entirely based on the work of Hennawi & Prochaska (2013), already adopted in Arrigoni Battaia et al. (2015b,a). To allow the Reader to fully understand the model used in the following Chapters, in this Chapter I adapted the description in Hennawi & Prochaska (2013) (see their Section 2).

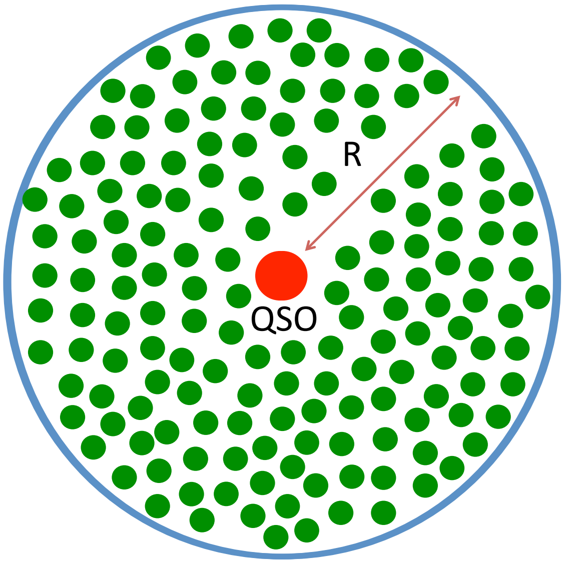

Figure 2.1: Toy-model of the cool halo gas of a QSO as described in Hennawi & Prochaska (2013). The halo is assumed to be spherical with a radius R, and a population of cool ($T \sim 10^4$ K) clouds with a single $n_{\rm H}$ is uniformly distributed within its volume.

Note that, in general, the covering factor can be larger than unity because there can be superposition of clouds along the line-of-sight.
The four parameters so far introduced, namely R, $n_{\rm H}$, $N_{\rm H}$, $f_{\rm C}$ can be directly observed or derived from both the absorption-line observations and the emission-line observations outlined in §1.2 and §1.3, and can be used to determine all other quantities of interest.

For example, the volume filling factor, i.e. the ratio of the volume occupied by the clouds to the total volume, is given by

$$f_{\rm V} = n_{\rm c} V_{\rm c} = \frac{3 f_{\rm C} N_{\rm H}}{4 R n_{\rm H}}, \tag{2.3}$$

where $V_{\rm c}$ is the volume occupied by the clouds, and Eqn. (2.2) is used in the second step. The total mass of cool gas within the spherical halo can then be calculated as

$$M_{\rm c} = \frac{4}{3}\pi R^3 f_{\rm V} \frac{n_{\rm H} m_{\rm p}}{X} = \pi R^2 f_{\rm C} N_{\rm H} \frac{m_{\rm p}}{X}, \tag{2.4}$$

where $m_{\rm p}$ is the mass of the proton and $X = 0.76$ is the hydrogen mass fraction (e.g, Boesgaard & Steigman 1985; Izotov et al. 1999).

The remainder of this Chapter is focused on obtaining analytical estimates for the Lyα emission expected from this population of cool clouds illuminated by the central quasar. Given the high redshift, these clouds are potentially unresolved in our observations, and thus, the observable of interest is the surface brightness [erg s^{-1} cm^{-2} arcsec^{-2}] averaged over the projected area on the sky as measured from Earth. The specific intensity of the Lyα line from the spherical halo is calculated by integrating the equation of radiative transfer through the gas distribution

$$I_{\mathrm{Ly}\alpha} = \int j_{\mathrm{Ly}\alpha} ds, \tag{2.5}$$

where $j_{\mathrm{Ly}\alpha}$ is the volume emissivity per steradian [erg s^{-1} cm^{-3} ster^{-1}] [1]. The average surface brightness observed from Earth can then be written as

$$\mathrm{SB}_{\mathrm{Ly}\alpha} \equiv \frac{1}{(1+z)^4}\langle I_{\mathrm{Ly}\alpha}\rangle = \frac{1}{(1+z)^4}\frac{1}{\pi R^2}\int j_{\mathrm{Ly}\alpha} dV \tag{2.6}$$

where the cosmological surface brightness dimming $(1+z)^{-4}$ is taken into account.

Note that in this work the UV background, i.e. the integrated ultraviolet emission from star-forming galaxies and AGNs that keep the IGM ionized (e.g., Haardt & Madau 2012; Faucher-Giguère et al. 2009 and references therein), is not taken into account. Indeed, as the systems of interest are hit by strong UV emission produced by the close AGN, and thus the gas is already ionized, the absence/presence of the UV background has a negligible effect on the Lyα emissivity of the cool halo gas.

2.1 FLUORESCENT LYα EMISSION

As mentioned in §1.1, a hydrogen atom emits a Lyα photon ($h\nu_{\mathrm{Ly}\alpha} = 10.2$ eV) in the highly probable transition $2p \rightarrow 1s$. Three processes can populate the $2p$ state, and hence produce a Lyα photon.

1) Collisional Excitation A free electron collides with a hydrogen atom, which is thus excited to a higher level, and may emit a Lyα photon when it relaxes back to the ground state. The collisional emissivity can be written as (e.g., Osterbrock & Ferland 2006; Rosdahl & Blaizot 2012)

$$j_{\mathrm{coll}} = \frac{h\nu_{\mathrm{Ly}\alpha}}{4\pi} C_{\mathrm{Ly}\alpha}(T)\, n_{\mathrm{e}} n_{\mathrm{HI}} \tag{2.7}$$

---

[1] The effect of resonant scattering of gas within the halo itself and in the IGM is ignored, as Zheng et al. (2011) showed that scattering by the IGM should be negligible at the redshift range considered here, i.e. $z \sim 2-3$. See section §2.3 for the impact of resonant scattering in the CGM. Also note that we ignore dust extinction, which should not be important in these systems, and thus should not produce a remarkable decrease of the Lyα emission (Hennawi & Prochaska 2013).

where $C_{\mathrm{Ly}\alpha}(T)$ is the rate of collisionally induced transitions to levels that could lead to a Lyα photon emission[2], and n_{e} and n_{HI} are the number densities of electrons and neutral hydrogen atoms, respectively.

2) Absorption of Photons with 10.2 **eV** $< h\nu <$ 13.6 **eV** These photons can excite a hydrogen atom to any level $n \geq 2$. The resulting cascade could produce a Lyα photon following the rules and probabilities of atomic physics (e.g., Menzel 1937; Chamberlain 1953).

3) Recombination A capture of a free electron by a proton to any excited level, i.e. $n \geq 2$, may produce a downward cascade by radiative transitions to the $2p$ level, and thus may result in the emission of a Lyα photon. The recombination emissivity can be written as (e.g., Osterbrock & Ferland 2006)

$$j_{\mathrm{rec}} = \frac{h\nu_{\mathrm{Ly}\alpha}}{4\pi}\,\eta\,\alpha(T)\,n_{\mathrm{e}}n_{\mathrm{p}} \tag{2.8}$$

where n_{p} is the number density of protons, η is the fraction of recombinations which result in a Lyα photon, and $\alpha(T)$ is the recombination rate coefficient. As it will be shown in the next Sections, the value of these last two factors depend on the physical conditions of the gas studied.

As shown in Chamberlain (1953), at the densities studied here ($n_{\mathrm{H}} < 100$ cm^{-3}), the total emissivity in the Lyα line can be written as a sum of the emissivity of these three processes. However, process 2) is likely subdominant with respect to process 3) in the case investigated here, because, given the hard ionizing flux of the QSO, the gas is presumably highly ionized. For the same reason, collisional excitation should be less important than recombination. However, collisional excitation can play an important role in the radiative cooling of $T \sim 10^4$ K gas, especially if the central quasar is faint or if there is not a clear bright source of ionizing photons.

Generally, the total Lyα emissivity can be then approximately written as (Rosdahl & Blaizot 2012)

$$j_{\mathrm{Ly}\alpha} = j_{\mathrm{rec}} + j_{\mathrm{coll}}, \tag{2.9}$$

but in what follows, I will consider the recombination emission (also called Lyα fluorescence) as the main powering mechanism of the Lyα emission[3]. In the next Sections, I examine the two limiting cases in which the gas clouds are (i) optically thin ($N_{\mathrm{HI}} \ll 10^{17.2}\,\mathrm{cm}^{-2}$), or (ii) optically thick ($N_{\rm HI} \gg 10^{17.2}\,{\rm cm}^{-2}$) to Lyman continuum photons, i.e. the ionizing radiation. For $N_{\rm HI} \sim 10^{17.2}\,{\rm cm}^{-2}$, the analytical expectations shown in the next Sections break down, and a full approach with radiative transfer calculations has to be adopted.

---

[2] The contribution to the coefficient $C_{\mathrm{Ly}\alpha}(T)$ from levels with $n > 4$ is of few percent (Osterbrock & Ferland 2006).

[3] Although the observations are not able to distinguish a photon produced from fluorescent emission or from cooling radiation, in the literature the two processes are treated separately, as in this work. It is important to separate both processes for two main reasons: to assess whether they have different observational signatures (morphology of the nebula, kinematics, etc.), and more importantly, because cooling radiation estimates are extremely sensitive to the gas temperatures, and usually simulations do not compute these self-consistently (mainly because they do not include self-shielding during dynamical evolution, e.g., Kollmeier et al. 2010).

2.1.1 OPTICALLY THIN REGIME

In this scenario, the gas is characterized by $N_{\rm HI} \ll 10^{17.2}\,{\rm cm}^{-2}$. The cool clouds are highly ionized by the hard QSO radiation, such that the optical depth (τ) to ionizing photons is $\tau \ll 1$, i.e. the nebula is transparent to ionizing photons[4].

By introducing in Eqn. (2.8) the values for the optically thin regime, the recombination emissivity from the cool clouds in the halo is given by

$$j_{\rm Ly\alpha} = f_{\rm V}\frac{h\nu_{\rm Ly\alpha}}{4\pi}\eta_{\rm thin}n_{\rm e}n_{\rm p}\alpha_{\rm A}(T), \tag{2.10}$$

where $f_{\rm V}$ takes into account that the clouds do not fill entirely the halo's volume (see Eqn. 2.3), $\eta_{\rm thin} = 0.42$ is the fraction of recombinations which result in a Lyα photon in the optically thin limit (Osterbrock & Ferland 2006), and $\alpha_{\rm A}(T)$ is the case A recombination coefficient weakly dependent on temperature T. At $T = 10{,}000\,{\rm K}$, $\alpha_A = 4.18 \times 10^{-13}\,{\rm cm}^{-3}\,{\rm s}^{-1}$ (Osterbrock & Ferland 2006).

Photoionization equilibrium is used to determine the electron and proton densities (Hennawi & Prochaska 2013),

$$n_{\rm HI}\Gamma = n_{\rm e}n_{\rm p}\alpha_{\rm A}, \tag{2.11}$$

where Γ is the photoionization rate given by

$$\Gamma = \frac{1}{4\pi r^2}\int_{\nu_{\rm LL}}^{\infty}\frac{L_\nu}{h\nu}\sigma_{\rm pi}(\nu)d\nu. \tag{2.12}$$

Here $\nu_{\rm LL}$ is the frequency at the Lyman limit, and $\sigma_{\rm pi}(\nu)$ is the hydrogen photoionization cross-section previously defined (see Eqn. 1.5). To estimate the specific luminosity L_ν, the QSO SED is approximated by a series of power-laws. In particular, I assume that the SED of the quasar is approximated by a series of power-laws at short wavelengths, in particular blueward of $\nu_{\rm LL}$. Specifically, for energies greater than 1 Rydberg, the SED is parameterized as $L_\nu = L_{\nu_{\rm LL}}(\nu/\nu_{\rm LL})^{\alpha_{\rm UV}}$, with

---

[4] A photon with wavelength shorter than $\lambda_{\rm LL} = 912$ Å (i.e. the hydrogen Lyman limit) and intensity I_0, experiences an attenuation by passing through a gas cloud with neutral column density $N_{\rm HI}$, and will thus come out with a weakened intensity

$$I(\lambda) = I_0(\lambda)\,e^{-\tau(\lambda)}$$

where $\tau(\lambda)$ is the optical depth for $\lambda \leq \lambda_{\rm LL}$, which can be written as in Eqn. (1.5) (Draine 2011; Mo et al. 2010).

$\alpha_{\rm UV} = -1.7$, consistent with the measurement of Lusso et al. (2015). One can thus estimate the luminosity at the Lyman limit $L_{\nu_{\rm LL}}$, i.e. the normalization of the spectral energy distribution, by integrating the composite SED against the SDSS filter curves, and choosing the amplitude to give the correct magnitudes at the rest-frame UV wavelengths of the quasar considered. In case the presence of a central hard ionizing source is not known, or the luminosity is not constrained because the central source is obscured from our viewing point, i.e. it is not detected in any UV rest-frame survey, this normalization will be a further free parameter in the modeling of the emission from the cool halo gas (e.g. in the case of LABs; see §3.4.1).

In all the cases studied in this work, optically thin gas will always be highly-ionized due to the presence of strong radiation fields. In this framework, the neutral fraction is $x_{\rm HI} \equiv \frac{n_{\rm HI}}{n_{\rm H}} \ll 1$, hence $n_{\rm p} \approx n_{\rm H}$ and $n_{\rm e} \approx (1 + Y/2X)\, n_{\rm H}$, where the helium and hydrogen mass fractions are Y and X, respectively, and all helium is assumed to be doubly ionized.

By inserting in Eqn. (2.6) all the above relations for the optically thin case, the observed Lyα surface brightness can be thus written as

$$\begin{aligned} {\rm SB}^{\rm thin}_{{\rm Ly}\alpha} &= \frac{\eta_{\rm thin} h\nu_{{\rm Ly}\alpha}}{4\pi(1+z)^4}\alpha_{\rm A}\left(1+\frac{Y}{2X}\right) f_{\rm C} n_{\rm H} N_{\rm H} \qquad (2.13) \\ &= 7.7\times10^{-18}\left(\frac{1+z}{3.0}\right)^{-4}\left(\frac{f_{\rm C}}{1.0}\right)\left(\frac{n_{\rm H}}{1.0\,{\rm cm}^{-3}}\right)\left(\frac{N_{\rm H}}{10^{20}\,{\rm cm}^{-2}}\right)\,{\rm erg\,s^{-1}\,cm^{-2}\,arcsec^{-2}} \end{aligned}$$

Thus, in the optically thin regime, if the central source is strong enough to maintain the gas highly ionized, the Lyα emission is independent of the luminosity of the quasar (or ionizing central source), and depends only on the physical properties and amount of the cool gas, i.e. ${\rm SB}^{\rm thin}_{{\rm Ly}\alpha} \propto f_{\rm C} n_{\rm H} N_{\rm H}$. This is due to the fact that photoionization equilibrium implies $j_{{\rm Ly}\alpha} \propto \Gamma n_{\rm HI}$, while at the same time, the neutral fraction is inversely proportional to the photoionization rate $x_{\rm HI} \approx \alpha_{\rm A} n_{\rm H}(1 + Y/2X)/\Gamma$. The result is that Γ (and any dependence on luminosity) cancels out when computing Eqn. (2.13).

2.1.2 OPTICALLY THICK REGIME

In this scenario, the gas is characterized by $N_{\rm HI} \gg 10^{17.2}\,{\rm cm}^{-2}$. In this case, the cool clouds are able to self-shield against the ionizing radiation, resulting in clouds with a core of neutral hydrogen ($\tau \gg 1$). For this reason, their Lyα emission is not proportional to the volume they occupy (i.e. no dependence on $f_{\rm V}$), but instead, practically all the recombinations and resulting Lyα photons will emerge from a highly ionized thin layer (Gould & Weinberg 1996). These optically thick clouds thus behave like a mirror, converting into Lyα photons a fraction $\eta_{\rm thick} = 0.66$ of the impinging ionizing radiation. The Lyα emissivity of each cloud would then be simply proportional to the area of the 'mirror' times the flux of ionizing photons that it intercepts, corrected by the factor $\eta_{\rm thick}$ (Gould & Weinberg 1996). The emissivity in the Lyα line from the cool clouds in the halo in the optically thick scenario can be thus written as

$$j_{{\rm Ly}\alpha} = \frac{h\nu_{{\rm Ly}\alpha}}{4\pi}\eta_{\rm thick} n_{\rm c}\sigma_{\rm c}\Phi, \tag{2.14}$$

where

$$\Phi = \int_{\nu_{\rm LL}}^{\infty} \frac{F_\nu}{h\nu} d\nu = \frac{1}{4\pi r^2}\int_{\nu_{\rm LL}}^{\infty} \frac{L_\nu}{h\nu} d\nu \tag{2.15}$$

is the ionizing photon number flux (phot $\rm s^{-1}\,cm^{-2}$).

Introducing Formulas (2.14) and (2.15), together with Eqn. (2.2) in Eqn. (2.6), yields an observed Lyα surface brightness given by

$$\begin{aligned} {\rm SB}^{\rm thick}_{{\rm Ly}\alpha} &= \frac{\eta_{\rm thick} h\nu_{{\rm Ly}\alpha}}{4\pi(1+z)^4} f_{\rm C}\Phi \qquad (2.16)\\ &= 6.0\times10^{-17}\left(\frac{1+z}{3.0}\right)^{-4}\left(\frac{f_{\rm C}}{1.0}\right)\left(\frac{R}{100\,{\rm kpc}}\right)^{-2}\left(\frac{L_{\nu_{\rm LL}}}{10^{30}\,{\rm erg\,s^{-1}\,Hz^{-1}}}\right) {\rm erg\,s^{-1}\,cm^{-2}\,arcsec^{-2}}. \end{aligned}$$

Thus in the optically thick case, the Lyα emission is proportional to the ionizing flux of the central source, and it is only marginally sensitive to the amount of cool gas in the halo through the covering factor $f_{\rm C}$, i.e. ${\rm SB}^{\rm thick}_{{\rm Ly}\alpha} \propto f_{\rm C} L_{\nu_{\rm LL}}$. This is opposite to the dependence shown in the previous section for the optically thin case (${\rm SB}^{\rm thin}_{{\rm Ly}\alpha} \propto f_{\rm C} n_{\rm H} N_{\rm H}$).

2.2 THE IMPACT OF RESONANT SCATTERING

In §1.1, I have introduced the resonance behavior of the Lyα emission. Given this property, one should be concerned about the resonant scattering of Lyα photons produced by the central quasar itself. However, radiative transfer simulations of radiation originating from a bright quasar and passing through a simulated gas distribution have shown that the scattered Lyα photons from the quasar do not contribute significantly to the Lyα surface brightness of the gas on large scales, i.e. $\gtrsim 50$ kpc (Cantalupo et al. 2014). Indeed, the aforementioned diffusion in velocity space of the resonant process is so efficient that the vast majority of resonantly scattered photons produced by the quasar itself escape the system at very small scales $\lesssim 10$ kpc, and hence do not propagate at larger distances (e.g. Dijkstra et al. 2006b; Verhamme et al. 2006; Cantalupo et al. 2005). As the focus of this work is on giant nebulae, i.e. with scales of hundreds of kpc, based on the results of the radiative transfer simulations of Cantalupo et al. (2014), the contribution of resonant scattering of the quasar photons to the Lyα emission is neglected in the following Chapters. Similar considerations also apply to the resonant lines of metals (e.g. C IV). However we note that resonant scattering of metal lines is expected to be much less efficient, because the much lower abundance of metals imply the gas in the halo is much less likely to be optically thick in these emissions. Note, that, on the other hand, the 'scattered' Lyα photons arising from the diffuse continuum emission produced by the gas itself are taken into account in all the calculations in this work.

The assumption of a negligible contribution of resonant scattering on large scales, clearly has to be verified with dedicated observations, e.g. imaging polarimetry could be a good choice (see §1.3.1.4 for first attempts). However, in the remaining of the work, we will stick to this assumption, and discuss it where needed.

2.3 CAVEATS

As already clearly stated, the model presented in the current Chapter is extremely simple. Nevertheless, it appears to be a powerful and intuitive tool to understand the physics behind the more complex problem (see next Chapters and Hennawi & Prochaska 2013). Here, I highlight the main issues which should be taken into account for a more detailed modeling.

Interaction with hot gas: the present model only considers clouds of cool gas ($T \sim 10^4$ K). However, as mentioned in Chapter 1, a QSO's halo is expected to be permeated by shock-heated gas at $T \sim 10^7$ K. Several previous studies, which have conducted a similar modeling (Mo & Miralda-Escude 1996; Maller & Bullock 2004) on extended Lyα emission (Rees 1988; Haiman & Rees 2001; Haiman et al. 2000; Dijkstra & Loeb 2009b), have nearly always taken into account the presence of a hot medium in pressure equilibrium with the cold gas. The conclusions of the model of Hennawi & Prochaska (2013) (used in this work) do not depend on the existence of a hot phase, however, dedicated observations and simulations are needed to quantify the importance of the interaction between these two phases (e.g., Nelson et al. 2015).

Geometry: it is assumed that the emitting clouds are spatially uniformly distributed throughout a spherical halo. This simple representation would need geometric corrections to take into account more complicated gas distributions, such as a radially varying covering factor or filamentary structures. However, these corrections are likely sub-dominant as compared to other effects.

Single Uniform Cloud Population: this simple model assumes a single population of clouds, all of which have the same constant physical parameters $N_{\rm H}$ and $n_{\rm H}$, following a uniform spatial distribution throughout the halo. In reality one expects a distribution of cloud properties, and a radial dependence. Indeed, Binette et al. (1996) argued that a single population of clouds is not able to simultaneously explain both the high and low ionization lines present in the extended emission line regions of HzRGs, and instead invoked a mixed population of completely ionized and partially ionized clouds. While, in the case of extended emission line regions (EELRs) around quasars, which are on smaller scales $R < 50\,{\rm kpc}$ than the ones studied here, detailed photoionization modeling of spectroscopic data has demonstrated that at least two density phases are required: a diffuse and abundant cloud population with $n_{\rm H} \sim 1\ {\rm cm}^{-3}$, and a much scarce and dense cloud population with $n_{\rm H} \sim 500\,{\rm cm}^{-3}$ (Stockton et al. 2002; Fu & Stockton 2007; Hennawi et al. 2009). These clouds might be in pressure equilibrium with the ionizing radiation (Dopita et al. 2002, Stern et al. 2014), as has been invoked in models of the narrow-line regions of AGN. Future detailed modeling of multiple emission lines from giant nebulae, analogous to previous work done on the smaller scales of EELRs (Stockton et al. 2002; Fu & Stockton 2007), might provide information on multiple density phases.

Ionization cones of the QSO: as mentioned in §1.3.1.2, the opening angle of the ionization cones of QSOs is not well constrained. This model assumes that the QSO is shining simultaneously on the gas and towards us, i.e. AGN unification model (e.g., Urry & Padovani 1995). This assumption, however, probably requires a particular orientation of the ionizing cone with respect to the large scale filaments (or generally, to the surrounding gas distribution). This point clearly needs further studies and simulations.

In order to properly address the aforementioned issues, the ideal approach would be to conduct a full radiative transfer calculation on a three dimensional gas distribution, possibly taken from a cosmological hydrodynamical simulation, to try to reproduce the observational data. At the moment, carrying out such a complete modeling is not possible, as is briefly discussed in Chapter 7.

> *"We must look for consistency. Where there is a want of it we must suspect deception."*
>
> Arthur Conan Doyle, *The Problem of Thor Bridge*

Chapter 3

A DEEP NARROWBAND IMAGING SEARCH FOR C IV AND HE II EMISSION FROM LYα BLOBS

As described in §1.3.1.4, an enigmatic population of giant Lyα nebulae, the so-called LABs, has been recently discovered at high redshift. Despite intense interest, their nature is still controversial, although there is growing evidence that they are associated with AGN activity (Overzier et al. 2013; Prescott et al. 2015b). Our ignorance of the physical process powering the emission in LABs likely results from the current lack of other emission-line diagnostics besides the strong Lyα line.

In this Chapter, I attempt to remedy this problem, by searching for emission in two additional rest-frame UV lines, namely C IV λ1549 and He II λ1640. As explained in §1.3.2, these lines are powerful diagnostics for the physical conditions of the emitting gas. Here, I present deep narrowband imaging observations tuned to the C IV and He II emission lines of 13 LABs at $z \sim 3.1$ in the well-known SSA22 proto-cluster field (Steidel et al. 2000; Hayashino et al. 2004; Matsuda et al. 2004). Our observations exploit a fortuitous match between two narrowband filters on VLT/FORS2 and the wavelengths of the redshifted C IV and He II emission lines of a dramatic overdensity of LABs (and Lyα emitters, LAEs) in the SSA22 field (Matsuda et al. 2004), and achieve unprecedented depth. This overdensity results in a large multiplexing factor allowing us to carry out a sensitive census of C IV/Lyα and He II/Lyα line ratios for a statistical sample of LABs in a single pointing.

---

[*] This chapter is adapted from Arrigoni Battaia et al. (2015b). I am the main contributor of this work: I have conducted the data reduction, analysis and the modeling here reported.

3.1 OBSERVATIONS AND DATA REDUCTION

3.1.1 VLT/FORS2 OBSERVATIONS AND DATA REDUCTION

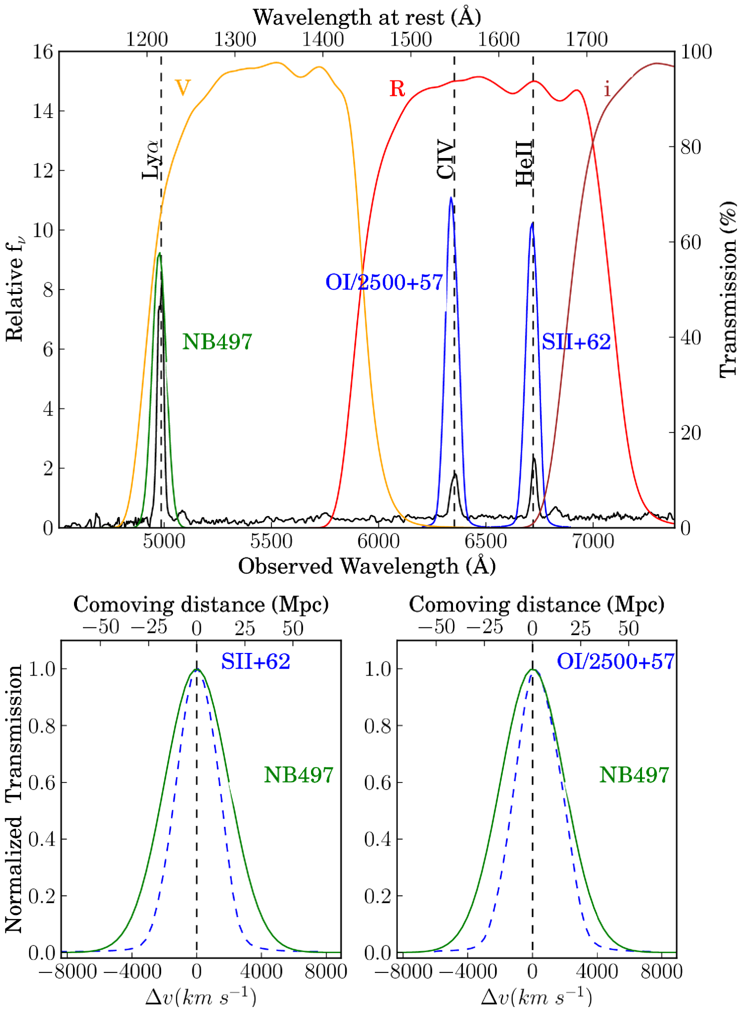

Figure 3.1: Top panel: Filter response profiles for the narrowband filters NB497 (green), SII+62 and OI/2500+57 (blue) and the broad-band filters *V* (orange), *R* (red) and *i* (brown) overplotted on a composite radio galaxy spectrum (McCarthy 1993). **Bottom panels:** Comparison between the NB497 (green) and the SII+62 and OI/2500+57 (dashed blue) filters shifted to match the narrowband filter used for Lyα (Matsuda et al. 2004). The filter curves are here normalized to their peak value and plotted with respect to the velocity and comoving distance probed. Note the nearly perfect match between the Lyα narrowband filter and the two FORS2 narrowband filters used for C iv λ1549 and He ii λ1640 in this work.

We obtained deep C iv and He ii narrowband images of 13 LABs in the SSA22 proto-cluster field, including the two largest LABs that were originally discovered by Steidel et al. (2000). Data were taken in service-mode using the FORS2 instrument on the VLT 8.2m telescope Antu (UT1) on 2010 August, September, October and 2011 September over 25 nights. We used two narrowband filters, O i/2500+57 and SII+62 matching the redshifted C iv λ1549 and He ii λ1640 at z = 3.1, respectively. The OI/2500+57 filter has a central wavelength of $\lambda_c \approx 6354$ Å and has a FWHM of $\Delta\lambda_{\rm FWHM} \approx 59$ Å, while the S ii+62 filter has $\lambda_c \approx 6714$ Å and $\Delta\lambda_{\rm FWHM} \approx 69$ Å (Fig. 3.1). These bandwidths provide a line-of-sight depth of $\Delta z \simeq 0.038$ and $\Delta z \simeq 0.042$, respectively for the O i/2500+57 and S ii+62 filter. Thus, given the typical uncertainties in the redshift measurements for the LABs (e.g. $z_{\rm LAB1} = 3.097 \pm 0.002$, Ohyama et al. 2003; $z_{\rm LAB2} = 3.103 \pm 0.002$, Matsuda

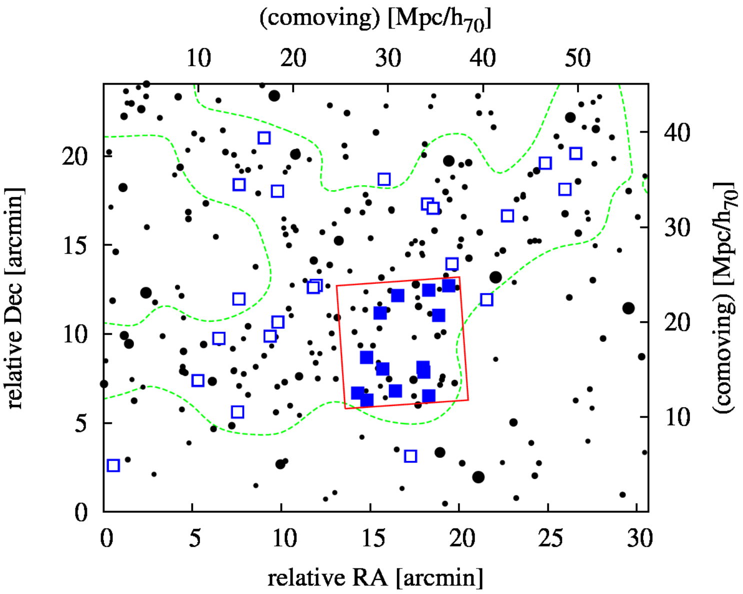

Figure 3.2: Spatial distribution of the Lyα emitters (black filled circles) and Lyα blobs (blue squares) in the SSA22 proto-cluster (Hayashino et al. 2004; Matsuda et al. 2004). The red box is the FOV of our FORS2 imaging (7′ × 7′) which includes 13 LABs (blue filled squares). The green dashed line indicates high-density region traced by the Lyα emitters.

et al. 2005), and the good agreement between the central wavelengths of the three narrow band filters used in this work (see Fig. 3.1), we are confident that, if present, the C IV and He II lines would fall within the targeted wavelength ranges. Note that very large velocity offsets (> 2000 km s^{-1}) with respect to the Lyα line would thus be required to bring the C IV or He II line outside our set of narrow-band filters. Such large kinematic offsets are not expected in these systems (e.g. Prescott et al. 2015b).

The FORS2 has a pixel scale of 0.25″ pixel^{-1} and a field of view (FOV) of 7′×7′ that allow us to observe a total of 13 LABs in a single pointing. The pointing was chosen to maximize the number of Lyα blobs while including the two brightest LABs, LAB1 and LAB2 (Steidel et al. 2000). In Figure 3.2, we show the spatial distribution of ~300 LAEs and 35 LABs in the SSA22 region, and mark the LABs within our FORS2 narrowband images.

The total exposure time was 19.9 and 19.0 hours for C IV and He II lines, respectively. These exposures consist of 71 and 68 individual exposures of ~17 minutes, taken with a dither pattern to fill in a gap between the two chips, and to facilitate the removal of cosmic rays. Because our targets are extended over 5″–17″ diameter and our primary goal is to detect the extended features rather than compact embedded galaxies, we carried out our observations under any seeing conditions (program ID: `085.A-0989`, `087.A-0297`). Figure 3.3 shows the distribution of FWHMs measured from stars in individual exposures. Although the observations were carried out under poor or variable seeing condition, the seeing ranges from 0.5″ to 1.4″ depending on the nights and the median seeing is ~0.8″ in both filters. In Table 1, we summarize our VLT/FORS2 narrowband observations.

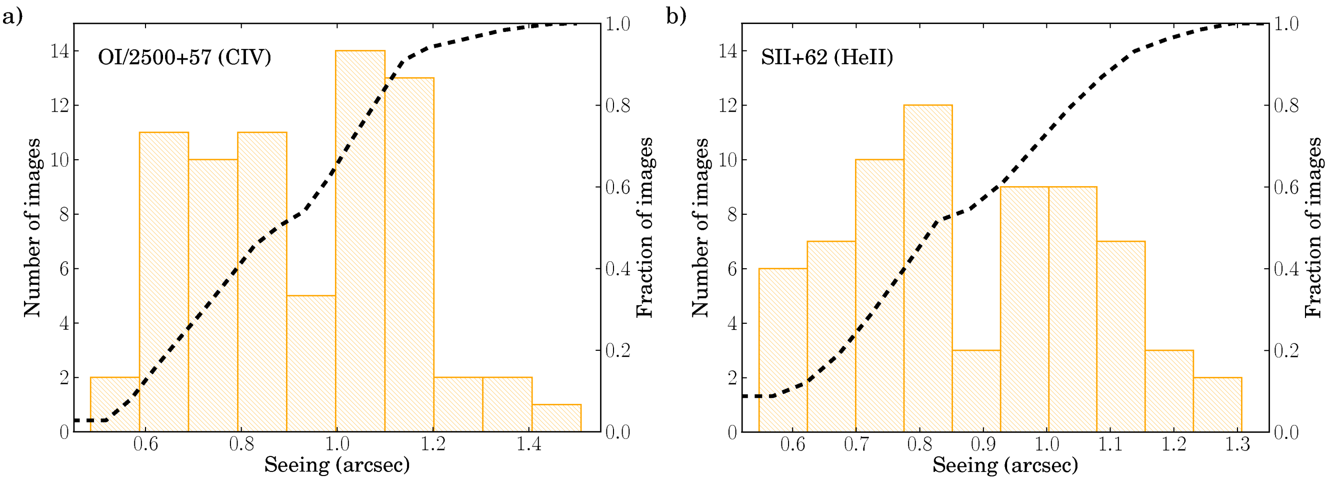

Figure 3.3: **(a)** Distribution of seeings for the OI/2500+57 (C iv λ1549) images. **(b)** Same for the SII+62 (He ii λ1640) images. The black dashed lines indicate the cumulative distribution. The median seeing is ~0.8″ for both C iv and He ii images.

The data were reduced with standard routines using `IRAF`[1]. The images were bias-subtracted and flat-fielded using twilight flats. To improve the flat-fielding essential for detecting faint extended emission across the fields, we further correct for the illumination patterns using night-sky flats. The night-sky flats were produced by combining the unregistered science frames with an average sigma-clipping algorithm after masking out all the objects. Satellite trails, CCD edges, bad pixels, and saturated pixels are masked. Each individual frame is cleaned from cosmic rays using the L.A.Cosmic algorithm (van Dokkum 2001). The astrometry was calibrated with the SDSS-DR7 *r*-band catalogue using `SExtractor` and `SCAMP` (Bertin 2006). The RMS uncertainties in our astrometric calibration are ~0.2″ for both C iv and He ii images.

The final stacks for each filter (C iv and He ii) were obtained using `SWarp` (Bertin et al. 2002): the individual frames were sky-subtracted using a background mesh size of 256 pixels (≈ 64″), then projected onto a common WCS using a *Lanczos3* interpolation kernel, and average-combined with weights proportional to flat and night-sky flat images. Note that we choose the mesh size to be large enough to ensure that we do not mistakenly subtract any extended emission as sky background. For flux calibration, we use four spectrophotometric standard stars (Feige110, EG274, LDS749B, and G158-100) that were repeatedly observed during our observations. Typical uncertainties in the derived zero-points are ≈0.03 mag.

---

[1] IRAF is the Image Analysis and Reduction Facility made available to the astronomical community by the National Optical Astronomy Observatories, which are operated by AURA, Inc., under contract with the U.S. National Science Foundation. STSDAS is distributed by the Space Telescope Science Institute, which is operated by the Association of Universities for Research in Astronomy (AURA), Inc., under NASA contract NAS 5–26555.

Table 3.1. VLT FORS2 Observations and Subaru Data

Telescope	Instrument	Filter (target line)	$\lambda^{a}_{\rm Central}$ (Å)	$\Delta\lambda^{b}_{\rm FWHM}$ (Å)	Seeing^{c} (arcsec)	Exp. Time (hours)	Depth^{d} (mag)	Pixel Scale (arcsec)
VLT	FORS2	OI/2500+57 (CIV)	6354	59	0.8	19.9	25.9	0.25
VLT	FORS2	SII+62 (HeII)	6714	69	0.8	19.0	26.5	0.25
Subaru^{e}	S-Cam	NB497 (Lyα)	4977	77	1.0	7.2	26.2	0.20
Subaru^{e}	S-Cam	R	6460	1177	1.0	2.9	26.7	0.20

[a] Central wavelength of the filter.

[b] FWHM of the filter.

[c] Median seeing of our FORS2 observations and average seeing of the Subaru data (Matsuda et al. 2004).

[d] 5σ detection limit for $2''$-diameter aperture.

[e] Images from Hayashino et al. (2004); Matsuda et al. (2004).

3.1.2 SUBARU SUPRIME-CAM DATA

To subtract continuum from our narrowband images and compare the C IV and He II line fluxes with those of Lyα, we rely on previous Subaru observations. The SSA22 field has been extensively observed in B, V, R, i', and NB497 bands (Hayashino et al. 2004, Matsuda et al. 2004) with the Subaru Suprime-Cam (Miyazaki et al. 2002). These images have a pixel scale of $0.20''$ pixel^{-1} and a FOV of $34'\times 27'$. The NB497 narrowband filter, tuned to Lyα line at $z \sim 3.1$, has a central wavelength of 4977 Å and a FWHM of 77 Å. The total exposure time for the Lyα narrowband image was 7.2 hours with a 5σ sensitivity of 5.5×10^{-18} erg s^{-1} cm^{-2} arcsec^{-2} per 1 arcsec^{2} aperture, which is roughly 1.5 – 2.5 times shallower than those of FORS2 He II and C IV images. In Table 1, we summarize the Subaru broadband and narrowband images that were used in this work.

Using these deep Subaru data, Matsuda et al. (2004) found 35 LABs, defined to be Lyα emitters with the observed EW(Lyα) $>$ 80 Å and an isophotal area larger than 16 arcsec^{2}, which corresponds to a spatial extent of 30 kpc at $z = 3$. The isophotal area was measured above the 2σ surface brightness limit (2.2×10^{-18} erg s^{-1} cm^{-2} arcsec^{-2}). In Table 3.2, we list the properties (e.g., Lyα luminosity and isophotal area) of the 13 LABs that were observed with VLT/FORS2. We refer the Reader to Matsuda et al. (2004) and to §1.3.1.4 for more details on this Lyα blob sample.

Table 3.2. Properties of the 13 LABs in our sample.

Object	F(Lyα) (1)	L(Lyα) (2)	Area (3)	SB (Lyα) (4)	SB (C IV) (5)	SB (He II) (6)	C IV/Lyα (7)	He II/Lyα (8)
LAB1	9.4	7.8	200	4.7	<0.74	<0.50	<0.16	<0.11
LAB2	8.2	6.8	145	5.6	<0.89	<0.63	<0.16	<0.11
LAB7	1.3	1.1	36	3.6	<1.19	<0.99	<0.33	<0.27
LAB8	1.5	1.3	36	4.2	<1.24	<0.93	<0.29	<0.22
LAB11	0.8	0.6	28	2.8	<1.23	<1.08	<0.44	<0.38
LAB12	0.7	0.6	27	2.7	<1.29	<1.06	<0.48	<0.39
LAB14	1.1	0.9	25	4.5	<1.38	<1.10	<0.31	<0.24
LAB16	1.0	0.9	25	4.1	<1.39	<1.07	<0.34	<0.26
LAB20	0.6	0.5	22	2.8	<1.35	<1.16	<0.48	<0.41
LAB25	0.6	0.5	22	2.7	<1.36	<1.12	<0.50	<0.41
LAB30	0.9	0.8	17	5.8	<1.45	<1.36	<0.25	<0.23
LAB31	1.2	1.0	19	6.6	<1.44	<1.18	<0.22	<0.18
LAB35	1.0	0.8	17	5.9	<1.52	<1.29	<0.26	<0.22

Note. — (1) Lyα line flux within the isophote in 10^{-16} erg s^{-1} cm^{-2}, (2) Lyα luminosity in 10^{43} erg s^{-1}, (3) isophotal area in arcsec^2 above 2.2×10^{-18} erg s^{-1} cm^{-2} arcsec^{-2}, (4) average surface brightness within the isophote, (5) 5σ upper limits on C IV surface brightness, (6) 5σ upper limits on He II surface brightness, (7–8) 5σ upper limits C IV/Lyα and He II/Lyα line ratios. All surface brighnesses are given in unit of 10^{-18} erg s^{-1} cm^{-2} arcsec^{-2}.

3.1.3 CONTINUUM SUBTRACTION

To identify the emission in the C IV λ1549 and He II λ1640 lines we subtract the continuum emission underlying the OI/2500+57 and SII+62 filter. We estimate the continuum using the deep Subaru R band image. Because the Subaru and FORS2 images have different pixel scales, we resample the R-band image to the FORS2 pixel scale and register them to our WCS in order to compare all the images pixel by pixel. We do not match the point spread functions (PSFs) given that FORS2 images were obtained with a wide range of seeing and we are mostly interested in the extended emission. We produce the continuum subtracted image for each filter (C IV and He II) using the following relations (Yang et al. 2009):

$$f^{BB}_{\lambda,\mathrm{cont}} = \frac{F_{BB} - F_{NB}}{\Delta\lambda_{BB} - \Delta\lambda_{NB}} \tag{3.1}$$

$$F_{\mathrm{line}} = F_{NB} - f^{BB}_{\lambda,\mathrm{cont}}\Delta\lambda_{NB}, \tag{3.2}$$

where F_{BB} is the flux in the R band, F_{NB} is the flux in one of the narrowband filters. $\Delta\lambda_{BB}$ and $\Delta\lambda_{NB}$ represent the FWHM of the R and narrowband filters, respectively. $f^{BB}_{\lambda,\mathrm{cont}}$ is the flux density of the continuum within the R band, and F_{line} is the line flux (C IV or He II).

Note that the R-band image includes both the C IV and He II lines, but here we adopt a simple approximation assuming that one emission line within the R-band (e.g. He II) is negligible in estimating the flux of the other emission line (e.g. C IV). For example, we would underestimate the line flux of C IV by $> 10\%$ if the flux in He II were $F_{\rm line} \gtrsim 2 \times 10^{-17}$ erg s^{-1} cm^{-2}, which is easily detectable in our deep images. We use these simple equations because we aim to minimize the systemic effects such as poor PSF matching and imperfect sky subtraction. Note that we have also tried the continuum subtraction with two off-band images (V and i'), as explained in Section §3.1.4.

3.1.4 SURFACE BRIGHTNESS LIMITS

We compute a global surface brightness limit for detecting He II and C IV lines using a global root-mean-square (rms) of the images. To calculate the global rms per pixel, we first mask out the sources, in particular the scattered light and halos of bright foreground stars, and compute the standard deviation of sky regions using a sigma-clipping algorithm. We convert these rms values into the surface brightness (SB) limits *per* 1 sq. arcsec aperture. We find that the 1σ detection limit per 1 arcsec^2 aperture (SB$_1$) is 4.2×10^{-19} and 6.8×10^{-19} erg s^{-1} cm^{-2} arcsec^{-2} for He II and C IV, respectively. These represent the deepest He II λ1640 and C IV λ1549 narrow-band images ever taken.

The sensitivity required to detect an extended source depends on its size because one can reach lower surface brightness levels by spatially averaging. In an ideal case of perfect sky and continuum subtraction, the 1σ SB limit for an extended source is given by ${\rm SB}_1/\sqrt{A_{\rm src}}$, where $A_{\rm src}$ is the isophotal area in arcsec^2 and SB$_1$ is the surface brightness limit per 1 arcsec^2 aperture. However, in practice the actual detection limits are limited by systematics resulting from imperfect sky and continuum subtraction. Therefore, we empirically determine the detection limits for extended sources with different sizes as follows.

In the continuum-subtracted line images, we mask all the artifacts (e.g., CCD edges and scattered light from bright stars) and also the locations of the LABs. For each LAB that we consider, we randomly place circular apertures with the same area of the LAB and extract the fluxes ($F_{\rm src}$) within these apertures. If the images have uniform noise properties in the absence of systematics, the fluxes ($F_{\rm src}$) from many random apertures should follow a Gaussian distribution with a width of $\sigma_{\rm src} \equiv {\rm SB}_1 \sqrt{A_{\rm src}}$. We find that the actual Gaussian width ($\sigma'_{\rm src}$) of the distribution is much broader than $\sigma_{\rm src}$ (Fig. 3.4 and 3.5). We adopt $F_{\rm limit} \equiv \sigma'_{\rm src}$ as a 1σ upper limit on the total line flux of each LAB. The corresponding upper limit for the surface brightness is given by ${\rm SB}_{\rm limit} \equiv F_{\rm limit}/A_{\rm src}$.

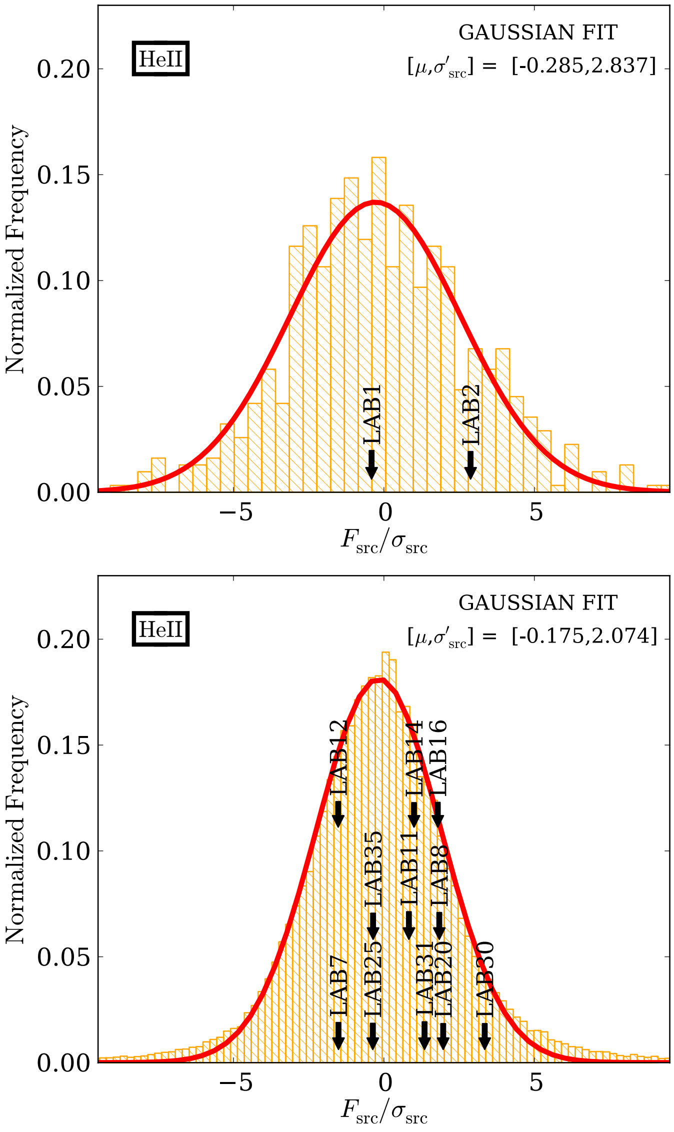

Figure 3.4: Analysis of the systematics in the He II line image. **Upper panel:** Distribution of the normalized flux, $F_{\rm src}/\sigma_{\rm src}$ for random circular apertures with the same extent as LAB1 and LAB2. Here, $F_{\rm src}$ is a total flux within an aperture and $\sigma_{\rm src}$ is the expected 1σ flux limit in an ideal case with uniform noise properties, i.e., $\sigma_{\rm src} = {\rm SB}_1 \sqrt{A_{\rm src}}$. The Gaussian fit to the histogram is highlighted in red. The observed values for LAB1 and LAB2 are shown by the black arrows. **Lower panel:** Same for all the other LABs with $A_{\rm src} < 40$ arcsec^2 in our sample. The black arrows indicate the value of each LAB. Note that in the absence of systematics, i.e., in ideal conditions when the sky and continuum subtractions are perfect, these histograms should be a Gaussian with unit variance, but they are ≈ 3 or ≈ 2 times broader, i.e., $\sigma'_{\rm src} \approx 2-3\,\sigma_{\rm src}$.

Figure 3.4 and 3.5 show the distribution of $F_{\rm src}/\sigma_{\rm src}$ for He II and C IV images, respectively. Note that we normalize the extracted fluxes to the $\sigma_{\rm src}$ in order to show the distributions for LABs with similar sizes in one plot. As the size of the LABs in our sample spans a large range, we show the distributions for two sub-samples: one for LAB1 and LAB2 with $A_{\rm src} > 100$ arcsec^2 and the other for the remaining LABs with $A_{\rm src} < 40$ arcsec^2. As previously stated, in the ideal case of no systematics, $\sigma_{\rm src}$ characterizes the noise in $F_{\rm src}$, and thus the distribution of the quantity $F_{\rm src}/\sigma_{\rm src}$ should be a Gaussian with unit variance. For both sub-samples, we find that $F_{\rm src}/\sigma_{\rm src}$ histograms show a variance greater than unity, suggesting that imperfect sky and continuum subtraction dominates our error budget. The normalized histograms have a standard deviation of ≈ 3 on the scale of the bigger LABs (LAB1 and LAB2), and ≈ 2 on the scale of the smaller LABs. Thus, as our 1σ limit on the total line flux of the largest LABs in our sample (LAB1 and LAB2), we adopt

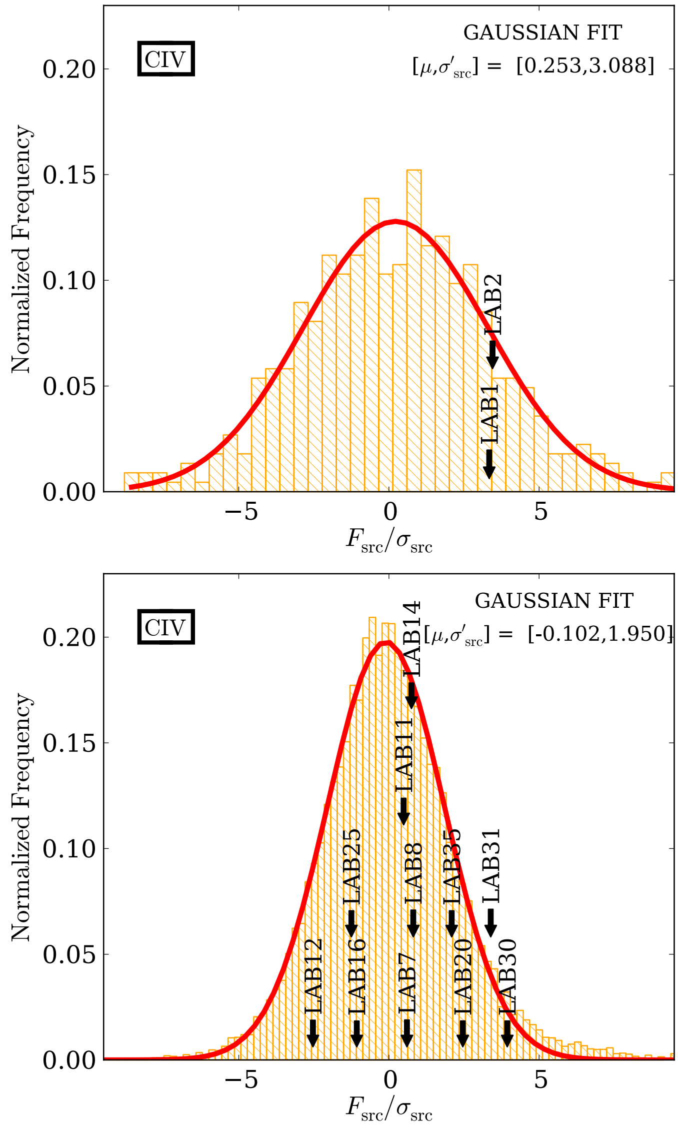

Figure 3.5: Analysis of the systematics in the C IV line image. **Upper panel:** Distribution of the normalized flux, $F_{\rm src}/\sigma_{\rm src}$ for random circular apertures with the same extent as LAB1 and LAB2. Here, $F_{\rm src}$ is a total flux within an aperture and $\sigma_{\rm src}$ is the expected 1σ flux limit in an ideal case with uniform noise properties, i.e., $\sigma_{\rm src} = {\rm SB}_1\sqrt{A_{\rm src}}$. The Gaussian fit to the histogram is highlighted in red. The observed values for LAB1 and LAB2 are shown by the black arrows. **Lower panel:** Same for all the other LABs with $A_{\rm src} < 40$ arcsec^2 in our sample. The black arrows indicate the value of each LAB. Note that in the absence of systematics, i.e., in ideal conditions when the sky and continuum subtractions are perfect, these histograms should be a Gaussian with unit variance, but they are ≈ 3 or ≈ 2 times broader, i.e., $\sigma'_{\rm src} \approx 2-3\,\sigma_{\rm src}$.

$F_{\rm limit} \equiv \sigma'_{\rm src} = 3\sigma_{\rm src}$, where $\sigma_{\rm src} \equiv {\rm SB}_1\sqrt{A_{\rm src}}$ is computed using the area of the blob. For all of the other blobs in our sample, we follow the same approach but use a value $F_{\rm limit} \equiv \sigma'_{\rm src} = 2\sigma_{\rm src}$. We conservatively define our detection threshold to be $5\sigma'_{\rm src}$, which formally means $15\sigma_{\rm src}$ for LAB1 and LAB2, and $10\sigma_{\rm src}$ for all the other blobs. In each histogram, we show the values extracted inside the isophotal contours of each LAB (black arrows). These values are well within the distribution of $F_{\rm src}/\sigma_{\rm src}$ determined from random apertures (see Table 3.3).

To test if our derived detection limits are reasonable, we visually confirm the detectability as a function of size by placing artificial model sources in He II and C IV narrowband images. We adopt circular top-hat sources with a uniform surface brightness corresponding to 1, 2, 3, 4, 5, 8, 10, 20 ${\rm SB}_{\rm limit}$, and an area of 200, 100, 40 and 20 arcsec^2, comparable to the size of the

Table 3.3. Extracted fluxes and significance for the 13 LABs in our sample.

Object	F(He II) (1)	F(C IV) (2)
LAB1	-2.98 (-0.41)	31.19 (3.34)
LAB2	17.81 (2.88)	27.47 (3.45)
LAB7	-4.63 (-1.51)	2.38 (0.60)
LAB8	5.69 (1.84)	3.22 (0.81)
LAB11	2.56 (0.83)	1.96 (0.49)
LAB12	-4.04 (-1.52)	-8.68 (-2.53)
LAB14	2.59 (1.00)	2.49 (0.75)
LAB16	4.64 (1.79)	-3.56 (-1.07)
LAB20	4.78 (1.97)	7.69 (2.46)
LAB25	-0.89 (-0.37)	-3.91 (-1.25)
LAB30	7.06 (3.35)	10.67 (3.94)
LAB31	3.02 (1.35)	9.74 (3.39)
LAB35	-0.76 (-0.36)	5.75 (2.09)

Note. — (1) He II line flux in 10^{-18} erg s^{-1} cm^{-2} extracted within the isophotal area defined in Matsuda et al. (2004), (2) C IV line flux in 10^{-18} erg s^{-1} cm^{-2}. For each value is given in brackets the statistical significance with respect to $\sigma_{\rm src}$.

LABs in our sample (see Table 3.2). After placing the simulated sources in the narrowband images, we subtract the continuum in the same way as explained in Section §3.1.3. Because the detectability strongly depends on the residual structure of the continuum subtraction, we place the model sources at different locations in the narrowband images after masking all the bad regions as explained above. Following Hennawi & Prochaska (2013), we construct a χ image by dividing the continuum-subtracted image by a "sigma" image. Here, the sigma image (or the square root of the variance image) is calculated by taking into account our stacking procedure, e.g., bad pixels, satellite trails and sky subtraction. In other words, this variance image is the theoretical photon counting noise variance, taking into account all the bad-behaving pixels. In this calculation, we do not include the variance due to R-band continuum, i.e., we ignore the photon counting noise from R-band image, thus it is likely that our sigma image might slightly underestimate the noise. Note however that the shallower NB images are very likely dominating the noise, thus the R-band contribution to the variance is a small correction.

To test the detectability of extended emission, we compute a smoothed χ image following the technique in Hennawi & Prochaska (2013). First, we smooth an image:

$$I_{\rm smth} = {\rm CONVOL[NB - CONTINUUM]}, \tag{3.3}$$

where the CONVOL operation denotes convolution of the stacked images with a Gaussian kernel with FWHM=2.35″. Then, we calculate the sigma image ($\sigma_{\rm smth}$) for the smoothed image ($I_{\rm smth}$) by propagating the variance image of the unsmoothed data:

$$\sigma_{\rm smth} = \sqrt{{\rm CONVOL}^2[\sigma^2_{\rm unsmth}]}, \tag{3.4}$$

where the CONVOL^2 operation denotes the convolution of variance image with the square of the Gaussian kernel. Thus, the smoothed χ image is defined by

$$\chi_{\rm smth} = \frac{I_{\rm smth}}{\sigma_{\rm smth}}. \tag{3.5}$$

This $\chi_{\rm smth}$ is more effective in visualizing the presence of extended emission.

Figure 3.6 and 3.7 show the $\chi_{\rm smth}$ for the simulated sources for He ii and C iv images, respectively. For each detection significance and source size, the simulated sources are shown for two different positions within the He ii or the C iv images. To guide the eye, these positions are highlighted by a black circle. These simulated $\chi_{\rm smth}$ images confirm that we should be able to detect extended emission down to a level of 5SB$_{\rm limit}$, justifying our choice for this detection threshold. Note again that SB$_{\rm limit}$ includes the correction we made to take into account the systematics.

In addition to the previous analysis, in order to further test our continuum subtraction, we also performed the continuum subtraction using two off-band images (V and i'; Hayashino et al.

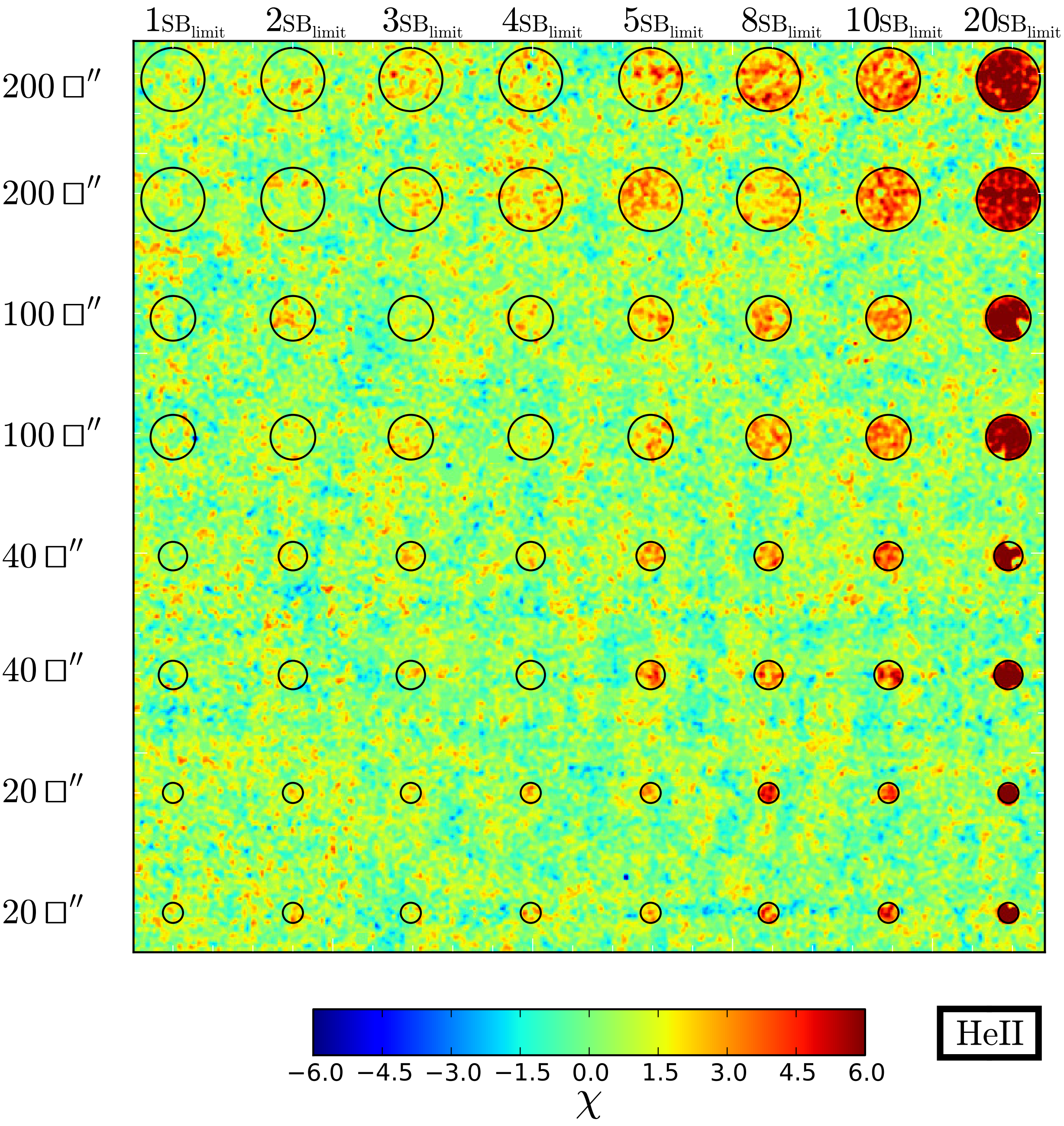

Figure 3.6: Illustration of detection significance of the simulated sources as a function of sizes in the He ɪɪ line. The panel shows the χ_{smth} image for the simulated sources with circular top-hat profile with uniform surface brightness. From top to bottom, the simulated sources are placed as follow: two rows for each area (200, 100, 40, 20 arcsec^2) with a surface brightness level of 1, 2, 3, 4, 5, 8, 10, 20 SB$_{\rm limit}$. The black circles indicate the position of the simulated sources. Note that we should be able to detect sources down to a sensitivity limit of 5SB$_{\rm limit}$, which corresponds to SB(HeII) = 5.02×10^{-19} erg s^{-1} cm^{-2} arcsec^{-2} for an area of 200 arcsec^2 (i.e. LAB1). The same stretch and color schemes are adopted in Figures 3.7 and 3.10.

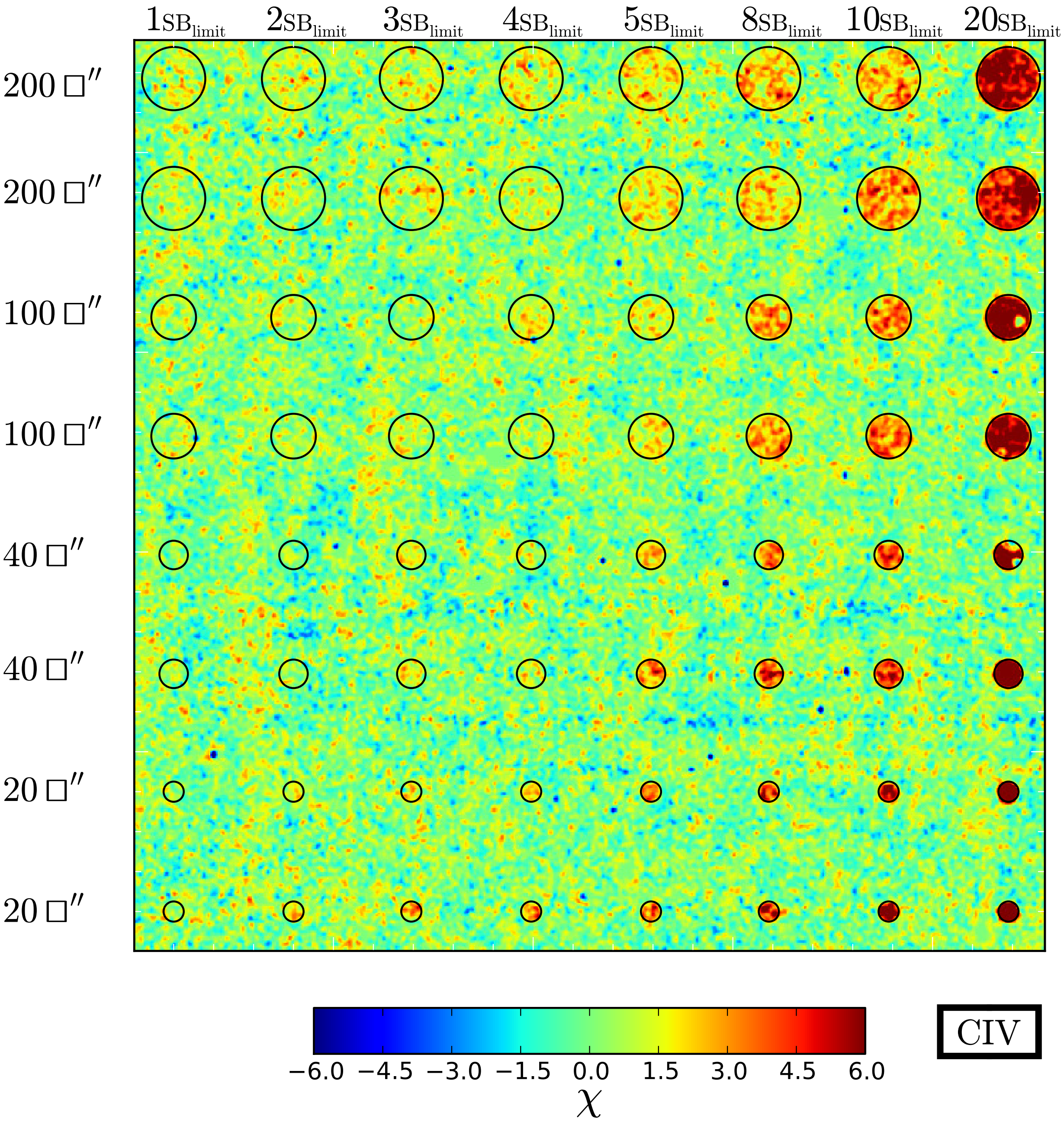

Figure 3.7: Illustration of detection significance of the simulated sources as a function of sizes in the C iv line. The panel shows the χ_{smth} image for the simulated sources with circular top-hat profile with uniform surface brightness. From top to bottom, the simulated sources are placed as follow: two rows for each area (200, 100, 40, 20 arcsec^2) with a surface brightness level of 1, 2, 3, 4, 5, 8, 10, 20 SB$_{\rm limit}$. The black circles indicate the position of the simulated sources. Note that we should be able to detect sources down to a sensitivity limit of 5SB$_{\rm limit}$, which corresponds to SB(CIV) = 7.36×10^{-19} erg s^{-1} cm^{-2} arcsec^{-2} for an area of 200 arcsec^2 (i.e. LAB1). The same stretch and color schemes are adopted in Figures 3.6 and 3.10.

2004), finding that the results remain unchanged. Note however, that due to the differences in the telescope PSFs and seeing of the observations, the use of two bands increases the noise. Thus, we prefer to estimate the continuum using only the *R*-band image.

3.2 OBSERVATIONAL RESULTS

In Figure 3.8 and 3.9, we show the postage-stamp images for the 13 LABs in our sample. Each row displays the *R*-band, the continuum-subtracted Lyα line image, the narrowband image of the C IV λ1549 line, the continuum-subtracted C IV line image, the He II λ1640 narrowband image, and the continuum-subtracted He II line image, respectively. The red contours indicate the isophotal aperture of LABs defined as the area above 2σ detection limit for the Lyα emission as originally adopted by Matsuda et al. (2004), i.e. 2.2×10^{-18} erg s^{-1} cm^{-2} arcsec^{-2}. The continuum-subtracted C IV and He II line images are nearly flat and lack significant large-scale residuals, indicating good continuum and background subtraction. Note that there could be still some residuals within the isophotal apertures (e.g., LAB2) because of minor mis-alignment between *R*-band and our narrowband images. However, these residuals do not affect our flux and surface brightness measurements. We do not detect any extended C IV or He II emission on the scale of the Lyα line in any of the LABs.

In order to better visualize these non-detections, we compute the χ and $\chi_{\rm smth}$ described in §3.1.4 for each LAB (using the pure photon counting noise estimates). Figure 3.10 shows the χ images and the $\chi_{\rm smth}$ images of $30'' \times 30''$ (corresponding to 230 kpc × 230 kpc at $z = 3.1$) centered on each LAB. A comparison of the $\chi_{\rm smth}$ images of the individual Lyα blobs with the simulated images in Figures 3.6 and 3.7 shows that we do not detect any extended emission in the HeII and CIV lines for the 13 LABs down to our sensitivity limits of 5SB$_{\rm limit}$ defined in Section §3.1.4. Note that we show images in Figures 3.6, 3.7 and 3.10 with the same stretch and color scheme for a fair comparison.

We thus place conservative upper limits, i.e. 5SB$_{\rm limit}$, on both C IV λ1549 and He II λ1640 surface brightness for each of the LABs. For LAB1 (area 200 arcsec^2), these limits correspond to SB(He II) = 5.02×10^{-19} erg s^{-1} cm^{-2} arcsec^{-2} and SB(C IV) = 7.36×10^{-19} erg s^{-1} cm^{-2} arcsec^{-2}. In Table 3.2, we summarize all of our upper limits, the properties of Lyα lines, and the resulting upper limits on the C IV/Lyα and He II/Lyα flux ratios. Note that the most stringent limits on these ratios are obtained for the brightest LAB1 and LAB2 given their larger Lyα isophotal area and luminosities. Coincidentally, these two LABs show the same values, F(He II)/F(Lyα) < 0.11 and F(C IV)/F(Lyα) < 0.16, because the difference in the area (LAB1 is larger than LAB2) is compensated by the difference in Lyα SB (LAB2 has a SB higher than LAB1). In what follows,

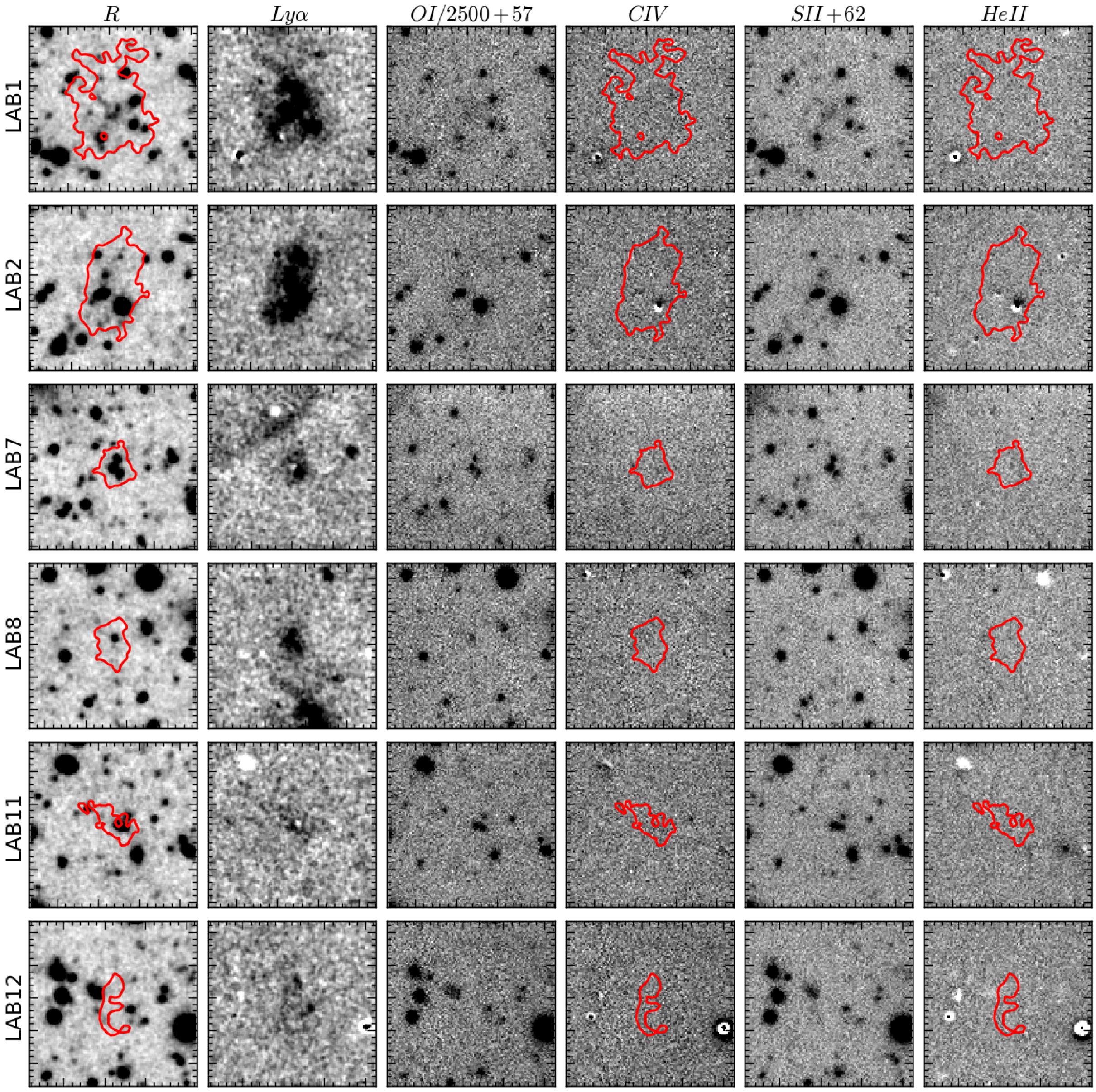
R
$Ly\alpha$
$OI/2500+57$
CIV
$SII+62$
$HeII$
LAB1
LAB2
LAB7
LAB8
LAB11
LAB12

Figure 3.8: Postage-stamp images of 30″× 30″(corresponding to about 230 kpc × 230 kpc at z = 3.1) centered on LAB1, LAB2, LAB7, LAB8, LAB11, and LAB12. From left to right: R-band, Lyα, O I/2500+57 (NB C IV), C IV λ1549, S II+62 (NB He II), and He II λ1640. On the R-band, C IV λ1549, and He II λ1640, is over-plotted the 2σ isophotal aperture of the Lyα emission (red line) as adopted by Matsuda et al. (2004). Note the lack of extended emission in the C IV λ1549 and He II λ1640 in comparison with the outstanding Lyα line. North is up, East is left.

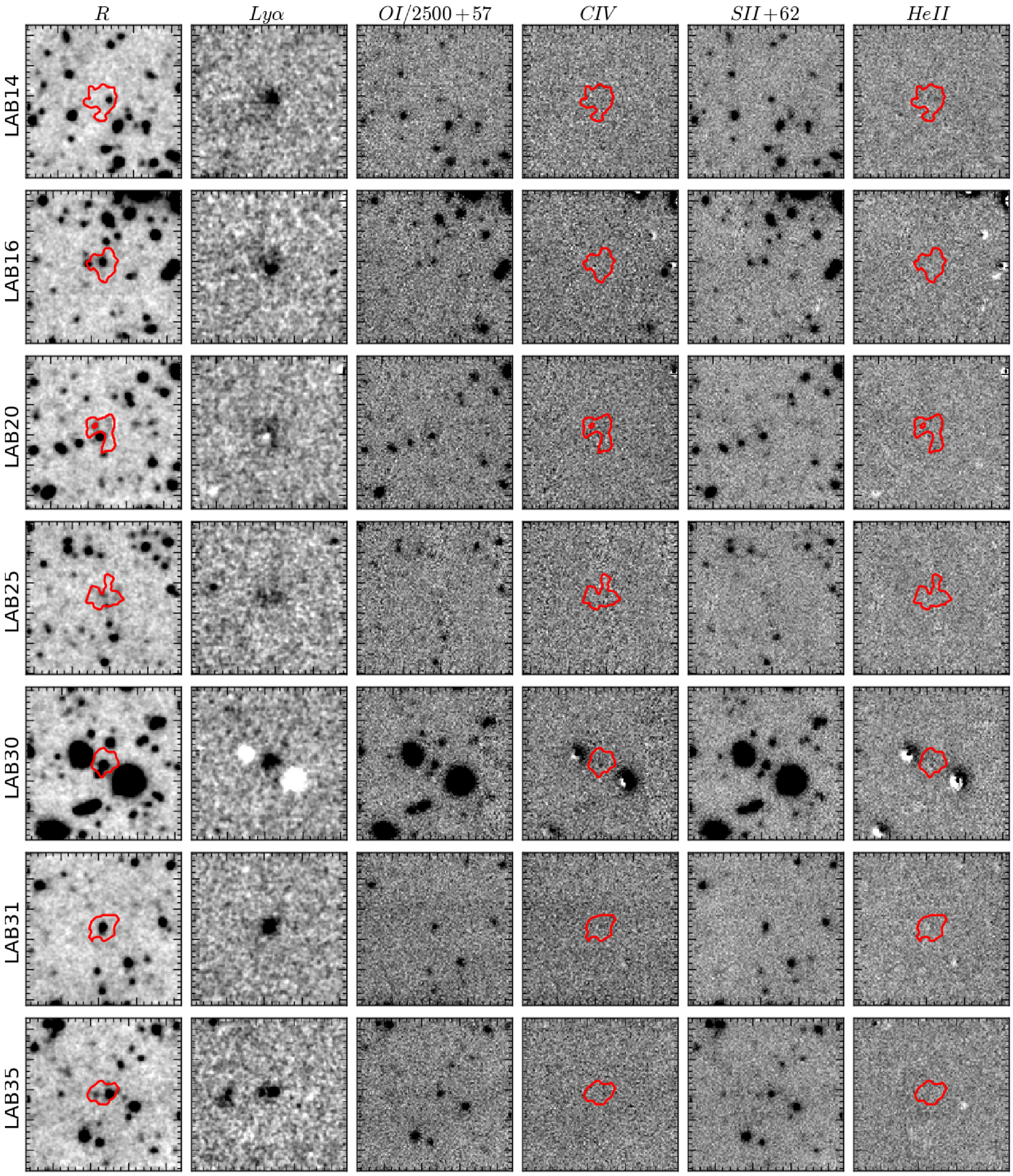
R
$Ly\alpha$
$OI/2500+57$
CIV
$SII+62$
$HeII$
LAB14
LAB16
LAB20
LAB25
LAB30
LAB31
LAB35

Figure 3.9: Postage-stamp images of 30″× 30″(corresponding to about 230 kpc × 230 kpc at $z = 3.1$) centered on LAB14, LAB16, LAB20, LAB25, LAB30, LAB31, and LAB35. From left to right: R-band, Lyα, O I/2500+57 (NB C IV), C IV λ1549, S II+62 (NB He II), and He II λ1640. On the R-band, C IV λ1549, and He II λ1640, is over-plotted the 2σ isophotal aperture of the Lyα emission (red line) as adopted by Matsuda et al. (2004). Note the lack of extended emission in the C IV λ1549 and He II λ1640 in comparison with the outstanding Lyα line. North is up, East is left.

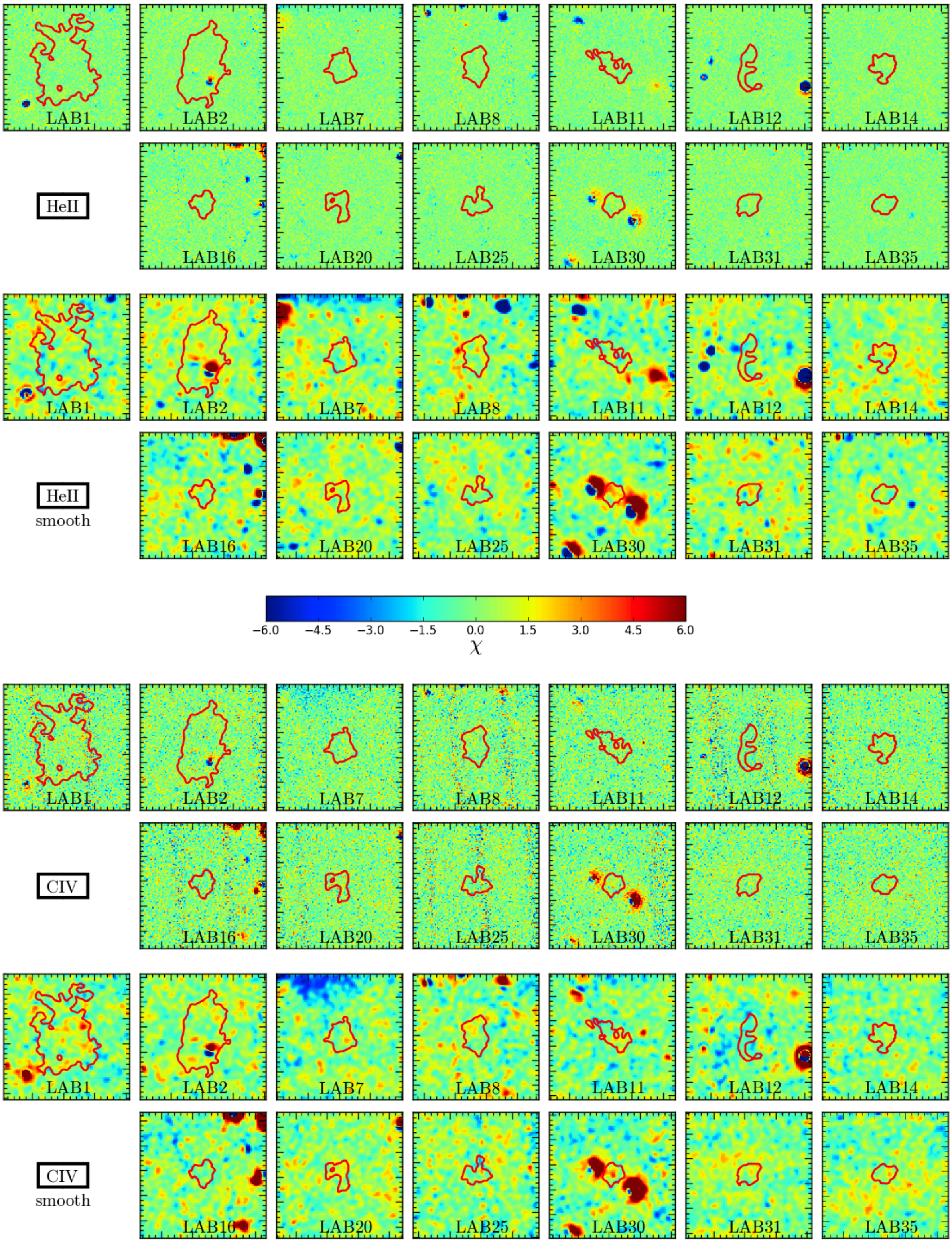
LAB1
LAB2
LAB7
LAB8
LAB11
LAB12
LAB14
HeII
LAB16
LAB20
LAB25
LAB30
LAB31
LAB35
LAB1
LAB2
LAB7
LAB8
LAB11
LAB12
LAB14
HeII
smooth
LAB16
LAB20
LAB25
LAB30
LAB31
LAB35
−6.0
−4.5
−3.0
−1.5
0.0
1.5
3.0
4.5
6.0
χ
LAB1
LAB2
LAB7
LAB8
LAB11
LAB12
LAB14
CIV
LAB16
LAB20
LAB25
LAB30
LAB31
LAB35
LAB1
LAB2
LAB7
LAB8
LAB11
LAB12
LAB14
CIV
smooth
LAB16
LAB20
LAB25
LAB30
LAB31
LAB35

Figure 3.10: Postage-stamp χ and $\chi_{\rm smth}$ images of the 13 LABs in our sample (§3.1.4). Each postage-stamp has a size of $30'' \times 30''$ (corresponding to about 230 kpc × 230 kpc at $z = 3.1$). To guide the eye, on each image is overplotted the 2σ isophotal aperture of the Lyα emission (red line) as adopted by Matsuda et al. (2004). A comparison with Figures 3.6-3.7 suggest that we did not detect any extended emission from any of the sources in our sample. Note that we used the same stretch and colormap as in Figure 3.6 and 3.7. Residuals from bright foreground objects due to minor mis-alignment between our data and SUBARU data are clearly visible. North is up, East is left.

we compare our limits to previous constraints on HeII and CIV in other nebulae, and then discuss the implications of our non-detections.

3.3 Previous Observations of He ii and C iv

We compile He ii and C iv line observations of extended Lyα nebulae from the literature, finding data for five Lyα blobs (Dey et al. 2005; Prescott et al. 2009, 2013, summarized in Table 3.4), Lyα nebulae associated with 53 high redshift radio galaxies (Humphrey et al. 2008; Villar-Martín et al. 2007a, which is a compilation mainly from De Breuck et al. 2001, Roettgering et al. 1997, and Vernet et al. 2001), and five radio-loud QSOs (Heckman et al. 1991a,b; Humphrey et al. 2013). However, a straightforward comparison is restrained by the following issues. First of all, these data are obtained with various different techniques (e.g., narrowband imaging, longslit spectroscopy, integral-field unit spectroscopy), and employ varied analysis methods (e.g., different extraction apertures), which result in different definitions of SB limits. Thus, a major uncertainty in comparing our data with the previous measurements are differences in the aperture for which these line fluxes or ratios are reported. In particular, our upper limits are computed over the entire Lyα nebulae defined by the 2σ Lyα isophotal apertures of Matsuda et al. (2004) (e.g. see Figures 3.8 and 3.9), above a Lyα surface brightness limit of 2.2×10^{-18} erg s^{-1} cm^{-2} arcsec^{-2}, and because of the use of narrow-band imaging, we can probe the whole extent of the source. On the other hand, in the case of LABs (Prescott et al. 2013; Dey et al. 2005) and HzRGs (Villar-Martín et al. 2007a), the lines are extracted from smaller aperture forcedly defined by the slit, sampling a particular position within the nebula. For example, in the case of HzRGs (De Breuck et al. 2000), the lines are typically measured from a one-dimensional spectra extracted by choosing the aperture which includes the most extended emission line, and typically the slit is oriented along the radio axis.

To further complicate the comparison, for HzRGs and QSOs where a bright central source is known to exist, it is difficult to separate the emission generated near the central source from the nebula itself. For example, for the radio-loud QSOs, Heckman et al. (1991a,b) carefully removed the contribution from the central QSOs in both the imaging and the spectroscopic analysis, thus these line ratios should only reflect the line emission in the extended nebulae[2]. In the case of HzRGs, the NLR can contaminate the emission on scales of a few kpc from the central source. However, in the measurements for HzRGs no attempt is made to exclude a possible contribution from this emission. While in the case of the LABs, the neglect of the contribution of the sources

---

[2] Heckman et al. (1991a,b) removed the continuum from the narrowband images and estimated the contribution of the QSO to the Lyα nebula by subtracting a scaled PSF. In the spectroscopic analysis, they iteratively subtracted a scaled version of the nuclear spectrum from the off-nuclear ones, until all traces of continuum flux near Lyα vanished.

Table 3.4. Properties of He ii and C iv emission from LABs in the literature.

Object	F (Lyα) (1)	SB (Lyα) (2)	Max. extent (3)	F (CIV) (4)	F (HeII) (5)	Aperture (6)	Reference
LABd05[a]	28.9(NB)/3.10 (spectrum)	9.20/45.9	20	0.42	0.41	4.5″× 1.5″	Dey et al. 2005
PRG1	4.36	58.1	5.0	0.21	0.57	5.0″× 1.5″	Prescott et al. 2009
PRG2	4.92	41.8	7.84	0.18	0.18	7.84″× 1.5″	Prescott et al. 2013
PRG3	1.02	12.1	5.60	<0.08	< 0.09	5.60″× 1.5″	Prescott et al. 2013
PRG4	1.03	40.9	1.68	<0.08	0.07	1.68″× 1.5″	Prescott et al. 2013

Note. — (1) Lyα line flux in 10^{-16} erg s^{-1} cm^{-2}, (2) Lyα surface brightness in 10^{-18} erg s^{-1} cm^{-2} arcsec^{-2}, (3) maximum extent in arcsec. (4) C iv line flux in 10^{-16} erg s^{-1} cm^{-2} arcsec^{-2}, (5) He ii line flux in 10^{-16} erg s^{-1} cm^{-2} arcsec^{-2}. (6) Apertures used to extract the values by the authors in the references.

[a] The authors of the reference quoted a conservative aperture of 10 arcsec radius in which they calculated all their quantities in the narrow-band image.

within the Lyα emission is not relevant because the star-forming galaxies embedded in the nebulae should scarcely emit in C iv and He ii lines (e.g. Shapley et al. 2003), and constitute only a small fraction of the area in the aperture.

Despite these caveats, in Figure 3.11 we plot all the available data in the literature for completeness to show the ranges spanned by these different types of sources in a He ii/Lyα versus C iv/Lyα diagram. But we caution again the reader that a direct comparison of objects from different studies in this plot could be problematic. The upper limits for the 13 Lyα blobs in our sample are shown in red.

Figure 3.11 illustrates that our upper limits are consistent with the previous measurements and more interestingly, that there are sources in the literature with line ratios even lower than our strongest upper limits (LAB1 and LAB2, gray shaded region). Indeed, although our narrow band images constitute the deepest absolute SB limits ever achieved in the C iv and He ii emission lines, some previous searches probed to smaller values of the line ratios because they observed brighter Lyα nebulae (e.g. in the case of HzRGs) or because they probed only the central part of the nebula where the Lyα emission is expected to be brighter. For example, Prescott et al. (2013) probed down to lower line ratios (e.g. the lowest green point in the plot, i.e. the LAB PRG2) because they focus on the brightest part of the blob in Lyα . Indeed, while the approximate isophotal area for this LAB is 103 arcsec^2, they covered only a smaller aperture (1.5″×7.84″) with their long-slit spectra. Thus, notwithstanding our efforts, Figure 3.11 is clearly indicating that in order to explore the full range of line ratios, one requires either deeper observations, or brighter samples of Lyα emission nebulae (see e.g. Chapter 5).

In addition to the sources with giant Lyα emission nebulae, Figure 3.11 also shows line ratios for star-forming galaxies at $z = 2 - 3$, for which the CIV and HeII line ratio is not powered by an AGN. In particular, we show the line ratios determined from the composite spectrum of Lyman break galaxies (LBGs) from (Shapley et al. 2003)[3] and for a peculiar galaxy (Q2343-BX418) studied in detail by Erb et al. (2010) which exhibits particularly strong He II emission. We show the corresponding line-ratios for LBGs because it has been proposed that some LABs could be powered by star-formation (Ouchi et al. 2009), albeit with extreme star-formation rates $\simeq 1000\,\mathrm{M}_{\odot}/\mathrm{yr}$. Indeed, the stacked Ly$\alpha$ narrowband images of LBGs also exhibit diffuse Lyα emission extending as far as ~50 kpc (Steidel et al. 2011), although the Lyα luminosity and surface brightness of these halos is $\gtrsim 10\times$ fainter than the LABs and the Lyα nebulae associated with HzRGs and QSOs. However, if the LABs represent some rare mode of spatially extended star-formation, then the C IV and He II line ratios of star-forming galaxies could thus be relevant.

The origin of the He II and C IV emission observed in the spectra of star-forming galaxies is not completely understood. Shapley et al. (2003) noted relatively broad (FWHM $\sim$ 1500 km s^{-1}) He II emission in the composite spectrum of LBGs, and speculated that it arises from the hot, dense stellar winds of Wolf-Rayet (W-R) stars, which descend from O stars with masses of $M > 20$–$30\ \mathrm{M}_{\odot}$. The C IV line in LBGs exhibits a characteristic P Cygni-type profile, which presumably arises from a combination of stellar wind and photospheric absorption, plus a strong interstellar absorption component due to outflows (Shapley et al. 2003). There could also be a narrow nebular emission component powered by a hard ionizing source. In Figure 3.11 we adopt the strict upper limit of C IV/Lyα < 0.02 of the non-AGN subsample in Shapley et al. (2003), whereas for the He II/Lyα ratio we use the global value for the first quartile with the Lyα line in emission because no He II/Lyα value was quoted for the non-AGN subsample. Erb et al. (2010) studied a young ($<$ 100 Myr), low metallicity ($Z \sim 1/6\ Z_{\odot}$) galaxy at $z = 2.3$ which exhibits exceptionally strong He II emission, which they however argued is not powered by an AGN. Erb et al. (2010) interpreted the He II emission as a combination of a broad component due to W-R stars and a narrow nebular component, powered by a hard ionizing spectrum. Although the He II emission is strong in comparison with other typical $z \sim 2 - 3$ LBGs, indicative of a harder ionizing spectrum, the He II/Lyα ratio of this galaxy is in fact lower than that of the average LBG owing to its extremely strong Lyα line.

---

[3] We use the values quoted for their subsample of LBGs that have strong Lyα emission, i.e. EW(Lyα) = 52.63 ± 2.74 Å (Shapley et al. 2003).

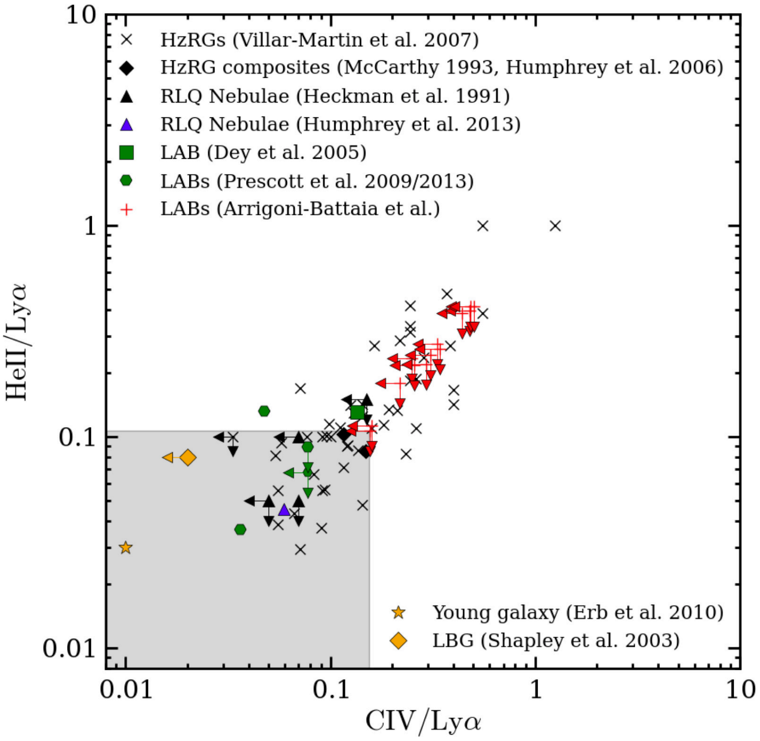

Figure 3.11: HeII/Lyα versus CIV/Lyα log-log plot. Our upper limits on the HeII/Lyα and CIV/Lyα ratios are compared with the values quoted in the literature for HzRG, QSOs, and LABs. Due to their larger extent, LAB1 and LAB2 define the strongest limits on these ratios: the gray shaded area highlights the regime constrained by these limits. Note however that these data are quite difficult to compare because of their heterogeneity.

3.4 Discussion

In what follows we discuss our upper limits in light of a photoionization or a shock scenario. The photoionization modeling is based on the assumptions described in Chapter 2 (Hennawi & Prochaska 2013), while the shock modeling is based on Allen et al. (2008). Both of these models are useful to build intuition on these powering mechanisms, but a more detailed analysis is needed.

3.4.1 Comparison with Photoionization Models

As reviewed in §1.3.1, it is well established that the ionizing radiation from a central AGN can power giant Lyα nebulae, with sizes up to ∼ 200 kpc, around high-z radio galaxies (HzRG) (e.g., Villar-Martín et al. 2003b; Reuland et al. 2003; Venemans et al. 2007) and quasars (e.g., Heckman et al. 1991b; Christensen et al. 2006; Smith et al. 2009; see Chapter 5), together with extended He ii and C iv emission (Villar-Martín et al. 2003a). Although HzRGs are more rare ($n \sim 10^{-8}$ Mpc^{-3}; Miley & De Breuck 2008a), the similarity between the volume density of LABs ($n \sim 10^{-5}$ Mpc^{-3}; Yang et al. 2010) and luminous QSOs ($n \sim 10^{-5}$ Mpc^{-3}; Hopkins et al. 2007), suggests that the LABs could represent the same photoionization process around obscured QSOs. Unified models of AGN invoke an obscuring medium which could extinguish a bright source of ionizing photons along our line of sight (e.g., Urry & Padovani 1995). Indeed, evidence for obscured AGNs have been reported for several LABs (e.g., Basu-Zych & Scharf 2004; Dey et al. 2005; Geach et al. 2007; Barrio et al. 2008; Geach et al. 2009; Overzier et al. 2013; Yang et al. 2014a), lending credibility to a photoionization scenario; however, this is not always the case (Nilsson et al. 2006; Smith & Jarvis 2007; Ouchi et al. 2009).

Despite these circumstantial evidences in favor of the photoionization scenario, detailed modeling for He ɪɪ and C ɪᴠ lines due to AGN photoionization in the context of large Lyα nebulae has not been carried out in the literature, with the exceptions of some studies focusing on the modeling of emission lines in the case of extended emission line regions (EELR) of HzRGs (e.g., Humphrey et al. 2008). Although many authors have modeled the narrow-line regions (NLR) of AGNs (e.g., Groves et al. 2004, Nagao et al. 2006, Stern et al. 2014), the physical conditions (i.e. gas density, ionization parameter) on these small scales $\gtrsim$ 1 kpc (e.g. Bennert et al. 2006, Hainline et al. 2014) are expected to be very different than the $\sim$ 100 kpc scale emission of interest to us here. As such, we model the photoionization of gas on scales of 100 kpc from a central AGN to predict the resulting level of the He ɪɪ and C ɪᴠ lines, relative to the Lyα emission.

To select the parameters of the models in order to recover the Lyα SB of LABs, we follow the simple picture described in Chapter 2, and assume a LAB to be powered by an obscured QSO with a certain luminosity at the Lyman limit ($L_{\nu_{\rm LL}}$). We remind the Reader that, in this framework, once the size of the halo is fixed, in the optically thick case ($N_{\rm HI} \gg 10^{17.2}$ cm^{-2}) the Lyα surface brightness scales with the luminosity at the Lyman limit of the central source, ${\rm SB}^{\rm thick}_{\rm Ly\alpha} \propto f_C L_{\nu_{\rm LL}}$ (see Eqn. (2.16)), while in the optically thin regime ($N_{\rm HI} \ll 10^{17.2}$ cm^{-2}) the SB does not depend on $L_{\nu_{\rm LL}}$, ${\rm SB}^{\rm thin}_{\rm Ly\alpha} \propto f_C n_{\rm H} N_{\rm H}$ (see Eqn. (2.13)), provided the AGN is bright enough to keep the gas in the halo ionized.

To cover the full range of possibilities, we thus construct a grid of ~5000 Cloudy models with parameters in the following range:

— $n_{\rm H} = 0.01$ to 100 cm^{-3} (steps of 0.2 dex);

— $\log N_{\rm H} = 18$ to 22 (steps of 0.2 dex);

— $\log L_{\nu_{\rm LL}} = 29.3$ to 32.2 (steps of 0.4 dex).

We restricted our photoionization modeling to cloud column densities of $\log N_{\rm H} \leq 22$ because for larger columns the implied total gas mass of the nebula alone becomes too large. Quasars at $z \sim 2-3$ are hosted by dark matter halos of $M_{DM} = 10^{12.5} M_{\odot}$ (White et al. 2012), and there is circumstantial evidence based on the strong clustering of LABs that they inhabit a similar mass scale (Yang et al. 2010). Using Eqn. (2.4), the total mass of cool ($\sim 10^4$ K) gas in our simple model can be written as:

$$M_c = 3.3 \times 10^{10} \left(\frac{R}{100\mathrm{kpc}}\right)^2 \left(\frac{f_C}{1.0}\right) \left(\frac{N_\mathrm{H}}{10^{20}\,\mathrm{cm}^{-2}}\right) \mathrm{M}_\odot. \tag{3.6}$$

Note that this value is reasonable, given the recent estimate by Prochaska et al. (2013a) that show that the cool gas mass of the CGM of such massive halos is $M_c > 10^{10}$ $\mathrm{M}_\odot$, based on absorption line spectroscopy. As the smooth morphology of LAB emission constraints the covering factor to be $f_\mathrm{C} \gtrsim 0.5$ (as we discuss below), we consider models up to $\log N_\mathrm{H} = 22$, which would result in very high cool gas masses $M_c = 10^{12.2} M_\odot$, for the lowest covering factor, $f_C = 0.5$.

Additionally, we limit n_H to be $\leq 100\,\mathrm{cm}^{-3}$. Although such high densities are typically adopted in the previous modeling of EELR around HzRGs (e.g., Humphrey et al. 2008, Matsuoka et al. 2009), for halo gas on a scales of $\sim$ 100 kpc, i.e. in the CGM, this would represent an extreme gas density. However, see the broader discussion in §5.4. Note further that the ratio $N_\mathrm{H}/n_\mathrm{H}$ is roughly the size of the emitting clouds, and even for the largest values of $N_\mathrm{H} \sim 10^{21}$ cm^{-2}, densities as large as $n_\mathrm{H} = 100$ cm^{-3} would imply extremely small cloud sizes of the order of parsecs, and even more implausibly small values for lower N_H. These limits on n_H and N_H are particularly important in the optically thin regime where $\mathrm{SB}^\mathrm{thin}_{\mathrm{Ly}\alpha} \propto n_\mathrm{H} N_\mathrm{H}$.

For the luminosity of the central QSO, we limit the models to $i > 16$ mag because the number density of sources with brighter ionizing fluxes is much less than the observed number density of the LABs that we study. At $z \sim 3$, QSOs with $i < 17$ have a number density of 1.16×10^{-9} Mpc^{-3} in comoving units (Hopkins et al. 2007), whereas, although current estimates are fairly rough, bright Lyα blobs with sizes of $\sim$ 100 kpc are much more abundant ($n \sim 10^{-5}$–10^{-6} Mpc^{-3}; Yang et al. 2009, Yang et al. 2010). For reference, the quasar luminosity function of Hopkins et al. (2007), implies that QSOs with $23 < i < 21$ have a number density of $\sim 3 \times 10^{-6}$ Mpc^{-3} at $z = 3.1$, comparable to that of LABs.

Finally, we decide to fix the covering factor to unity $f_C = 1.0$. The assumption of a high or unit covering factor is driven by the observed diffuse morphology of the Lyα nebulae, which do not show evidence for clumpiness arising from the presence of a population of small rare unresolved clouds. We directly test this assumption as follows. We randomly populate an area of 200 arcsec^2 (area of LAB1) with point sources such that $f_C = 0.1 - 1.0$, and we convolve the images with a Gaussian kernel with a FWHM equal to our median seeing value, in order to mimic the effect of seeing in the observations. We find that the smooth morphology observed for LABs cannot be reproduced by images with $f_C < 0.5$, as they appear too clumpy.

We preform photoionization calculations using the Cloudy photoionization code (v10.01), last described by Ferland et al. (2013). As the LABs are extended over $\sim$ 100 kpc, whereas the radius of the emitting clouds is expected to be much smaller, we assume a standard plane-parallel geometry for the emitting clouds illuminated by the distant central source. Note that we evaluate the ionizing flux at a single location for input into Cloudy, specifically at $R/\sqrt{3}$ (where $R = 100$ kpc). Capturing the variation of the physical properties of the nebula with radius is beyond the purpose of this work. Indeed, given that for the objects in the literature are not reported radial trends for the C IV/Lyα and He II/Lyα ratios, and given that we have non detections, modeling the emission as coming from a single radius is an acceptable first order approximation.

We model the input quasar SED using a composite quasar spectrum which has been corrected for IGM absorption (Lusso et al. 2015). This IGM corrected composite is important because it allows us to relate the i-band magnitude of the central source to the specific luminosity at the Lyman limit $L_{\nu_{\rm LL}}$. For energies greater than one Rydberg, we assume a power law form $L_\nu = L_{\nu_{\rm LL}}(\nu/\nu_{\rm LL})^{\alpha_{\rm UV}}$ and adopt a slope of $\alpha_{\rm UV} = -1.7$, consistent with the measurements of Lusso et al. (2015). We determine the normalization $L_{\nu_{\rm LL}}$ by integrating the Lusso et al. (2015) composite spectrum against the SDSS filter curve, and choosing the amplitude to give i-band apparent magnitudes of $i = 16-23$, in steps of unity. We extend this UV power law to an energy of 30 Rydberg, at which point a slightly different power law is chosen $\alpha = -1.65$, such that we obtain the correct value for the specific luminosity at 2 keV $L_\nu(2\,\rm keV)$ implied by measurements of $\alpha_{\rm OX}$, defined to be $L_\nu(2\,{\rm keV})/L_\nu(2500\,\text{Å}) \equiv (\nu_{2\,\rm keV}/\nu_{2500\,\text{Å}})^{\alpha_{\rm OX}}$. We adopt the value $\alpha_{\rm OX} = -1.5$ measured by Strateva et al. (2005) for SDSS quasars. An X-ray slope of $\alpha_{\rm X} = -1$, which is flat in νf_ν is adopted in the interval of 2-100 keV, and above 100 keV, we adopt a hard X-ray slope of $\alpha_{\rm HX} = -2$. For the rest-frame optical to mid-IR part of the SED, we splice together the composite spectra of Lusso et al. (2015), Vanden Berk et al. (2001), and Richards et al. (2006). These assumptions about the SED are essentially the standard ones used in photoionization modeling of AGN (e.g. Baskin et al. 2014). See also §5.4.3.3 and Figure 5.12 for further details on the SED.

As last step, we consider only models with solar metallicity, and from our model grid, we select only models with $\rm SB_{Ly\alpha} = (1–9) \times 10^{-18}$ erg s^{-1} cm^{-2} arcsec^{-2}, comparable to LABs. Note that, as already stressed in §2.2, we neglect the contribution due to the resonant scattering of Lyα photons produced by the quasar itself. Indeed, the scattered Lyα line photons from the quasar should not contribute significantly to the Lyα surface brightness on the large scales considered here (Cantalupo et al. 2014). This is due to the great efficiency of the resonant scattering in diffusing the photons both spatially and in the velocity space.

In Figure 3.12 we compare our photoionization model predictions in the He II/Lyα versus C IV/Lyα diagram to our LAB limits and the data points from the literature. The left panel and right panels show the optically thin and optically thick regimes, respectively. Note that this division into optically thin and thick models, corresponds to a division in the ionizing luminosity of the central source (which in the case of LABs and HzRGs is obscured from our vantage point and is thus unknown). Specifically, in the optically thin regime we find that for the range of $\rm SB_{Ly\alpha}$ considered, the central source must have $L_{\nu_{\rm LL}} \gtrsim 10^{30.5}$ erg s^{-1} Hz^{-1} or $i \lesssim 20$ [4]. On the other hand, because in the optically thick limit SB$_{\rm Ly\alpha} \propto L_{\nu_{\rm LL}}$, the ionizing luminosity is fixed to be in a relatively narrow range $L_{\nu_{\rm LL}} \simeq 10^{29.7} - 10^{29.3}$ erg s^{-1} Hz^{-1} ($i \simeq 22 - 23$).

For clarity, in Figure 3.12 we show only the models with $N_{\rm H} = 10^{18}, 10^{19}, 10^{20}, 10^{21}, 10^{22}$ cm^{-2}. The model grids are color-coded according to the ionization parameter U, which is defined to be the ratio of the number density of ionizing photons to hydrogen atoms ($U \equiv \Phi_{\rm LL}/cn_{\rm H} \propto L_{\nu_{\rm LL}}/n_{\rm H}$), and provides a useful characterization of the ionization state of the nebulae. Because photoionization models are self-similar in this parameter (Ferland 2003), our models will exhibit a degeneracy between $n_{\rm H}$ and $L_{\nu_{\rm LL}}$. Nevertheless, we decided to construct our model grid in terms of $n_{\rm H}$ and $L_{\nu_{\rm LL}}$, in order to explore the possible ranges of both parameters.

Figure 3.12 illustrates that, overall, our photoionization models can cover the full range of HeII/Lyα and CIV/Lyα line ratios that are observed in the data. Note that previous studies of EELR around HzRGs favored models with log$U \sim -1.46$ (e.g. Humphrey et al. 2008), which are consistent with our results. Note however that two HzRGs with He II/Ly$\alpha \approx 1$ and C IV/Ly$\alpha \approx 1$, are not covered by our models. For both of these data, emission from the central source has not been excluded, and thus we speculate that these very high line ratios arise because of contamination from the narrow-line region of the obscured AGN, where Lyα photons have been destroyed by dust. Indeed, both of these objects, MG1019+0535 and TXS0211-122, have a C IV/He II ratio similar to the bulk of the HzRGs population, but they exhibit unusually weak Lyα lines (Dey et al. 1995, van Ojik et al. 1994). Note however, that while destruction of Lyα by dust grains can have a large impact on these line ratios for emission emerging from the much smaller scale narrow line region, dust is not expected to significantly attenuate the Lyα emission in the extended nebulae around QSOs (see discussion in Appendix A of Hennawi & Prochaska 2013) given the physical conditions characteristic of the CGM, and thus we neglect destruction of Lyα photons by dust in our modeling.

The optically thin regime (see upper panel) seems to better reproduce the range of high He II/Lyα and C IV/Lyα ratios, and seems to have difficulties in reproduce the low ratios implied by our observations (see below). To understand why the optically thin models do not cover low He II/Lyα ratio, we describe here the trajectory of the optically thin models through the He II/Lyα and C IV/Lyα diagram. We follow the curves from low to high U. Recall that in the optically thin regime SB$_{Ly\alpha} \propto n_{\rm H}N_{\rm H}$, but is roughly independent of the source luminosity $L_{\nu_{\rm LL}}$ [5]. Thus by fixing $N_{\rm H}$, and requiring that SB$_{\rm Ly\alpha}$ =(1–9)×10^{-18} erg s^{-1} cm^{-2}, we also fix $n_{\rm H}$. Thus U is increases along this track because the central source luminosity is increasing $L_{\nu_{\rm LL}}$, which hardly changes the Lyα emission, but results in significant variation in both He II and C IV .

---

[4] This constraint follows from the definition of an optically thin cloud, i.e. $N_{\rm HI} \ll 10^{17.2}$ cm^{-2}.

[5] Note that in this regime the Lyα emission is not completely independent on the luminosity of the central source. Indeed, this scaling neglects small variations due to temperature effects, which Cloudy is able to trace.

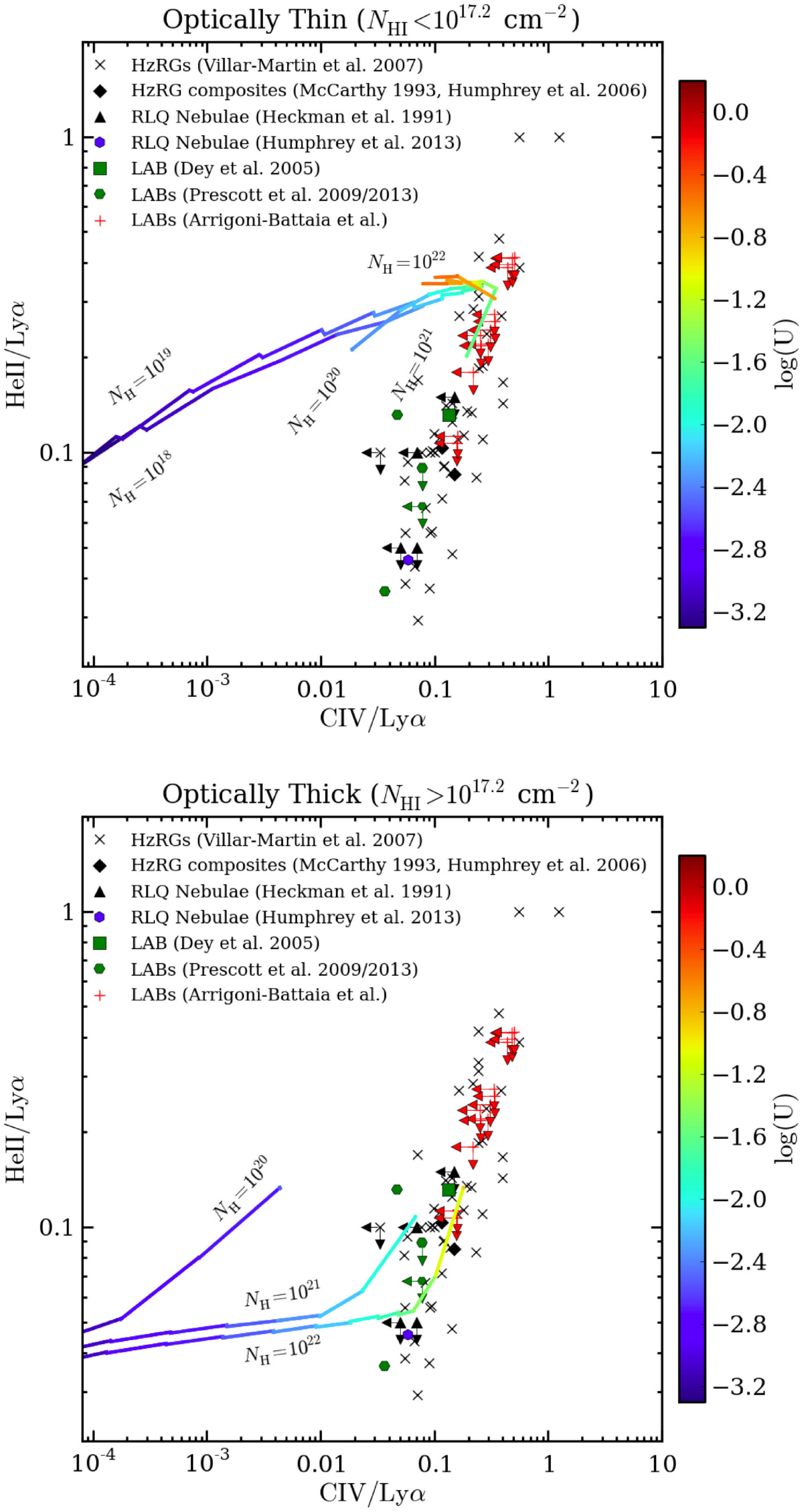

Optically Thin ($N_{\mathrm{HI}} < 10^{17.2}$ cm^{-2})

Optically Thick ($N_{\mathrm{HI}} > 10^{17.2}$ cm^{-2})

Figure 3.12: HeII/Lyα versus CIV/Lyα log-log plot. Same data points as in Figure 3.11. Our upper limits on the HeII/Lyα and CIV/Lyα ratios are compared with the Cloudy photoionization models. In the upper panel we plot the optically thin models, while in the lower panel is shown the optically thick regime. For clarity, we plot only the models with $N_{\mathrm{H}} = 10^{19}, 10^{20}, 10^{21}, 10^{22}$ cm^{-2}. The grids are color coded following the ionization parameter (see colorbar on the right) and the value of hydrogen column density is indicated. Note that there are no optically thick models with $N_{\mathrm{H}} = 10^{19}$ cm^{-2}. Note that the x-axis is on different scale than Figure 3.11.

First consider the trend of the He II/Lyα ratio. He II is a recombination line and thus, once the density is fixed, its emission depends basically on what fraction of Helium is doubly ionized. For this reason, the He II/Lyα ratio is increasing from $\log U = -3.3$ and reaches a peak at $\log U \sim -2.0$, corresponding to an increase in the fraction of the He^{++} phase from about 20% to 90% of the total Helium. Further increases U, result in only modest changes to the He^{++} fraction, but result in an increase in gas temperature. These higher temperatures change the value at which the He II/Lyα ratio saturates. In particular, at higher temperatures, if both Hydrogen and Helium are completely ionized, the He II/Lyα saturation value decreases (see also §5.4.4 and Eqn. 5.8).

Our photoionization models indicate that the C IV emission line is an important coolant and is powered primarily by collisional excitation. Figure 3.12 shows that our models span a much wider range in the C IV/Lyα ($\sim$ 3 dex) ratio than in He II/Lyα ($\lesssim$ 2 dex). The strong evolution in C IV/Lyα results from a combination of two effects. First, increasing U increases the temperature of the gas, and the C IV collisional excitation rate coefficient has a strong temperature dependence (Groves et al. 2004). Second, the efficacy of C IV as a coolant depends on the amount of Carbon in the C^{+3} ionic state. As $\log U$ increases from $\simeq -3.3$ to $\simeq -2$, the C^{+3} fraction increases from 1% to 37%. These two effects conspire to give rise to nearly three orders of magnitude of variation in the C IV emission.

From the left panel of Figure 3.12, it is clear that our optically thin models with solar metallicities populate the region below our most stringent upper limits (LAB1 and LAB2) only for very low U ($\log U \sim -3.0$), i.e. which means at very high density $n_{\rm H} \gtrsim 6$ cm^{-3} [6]. These are models for which Helium is not completely ionized, and thus low He II/Lyα ratios are allowed. This result agrees with the analysis of a newly discovered giant Lyα nebula around a $z \sim 2$ radio-quiet QSO (see Chapter 5). Also in that case, it is invoked the presence of dense clouds to explain the Lyα emission in the optically thin regime.

On the other hand, the optically thick models (see lower panel of Figure 3.12) can also populate the area below the upper limits for LAB1 and LAB2, namely the lower part of the observed He II/Lyα – C IV/Lyα diagram. Note that given the range of $L_{\nu_{\rm LL}}$ and $n_{\rm H}$ in our parameter grid, models with $N_{\rm H} = 10^{18} - 10^{19}$ cm^{-2} are never optically thick[7], which explains why we only show optically thick models with $N_{\rm H} = 10^{20}, 10^{21}, 10^{22}$ cm^{-2}. The bulk of these models reside on a sequence with almost constant He II/Lyα (around He II/Lyα = 0.04 – 0.05) for a wide range of C IV/Lyα, which is driven by variation in U. The models departing from this sequence are characterized by $N_{\rm HI}$ slightly greater than $10^{17.2}$ cm^{-2} and they can thus be seen as a transition between the optically thick case and the optically thin case.

---

[6] This lower limit on the density is determined by the lower luminosity for which our models are optically thin, i.e. i-mag$\sim$ 20. Higher luminosities select even higher densities.

[7] We found optically thick models for $N_{\rm H} > 10^{19.2}$ cm^{-2}.

It is worth to stress here that some of the HzRGs show lower Lyα emission, and thus higher ratios in these plots, because of intervening neutral Hydrogen (e.g. Wilman et al. 2004). It has been shown that this absorption is mainly caused by strong absorbers, i.e. $N_{\rm HI} > 10^{18}{\rm cm}^{-2}$. For example, van Ojik et al. (1997) show that strong HI absorption ($10^{18}{\rm cm}^{-2} < N_{\rm HI} < 10^{20}{\rm cm}^{-2}$) is found in 11 out of 18 sources in their sample. As we are not taking into account the absorption in our modeling and as we do not have complete information to correct the data for absorption, one needs to be cautious, particularly when comparing our models with the data of HzRGs.

To summarize, the photoionization models produce line ratios which are consistent with our upper limits and which span the values observed in the literature. In the next Section we consider the degree to which shock powered emission can explain line ratios in Lyα nebulae.

3.4.2 Comparison with Shock Models

Taniguchi & Shioya (2000) and Mori & Umemura (2006) have speculated that intense star-formation accompanied by successive supernova explosions could power a large scale galactic superwind, and radiation generated by overlapping shock fronts could power the Lyα emission in the LABs. However, it is well known that it is difficult to distinguish between photoionization and fast-shocks using line-ratio diagnostic diagrams (e.g. Allen et al. 1998). Furthermore, for AGN narrow line regions, the Lyα line is typically avoided in these diagrams because of its resonant nature and the fact that it may be more likely to be destroyed by dust, although we have argued that it is not an issue for CGM gas. It is thus interesting to study how shock models populate the He ii/Lyα versus C iv/Lyα diagram in comparison with photoionization models and our observational limits.

To build intuition about the line ratios expected in a shock scenario we rely on the modeling of fast shocks by Allen et al. (2008). We thus imagine the Lyα emission as the sum of overlapping shock fronts with shock velocity $v_{\rm s}$, moving into a medium with preshock density $n_{\rm H}$. In the case of such shocks, Allen et al. (2008) showed that the Lyα emission depends strongly on $v_{\rm s}$, i.e. $F_{{\rm Ly}\alpha} \propto n_{\rm H} v_s^3$ (their Table 6). In order to test a realistic set of parameters in the case of LABs, we limit the grid of models presented by Allen et al. (2008) to:

- $n_{\rm H} = 0.01, 0.1, 1.0, 10, 100$ cm^{-3},

- shock velocities, $v_{\rm s}$, from 100 km s^{-1} to 1000 km s^{-1} in steps of 25 km s^{-1}.

We consider only models with solar metallicity[8]. The magnetic parameter $B/n^{1/2}$, where B is the magnetic field in μG, determines the relative strength of the thermal and magnetic pressure. We adopt a magnetic parameter $B/n^{1/2} = 3.23\ \mu\mathrm{G\ cm}^{3/2}$, which represents a value expected for ISM gas assuming equipartition of magnetic and thermal energy. However, note that, given the very strong dependence of the ionizing flux on the shock velocity $F_{\mathrm{UV}} \propto v_{\mathrm{s}}^3$, the line ratios do not vary so markedly with either the metallicity or the magnetic field (see Allen et al. 2008 for further details).

In Figure 3.13 we show two sets of shock models. In the upper panel, we plot the models for which the emission is coming solely from the shocked region, where the gas, moving at about v_{s} is ionized and excited to high temperatures by the shock. Temperatures ahead of the shock-front are of the order of 10^4 K , whereas temperatures as high as 10^6 K can be reached in the post-shock gas (Allen et al. 2008). In the lower panel, we plot a combination of the emission coming from the shocked gas and from the ‘static’ precursor, i.e. the pre-shock region which is photoionized by the radiation emitted upstream from the shocked region. The trends of the models can be explained as follows. The models for the shock component (upper panel of Figure 3.13) show a rapid decrease in the C iv/Lyα ratio for increasing v_{s}. This is due to a rapid increase in the Lyα line due to the strong scaling of the ionizing flux with v_{s}, and to a decrease in the C iv line due to the lack of carbon in the C^{3+} phase for high velocities (i.e. carbon is in higher ionization species, see Figure 9 of Allen et al. 2008). The He ii/Lyα ratio depends more strongly on the gas density because n_{H} sets the volume of the shocked region and thus the recombination luminosity of Helium, i.e. at fixed v_{s}, a higher density corresponds to a smaller shocked volume and less Helium emission (see Figure 6 of Allen et al. 2008).

The combination of shock and precursor models mainly alter the ratios for models with high v_{s} (see lower panel of Figure 3.13). This is because the precursor component is adding the contribution of a photoionized gas at temperature of the order of 10^4 K, and the ionizing flux scales strongly with shock velocity $F_{\mathrm{UV}} \propto v_{\mathrm{s}}^3$. For velocities $v_{\mathrm{s}} \gtrsim 400$ km s^{-1}, the resulting hard radiation field results in a large fraction of double ionized Helium He^{++} over a significant volume of the precursor, significantly increasing the He ii emission and the He ii/Lyα ratio. This photoionized precursor similarly increases the abundance of the C^{3+} phase giving rise to a higher C iv/Lyα ratio. Thus, adding the precursor contribution to the shock models causes the models to fold over each other at high velocities.

Figure 3.13 illustrates that the shock models with $v_{\mathrm{s}} > 250$ km s^{-1} are capable of populating the line ratio diagram below our tightest upper limits (i.e. LAB1 and LAB2) (see Figure 3.13). However, the shock velocities above $\sim$ 250 km s^{-1} could be in potential disagreement with recent observations of outflow velocities (Yang et al. 2011, 2014a,b). Using the velocity offset

---

[8] Note that the solar values used by Allen et al. (2008) are slightly different from what is used in Cloudy (and thus in our previous section).

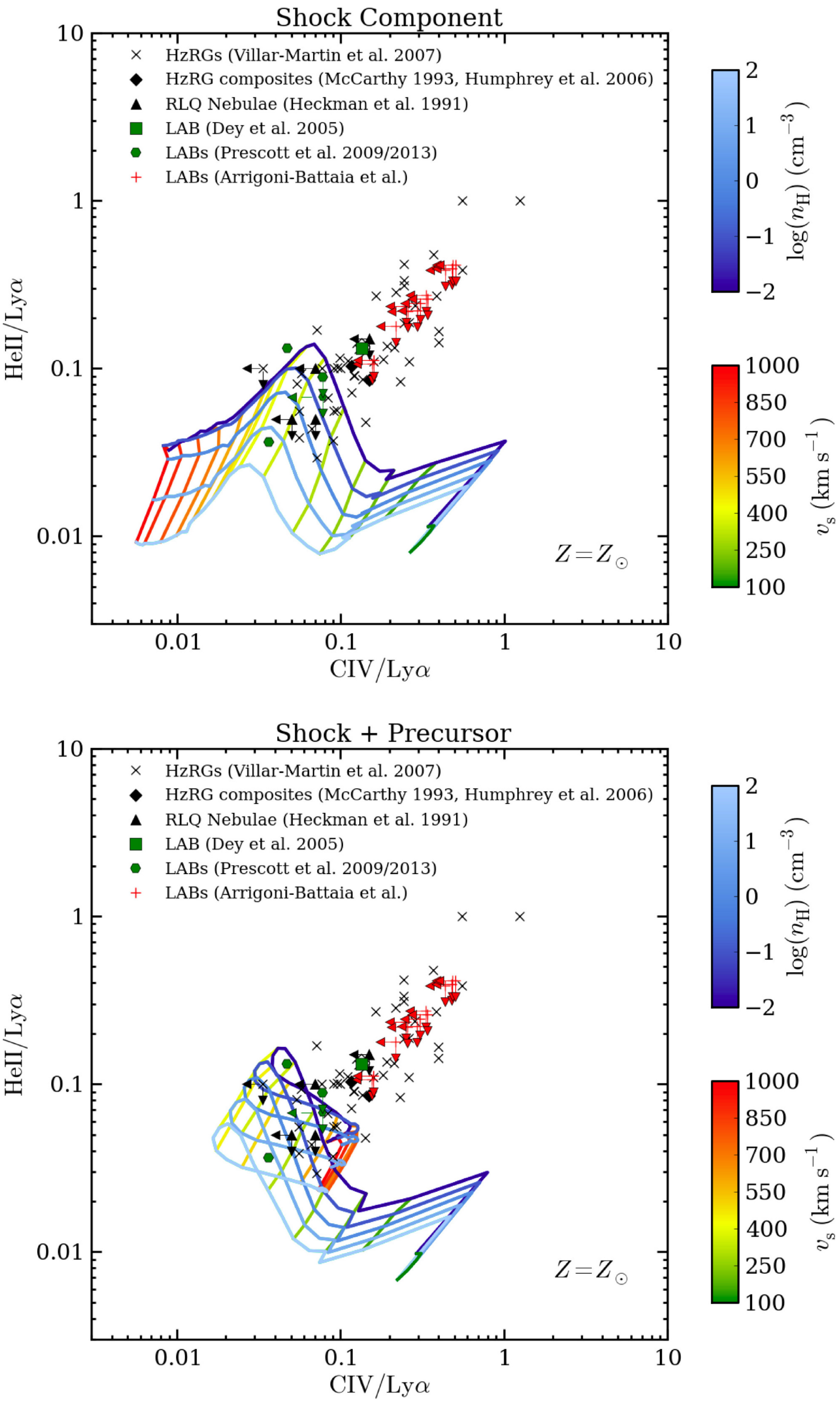

Figure 3.13: HeII/Lyα versus CIV/Lyα log-log plot. Same data points as in Figure 3.11. Our upper limits on the HeII/Lyα and CIV/Lyα ratios are compared with the models by Allen et al. (2008). In the upper panel we plot the shock models, while in the lower panel is shown the combination of shock and precursor. The grids are color coded following the density of the pre-shock region, N_{H}, and the velocity of the shock, v_{s}. The models are not taking into account the possible additional contribution due to Lyα scattering.

between the Lyα and the non-resonant [O III] or Hα line, the offset of stacked interstellar metal absorption lines, and the [O III] line profile, Yang et al. (2011, 2014b) find that the kinematics of gas along the line of sight to galaxies in LABs are consistent with a simple picture in which the gas is stationary or slowly outflowing at velocities of a few hundred km s^{-1} from the embedded galaxies. In addition, Prescott et al. (2009) showed that the He II line detected in a LAB at $z = 1.67$, is narrow: FWHM $\lesssim$ 500 km s^{-1}. Therefore, these observations seem to rule out the shock-only models (upper panel of Figure 3.13), where the gas velocities, i.e. the observed velocities, are expected to be similar to the shock velocity v_s.

In the case of a combination of shock and precursor (lower panel of Figure 3.13), the interpretation is more complicated. As we explained above, the emission from the precursor dominate the line ratios at $v_s \gtrsim 250$ km s^{-1}, where the models lie below our upper limits. As the precursor is static, if we are preferentially seeing this state of the gas, we would measure velocities lower than v_s. In this case, as the shock is behaving as a photoionizing source, it would be difficult to disentangle the combination of shock and precursor from the photoionization case. Furthermore, it is important to note that we are not taking into account any deceleration of the shock. A detailed modeling of a superposition of blast waves that are slowing down with time is beyond the scope of this work.

It is worth to stress again here, that these models suffer from uncertainty in the Lyα calculation. In particular, the additional contribution from scattering is not taken into account, thus making the Lyα line weaker. As a consequence, these grids may be shifted to lower values on both axes. Note also that we fix the metallicity to the solar value. However, a decrease in the C IV emission is expected for sub-solar metallicity, weakening the constraints on the shock velocities. The trends with metallicity are beyond the scope of this work and we are going to address them in future works. Another caveat is that the line ratios of HzRGs can be biased because the absorption of Lyα due to the intervening Hydrogen was not taken into account.

Thus, even though our models can give us a rough idea of the line emission in the shock scenario, these plots should be treated with caution.

3.4.3 COMPARISON TO PREVIOUS MODELING OF EXTENDED LYα EMISSION NEBULAE

As stated in §1.3.2, rigorous modeling of photoionization of large Lyα nebulae in the context of LABs has never been performed. However, Prescott et al. (2009) reported a detection of extended He II and modeled simple, constant density gas clouds assuming illumination from an AGN, Pop III, and Pop II stars. They are not quoting all the parameters of their Cloudy models (e.g., N_H) and thus it is not possible to make a direct comparison. However, they found that the data are in agreement with photoionization from a hard ionizing source, either due to an AGN or a very low metallicity stellar population ($Z < 10^{-2} - 10^{-3} Z_{\odot}$). They conclude that, in the case of an AGN, this source must be highly obscured along the line of sight. They also showed that their observed ratios are inconsistent with shock ionization in solar metallicity gas.

On smaller scales, photoionization has been modeled in the case of EELR of HzRGs. In particular, Humphrey et al. (2008) using the code *MAPPINGS Ic* (Binette et al. 1985), shows that the data are best described by AGN photoionization with the ionization parameter U varying between objects, in a range comparable with our grid. However, they found that a single-slab photoionization model is unable to explain adequately the high-ionization (e.g. N v) and low-ionization (e.g. C ii, N ii, O ii) lines simultaneously, with higher U favored by the higher ionization lines. They also demonstrated that shock models alone are overall worse than photoionization models in reproducing HzRGs data. In the shock scenario is required an additional source of ionizing photons, i.e. the obscured AGN, in order to match most of the line ratios studied by Humphrey et al. (2008). However, note that shock with precursor models can explain some ratios, e.g. N v/N iv, which are hardly explained by a single-slab photoionization model (Humphrey et al. 2008).

3.5 SUMMARY AND CONCLUSIONS

We obtained the deepest ever narrowband images of He ii and C iv emission from 13 Lyα blobs in the SSA22 proto-cluster region to study the poorly understood mechanism powering the Lyα blobs. By exploiting the overdensity of LABs in the SSA22 field, we were able to conduct the first statistical multi emission line analysis for a sample of 13 LABs, and compared their emission line ratios to Lyα nebulae associated with other Lyα blobs, high-z radio galaxies (HzRGs), and QSOs. We compared these results to detailed models of He ii/Lyα and C iv/Lyα line ratios assuming that the Lyα emission is powered by a) photoionization from an AGN or b) in a shock scenario. The primary results of our analysis are:

- We do not detect extended emission in the He ii and C iv lines in any of the 13 LABs down to our sensitivity limits, 2.1× and 3.4×10^{-18} erg s^{-1} cm^{-2} arcsec^{-2} (5σ in 1 arcsec^{2}) for He ii and C iv , respectively.

- Our strongest constraints on emission line ratios are obtained for the brightest LABs in our field (LAB1 and LAB2), and are thus constrained to be lower than 0.11 and 0.16 (5σ), for He ii/Lyα and C iv/Lyα, respectively.

- Photoionization models, accompanied by a reasonable variation of the parameters ($N_{\rm H}$, $n_{\rm H}$, i) describing the gas distribution and the ionizing source, are able to produce line ratios smaller than our upper limits in the He II/Lyα versus C IV/Lyα diagram. Although our data constitute the deepest observations of these lines, they are still not deep enough to rule out photoionization by an obscured AGN as the power source in LABs. These same photoionization models can also accommodate the range of line ratios in the literature for other Lyα nebulae. In particular, optically thin models populate the region below our upper limits only for really low ionization parameters ($\log U \sim -3.0$) and high densities ($n_{\rm H} \gtrsim 6$ cm^{-3}). On the other hand, the bulk of the optically thick models lies below our LAB limits, on a sequence with almost constant He II/Lyα (around He II/Lyα = 0.04 − 0.05).
- Shock models can populate a He II/Lyα versus C IV/Lyα diagram below our LAB limits only if high velocities are assumed, i.e. $v_{\rm s} \gtrsim 250$ km s^{-1}, but they do not reproduce the higher line ratios implied by detections of He II and C IV in the HzRGs. While the 'shock-only' models seem to be ruled out by observations of relatively weak outflow kinematics in the central galaxies embedded in LABs (Prescott et al. 2009; Yang et al. 2011, 2014b), we note that the composite models of shock and precursor might be in agreement with observed gas velocities lower than $v_{\rm s}$ and thus allow $v_{\rm s} \gtrsim 250$ km s^{-1}.

Deeper observations of the He II and C IV emission lines in the SSA22 field are required in order to make more definitive statements about the mechanism powering the LABs. For example, our photoionization modeling suggests that line ratios as low as He II/Ly$\alpha \simeq 0.05$ and C IV/Ly$\alpha \simeq 0.07$ can be produced by combinations of physical parameters ($N_{\rm H} = 10^{19} - 10^{21}$ cm^{-2}, $n_{\rm H} = 1 - 10$ cm^{-3}, $i = 17$) which are still plausible. This implies that SBs as low as 1× and 1.5×10^{-18} erg s^{-1} cm^{-2} arcsec^{-2} per 1 arcsec^2 aperture (5σ) must be achieved to start to rule out photoionization.

For bright giant Lyα nebulae around QSOs, as I show in Chapter 5, photoionization modeling are much more constrained, because the ionizing luminosity of the central source is known. Sensitive measurements of line ratios from deep observations can thus constrain the properties of gas in the CGM. Further, by probing an order of magnitude deeper than our current observations, a new generation of image-slicing integral field units, such as the Multi Unit Spectroscopic Explorer (MUSE, Bacon et al. 2004) on VLT or the Keck Cosmic Web Imager (KCWI, Morrissey et al. 2012), will probably be able to make an important step forward in solving the mystery of LABs.

"If you look in the dark for a long time, there is always something."

William Butler Yeats

Chapter 4

FLASHLIGHT: FLUORESCENT LYMAN-ALPHA SURVEY OF COSMIC HYDROGEN ILLUMINATED BY HIGH-REDSHIFT QUASARS.

As mentioned in Chapter 1, although there have been many efforts in detecting extended emission from the CGM around QSOs (e.g. Heckman et al. 1991b; Christensen et al. 2006), before 2011 most of the observations were carried out at $z \sim 3$, where the $(1+z)^4$ cosmological surface brightness dimming dictates that one must integrate ~ 10 times longer than at $z \sim 2$, to achieve the same depth. Further, these studies were hindered by the use of wide low throughput filters (FWHM= 70 − 100 Å) and also by older, and thus less sensitive CCDs. New statistical surveys targeting the Lyα line around $z \sim 2$ QSOs with narrower filters are needed, since they would be more effective in determining the properties of extended emission in the QSOs environment.

With this idea in mind, I started the FLASHLIGHT survey (Arrigoni Battaia et al. 2014) in November 2012 together with Joseph F. Hennawi, Sebastiano Cantalupo, and J. Xavier Prochaska.

---

[*] This Chapter refers to the work advertised in Arrigoni Battaia et al. (2014), which is a proceeding of the Symposium #304 of the International Astronomical Union. As part of the FLASHLIGT survey, I took part at three observing runs at the Gemini-South telescope, for a total of 12 nights. The first of these runs was used to mount and test our narrow-band filter on GMOS-S. I also took part at two observing runs at the Keck telescope for a total of 4 nights. In the first of these runs, we discovered the Slug Nebula and also a system with a quasar quartet (Hennawi et al. 2015). The former is included in this work in Chapter 5, while the latter, being follow-up observations of a giant nebula candidate (Hennawi & Prochaska 2013) and thus not part of FLASHLIGHT, is not discussed here. Finally, I perform the data reduction and ongoing analysis.

4.1 THE FLASHLIGHT IDEA: USING QSOS AS SEARCHLIGHTS

As introduced previously in §1.3, QSOs are one of the most powerful sources of ionizing radiation in the universe, and are believed to be hosted in centers of galaxies in a dark matter halos of mass $M_{\rm DM} \sim 10^{12.5}$ M$_\odot$ (White et al. 2012). The ionizing flux emitted by the QSO may thus impinge on the surrounding complex gas distribution (e.g. CGM, cooling flow filaments, nearby satellite galaxies, IGM), allowing us to detect the reprocessed emission, and thus directly study the properties of the emitting gas. In particular, the gas is likely to be photoionized by the QSO, and thus, a strong signal from the Lyα line is expected (see Chapter 2). Indeed, acting like a flashlight, a QSO is able to boost the fluorescence emission expected from cold gas in the presence of the UV background (e.g., ${\rm SB}_{\rm Ly\alpha} \sim 10^{-20}$ erg s^{-1} cm^{-2} arcsec^{-2}, Lowenthal et al. 1990; Rauch et al. 2008) by roughly a factor of $\sim 100 - 1000$ (e.g. ${\rm SB}_{\rm Ly\alpha} \sim 10^{-18}$ erg s^{-1} cm^{-2} arcsec^{-2}, Hogan & Weymann 1987; Binette et al. 1993; Gould & Weinberg 1996; Cantalupo et al. 2005), making it detectable by current facilities. Indeed, as already mentioned in Chapter 1, recently Cantalupo et al. (2012) identified a population of compact Lyα emitters around a $z \sim 2$ QSO, which seems not powered by normal star formation. These objects show rest-frame equivalent widths exceeding the maximum value expected from star-formation, $EW_0^{\rm Ly\alpha} > 240$Å (e.g., Charlot & Fall 1993), and are thus the best candidates to date for fluorescent emission powered by a proximate quasar on scales of $\sim$ Mpc. These objects are thought to be 'dark-galaxies', i.e. gas-rich, low-mass haloes ($10^9 - 10^{11}$ M$_\odot$) with very low star formation efficiencies (e.g., Gnedin & Kravtsov 2010; Krumholz & Dekel 2012).

The idea of using a QSO as a searchlight inevitably comes with all the uncertainties on the nature of the QSO itself. Specifically of relevance here, is its not well constrained ultraviolet continuum (e.g., Lusso et al. 2015), and opening angle (Trainor & Steidel 2013). However, these points can also be tested by studying the extended emission around the QSOs (e.g. morphology, covering factor, ionization level within the detected gas, frequency of giant Lyα nebulae), in a survey like ours.

4.2 OBSERVATIONS

The FLASHLIGHT survey comprises our efforts of the past three years (2012-2015) to search for fluorescent Lyα emission powered by luminous $z \sim 2$ QSOs, using custom designed narrow-band (NB) filters. The filters have been purchased from Andover Corporation, and have been designed to have a very narrow band-pass FWHM of $\sim$ 30 Å to minimize sky background, while maintaining a reasonable throughput ($\sim$ 50%). Each filter has been crafted to meet the characteristics of the specific telescope used. These observations have been conducted on two

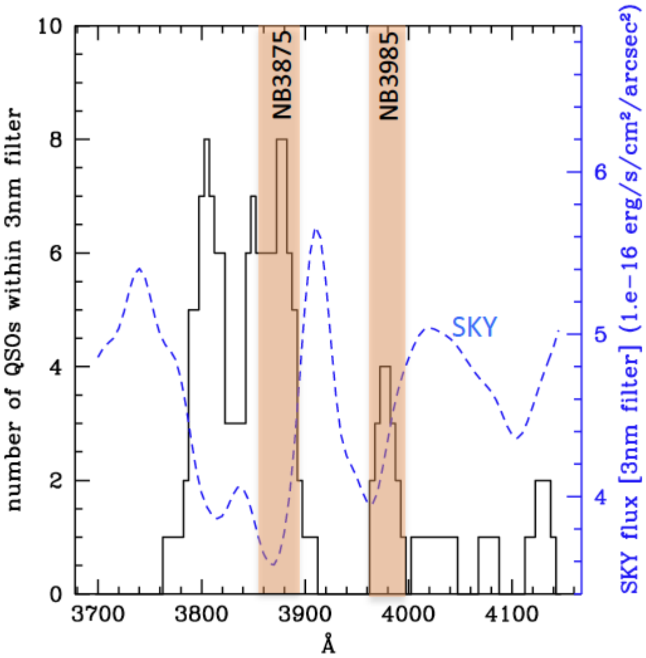

Figure 4.1: Selection of the central wavelength of the two custom-built NB filters (NB3875 and NB3985) used with the LRIS/Keck instrument (Figure courtesy of Sebastiano Cantalupo). These filters have been designed to maximize the number of possible targets (black histogram) and system throughput, while minimizing the sky background (blue dotted line).

distinct telescopes: the Keck 10m telescope and the Gemini-South 8.1m telescope. The narrow-band technique requires very accurate z measurements for each QSO. These were obtained by targeting narrow lines in the QSO spectra, using near infrared (NIR) spectroscopic observations, e.g. [O III]λ5007 [1]. We have thus selected the central wavelengths of our filters to cover ‘sweet’ spots in the redshift distribution of QSOs, i.e. to maximize the number of possible targets, while trying to minimize the sky background (see Figure 4.1).

The program on the Keck telescope is led by Sebastiano Cantalupo and J. Xavier Prochaska, and consists of a total of eight QSOs imaged in about 10 nights of observations (2-3 nights were lost due to bad weather), of which I have conducted two observing runs (4 nights). As this program is still under development and I am not the main contributor, I briefly summarize here its main aspects, while below I describe in detail the Gemini program. During this campaign, we obtained deep narrow-band images in parallel with broad-band V images thanks to the possibility of employing a dichroic[2] within the Low Resolution Imaging Spectrograph (LRIS; Oke et al. 1995) on the Keck I telescope. This technique spares us a lot of observing time, and simultaneously achieves unprecedently deep broad-band images, necessary to firmly constrain the equivalent width of Lyα emitting objects undetected in the continuum.

---

[1] For this reason, I have been involved in observing runs at the NTT telescope with the SOFI instrument (Moorwood et al. 1998).

[2] Specifically, we employed the D460 dichroic.

Three QSOs were observed with the filter NB3985 centered on the Lyα line redshifted to $z = 2.279$ ($\lambda_{\rm center} = 3986$ Å, FWHM= 31.6 Å), and five with one centered at $z = 2.190$ ($\lambda_{\rm center} = 3878$ Å, FWHM= 30 Å). The exposure times of these observations vary from 2 to 10 hours, in series of 1280s exposures, resulting in sensitivity limits (1σ in 1 square arcsec) ranging from $\rm SB_{Ly\alpha} = 1.2 \times 10^{-18}\ erg\,s^{-1}\,cm^{-2}\,arcsec^{-2}$ to $\rm SB_{Ly\alpha} = 5 \times 10^{-19}\ erg\,s^{-1}\,cm^{-2}\,arcsec^{-2}$. All of the targeted quasars were selected to be hyper-luminous, i.e. $V \lesssim 17$, based on the simple idea that brighter QSOs would highly facilitate the detection of fluorescently emitting 'dark' galaxies (Cantalupo et al. 2012). These observations led to the surprising discovery of a giant (~ 500 kpc) Lyα nebula around the quasar UM 287 at $z = 2.279$ (Cantalupo et al. 2014), which will be extensively presented in Chapter 5. All the other 7 quasars do not show extended Lyα emission, i.e. > 50 kpc.

On the other hand, Joseph F. Hennawi and I led the effort with the Gemini-South telescope. We successfully installed the *first*[3] custom-built filter for the Gemini Multi Object Spectrograph (GMOS, Hook et al. 2004), targeting Lyα emission at $z = 2.253$ ($\lambda_{\rm center} = 3955$ Å, FWHM = 32.7 Å, peak transmission $\rm T_{peak} = 53.88\%$). We have observed a total of 17 quasars, three of which have longer integrations, typically of 5 hours in series of dithered 1800s exposures, achieving a depth of $\rm SB_{Ly\alpha} \sim 2 \times 10^{-18}\ erg\,s^{-1}\,cm^{-2}\,arcsec^{-2}$ (1σ in 1 square arcsec); whereas the other 14 quasars were observed in a fast survey mode, to try to uncover new giant Lyα nebulae similar to UM 287. To have a more representative sample, we selected our targets from the SDSS/BOSS catalogue (Pâris et al. 2014) without imposing any constraint on their luminosity. As NIR spectra are not available for most of the SDSS QSOs, redshifts are determined using a custom line centering code that corrects for the known relative shifts among broad rest-frame UV emission lines, as in Hennawi & Prochaska (2013) (for details see also Hennawi et al. 2006; Shen et al. 2007). The typical uncertainty on these redshift estimates is $\sigma_z \sim 0.003$ (or equivalently ~ 270 km s^{-1}), which is much smaller than the width of the narrow-band filter used, i.e. $\Delta z = 0.027$ (or equivalently $\Delta v = 2479$ km s^{-1}). Thus, to be sure that our targets fall within the narrow band filter, we selected only QSOs whose redshift gives a maximum shift of ± 5 Å from the filter's center (or equivalently $\delta v = 370$ km s^{-1}).

The 'fast survey' observations were carried out using typical exposure times of $\sim$ 2 hours in series of dithered 1200s exposures, achieving an average depth of $\rm SB_{Ly\alpha} \sim 4.5 \times 10^{-18}\ erg\,s^{-1}\,cm^{-2}\,arcsec^{-2}$. In addition to the NB data, we have observed the same fields in g-band with a typical exposure time of 3 hours in series of dithered 240s, or 40 minutes in series of dithered 300s exposures, for the long integrations and for the fast survey mode, respectively. I took the data of the 'fast-survey' in March 2014 in a 4 nights run (program ID: `GS-2014A-C-2`), while the longer exposures were obtained in service mode during 2013-2014 (program ID:

---

[3] Bernadette Rodgers and Pascale Hibon private communication.

`GS-2013A-Q-36`)[4]. The seeing was ~0.7″ for the service mode program, while it ranged between 0.5″ and 1.9″ during the visitor run, with a median seeing of ∼ 1.2″. A 4 nights run (program ID: `GS-2013B-C-4`) was completely lost in September 2013, due to bad weather conditions. However, it allowed us to get familiar with the instrument and to implement a robust custom pipeline for the data reduction. The observations taken with GMOS/Gemini-South and used in this work[5] are summarized in Table 4.1. Note that in June 2014 the CCDs of GMOS-S were updated to the new Hamamatsu CCDs, more sensitive at longer wavelengths, e.g. $\lambda > 5000$ Å. For this reason, the overall efficiency of the system at 4000 Å has been degraded by 25% (for the blue sensitive CCD), which means that we are not able anymore to observe $z \sim 2$ targets in a reasonable amount of time with this instrument.

Taking all the Keck and Gemini observations together, we have observed a total of 25 quasars. The size of our sample and the depth achieved make this survey the first one of this kind.

4.3 DATA REDUCTION OF THE GEMINI DATA

As we are interested in detecting very faint surface brightness levels, we prefer to handle all the data reduction and not rely on the full GMOS package[6] based on IRAF for the data reduction. For this purpose, we have written a new custom pipeline code in the Interactive Data Language (IDL). We used only the available IRAF routine `gmosaic` from the GMOS package, to correctly mosaic the three different chips of the CCD. Specifically, the images were bias-subtracted and flat-fielded using twilight flats. To improve the flat-fielding, essential for detecting faint extended emission across the fields, we further correct for the illumination patterns using night-sky flats. The night-sky flats were produced by combining the unregistered science frames with an average sigma-clipping algorithm after masking out all the objects. Satellite trails, CCD edges, bad pixels, and saturated pixels were masked. In particular, we produced a mask of bad behaving pixels, using an average dark-current frame obtained from dark-current images with the same exposure time as the science frames. We notice that this mask is important, given our binning of 4 pixels (resulting in a pixel scale of 0.29″ pixel^{-1}), needed to achieve ‘sky-limited’ observations, i.e. to minimize read-noise. Each individual frame is cleaned from cosmic rays using the L.A.Cosmic algorithm (van Dokkum 2001).

---

[4] Due to bad weather conditions, our queue program was rescheduled two times, i.e. it took roughly three semesters to get the data.

[5] We observed for only 1 hour the quasar HDFS J2233-606, known to have a large Lyα nebula (Bergeron et al. 1999) to confirm it. Further, we got some data on the quasar SDSSJ212747.43+004929.5 from the queue program, which are not included in the current analysis given the different setup used for its observation.

[6] http://www.gemini.edu/sciops/data-and-results/processing-software

Table 4.1. Summary of the GMOS/Gemini-South Observations used in this work.

Target	z	i-mag (AB)	Exp. Time NB[a] (hours)	Exp. Time g[b] (hours)	Depth[c] (cgs/arcsec^2)
SDSSJ081846.64+043935.2	2.255	19.38	2	0.5	3.8×10^{-18}
SDSSJ082109.79+022128.4	2.254	18.91	2	0.5	3.8×10^{-18}
SDSSJ084117.87+093245.3	2.254	18.02	5	3	2.5×10^{-18}
SDSSJ085233.00+082236.2	2.253	18.31	2	0.7	4.4×10^{-18}
SDSSJ093849.67+090509.7	2.255	17.33	5	3	2.1×10^{-18}
SDSSJ100412.88+001257.6	2.253	18.62	2	0.5	5.0×10^{-18}
SDSSJ104330.46-023012.6	2.252	18.37	2	0.5	4.8×10^{-18}
SDSSJ110650.53+061049.9	2.253	18.74	1.7	0.4	6.1×10^{-18}
SDSSJ113240.86-014818.9	2.251	19.19	2	0.7	5.2×10^{-18}
SDSSJ121503.13+003450.6	2.255	19.36	2	0.7	4.9×10^{-18}
SDSSJ131433.84+032322.0	2.251	18.52	1.7	0.4	5.8×10^{-18}
SDSSJ141027.12+024555.8	2.252	19.31	2	0.5	4.9×10^{-18}
SDSSJ141936.61+045430.8	2.254	19.51	1.7	0.4	4.6×10^{-18}
SDSSJ151521.88+070509.8	2.254	19.96	2	0.3	4.2×10^{-18}
SDSSJ160121.02+064530.3	2.257	19.45	1.7	0.5	4.5×10^{-18}

[a] Total exposure time for the observations with the narrow-band filter.

[b] Total exposure time for the observations in the g-band.

[c] 1σ surface brightness limit [$\mathrm{erg\,s^{-1}\,cm^{-2}\,arcsec^{-2}}$] in 1 square arcsec for the NB images (see Section for details).

The final stacks for each filter (NB and g-band) were obtained by average-combining the science frames with weights (based on the S/N) and a sigma clipping algorithm. The sky-subtraction is performed on the individual frames before the final stack. To ensure that we do not mistakenly subtract any extended emission, or introduce systematics during the sky subtraction, we simply estimate an average sky value, after masking out all sources in each individual image. We then subtract this constant value from each image. Given the very small field distortions of GMOS[7], we calibrate the astrometry after the stacking[8]. The astrometry was calibrated with the SDSS-DR9 catalogue using `SExtractor` (Bertin & Arnouts 1996) and `SCAMP` (Bertin 2006). The RMS uncertainties in our astrometric calibration are $\sim 0.2''$. For the flux calibration of the NB imaging, we use the standard stars (H600, G60-54, G138-31) that were repeatedly observed during the observations, typically at the beginning and at the end of the night. To avoid systematics in the flux calibration, these spectrophotometric stars are selected to be free of any feature at the wavelength of interest, and to have a good sampling of their tabulated spectrum (at least 1Å). All data show consistent zero points, with good agreement between the queue program and the 'fast-survey', and stable during the whole night ($\text{ZP}_{NB} = 22.11$). The uncertainty in the derived zero-point is ≈ 0.03 mag. Regarding the g-band images, the flux calibration is performed using several photometric stars in different PG-fields (PG0918+029,PG1047,PG1633+099) observed at the beginning and at the end of each night. Also in this case, all data show consistent zero points, with good agreement between the queue program and the 'fast-survey', and stable during the whole night ($\text{ZP}_{NB} = 28.45$). Note that this value is consistent with the GMOS tabulated values[9]. The uncertainty in the derived zero-points is ≈ 0.03 mag.

During the data reduction steps (e.g. bad pixel masking, satellite trails masking, etc.), our pipeline consistently propagates the errors, and produces a variance image $\sigma^2 = \text{SKY}+\text{OBJECTS}+\text{READNOISE}$. A correct final variance image for each stack, and thus a correct knowledge of the errors, is of fundamental importance for the measurement of very low signals. This has been already stressed in Chapter 3, and will be again evident in Chapter 6. We compute a global surface brightness limit for detecting the Lyα line using a global root-mean-square (rms) of the images. To calculate the global rms per pixel, we first mask out all the sources in the images, paying particular attention to the scattered light and halos of bright foreground stars, and then compute the standard deviation of sky regions using a sigma-clipping algorithm. We convert these rms values into the surface brightness limits *per* 1 sq. arcsec aperture listed in Table 4.1.

---

[7] The field distortions of GMOS-S are regularly checked. For the E2V detector they were estimated to be 1 pixel in the x-direction and 2 pixels in the y-direction at the edge of the field on March 2014 (Pascale Hibon private communication). Note that these values correspond to the unbinned CCD, and thus 1 pixel corresponds to $0.07''$, resulting in negligible distortions with our binning. This scenario was confirmed by comparing the SDSS-DR9 catalogue with our individual frames.

[8] In this way, we avoid the problem of getting a good astrometry solution for individual NB images with very few sources.

[9] http://www.gemini.edu/sciops/instruments/performance-monitoring/data-products/gmos-n-and-s/photometric-zero-points

4.4 Overview of the Current Results of the Survey

Currently, to our knowledge, this dataset represents the deepest and largest survey targeting $z \sim 2$ QSOs. In this section I briefly summarize the results that we have so far in hand, while in the next Chapters I will extensively discuss some of these points.

The Slug Nebula The first observing run at the Keck telescope in November 2012 led to the discovery of a giant ($\sim$ 500 kpc) Lyα nebula around the UM 287 quasar[10] . This luminous ($L \simeq 1.43 \times 10^{45}$ erg s^{-1}) nebula represents the largest reservoir of cool gas ever observed at high redshift, and poses a great challenge to our current understanding of the astrophysics of the halos hosting massive $z \sim 2$ galaxies (see Chapter 5). Either an enormous reservoir of cool gas is required $M \simeq 10^{12}$ M$_{\odot}$, exceeding the expected baryonic mass available, or one must invoke extreme gas clumping factors, not present in high-resolution cosmological simulations. This nebula is mainly known as the 'Slug Nebula', name inspired by its shape, which also recalls the mascot of the University of California, Santa Cruz.

Fraction of Large Nebulae Immediately after the surprising discovery of the Slug Nebula, the question *"How often a $z \sim 2$ QSO shows such huge nebulosity?"* was in the air. To answer this question, we can define a giant Lyα nebula to be extended emission on a scale > 50 kpc from the QSO with an average SB$_{\rm Ly\alpha} \sim 10^{-17}$ erg s^{-1} cm^{-2} arcsec^{-2}, achieved in both our Keck and Gemini data. Given that we have observed a total of 25 QSOs, and detected only a single giant Lyα nebula (around UM 287), it seems that 4% of the QSOs should show giant Lyα nebulae. By taking into account the 1σ confidence level for the Poisson distribution in the small number regime, the frequency of occurance of giant nebulae is in the range $3-9\%$ (Hennawi et al. 2015). An independent answer to the above question comes from narrow-band imaging of 8 QSOs at $z \sim 2.7$, as part of the Keck Baryonic Structure Survey (KBSS, by C.Steidel and Collaborators). We are aware of a single giant Lyα nebula in these observations, i.e. around the quasar HS1549+19 (Martin et al. 2014a). Thus, the 1σ Poisson confidence interval for the frequency of giant nebulae in this sample is $10-29\%$. Further, Hennawi et al. (2015) shows that the detection of a single extended nebula in the sample of 23 quasar spectra of Hennawi & Prochaska (2013), can again suggest that 10% of the quasars should show such giant nebulosities[11]. Thus, three independent surveys indicate that roughly 10% of the QSOs should show such giant Lyα nebulosities. However, larger statistical samples are needed to confirm this scenario (see Chapter 7).

---

[10] I took the data together with Sebastiano Cantalupo. J. Xavier Prochaska was connected remotely from Santa Cruz, while Joseph F. Hennawi was connected from Heidelberg.

[11] This argument is derived from geometrical considerations. See Hennawi et al. (2015) for details.

LAEs Catalogues I have compiled catalogues of Lyα emitters (LAEs) for each of the fields already reduced. The overall analysis will be conducted in the next years. The main aims of this analysis are 1) build up a large sample of 'dark-galaxies' candidates (Cantalupo et al. 2012), to be followed-up and confirmed with other facilities (e.g., HST); 2) to characterize the environment of the observed quasars, i.e. is a typical QSO sitting in an overdensity or not? Do the QSO has an impact on the distribution of detected Lyα emitting objects (e.g. Trainor & Steidel 2013)?

Discovery of a new LAB During the 'fast-survey' with Gemini-South we discovered a new LAB in the field of the QSO SDSSJ121503.13+003450.6 (see Figure 4.2). This LAB, with its maximum size of $\sim$ 70 kpc (from the 2σ isophote) and average $\mathrm{SB}_{\mathrm{Ly}\alpha} = 8.2\times10^{-18}$ erg s^{-1} cm^{-2} arcsec^{-2}, demonstrates that we have reached a sufficient depth to detect giant Lyα nebulae around the observed QSOs. Obviously, further observations are needed to fully characterize this source.

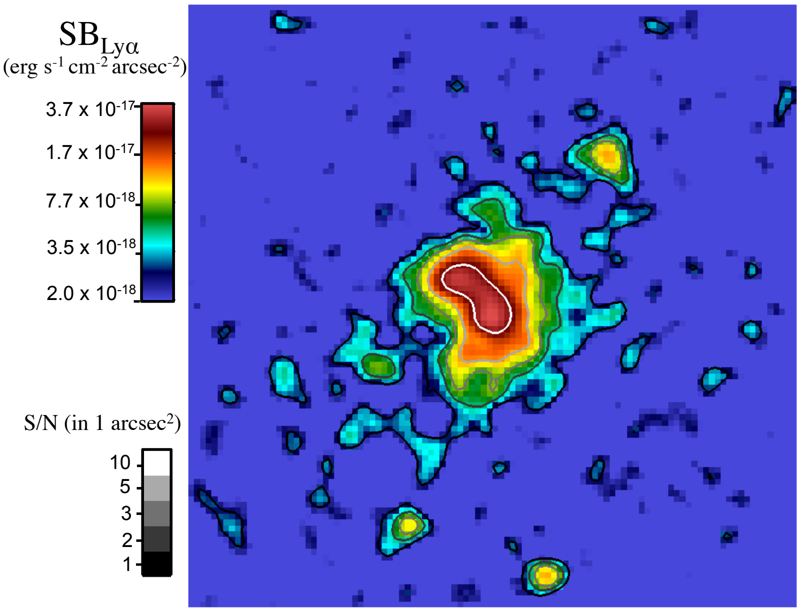

Figure 4.2: Lyα surface brightness map of the LAB discovered in the field of the quasar SDSSJ121503.13+003450.6. The image shows a $30'' \times 30''$field of view. The LAB has an average surface brightness of $\mathrm{SB}_{\mathrm{Ly}\alpha} = 8.2 \times 10^{-18}$ erg s^{-1} cm^{-2} arcsec^{-2}, and an extent of $\sim$ 70 kpc. Both measurements are within the 2σ isophote of our observations, see Table 4.1.

Constraining the Lyα Extended Emission around the Average QSO From the foregoing discussion, it is clear that only 10% of the observed QSOs show giant Lyα nebulosities. What is the Lyα emission level expected around the average QSO population? To answer this question, I performed a stacking analysis of all the Gemini data, showing that the signal is expected to be very faint, i.e. $\mathrm{SB}_{\mathrm{Ly}\alpha} \sim 5 \times 10^{-20}$ erg s^{-1} cm^{-2} arcsec^{-2}, and thus difficult to achieve even with new instruments, e.g. MUSE. As far as I know, this is the first attempt to characterize the CGM of QSOs to these depths. See Chapter 6 for the detailed analysis.

> *"The beginning of knowledge is the discovery of something we do not understand."*
>
> Frank Herbert

Chapter 5

DISCOVERY AND ANALYSIS OF THE LARGEST LYα NEBULA EVER OBSERVED

In this Chapter, I discuss the largest Lyα nebula ever observed at high redshift, found during the observations of the FLASHLIGHT survey, as anticipated in §4.4. This Chapter starts with a brief introduction on the discovery of the UM 287 nebula, explaining why its size and luminosity are a challenge for the current interpretation of the astrophysics of massive halos (§5.1). In §5.2, the observations and data reduction are then extensively presented. §5.3.1 presents a comparison of the environment of the newly discovered Lyα nebula to other Lyα nebulae known, and §5.3.2 describes how its observed Lyα surface brightness has been compared to radiative transfer simulations. Finally, in §5.4, I show how deep observations in the He II and C IV lines, together with a detailed photoionization modeling, help in constraining the properties of the Lyα nebula and suggest a solution to the tension between our discovery and current cosmological simulations.

---

[*] This chapter is adapted from Cantalupo et al. (2014), and Arrigoni Battaia et al. (2015a). My personal contribution to the former paper (which appeared on Nature doi:10.1038/nature12898) was mainly related to data reduction and analysis. Specifically, I reduced and calibrated the images, produced the continuum-subtracted image, the catalogues of the LAEs, and compiled data on all Lyα nebulae in the literature. I have also assisted with the observations at the Keck telescope, contributed to the text and the figures. For the sake of clarity and because it is relevant for the subsequent Sections, I decided to include in this Thesis the comparison with simulations performed by Sebastiano Cantalupo. Regarding the latter paper, I am the main contributor. However, Joseph F. Hennawi performed the data reduction of the spectra.

5.1 THE DISCOVERY

As emphasized in §4.1, a bright quasars can, like a flashlight, 'illuminate' the densest knots in the surrounding cosmic web and boost fluorescent Lyα emission to detectable levels. Following this idea, we imaged UM 287 on 2012 November 12 and 13 UT with a custom narrow-band filter (NB3985) tuned to Lyα at $z = 2.28$ inserted into the camera of the Low Resolution Imaging Spectrometer (LRIS) on the 10m Keck I telescope. Figure 5.1 presents the processed and combined images, centered on UM 287. In the NB3985 image, we identify a very extended nebula originating near the quasar with a projected size of about $1'$. In the broad-band images no extended emission is observed. This requires the narrow-band light to be line-emission, and we identify it as Lyα at the redshift of UM 287.

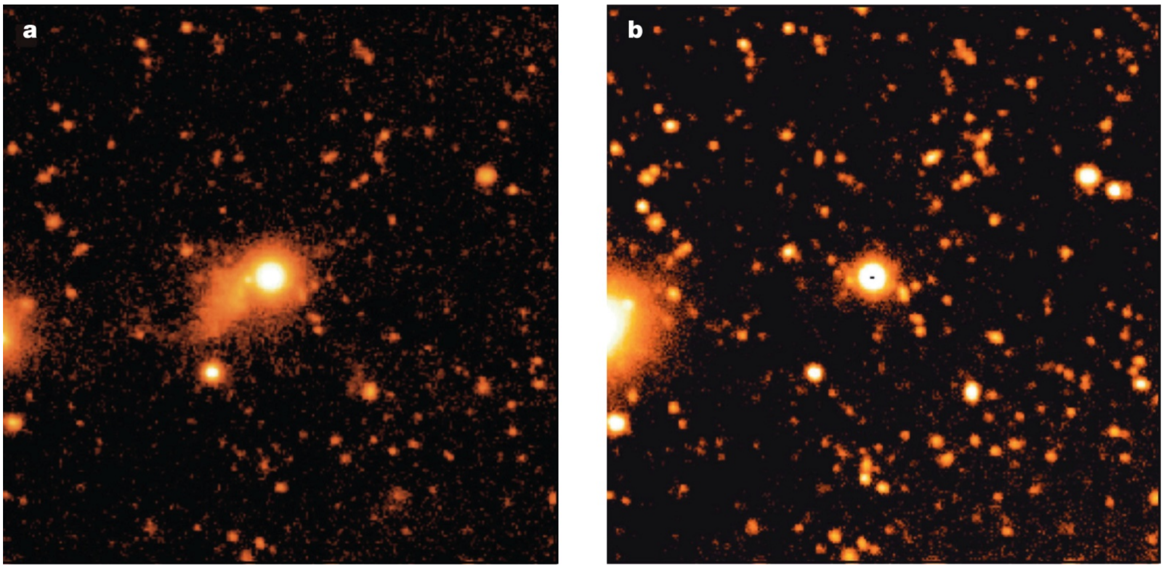

Figure 5.1: Processed and combined images of the field surrounding the quasar UM 287. Each image is $2' \times 2'$, and the quasar is located at the center. In the narrow-band (NB3985) image (Panel a), which is tuned to the Lyα line of the systemic redshift of UM 287, we identify very extended ($\sim 55''$ across) emission. The deep V-band image (Panel b) does not show any extended emission associated with UM 287. This requires the nebula to be line-emission, and we identify it as Lyα at the redshift of the quasar. Figure adapted from Cantalupo et al. (2014).

Figure 5.2 presents the NB3985 image, continuum subtracted using standard techniques (see §5.2.1) and smoothed with a $1''$ Gaussian kernel. This image is dominated by the filamentary and asymmetric nebula that has a maximum projected extent of $55''$ as defined by the 10^{-18} erg s^{-1} cm^{-2} arcsec^{-2} isophotal contour, corresponding to about 460 physical kpc or 1.5 Mpc in co-moving coordinates. Including (excluding) the emission from the quasar UM 287 falling within the narrow-band filter, the structure has a total line luminosity $L_{\mathrm{Ly}\alpha} = (1.43 \pm 0.05) \times 10^{45}$ erg s^{-1} ($L_{\mathrm{Ly}\alpha} = (2.2 \pm 0.2) \times 10^{44}$ erg s^{-1}).

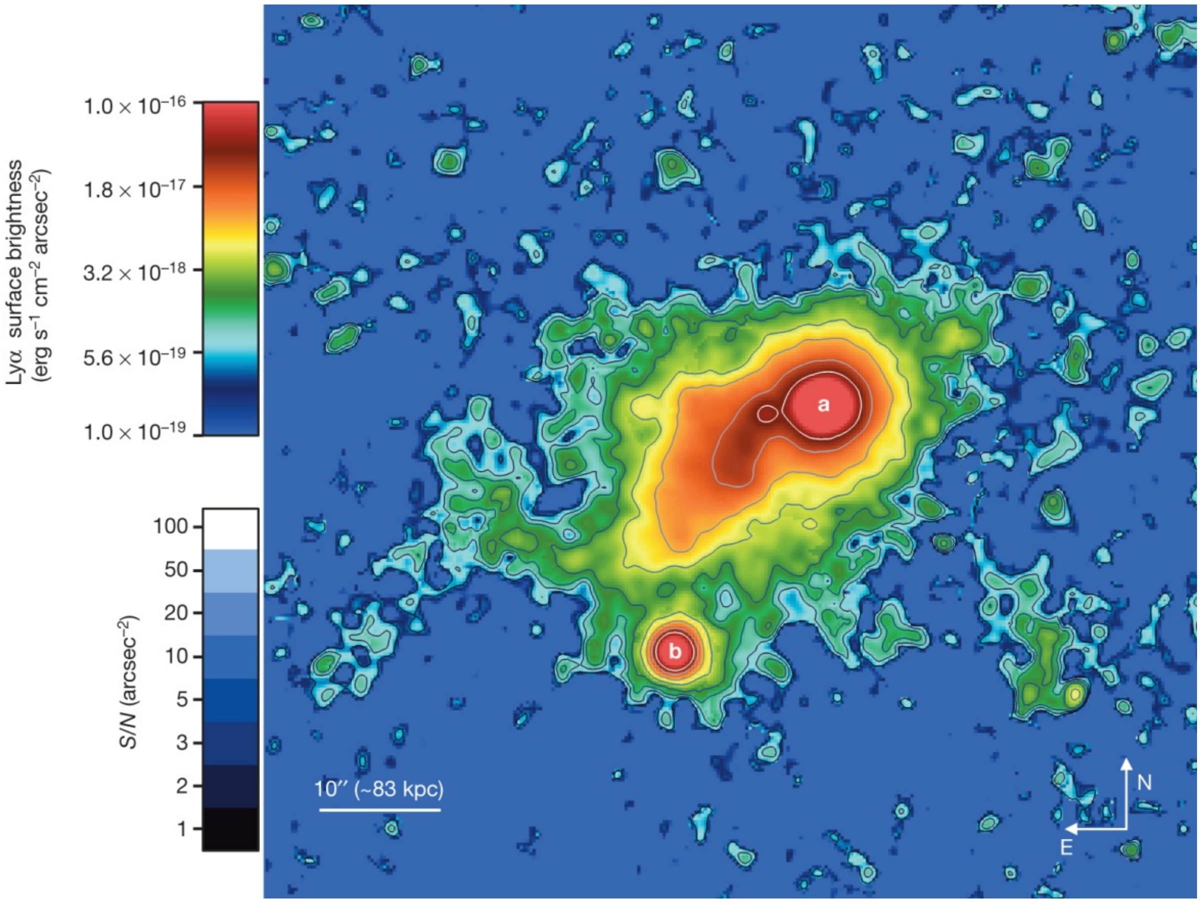

Figure 5.2: Lyα image of the UM 287 nebula (also known as Slug Nebula). We subtracted from the narrow-band image the continuum contribution estimated from the broad-band images (see §5.2.1). The location of the quasar UM 287 is labelled with 'a'. The color map and the contours indicates, respectively, $\mathrm{SB}_{\mathrm{Ly}\alpha}$ (upper color scale) and the signal-to-noise ratio per arcsec^2 aperture (lower color scale). The extended emission spans a projected angular size of ~ 55 arcsec (about 460 kpc), measured from the 2σ ($\sim 10^{-18}$ erg s^{-1} cm^{-2} arcsec^{-2}) contours. The object marked with 'b' is an optically faint ($V \approx 21.5$) quasar at the same redshift as UM 287 (see §5.2.2). The nebula appears broadly filamentary and asymmetric, extending mostly on the eastern side of the quasar UM 287 up to a projected distance of about 35″ (~ 285 kpc) measured from the 2σ isophote. The nebula extends towards the southeast in the direction of the optically faint quasar. However, the two quasars do not seem to be directly connected by this structure that continues as a fainter and spatially narrower filament. The large distance between the two quasars and the very broad morphology of the nebula argue against the possibility that it may originate from an interaction between the quasar host galaxies (see §5.2.2). Figure adapted from Cantalupo et al. (2014).

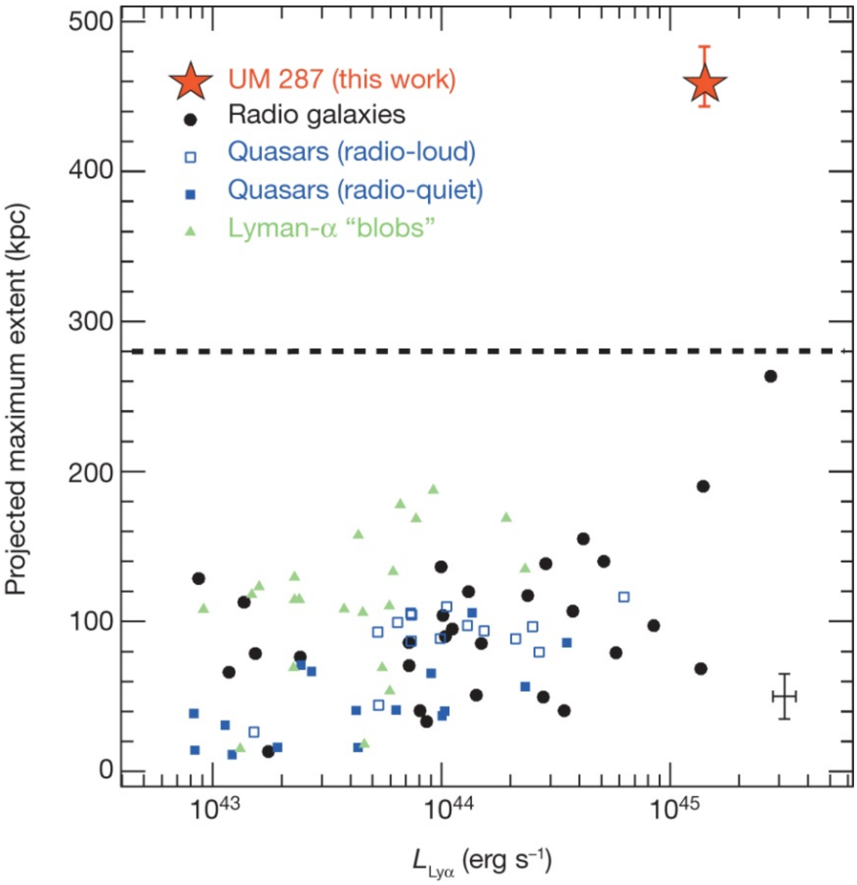

Figure 5.3: Luminosity-size relations for previously detected, bright Lyα nebulae and UM 287. The plot includes nebulae surrounding radio galaxies (black circles), radio-loud quasars (blue open squares), radio-quiet quasars (blue filled squares) and LABs (green triangles). Here, to make the plot more readable, I do not show all the sources in Table 1.2, but a representative sample. Excluding the contribution coming directly from the quasar broad line region, the luminosity of the UM 287 nebula corresponds to $L_{\mathrm{Ly}\alpha} = (2.2 \pm 0.2) \times 10^{44}$ erg s^{-1} (about 16% of the total luminosity). Error bars for UM 287 represent the 1σ photometric error including continuum-subtraction (error bar is smaller than the symbol size) and an estimate of the error on the projected maximum extent using $\pm 1\sigma$ with respect to the 2σ isophote. The typical errors for other sources are presented separately in the bottom-right corner. The dashed line indicates the virial diameter of a dark-matter halo with mass $\sim 10^{12.5}$ M$_\odot$, the typical host of radio-quiet quasars including UM 287, as confirmed by the analysis of the galaxy overdensity in our field (see §5.3.1). The UM 287 nebula, differently from any previous detection, extends on IGM scales that are well beyond any possible associated dark-matter halo. Note that even if we restrict the size measurement of the UM 287 nebula to the 4×10^{-18} erg s^{-1} cm^{-2} arcsec^{-2} isophote to be comparable with the majority of the previous surveys, the measured apparent size of the UM 287 nebula will be reduced only by about 20%. Figure adapted from Cantalupo et al. (2014).

Although few Lyα nebulae extending up to about 250 kpc have been previously detected (see Table 1.2, and §1.3.1) the UM 287 nebula represents a system that is unique so far: given its size, it extends well beyond any plausible dark-matter halo associated with the quasar UM 287 (see §5.3.1), representing an exceptional example of emitting gas on intergalactic scales.

We remind again the Reader that (see section §1.3.1) the largest Lyα nebulae previously discovered (see Fig. 5.3) are associated with the most massive dark-matter haloes present in the high-redshift Universe. High-redshift radio galaxies (HzRGs), inferred to host obscured but luminous AGN, are often surrounded by giant Lyα envelopes extending up to about 250 kpc at $z \sim 3$. Clustering arguments and the observation of large overdensities of Lyα galaxies, together with the lack of X-ray detection from a possible intracluster medium, suggest that HzRGs are associated with haloes of 10^{13} M$_\odot$ (Venemans et al. 2007). With a virial diameter of about 300 kpc at $z \sim 3$, these haloes are therefore able to contain the largest HzRG Lyα nebulae. Blind narrow-band surveys have derived an apparently different population of large nebulae (termed LABs) with sizes extending up to 180 kpc. The rarity and the strong clustering of these sources, suggest, as for HzRGs, an association with proto-cluster environments and haloes with masses of about 10^{13} M$_\odot$ (Yang et al. 2010). Although the detailed origin of the emission of the Lyα blobs is still unclear, the sizes of the associated haloes strongly suggest that the emitting gas is confined within the halo itself. This is also the case for the Lyα nebulae previously detected around a small number of bright quasars, extending up to about 100 kpc (see Table 1.2). Clustering studies demonstrate that bright quasars at $z < 3$ populate haloes of mass $\sim 10^{12.5}$ M$_\odot$ (that have a virial diameter of about 280 kpc at $z \approx 2.3$)[1] independently of their redshift or luminosity (da Ângela et al. 2008; Trainor & Steidel 2012).

The exceptional nature of the nebula is due not only to its size (about 460 kpc) but also to the fact that it is associated with a radio-quiet quasar. Radio-quiet quasars have the smallest host halo mass ($\sim 10^{12.5}$ M$_\odot$) and virial diameter (280 kpc) among previously detected objects and do not have radio-emitting jets that may power Lyα emission on large scales (Villar-Martín et al. 2007a). In order for the nebula to be fully contained within the virial radius of a dark-matter halo centered on UM 287, a halo mass would be required that is at least ten times larger than the typical value associated with radio-quiet quasars. This would make the host halo of UM 287 one of the largest known at $z > 2$, a possibility that is excluded by the absence of a significant overdensity of LAEs around UM 287 compared to other radio-quiet quasars (see §5.3.1). Differently from any previous detection, the nebula is therefore an image of intergalactic gas at $z > 2$ extending beyond any individual, associated dark-matter halo. The rarity of these systems may be explained by the combination of anisotropic emission from the quasars (typically only about 40% of the solid angle around a bright, high-redshift quasar is unobstructed (Polletta et al. 2008), the anisotropic distribution of dense filaments and light travel effects that, for quasar ages of less than a few million years, further limit the possible 'illuminated' volume.

---

[1] Other studies show that the virial diameter at these redshifts for a halo of $M_{\rm DM} \sim 10^{12.5}$ M$_\odot$ is $\sim$ 320 kpc (e.g., Prochaska et al. 2013a). The difference between the two measurements reflects the uncertainties of each study. In this work, , for consistency, I stick to the values I used when I wrote my papers.

In order to constrain the physical properties of this system, we use a set of Lyα radiative transfer calculations (Cantalupo & Porciani 2011) combined with adaptive mesh refinement simulation of cosmological structure formation around a dark-matter halo with mass $M_{\rm DM} \approx 10^{12.5}$ (see §5.3.2). We consider two possible, extreme scenarios for the Lyα emission mechanism of the intergalactic gas associated with the nebula: (1) the gas is highly ionized by the quasar and the Lyα emission is mainly produced by hydrogen recombinations, i.e. the fluorescence scenario ; and (2) the gas is mostly neutral and the emission is mainly due to scattering of the Lyα and continuum photons produced by the quasar broad line region. The models are used to obtain scaling relations between the observable Lyα surface brightness from the intergalactic gas surrounding the quasar and the hydrogen column densities (see §5.3.2). These scaling relations are consistent with analytical expectations. Note that the estimated column densities for scenario (1) depend on the ionized gas clumping factor ($C = \langle n_{\rm e}^2 \rangle / \langle n_{\rm e} \rangle^2$, where $n_{\rm e}$ is the electron density) below the simulation resolution scale, ranging from about 10 physical kpc for diffuse intergalactic gas to $\sim$ 160 physical pc for the densest regions within galaxies.

The results are presented in Figure 5.4. The observed Lyα emission requires very large column densities of 'cold' ($T < 5 \times 10^4$ K) gas, up to $N_{\rm H} \approx 10^{22}$ cm^{-2}. The implied total, cold gas mass 'illuminated' by the quasar is $M_{\rm gas} \approx 10^{12\pm0.5}$ M$_\odot$ for the 'mostly ionized' case (scenario (1)) assuming $C = 1$ and $M_{\rm gas} \approx 10^{11.4\pm0.6}$ M$_\odot$ for the 'mostly neutral' case (scenario (2)). Note that the total estimated mass for case (1) scales as $C^{-1/2}$. For comparison, a typical simulated filament in our cosmological simulation of structure formation with size and morphology similar to the nebula around a dark-matter halo of mass $M_{\rm DM} \approx 10^{12.5}$ M$_\odot$ has a total gas mass of about $M_{\rm gas} \approx 10^{11.3}$ M$_\odot$, but only about 15% of this gas is 'cool' ($T < 5 \times 10^4$ K) – that is, $M_{\rm gas} \approx 10^{10.5}$ M$_\odot$ – and therefore able to emit substantial Lyα emission. These estimates are consistent with a large sample of simulated haloes obtained by other recent works based on cosmological adaptive mesh refinement simulations (Fumagalli et al. 2014). These simulations also show a (weak) decreasing trend of the cool gas fraction with halo mass.

How can we explain the large differences between the estimated mass of cool gas in the nebula and the available amount of cool gas predicted by numerical simulations on similar scales? One possibility is to assume that the simulations are not resolving a large population of small, cool gas clumps within the low-density intergalactic medium that are illuminated and ionized by the intense radiation of the quasar (see the discussion in §5.4). In this case, an extremely high clumping factor, up to $C \approx 1000$, on scales below a few kiloparsecs would be required in order to explain the large luminosity of the nebula with the cold gas mass predicted by the simulations. On the other hand, if some physical process that is not fully captured by current grid-based sim-

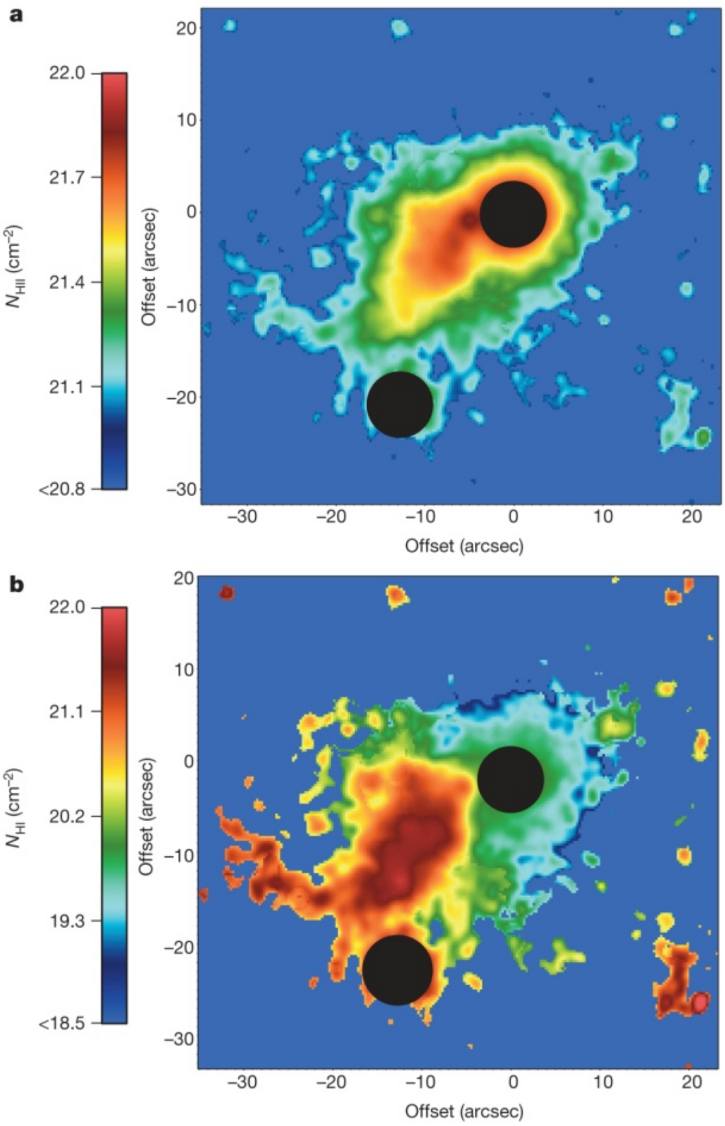

Figure 5.4: Inferred hydrogen column densities associated with the UM 287 nebula. We have converted the observed $SB_{Ly\alpha}$ into gas column densities N using a set of scaling relations obtained with detailed radiative transfer simulations and consistent with analytical expectations (see §5.3.2 and Figure 5.7). We have explored two extreme cases: (1) the gas is mostly ionized by the quasar radiation (Panel a; N_{HII}) and (2), the gas is mostly neutral (Panel b; N_{HI}). Two circular regions with a diameter of $7''$ ($\sim$ 8 times the seeing radius) have been masked at the location of the quasars (black circles). The inferred hydrogen column density in Panel 'a' scales as $C^{-1/2}$, where C is the gas clumping factor on a spatial scale of about 10 physical kpc at moderate overdensities (less than about 40 times the mean density of the Universe at $z \sim 2.279$). The implied column densities and gas masses, in both cases, are at least a factor of ten larger than what is typically observed within cosmological simulations around massive haloes, suggesting that a large number of small clumps within the diffuse intergalactic medium may be missing within current numerical models. Figure adapted from Cantalupo et al. (2014).

ulations increases the fraction of cold gas around the quasar – for example, a proper treatment of metal mixing – a smaller clumping factor may be required. In the extreme (and rather unrealistic) case that all the hot gas is turned into a cool phase, the required clumping factor would be $C \approx 20$. Even if the gas is not ionized by the quasar (scenario (2) above), the simulations are able to reproduce the observed mass only if a substantial amount of hot gas is converted into a cool phase. Incidentally, this is exactly the same result produced by comparing the properties of Lyα absorption systems around a large statistical sample of quasars with simulations (Prochaska et al.

2013b). Proper modeling of this gas phase will require a new generation of numerical models that are able – simultaneously – to spatially resolve these small intergalactic clumps within large simulation boxes, and to treat the multiphase nature of this gas and its interaction with galaxies and quasars.

5.2 OBSERVATIONS AND DATA REDUCTION

As part of the FLASHLIGHT survey (see Chapter 4), we obtained deep, narrow-band imaging of the field surrounding UM 287, also known as PHL 868 and LBQS 0049+0045. UM 287 was discovered in the University of Michigan emission-line survey, has a precisely measured redshift $z = 2.279 \pm 0.001$ based on analysis of [O III] emission lines (McIntosh et al. 1999), and has a bolometric luminosity $L_{\rm bol} \approx 10^{47.3}$ erg s^{-1} estimated from its 1450Å rest-frame flux using standard cosmology. This places it in the upper quartile of ultraviolet-bright quasars at this redshift. Assuming that the spectral energy distribution follows a power law (Lusso et al. 2015) with frequency index $\alpha = -1.7$ at energies exceeding 1 Rydberg, we estimate the luminosity of ionizing photons to be $\Phi = 10^{57.1}$ s^{-1} assuming isotropic emission.

The quasar has no counterpart in the FIRST (Becker et al. 1994) images at 20 cm (1.4 GHz), and based on the FIRST coverage maps we obtain a 5σ flux limit $F_{\rm radio} < 0.76$ mJy, which, given its large ultraviolet luminosity, classifies this quasar as radio-quiet (Ivezić et al. 2002). We selected this source for imaging based solely on its high luminosity, its precisely measured redshift, and its radio-quiet characteristics. As previously mentioned in §4.2, we purchased a custom-designed narrow-band filter from Andover Corporation, sized to fit within the grism holder of the Keck/LRISb camera. The filter was tuned to Lyα at the source's systemic redshift and we requested a narrow band-pass (FWHM $\approx$ 30 Å) that minimized sky background, while maximizing throughput. Figure 5.5 presents the as-measured transmission curve of the NB3985 filter used in these observations.

We observed UM 287 on the nights of UT 12-13 November 2012 for a total of 10 hours, in a series of dithered, 1200s exposures. Conditions were clear, with atmospheric seeing varying from FWHM $\approx 0.6 - 1$ arcsec. As explained in §4.2, LRIS allows us to take broad-band images in parallel. In this way, we obtained 10 hours of broad-band V images with the LRISr camera and 1hour of B-band imaging. For all observations, we employed the D460 dichroic beam splitter. We binned the blue CCDs 2×2 to minimize read noise.

All these data were processed with standard techniques. Bias subtraction was performed using measurements from the overscan regions of each image. The images have been reduced using standard routines within the reduction software IRAF, including bias subtraction, flat fielding

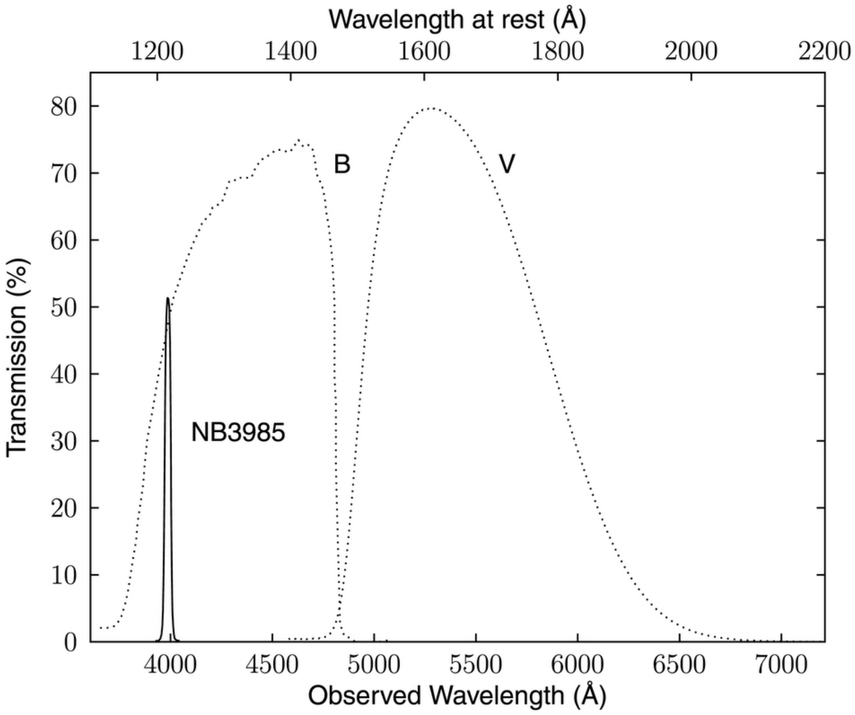

Figure 5.5: Measured transmission curves of the filters used in the discovery of the UM 287 nebula. Solid line, NB3985; dotted lines, *B*-band (left) and *V*-band (right). Bottom axis, observed wavelength; top axis, the rest-frame wavelength for sources at $z = 2.279$. Figure adapted from Cantalupo et al. (2014).

and illumination correction. A combination of twilight sky flats and unregistered science frames has been used to produce flat-field images and illumination corrections for each band. Each individual frame has been registered on the SDSS-DR7 catalogue using `SExtractor` (Bertin & Arnouts 1996) and `SCAMP` (Bertin 2006) in sequence. The astrometric uncertainty of our registered images is about $0.2''$. Finally, for each band (NB3985, *B*, *V*), the corrected frames were average-combined using `SWarp` (Bertin et al. 2002).

We have calibrated the photometry of our images in the following manner. First, we observed during the two nights two spectrophotometric stars (Feige 110 and Feige 34) through the narrow-band filter, under clear conditions. For the broad band images, we observed the standard star field PG 0231+051.

To compute the zero-point for the narrow-band images, we first measured the number of counts per second of the standard stars Feige 110 and Feige 34. We then compared this measurement with the flux expected, estimated by convolving the spectrum of the standard star with the normalized filter transmission curve (see Fig. 5.5). The two measurements agreed to within 0.1 mag. We attribute the difference to small variations in the transparency and adopt an average zero-point of $\mathrm{ZP_{NB}} = 24.14$. The surface brightness limit for our observation in the central region of the image occupied by the nebula is about 5×10^{-19} erg s^{-1} cm^{-2} arcsec^{-2} at 1σ level within an aperture of 1 square arcsec.

For the broad-band images, we compared the number of counts per second of the five stars in the PG 0231+051 field with their tabulated V and B magnitudes (Landolt 1992). The derived zero-point for the five stars are consistent with each other within a few percent and we adopt the average values: $\mathrm{ZP}_B = 28.40$ and $\mathrm{ZP}_V = 28.07$.

As the standard stars and the PG 0231+051 field were observed with a similar airmass of approximately 1.2, which corresponds to the average airmass of our observations, we did not correct the individual images before combination. Moreover, by monitoring unsaturated stars on several exposures, we estimated that the correction would be of the order of a few percent.

5.2.1 CONTINUUM SUBTRACTION

To isolate the emission in the Lyα line we estimated and then subtracted the continuum emission from discrete and extended sources contained within the NB3985 filter. We estimated the continuum using a combination of the V-band and B-band images as follows. First, we smoothed both of the broad-band images using a Gaussian kernel of $1''$ and set to zero all of the pixels with values less than the measured root-mean-square (1σ). Additionally, in the V-band we set to zero all of the pixels which have signal above 1σ in the B-band, as we prefer to use the latter image when possible given that it lies closer in wavelength to the Lyα line (e.g. see Fig. 5.5 for the position of the filters).

After matching the seeing between the narrow-band and the broad-band images, the continuum subtraction has been applied using the following formula

$$\mathrm{Ly}\alpha = \mathrm{NB3985} - a\left(\frac{\mathrm{FWHM}_{\mathrm{NB3985}}}{\mathrm{FWHM}_B}\right)\left(\frac{\mathrm{Tr}_{\mathrm{NB3985}}}{\mathrm{Tr}_B}\right)B - b\left(\frac{\mathrm{FWHM}_{\mathrm{NB3985}}}{\mathrm{FWHM}_V}\right)\left(\frac{\mathrm{Tr}_{\mathrm{NB3985}}}{\mathrm{Tr}_V}\right)V \qquad (5.1)$$

where Lyα is the final subtracted image, NB3985 is the smoothed narrow-band image, B and V are the smoothed and masked broad-band images, and $\mathrm{Tr}_{\mathrm{NB3985}}$, Tr_B and Tr_V are the transmission peak values for NB3985, B-band and V-band filters, respectively. The parameters $a = 0.85$ and $b = 0.65$ allow a better match to the continuum. Following this procedure, we primarily used the smoothed B-band image to estimate the continuum and we included the V-band to achieve deeper sensitivity and to correct those objects not detected in the B-band image.

5.2.2 Data Reduction and Analysis for the Companion Quasar

Upon analysing the continuum-subtracted Lyα image, we identified a compact Lyα excess source at 24.3$''$ separation from UM 287 (corresponding to about 200 kpc), which has a faint counterpart in our deep LRIS continuum image ($V = 21.54 \pm 0.06$). Further exploration of this source reveals it is detected by the FIRST survey (FIRST J005203.26+010108.6) with a flux $F_{\rm peak} =$ 21.38 mJy, strongly suggesting that this source is a radio-loud, but optically faint quasar. On UT 08 December 2012, we obtained a long-slit spectrum of J005203.26+010108.6 using the Keck/LRIS spectrometer configured with the D560 dichroic, the 600/4000 grism in the LRISb camera, and the 600/10000 grating in the LRISr camera. We oriented the long slit to also cover UM 287.

These data were reduced with the LowRedux (http://www.ucolick.org/~xavier/LowRedux/index.html) software package using standard techniques. Figure 5.6 presents the two, optimally extracted spectra from the LRISb camera. One recognizes the broad and bright emission lines characteristic of type I quasars. The redshift estimated from these lines – that has an error of about 800 km s^{-1} (1σ) – is consistent with the systemic redshift of UM 287, suggesting that UM 287 is actually a member of a binary system with a fainter companion. We emphasize, however, that there is very little (if any) Lyα emission apparent in the narrow-band image that may be associated with J005203.26+010108.6 apart from that produced by its own nuclear activity.

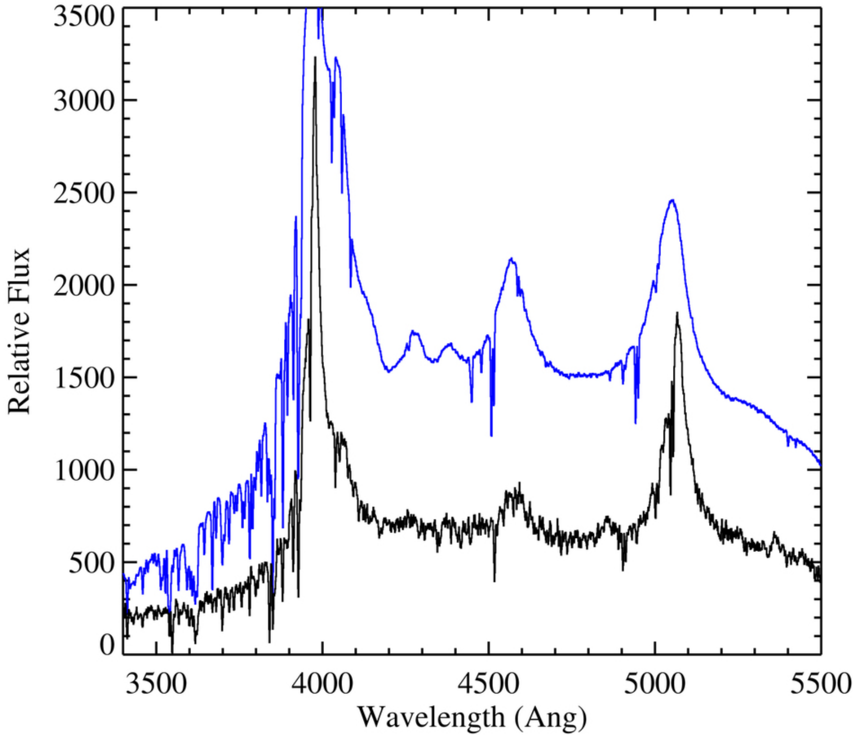

Figure 5.6: Keck/LRIS spectrum of the quasar UM 287 and of the faint, radio-loud companion quasar. Black line, spectrum of the companion quasar which is indicated by ‘b’ in Fig. 5.2 and is separated by about 24$''$ from UM 287. Blue line, spectrum of UM 287. Comparison of the two spectra clearly shows that this companion is a quasar at a redshift similar to that of UM 287. Figure adapted from Cantalupo et al. (2014).

Because of the large distance from UM 287 – at least 200 kpc and up to 4 Mpc considering the 1σ redshift error – and the morphology of the nebula we can exclude the possibility that the UM 287 nebula is the result of tidal interaction due to a merging event between the two quasar hosts. Indeed, such a large separation would imply that any possible encounter between the two quasars is probably a high velocity interaction or an encounter with large impact parameter. We note that it is not impossible but extremely difficult to produce a long and massive tidal tail during a 'fast' encounter (Barnes & Hernquist 1992) and the amount of gas stripped by the quasar host galaxies in the best scenario would probably be a very small fraction ($< 10\%$) of its total interstellar medium. Irrespective of the details of the possible interaction between the two quasar host galaxies, any resulting, long tidal tail would be very thin with sizes of the order of few kpc or less (Barnes & Hernquist 1992) whereas the observed nebula has a FWHM thickness of at least 100 kpc in its widest point.

5.3 ANALYSIS OF THE NEBULA'S ENVIRONMENT AND EMISSION

5.3.1 GALAXY OVERDENSITY ANALYSIS

We have obtained a sample of 60 Lyα emitter (LAE) candidates above a flux limit of 3×10^{-18} erg s^{-1} cm^{-2} (corresponding to a Lyα luminosity of about 2×10^{41} erg s^{-1}) within the volume probed by our narrow-band imaging ($\sim$ 3100 co-moving Mpc^{-3}) around UM 287. The selection is based on the same technique applied by Cantalupo et al. (2012).

How does the number density in our survey compare to other similar searches around massive objects? As anticipated in §1.3.1.3, surveys of LAE around HzRGs (Venemans et al. 2007; Kurk et al. 2000) have revealed large overdensities of LAEs with respect to field studies at similar redshifts (Guaita et al. 2010; Ciardullo et al. 2012), that are compatible with the presence of a massive halo of $\sim 10^{13}$ M$_\odot$, as estimated from clustering. Narrowband imaging of the radio-galaxy MRC 1138-262 at $z = 2.16$ (Kurk et al. 2000), associated with a 200-kpc-scale Lyα nebula (see Table 1.2 for precise values), found a number density of LAE above $L_{\mathrm{Ly}\alpha} = 1.4\times10^{42}$ erg s^{-1} of $n_{\mathrm{HzRG}} \approx (10\pm2)\times10^{-3}$ co-moving Mpc^{-3} (Venemans et al. 2007). By comparison, the number density of LAE above the same limit at the same redshift in the field is $n_{\mathrm{field}} \approx (1.5 \pm 0.5) \times 10^{-3}$ co-moving Mpc^{-3}, corrected for completeness (Guaita et al. 2010). If we restricted our sample to the same luminosity cut, we found a number density of $n_{\mathrm{UM\ 287}} \approx (5 \pm 1) \times 10^{-3}$ co-moving Mpc^{-3}. Note that, at this luminosity, our sample is complete. Despite the large statistical errors, we note that the overdensity with respect to the field around UM 287 (about a factor of three) is significantly smaller than the overdensity of LAE around MRC 1138-262 (about a factor six). A similar result is obtained comparing the overdensity of LAE around UM 287 with other HzRGs

(Venemans et al. 2007), suggesting that UM 287 is hosted by a smaller halo than typical HzRG hosts. Moreover, the modest overdensity of our field is strong evidence against the possibility that the UM 287 nebula may be fully contained by an individual dark-matter halo of mass $10^{13.5}$, as would be required by its size. Note that the galaxy number density estimate around UM 287 is a conservative upper limit. Indeed, as already explained in §4.1, if the quasar is illuminating the surrounding volume, we expect a boost in the number of detectable LAE objects due to fluorescence, as demonstrated by Cantalupo et al. (2012). Our measurement is also compatible with the number density of LAEs found by another recent, shallower search for Lyα emission around eight radio-quiet, bright quasars at $z \sim 2.7$, as part of the Keck Baryonic Structure Survey (KBSS). These studies found number densities ranging from 6×10^{-3} to 22×10^{-3} co-moving Mpc^{-3} around individual quasars above a Lyα luminosity of $L_{\mathrm{Ly}\alpha} = 5.8 \times 10^{41}$ erg s^{-1} (Trainor & Steidel 2013). Combining the eight fields, the average number density from their survey is $(12.0 \pm 0.4) \times 10^{-3}$ co-moving Mpc^{-3}.

Using the same luminosity cut, we find a number density of $(12 \pm 2) \times 10^{-3}$ co-moving Mpc^{-3}, suggesting that the halo mass of UM 287 is indeed within the typical range for the host haloes of radio-quiet quasars, i.e. $M_{\mathrm{DM}} \sim 10^{12.5}$ $\mathrm{M}_{\odot}$ (White et al. 2012).

5.3.2 CONVERTING THE OBSERVED LYα EMISSION TO GAS COLUMN DENSITIES

As anticipated in §5.1, we derived a relation between the observable Lyα emission from diffuse gas illuminated by a quasar and the gas column densities by combining a Lyα radiative transfer model with the results of a cosmological hydrodynamical simulation of structure formation at $z = 2.3$ (Cantalupo et al. 2012). The cosmological simulations have been obtained with the adaptive mesh refinement code RAMSES (Teyssier 2002) and consist of a 403 co-moving Mpc^3 cosmological volume with a 103 co-moving Mpc^3 high-resolution region containing a massive halo compatible with the expected quasar hosts, i.e. a dark-matter mass $M_{\mathrm{DM}} \sim 10^{12.5}$ $\mathrm{M}_{\odot}$. The equivalent base-grid resolution in the high-resolution region corresponds to a (1024^3) grid with a dark-matter particle mass of about 1.8×10^6 $\mathrm{M}_{\odot}$. We used other additional six grid refinement levels, reaching a maximum spatial resolution of about 0.6 co-moving kpc, that is, about 165 physical pc at $z = 2.3$. Star formation, supernova feedback, and an optically thin ultraviolet background with an on-the-fly self-shielding correction are included using a typical choice of sub-grid parameters for the simulation resolution (Cantalupo et al. 2012). We have then applied in post processing an ionization and Lyα radiative transfer using the RADAMESH adaptive mesh refinement code (Cantalupo & Porciani 2011). Ionization, Lyα and non-ionizing continuum radiation from the quasar broad line region is propagated within two symmetric cones that cover half of the solid angle around the quasar. We included light-travel and finite light-speed effects for both ionizing and Lyα radiation transfer and varied the quasar age (from 1 Myr to

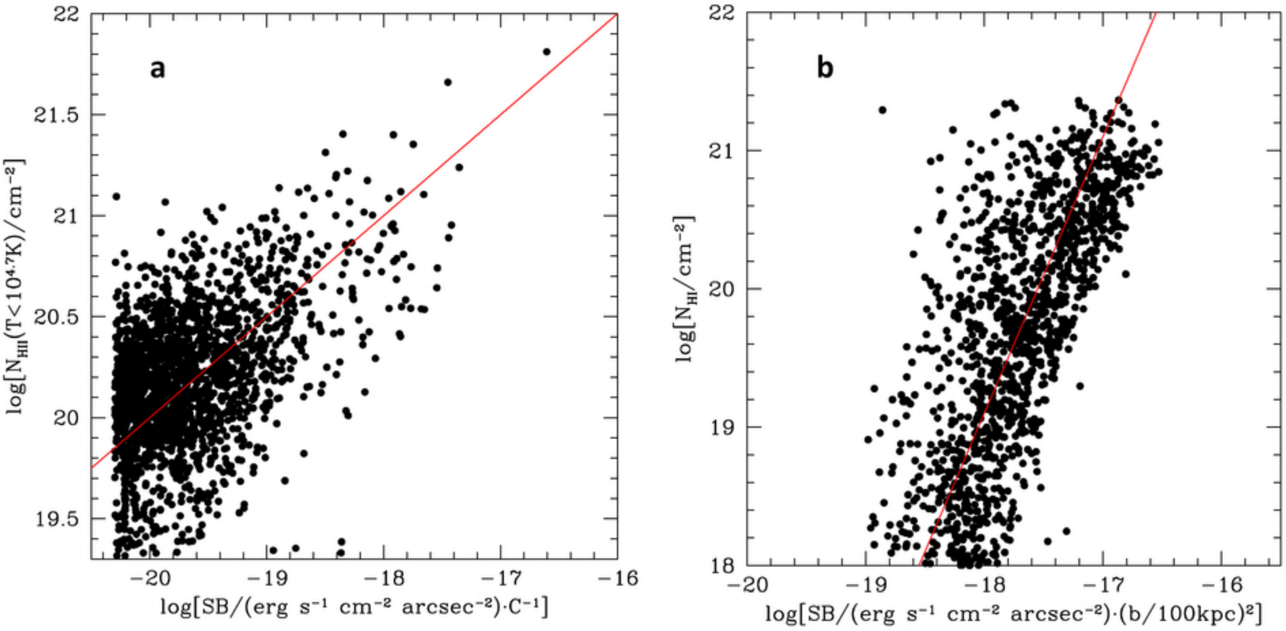

Figure 5.7: Pixel-to-pixel correlations for $\mathrm{SB}_{\mathrm{Ly}\alpha}$ for scenarios (1) and (2). **Panel a:** Pixel-to-pixel correlation between simulated $\mathrm{SB}_{\mathrm{Ly}\alpha}$ divided by the clumping factor (C) and corresponding cool ($T < 5 \times 10^4$ K) ionized hydrogen column densities $\mathrm{N}_{\mathrm{HII}}$ for scenario (1) (see §5.1 for details). The solid line indicates the Relation (5.2). **Panel b:** Pixel-to-pixel correlation between simulated $\mathrm{SB}_{\mathrm{Ly}\alpha}$ (normalized by the quasar impact parameter squared, b^2) and corresponding N_{HI} for scenario (2) (see §5.1 for details). The solid line represents the relation $N_{\mathrm{HI}} = 10^{19.1}\,[\mathrm{SB}_{\mathrm{Ly}\alpha}(b/100)^2]^2$ cm^{-2} (here $\mathrm{SB}_{\mathrm{Ly}\alpha}$ is in unit of 10^{-18} erg s^{-1} cm^{-2} arcsec^{-2} , and b is in units of kpc). Figure adapted from Cantalupo et al. (2014).

10 Myr) and the orientation of the emission cones with respect to the observer line-of-sight and the cosmic web surrounding the simulated halo. We note that these effects are able to produce asymmetric Lyα nebulae with sizes and morphologies similar to the observations for short quasar ages (< 5 Myr).

In order to produce a calibrated relation for scenario (1) as discussed in §5.1, we have fixed the quasar ionizing and Lyα luminosity to the observed value and assumed that the ionizing and Lyα emitting cones are coincident. We have then produced mock images with the same angular resolution of the observation that have been convolved with a point spread function (PSF) with 1 arcsec size to simulate atmospheric seeing. A column density map of cool ($T < 5 \times 10^4$ K) ionized hydrogen was produced from the simulations considering only the gas ‘illuminated’ by the quasar and convolved with the same PSF. We have then cross-correlated the two quantities pixel by pixel and fitted the calibrated relation shown as a solid line in the left panel of Figure 5.7. We find that

$$N_{\rm HII} = 10^{21} \left(\frac{\rm SB_{Ly\alpha}}{10^{-18}\,{\rm erg\,s^{-1}\,cm^{-2}\,arcsec^{-2}}} \right)^{1/2} C^{-1/2}\,{\rm cm}^{-2}, \tag{5.2}$$

where $N_{\rm HII}$ is the ionized hydrogen column density, which, in this highly ionized scenario, basically represents the total hydrogen column density $N_{\rm H}$.

This relation is consistent with analytical expectations[2] from highly ionized gas where the Lyα emission is mostly produced by hydrogen recombination with a negligible contribution from collisional excitations and Lyα scattering (or photon-pumping) from the quasar non-ionizing continuum and Lyα radiation (Cantalupo et al. 2012). We have repeated the experiment varying the sub-grid clumping factor (C) below the simulation resolution and found, as expected for highly ionized gas, that the simulated surface brightness scales linearly with C at a given gas column density.

We have also considered the extreme case (scenario (2) in §5.1) in which the simulated gas is only illuminated by non-ionizing radiation from the quasar, and therefore that dense gas in the simulation remains mostly neutral above the self-shielding number density to the cosmic ultraviolet background ($n \sim 0.01$ cm^{-3}). We obtained and post-processed a mock image as in the previous case and cross-correlated the resulting $\rm SB_{Ly\alpha}$ with the neutral hydrogen column densities ($N_{\rm HI}$). Despite the large scatter, we found a good correlation between these two quantities (panel 'b' of Fig. 5.7) if the surface brightness is normalized by the impact parameter (b) squared. The relation between $\rm SB_{Ly\alpha}$, $N_{\rm HI}$, and b is consistent with simple analytical expectations from pure Lyman scattering from the broad line region of the quasar for Lyα optical depth much larger than unity. In this case, the amount of photon-pumping (or, analogously, the equivalent width of the absorbed quasar Lyα and continuum emission) is dominated by the line damping wing and therefore is proportional to $N_{\rm HI}^{1/2}$.

5.4 DEEP He II AND C IV SPECTROSCOPY: DENSE COMPACT GAS CLUMPS

In §5.1, we have shown that the discovery of the UM 287 nebula rises tension between observations and current cosmological simulations. In an effort to better understand the mechanism powering the emission in UM 287, and further constrain the physical properties of the emitting gas, in the following I present the result of a sensitive search for emission in two additional diagnostics, namely He II and C IV, already studied in the case of LABs (Chapter 3). The importance of detecting such lines has been illustrated in §1.3.2, however here I briefly remind the basics.

---

[2] It is indeed equivalent to Eqn. (2.13), derived in the optically thin regime.

The detection of either of these high-ionization emission lines in the extended UM 287 nebula, would indicate that the gas is 'illuminated' by an intense source of hard ionizing photons $E \gtrsim 4$Ryd, and would thus establish that photoionization by the quasar is the primary mechanism powering the giant Lyα nebula. As we will show, in a photoionization scenario where He II emission results from recombinations, the strength of this line is sensitive to the density of the gas in the nebula, which can thus break the degeneracy between gas density and gas mass, mentioned above. In addition, because He II is not a resonant line, a comparison of its morphology and kinematics to the Lyα line can be used to test whether Lyα photons are resonantly scattered. On the other hand, a detection of extended emission in the C IV line can provide us information on the metallicity of the gas in the CGM, and simultaneously constrain the size at which the halo is metal-enriched.

5.4.1 OBSERVATIONS AND DATA REDUCTION

Two moderate resolution (FWHM$\sim$ 300 km s^{-1}) spectra of the UM 287 nebula were obtained using the Low Resolution Imaging Spectrograph (LRIS; Oke et al. 1995) on the Keck I telescope on UT 2013 Aug 4, in multi-slit mode with custom-designed slitmasks. We used the 600 lines mm^{-1} grism blazed at 4000 Å on the blue side, resulting in wavelength coverage of $\approx 3300 - 5880$ Å, which allows us to cover the location of the C IV and He II lines. The dispersion of this grism is $\sim$ 4 Å per pixel and our 1$''$slit give a resolution of FWHM $\simeq$ 300 km s^{-1}. We observed each mask for a total of $\sim$ 2 hours in a series of 4 exposures.

Figure 5.8 shows the position of the two 1$''$-slits (red and blue) on top of the narrow-band image (matching the Lyα line at the redshift of UM 287) presented in Figure 5.1. As previously said in §5.2.2, there is a optically faint ($V = 21.54 \pm 0.06$) radio-loud quasar ('QSO b') at the same redshift, and at a projected distant of 24.3 arcsec ($\sim$ 200 kpc) from the bright UM 287 quasar ('QSO a'). The first slit orientations was chosen to simultaneously cover the extended Lyα emission and the UM 287 quasar (blue slit), whereas the second (red slit) was chosen to cover the companion quasar 'b' together with the diffuse nebula. By covering one of the quasars with each slit orientation we are thus able to cleanly subtract the PSF of the quasars from our data (see Section §5.4.2).

The 2-d spectroscopic data reduction is performed exactly as described in Hennawi & Prochaska (2013) and we refer the reader to that work for additional details. In what follows, we briefly summarize the key elements of the data reduction procedure. All data were reduced using the LowRedux pipeline[3], which is a publicly available collection of custom codes written in the Interactive Data Language (IDL) for reducing slit spectroscopy. Individual exposures are pro-

---

[3] http://www.ucolick.org/~xavier/LowRedux

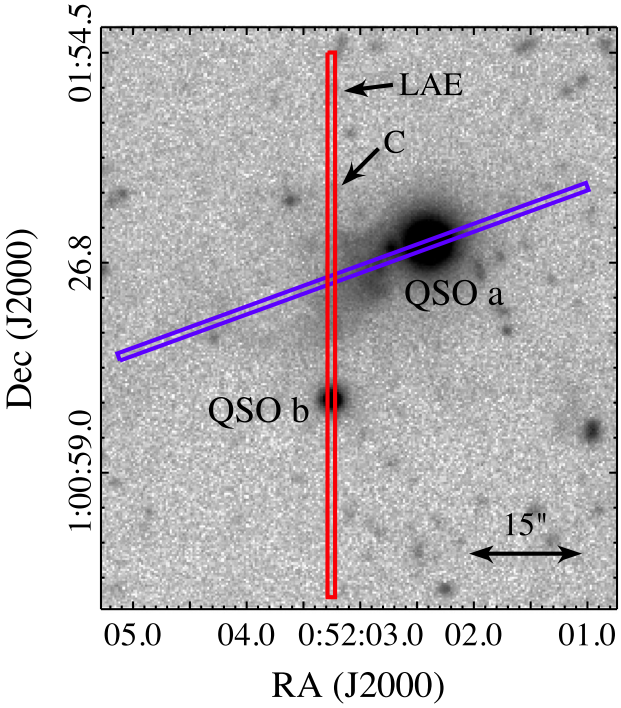

Figure 5.8: 10-hours narrow-band image matching the Lyα line at the redshift of UM 287. 'QSO a' is the quasar UM 287, while 'QSO b' is the faint companion quasar . The red and blue lines highlight the position of the 1″slits chosen to study the extended emission in this work. Note that a Lyman Alpha Emitter ('LAE') and a continuum source ('C') fall within the 'red' slit (see Figure 5.9).

cessed using standard techniques, namely they are overscan and bias subtracted and flat fielded. Cosmic rays and bad pixels are identified and masked in multiple steps. Wavelength solutions are determined from low order polynomial fits to arc lamp spectra, and then a wavelength map is obtained by tracing the spatial trajectory of arc lines across each slit.

We then perform the sky and PSF subtraction as a coupled problem, using a novel custom algorithm that we briefly summarize here (see Hennawi & Prochaska 2013 for additional details). We adopt an iterative procedure, which allows us to obtain the sky background, the 2-d spectrum of each object, and the noise, as follows. First, we identify objects in an initial sky-subtracted image[4], and trace their trajectory across the detector. We then extract a 1-d spectrum, normalize these sky-subtracted images by the total extracted flux, and fit a B-spline profile to the normalized spatial light profile of each object relative to the position of its trace. Given this set of 2-d basis functions, i.e. the flat sky and the object model profiles, we then minimize chi-squared for the best set of spectral B-spline coefficients which are the spectral amplitudes of each basis component of the 2-d model. The result of this procedure are then full 2-d models of the sky-background, all object spectra, and the noise (σ^2). We then use this model sky to update the sky-subtraction, the individual object profiles are re-fit and the basis functions updated, and chi-square fitting is repeated. We iterate this procedure of object profile fitting and subsequent chi-squared modeling four times until we arrived at our final models.

---

[4] By construction, the sky-background has a flat spatial profile because our slits are flattened by the slit illumination function.

For each slit, each exposure of a given slit is modeled according to the above procedure, allowing us to subtract both the sky and the PSF of the quasars. These images are registered to a common frame by applying integer pixel shifts (to avoid correlating errors), and are then combined to form final 2-d stacked sky-subtracted and sky-and-PSF-subtracted images. The individual 2-d frames are optimally weighted by the $(S/N)^2$ of their extracted 1-d spectra. The final result of our data analysis are three images: 1) an optimally weighted average sky-subtracted image, 2) an optimally weighted average sky-and-PSF-subtracted image, and 3) the noise model for these images σ^2. The final noise map is propagated from the individual noise model images taking into account weighting and pixel masking entirely self-consistently.

Finally, we flux calibrate our data following the procedure in Hennawi & Prochaska (2013). As standard star spectra were not typically taken immediately before/after our observations, we apply an archived sensitivity function for the LRIS B600/4000 grism to the 1-d extracted quasar spectrum for each slit, and then integrate the flux-calibrated spectrum against the SDSS g-band filter curve. The sensitivity function is then rescaled to yield the correct SDSS g-band photometry. Since the faint quasar is not clearly detected in SDSS, we only used the g-band magnitude of the UM 287 quasar to calculate this correction. Note that this procedure is effective for point source flux-calibration because it allows us to account for the typical slit-losses that affect a point source. However, this procedure will tend to underestimate our sensitivity to extended emission, which is not affected by these slit-losses. Hence, our procedure is to apply the rescaled sensitivity functions (based on point source photometry) to our 2-d images, but reduce them by a geometric slit-loss factor so that we properly treat extended emission. To compute the slit-losses we use the measured spatial FWHM to determine the fraction of light going through our 1.0″ slits, but we do not model centering errors (see Section §5.4.2 for a test of our calibration, and see Hennawi & Prochaska 2013 for more details).

Given this flux calibration, the 1σ SB limit of our observations are $\mathrm{SB}_{1\sigma} = 1.3\times10^{-18}$ erg s^{-1} cm^{-2} arcsec^{-2}, and $\mathrm{SB}_{1\sigma} = 1.5\times10^{-18}$ erg s^{-1} cm^{-2} arcsec^{-2} for C IV and He II , respectively. This limits are obtained by averaging over a 3000 km s^{-1} velocity interval, i.e. ±1500 km s^{-1} on either side of the systemic redshift of the UM 287 quasar, i.e. $z = 2.279 \pm 0.001$ (McIntosh et al. 1999), at the C IV and He II locations, and a $1'' \times 1''$ aperture[5]. This limits (approximately independent of wavelength) are about 3× the 1σ limit in 1 arcsec^2 for the $\sim$ 10 hours narrow-band exposure targeting the Lyα line (Fig. 5.2), i.e. 5×10^{-19} erg s^{-1} cm^{-2} arcsec^{-2} [6]. Note that we choose this velocity range to enclose all the extended Lyα emission, even after smoothing (see next Section

---

[5] Obviously, if we use a smaller velocity aperture we get a more sensitive limit, i.e. $SB_{\rm limit} = SB_{1\sigma}\sqrt{\frac{\Delta v_{\rm new}}{3000\ {\rm km\ s^{-1}}}}$, e.g. we obtain $SB_{1\sigma} = 7.3\times10^{-19}$ erg s^{-1} cm^{-2} arcsec^{-2} for a 700 km s^{-1} velocity interval.

[6] Note that spatial averaging allow us to achieve more sensitive limits. If we consider an aperture of 1″×20″, we reach $SB_{1\sigma}^{A=20} = 3.7\times10^{-19}$ erg s^{-1} cm^{-2} arcsec^{-2} at the location of the Lyα line.

§5.4.2), and because the narrow-band image presented in §5.1, covers approximately this width, i.e. $\Delta v \sim 2400$ km s^{-1}.

Further, it is important to stress here that the line ratios we use in this work are only from the spectroscopic data (we do *not* use the NB data for the Lyα line), and hence they are independent of any errors in the absolute calibration. Although we do not use the NB data in our analysis, we show in the next section that our results are consistent with the NB imaging, and thus robustly calibrated.

5.4.2 OBSERVATIONAL RESULTS

Following Hennawi & Prochaska (2013), we search for extended Lyα , C IV , and He II emission by constructing a χ image

$$\chi^2 = \sum_i^{N_{\rm pix}} \frac{({\rm DATA}_i - {\rm MODEL}_i)^2}{\sigma_i^2} \tag{5.3}$$

where the sum is taken over all $N_{\rm pix}$ pixels in the image, 'DATA' is the image, 'MODEL' is a linear combination of 2-d basis functions multiplied by B-spline spectral amplitudes, and σ is a model of the noise in the spectrum, i.e. σ^2 = SKY + OBJECTS + READNOISE. The 'MODEL' and the σ^2 are obtained during our data reduction procedure (see Section §5.4.1, and Hennawi & Prochaska 2013 for details).

Figures 5.9 and 5.10 show the two-dimensional spectra for the slits in Figure 5.8 plotted as χ-maps. Note that if our noise model is an accurate description of the data, the distribution of pixel values in the χ-maps should be a Gaussian with unit variance. In these images, emission will be manifest as residual flux, inconsistent with being Gaussian distributed noise. The bottom row of each Figure shows the $\chi_{\rm sky}$ map (only sky subtracted) at the location of the Lyα, C IV, and He II, respectively. Even in these unsmoothed data the extended Lyα emission is clearly visible up to ~ 200 kpc (~ 24″) from 'QSO b', along the 'red' slit (Figure 5.9). This emission has $\mathrm{SB}_{\mathrm{Ly}\alpha} = (6.3 \pm 0.4) \times 10^{-18}$ erg s^{-1} cm^{-2} arcsec^{-2}, calculated in a 1″ × 20″aperture[7] and over a 3000 km s^{-1} velocity interval (blue box in Fig. 5.9). This value is in agreement with the emission detected in the continuum-subtracted image (Fig. 5.2) within a 1″×20″aperture at the same position within the slit, i.e. $\mathrm{SB}_{\mathrm{Ly}\alpha} = (7.0 \pm 0.1) \times 10^{-18}$ erg s^{-1} cm^{-2} arcsec^{-2}. Along the 'blue' slit, the extended emission is inevitably mixed with the PSF of the hyper-luminous UM 287 QSO, making PSF subtraction much more challenging. Nevertheless, we compute the emission in the extended Lyα line in an aperture of about 1″×13″aperture (from 40 to 150 kpc) and within 3000 km s^{-1}, after subtracting the PSF of the quasar (see Figure 5.10). Again, we find that surface brightness measured from spectroscopy ($\mathrm{SB}_{\mathrm{Ly}\alpha} = 1.4 \times 10^{-17}$ erg s^{-1} cm^{-2} arcsec^{-2}),

---

[7] Note that one spatial dimension is set by the width of the slit, i.e. 1″.

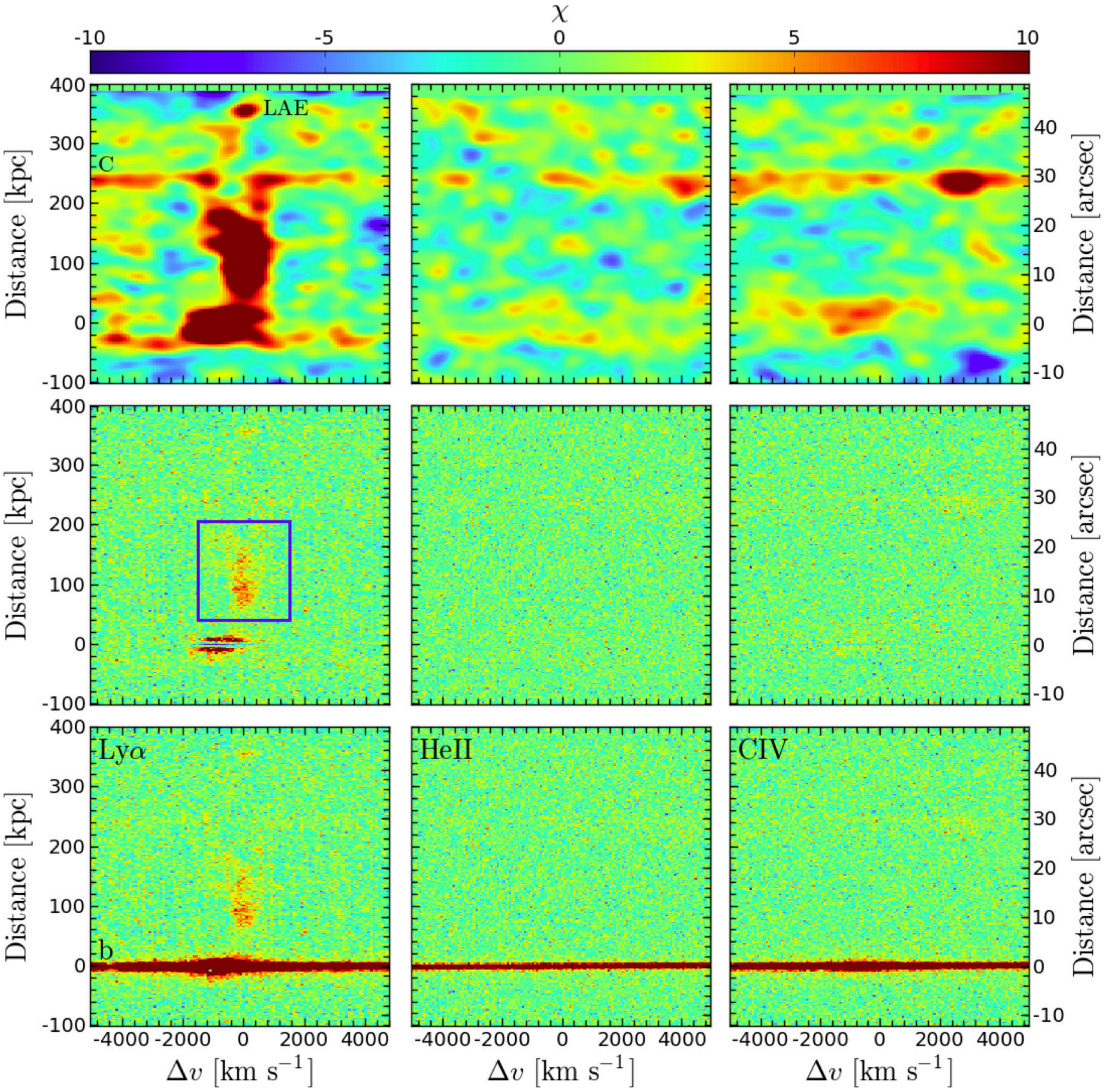

Figure 5.9: Two-dimensional spectra for the red slit shown in Figure 5.8, plotted as χ-maps following Hennawi & Prochaska (2013). In all panels, $v = 0$ km s^{-1} indicates the systemic redshift of the UM 287 quasar, while the distance is computed from the companion quasar, i.e. 'QSO b'. **Bottom row:** $\chi_{\rm sky}$ (sky-subtracted only) at the location of Lyα, He II, and C IV. **Middle row:** $\chi_{\rm sky+PSF}$ (sky and PSF subtracted) at the location of Lyα, He II, and C IV. **Upper row:** smoothed maps $\chi_{\rm smth}$ after the PSF subtraction of the companion QSO ('QSO b' in Figure 5.8). As expected, the extended Lyα emission is well visible in these panels up to 200 kpc from the companion QSO. Note also that within this slit we have a continuum source (source 'C' in Figure 5.8) at ~ 230 kpc, and a Lyman Alpha emitter ('LAE', also highlighted in Figure 5.8) at ~ 350 kpc (see Section §5.4.2 for details). The blue box indicates the aperture used to compute the SB$_{\rm Ly\alpha}$, and the limits on He II/Lyα and C IV/Lyα line ratios, i.e. $1'' \times 20''$and $\Delta v = 3000$ km s^{-1}.

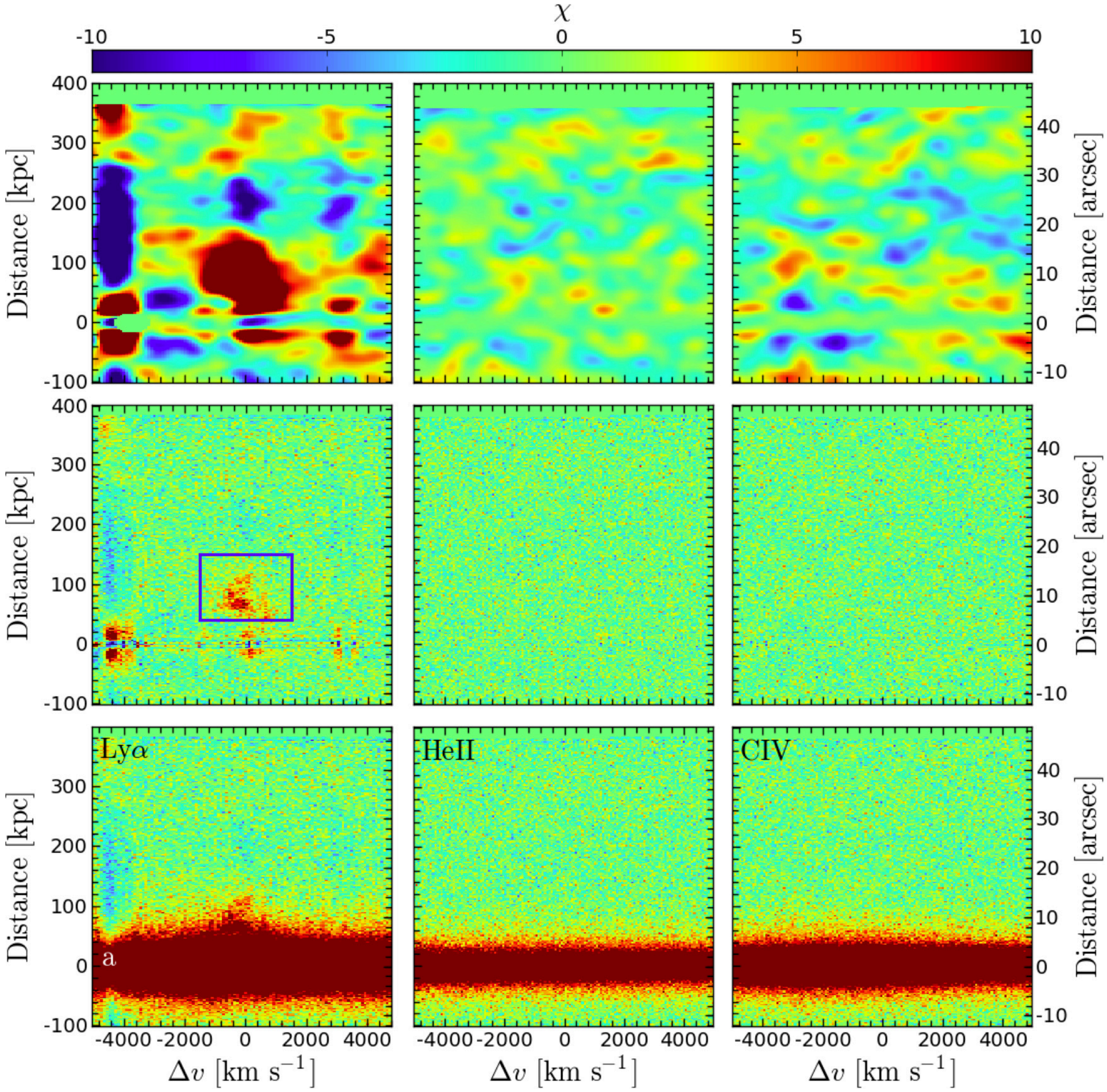

Figure 5.10: Two-dimensional spectra for the blue slit shown in Figure 5.8, plotted as χ-maps following Hennawi & Prochaska (2013). In all panels, v = 0 km s^{-1} indicates the systemic redshift of the UM 287 quasar. The distance is also computed from the UM 287 quasar, i.e. 'QSO a'. **Bottom row:** $\chi_{\rm sky}$ (sky-subtracted only) at the location of Lyα, He ii, and C iv. **Middle row:** $\chi_{\rm sky+PSF}$ (sky and PSF subtracted) at the location of Lyα, He ii, and C iv. **Upper row:** smoothed maps $\chi_{\rm smth}$ after the PSF subtraction of the UM 287 QSO ('QSO a' in Figure 5.8). As expected, also along this slit we detect extended Lyα emission. Given our sensitivity limits, the Lyα line is detected up to ~150 kpc from the UM 287 QSO. Note that for such a bright QSO, it is difficult to cleanly subtract its PSF. The blue box indicates the aperture used to compute the SB$_{\rm Ly\alpha}$ as outlined in section §5.4.2.

and from narrow-band imaging ($\mathrm{SB_{Ly\alpha}} = 1.7 \times 10^{-17}$ erg s^{-1} cm^{-2} arcsec^{-2}) agree within the uncertainties[8]. The agreement between the Lyα spectroscopic and narrow band imaging surface brightnesses for both slit orientations confirm that our spectroscopic calibration procedure is robust.

We do *not* detect any extended emission in either the C IV or in the He II line, for either of the slit orientations. To better visualize the presence of extended emission, we first subtract the PSF of the QSOs for each position angle (see middle rows in Figures 5.9, and 5.10), and finally, we show in the upper rows the smoothed $\chi_{\rm smth}$ maps. These smoothed maps are of great assistance in identifying faint extended emission (see Hennawi & Prochaska 2013 for more details on the PSF subtraction and the calculation of the smoothed χ-maps). The lack of compelling emission features in the PSF-subtracted smoothed maps confirm the absence of extended C IV and He II at our sensitivity limits in both slit orientations.

As our goal is to measure line ratios between the Lyα emission and the C IV and He II lines, we compute the surface brightness limits within the same aperture in which we calculated the Lyα emission along the 'red' slit, i.e. $1''\times20''$and Δv = 3000 km s^{-1}. Because the companion quasar is much fainter than the UM 287 quasar, the PSF subtraction along the 'red' slit does not suffer from systematics, whereas the large residuals in the left panel of Figure 5.10 indicate that there are significant PSF subtraction systematics for the Lyα emission in the 'blue' slit covering the UM 287 quasar. We have thus decided to focus on the line ratio obtained from the 'red' slit, although the constraints we obtain from the 'blue' slit are comparable. We find $\mathrm{SB}^{A=20}_{1\sigma,\mathrm{C\ IV}} = 3.3 \times 10^{-19}$ erg s^{-1} cm^{-2} arcsec^{-2} and $\mathrm{SB}^{A=20}_{1\sigma,\mathrm{He\ II}} = 3.7 \times 10^{-19}$ erg s^{-1} cm^{-2} arcsec^{-2}, respectively at the C IV and He II locations.

To better understand how well we can recover emission in the He II and C IV lines in comparison to the Lyα , we visually estimate the detectability of extended emission in these lines by inserting fake sources as follows. First, we select the Lyα emission above its local 1σ limit along the 'red' slit, we smooth it and scale it to be 1, 2, 3, and 5× $\mathrm{SB}^{A=20}_{1\sigma}$ at the location of the He II and C IV line. Finally, we add Poisson realizations of these scaled models into our 2-d PSF and sky-subtracted images. In Figure 5.11 we show the χ-maps for this test at the location of He II . This test suggests that we should be able to clearly detect extended emission on the same scale as the Lyα line if the source is $\gtrsim 3\times\,\mathrm{SB}^{A=20}_{1\sigma}$. Thus, in the remainder of the paper we use 3σ ($\sigma \equiv \mathrm{SB}^{A=20}_{1\sigma}$) upper limits on the He II/Lyα and C IV/Lyα ratios. Given the values for the $\mathrm{SB_{Ly\alpha}}$ and the surface brightness limits at the location of the C IV and He II lines (within the $1'' \times 20''$aperture and 3000 km s^{-1} velocity window for the red slit) we get (He II/Lyα)$_{3\sigma} \lesssim 0.18$ and (C IV/Lyα)$_{3\sigma} \lesssim 0.16$. Note that given the brighter Lyα emission at the location of the 'blue' slit, the limits implied are about 2× lower than these quoted limits for the 'red' slit.

---

[8] We do not quote errors for these second set of measurements because there are significant systematics associated with the PSF subtraction in both imaging and spectroscopic data.

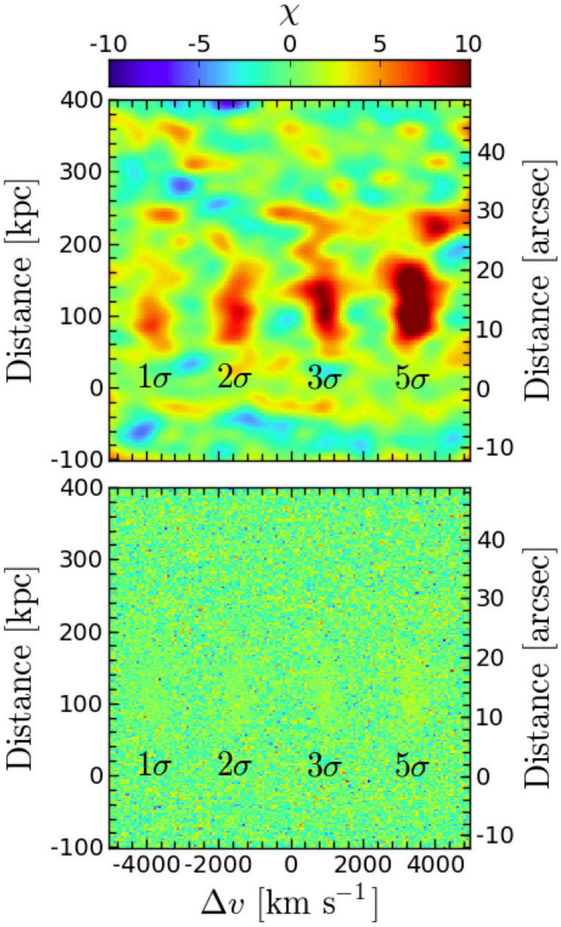

Figure 5.11: Illustration of detection significance of scaled models of the Lyα emission at the location of the He II line along the 'red' slit (Figure 5.9). The synthetic sources corresponds to 1, 2, 3, and 5× $\mathrm{SB}^{A=20}_{1\sigma,\mathrm{He\,II}}$. The bottom panel shows the $\chi_{\rm sky}$ (sky-subtracted only) map, while the upper panel shows the smoothed map. This figure suggests that we should be able to clearly detect extended emission $\gtrsim 3\sigma$ on the scale of the Lyα line.

It is important to note that we detect extended C IV emission around the faint companion quasar 'b' (see the smoothed maps in Figure 5.9). As this line is physically distinct from the UM 287 nebula and essentially follows the extended Lyα emission around the faint quasar (compare the smoothed maps for Lyα and C IV), this suggests that we have detect the extended narrow emission line region (EELR) of this source. This kind of emission, produced by the gas excited by an AGN on scales of tens of kpc, is usually observed around low redshift $z < 0.5$ type-I (e.g. Stockton et al. 2006; Husemann et al. 2013) and type-II quasars (e.g. Greene et al. 2011), traced by [O III] and Balmer lines. We do not quote a value for the emission because, given the much smaller scales in play here, its accuracy depends on the PSF-subtraction. However note that this detection, near the limit of our sensitivity, clearly demonstrates that we could have detected faint extended emission in the C IV and He II lines within the Lyα nebula itself if this emission were characterized by higher line ratios.

Finally, we briefly comment on the nature of two other sources which fall within the 'red' slit, i.e. a Lyman Alpha emitter (LAE) (i.e. $EW^{rest}_{\rm Ly\alpha} > 20$Å) and a continuum source (see Figure 5.9). Indeed, this slit orientation was also chosen to confirm the presence of a LAE at about 350 kpc northward of ‘QSO b’, clearly visible in Figure 5.2 (its position is also indicated in Figure 5.8). Our LRIS data confirm the presence of a line emission from a LAE at a redshift $z = 2.280 \pm 0.002$, which is consistent with the redshift of the UM 287 quasar, within our uncertainties. We ascribe this emission to the Lyα line, and we compute a flux of $F_{Ly\alpha} = (9.2 \pm 0.9) \times 10^{-18}$ erg s^{-1} cm^{-2} (in an aperture of Δv = 1400 km s^{-1}, and 4 arcsec^2), in agreement with $F_{Ly\alpha} = (8.4 \pm 0.4) \times 10^{-18}$ erg s^{-1} cm^{-2} computed in an aperture of 4 arcsec^2 in the map shown in Fig. 5.2. We also serendipitously obtained a spectrum of a source at $\sim$ 230 kpc from quasar ‘b’, which coincides with a continuum sources in our deep V-band image (Fig. 5.1). In our 2-d spectrum, we detect a faint continuum associated with this source and an emission line at a wavelength of 5123Å, which appears at a velocity $\sim$ 2750 km s^{-1} from the C IV line in the right panel of Figure 5.9. However, given the low signal-to-noise ratio of the continuum, and the detection of a single emission line, we are unable to determine the redshift of this source.

5.4.2.1 KINEMATICS OF THE NEBULA

With these slit spectra for two orientations, we can begin to study the kinematics of the Lyα emission of the UM 287 giant nebula. We first focus on the ‘red’ slit (see Figure 5.9), which covers the companion quasar (‘QSO b’) and the extended Lyα emission at a projected distance of 100−160 kpc ($\sim 13''-19''$) from UM 287 (‘QSO a’). We tested the kinematics of the detected emission by measuring the flux-weighted line centroid and the flux-weighted velocity dispersion (σ) around the centroid velocity in 2-pixels wide bins ($\sim 0.54''$) across the spatial slit direction. We then converted the velocity dispersion to a gaussian-equivalent FWHM$_{\rm gauss}$ assuming FWHM$_{\rm gauss} \sim 2.35\sigma$. Note that, because of the resonant nature of the Lyα emission, the line width may be broadened by radiative transfer effects (e.g., Cantalupo et al. 2005) and representing, thus, only an upper limit for the thermal or kinematical broadening. The extended emission has an average FWHM$_{\rm gauss} \sim$ 500 km s^{-1} at a redshift of $z = 2.279$, which is centered on the systemic redshift of the UM 287 quasar. Although the emission appears coherent on this large scales, the gaussian FWHM calculated at each location ranges between $\sim$ 370 km s^{-1} and $\sim$ 600 km s^{-1}, suggesting the need of higher resolution data to better characterize its width and shape. The line emission is red-shifted by $\sim$ 750 km/s from quasar ‘b’. However note that our estimate for the redshift of quasar ‘b’ $z = 2.275$ has a large 800 km s^{-1} error, because it is estimated from broad rest-frame UV emission lines which are poor tracers of the systemic frame (see §5.2.2).

As for the ‘blue’ slit, statements about kinematics are limited by the challenge of accurately subtracting the PSF of the bright UM 287 quasar. Given our SB limit, we detect the Lyα emission out to $\sim$ 150 kpc. As expected from the narrow-band imaging, the Lyα is stronger at this location in comparison with the other slit orientation. In particular, the emission shows a peak at ~63 kpc ($\sim 7.7''$) in agreement with the narrow-band data (see Fig. 5.2). At this second location, the Lyα

line appears broader FWHM$_{\rm gauss}$ ~ 920 km s^{-1} and appears to vary more with distance along the slit. This larger width may arise from the fact we are probing smaller distances from the UM 287 quasar than in the 'red' slit.

Note that, at our spectral resolution (FWHM ~ 320 km s^{-1}), there is no evidence for "double-peaked" kinematics characteristic of resonantly-trapped Lyα (e.g. Cantalupo et al. 2005) along either slit. This may indicate that resonant scattering of Lyα photons does not play an important role in the Lyα kinematics, however, data at a higher resolution are needed to confirm this conclusion.

These estimates for the widths of Lyα emission are comparable to the velocity widths observed in absorption in the CGM surrounding z ~ 2 quasars ($\Delta v \approx 500$ km s^{-1}; Prochaska & Hennawi 2009; Lau et al. 2015), pheraps suggesting that the kinematics traced in emission are dominated by the motions of the gas as opposed to the effects of radiative transfer. Both the emission and absorption kinematics are comparable to the virial velocity ~ 300 km s^{-1} of the massive dark matter halos hosting quasars (M$_{\rm DM}$ ~ $10^{12.5}$ M$_\odot$, White et al. 2012), and thus appear consistent with gravitational motions.

5.4.3 MODELING THE LYα, C IV AND HE II EMISSION AROUND UM 287

As anticipated previously, to further constrain the properties of the gas in this huge nebula, in this Section we exploit the simple model for cool clouds in a quasar halo introduced in Chapter 2 (Hennawi & Prochaska 2013) and the consequent photoionization modeling procedure introduced in Chapter 3. Our main goal is to show how our line ratio constraints on C IV/Lyα and He II/Lyα can be used to constrain the physical properties of the gas in the UM 287 nebula, such as the volume density ($n_{\rm H}$), column density ($N_{\rm H}$), and gas metallicity (Z).

We reiterate that as in §5.1, model the Lyα emission alone cannot break the degeneracy between the clumpiness or density of the gas, and the total gas mass. In the next sections we show how information on additional lines (in particular He II) can constrain the density of the emitting gas and thus break this degeneracy.

5.4.3.1 BRIEF REMINDER OF THE PHOTOIONIZATION MODELING

In the following, we briefly outline the simple model for cool halo gas (Chapter 2) for the case of UM 287. We assume a simple picture where UM 287 has a spherical halo populated with spherical clouds of cool gas (T ~ 10^4 K) at a single uniform hydrogen volume density $n_{\rm H}$, and uniformly distributed throughout the halo. We model a scale length of $R = 160$ kpc from the central quasar, which approximately corresponds to the distance probed by the 'red' slit, and represents the expected virial radius for a dark matter halo hosting a quasar at this redshift. In this configuration, the spatial distribution of the gas is completely specified by $n_{\rm H}$, R, the hydrogen column density $N_{\rm H}$, and the cloud covering factor f_C.

If we plug typical values for these parameters in Eqn. (2.4), the total mass of cool gas in our simple model can be written as:

$$M_{\rm c} = 2.7 \times 10^{10} \left(\frac{R}{160\,{\rm kpc}}\right)^2 \left(\frac{N_{\rm H}}{10^{19.5}\,{\rm cm}^{-2}}\right) \left(\frac{f_{\rm C}}{1.0}\right) M_{\odot}. \tag{5.4}$$

Further, as introduced in Chapter 2, in this simple model, the Lyα SB is determined by simple relations which depend only on $n_{\rm H}$, $N_{\rm H}$, f_C, and the luminosity of the QSO at the Lyman limit ($L_{\nu_{\rm LL}}$). To build intuition, it is useful to consider two limiting regimes for the recombination emission, for which the clouds are optically thin ($N_{\rm HI} \ll 10^{17.2}$ cm^{-2}) and optically thick ($N_{\rm HI} \gg 10^{17.2}$ cm^{-2}) to the Lyman continuum photons. In the optically thick case the Lyα surface brightness scales with the luminosity of the central source, ${\rm SB}^{\rm thick}_{\rm Ly\alpha} \propto f_C L_{\nu_{\rm LL}}$, while in the optically thin regime the SB does not depend on $L_{\nu_{\rm LL}}$, ${\rm SB}^{\rm thin}_{\rm Ly\alpha} \propto f_C n_{\rm H} N_{\rm H}$, provided the AGN is bright enough to keep the gas in the halo ionized enough to be optically thin (see Chapter 2 for the complete formulas).

We now argue that the Lyα emitting gas is unlikely to be optically thick $N_{\rm HI} \gtrsim 10^{17.2}$ cm^{-2}. Equations (2.16) expresses the ${\rm SB}^{\rm thick}_{\rm Ly\alpha}$ in terms of $L_{\nu_{\rm LL}}$, the luminosity at the Lyman edge. To compute this luminosity, we assume, as usual, that the quasar spectral energy distribution obeys the power-law form $L_\nu = L_{\nu_{\rm LL}}(\nu/\nu_{\rm LL})^{\alpha_{\rm UV}}$, blueward of $\nu_{\rm LL}$ and adopt a slope of $\alpha_{\rm UV} = -1.7$ consistent with the measurements of Lusso et al. (2015). The quasar ionizing luminosity is then parameterized by $L_{\nu_{\rm LL}}$, the specific luminosity at the Lyman edge[9]. We determine the normalization $L_{\nu_{\rm LL}}$ by integrating the Lusso et al. (2015) composite spectrum against the SDSS filter curve, and choosing the amplitude to give the correct i-band magnitude of the UM 287 quasar (i-mag= 17.28), which gives a value of $L_{\nu_{\rm LL}} = 5.4 \times 10^{31}$ erg s^{-1} Hz^{-1}.

Substituting this value of $L_{\nu_{\rm LL}}$ for UM 287 into Eqn. (2.16), we thus obtain

$$\begin{aligned} {\rm SB}^{\rm thick}_{\rm Ly\alpha} &= 8.8 \times 10^{-16} \left(\frac{1+z}{3.279}\right)^{-4} \left(\frac{f_{\rm C}}{1.0}\right) \left(\frac{R}{160\,{\rm kpc}}\right)^{-2} \\ &\times \left(\frac{L_{\nu_{\rm LL}}}{10^{31.73}\,{\rm erg\,s^{-1}\,Hz^{-1}}}\right) {\rm erg\,s^{-1}\,cm^{-2}\,arcsec^{-2}}. \end{aligned} \tag{5.5}$$

This value is over two order of magnitude larger than the observed SB value of the Lyα emission at 160 kpc from UM 287. Even if we consider a larger radius, R = 250 kpc, in order to get the observed $\mathrm{SB}_{\mathrm{Ly}\alpha}$ we would need a very low covering factor, i.e. $f_{\mathrm{C}} \sim 0.02$. Such a small covering factor would be strictly at odds with the observed smooth morphology of the diffuse nebula as seen in Figures 5.1 and 5.2. Analogous to what done in the case of LABs (§3.4.1), we directly test this assumption as follows. We randomly populate an area comparable to the extent of the Lyα nebula with point sources such that $f_C = 0.1 - 1.0$, and we convolve the images with a Gaussian kernel with a FWHM equal to our seeing value, in order to mimic the effect of seeing in the observations. We find that the smooth morphology observed cannot be reproduced by images with $f_C < 0.5$, as they appear too clumpy. Thus, the smooth morphology of the emission in the Lyα nebula implies a covering factor of $f_C \gtrsim 0.5$.

---

[9] We describe in detail the assumed quasar spectral-energy distribution (SED) in Section §5.4.3.3.

In the following sections we construct photoionization models for a grid of parameters governing the physical properties of the gas to estimate the expected He II and C IV emission. Following the discussion here, we shall see that the models which reproduce the observed Lyα SB will be optically thin, because given the high covering factor optically thick models would be too bright.

5.4.3.2 THE IMPACT OF RESONANT SCATTERING

In §1.1 and §2.2, I have stressed that the Lyα photons should be subject to substantial resonant scattering under most of the astrophysical conditions, given the large optical depth at line center (see e.g. Gould & Weinberg 1996). Thus, typically, a Lyα photon experiences a large numbers of scattering before escaping the system in which it is produced. This process thus leads to double-peaked emission line profiles as Lyα photons must diffuse in velocity space far from the line center to be able to escape the system (e.g. Neufeld 1990; Gould & Weinberg 1996; Cantalupo et al. 2005; Dijkstra et al. 2006b; Verhamme et al. 2006). Although our models are optically thin at the Lyman limit, i.e. to ionizing photons, for the model parameters required to reproduce the SB of the emission, they will almost always be optically thick to the Lyα transition (i.e. $N_{\mathrm{HI}} \gtrsim 10^{14}$ cm^{-2}). Hence one should be concerned about the resonant scattering of Lyα photons produced by the central quasar itself. However, the same radiative transfer simulations used in §5.1 have shown that the scattered Lyα line photons from the quasar do not contribute significantly to the Lyα surface brightness of the nebula on large scales, i.e. $\gtrsim 100$ kpc (Cantalupo et al. 2014). This is because the resonant scattering process results in very efficient diffusion in velocity space, such that the vast majority of resonantly scattered photons produced by the quasar itself escape the system at very small scales $\lesssim 10$ kpc, and hence do not propagate at larger distances (e.g. Dijkstra et al. 2006b; Verhamme et al. 2006; Cantalupo et al. 2005). For this reason, we do not model the contribution of resonant scattering of the quasar photons to the Lyα emission. Similar considerations also apply to the resonant C IV line, however we note that resonant scattering of C IV is expected to be much less efficient, because the much lower abundance of metals imply the gas in the nebula is much less likely to be optically thick to C IV .

To avoid a contribution to the Lyα and C IV emission from scattering of photons from the QSO we have thus masked both lines in our assumed input quasar spectrum. Note that with this approach we do not neglect the 'scattered' Lyα photons arising from the diffuse continuum produced by the gas itself, which however turn out to be insignificant [10].

5.4.3.3 MODELING THE UM 287 QUASAR SED

We assume that the spectral energy distribution (SED) of UM 287 has the form shown in Figure 5.12. As we do not have complete coverage of the spectrum of this quasar, we adopt the same assumptions used in the case of LABs in Chapter 3, here briefly summarized again. Given the ionization energies for the species of interest to us in this work, i.e. 1 Ryd=13.6 eV for Hydrogen, 4 Ryd=54.4 eV for He II , and 48 eV for C IV , we have decided to stick to power-law approximations above 1 Ryd. However, note that the UV range of the SED is so far not well constrained (see Lusso et al. 2015 and reference therein).

In particular, we model the quasar SED using a composite quasar spectrum which has been corrected for IGM absorption (Lusso et al. 2015). This IGM corrected composite is important because it allows us to relate the i-band magnitude of the UM 287 quasar to the specific luminosity at the Lyman limit $L_{\nu_{\rm LL}}$. For energies greater than one Rydberg, we assume a power law form $L_\nu = L_{\nu_{\rm LL}}(\nu/\nu_{\rm LL})^{\alpha_{\rm UV}}$ and adopt a slope of $\alpha_{\rm UV} = -1.7$, consistent with the measurements of Lusso et al. (2015). While in §5.4.6 we test also the cases for $\alpha_{\rm EUV} = -1.1$, and -2.3. We determine the normalization $L_{\nu_{\rm LL}}$ by integrating the Lusso et al. (2015) composite spectrum against the SDSS filter curve, and choosing the amplitude to give the correct i-band magnitude of the UM 287 quasar (i.e. i=17.28), which gives a value of $L_{\nu_{LL}} = 5.4 \times 10^{31}$ erg s^{-1} Hz^{-1}. We extend this UV power law to an energy of 30 Rydberg, at which point a slightly different power law is chosen $\alpha = -1.65$, such that we obtain the correct value for the specific luminosity at 2 keV $L_\nu(2\,{\rm keV})$ implied by measurements of $\alpha_{\rm OX}$, defined to be $L_\nu(2\,{\rm keV})/L_\nu(2500\,{\rm \AA}) \equiv (\nu_{2\,{\rm keV}}/\nu_{2500\,{\rm \AA}})^{\alpha_{\rm OX}}$. We adopt the value $\alpha_{\rm OX} = -1.5$ measured by Strateva et al. (2005) for SDSS quasars. An X-ray slope of $\alpha_{\rm X} = -1$, which is flat in νf_ν is adopted in the interval of 2-100 keV, and above 100 keV, we adopt a hard X-ray slope of $\alpha_{\rm HX} = -2$. For the rest-frame optical to mid-IR part of the SED, we splice together the composite spectra of Lusso et al. (2015), Vanden Berk et al. (2001), and Richards et al. (2006). These assumptions about the SED are essentially the standard ones used in photoionization modeling of AGN (e.g. Baskin et al. 2014). Summarizing, given the lack

---

[10] Note that this value depends on the broadening of the line due to turbulent motions of the clouds. Given current estimates of typical equivalent widths of optically thick absorbers in quasar spectra, i.e. ~ 1Å (Prochaska et al. 2013b), in our calculation we consider turbulent motions of 30 km s^{-1}. However, note that our results are not sensitive to this parameter.

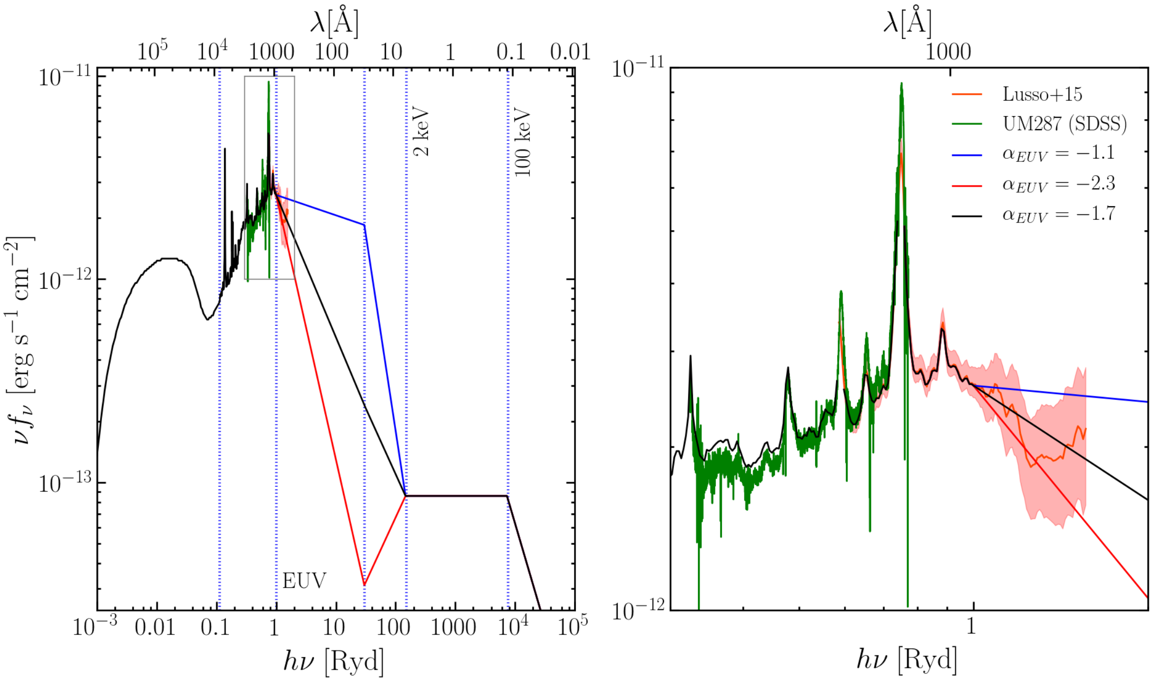

Figure 5.12: Spectral energy distribution (SED) of UM 287 used as incident radiation field in our modeling. The black solid line indicate our fiducial input spectrum characterized by a slope in the EUV of $\alpha_{\rm EUV} = -1.7$ (Lusso et al. 2015), while the red and blue line indicate the values of $\alpha_{\rm EUV} = -2.3$ and $\alpha_{\rm EUV} = -1.1$, respectively, tested in §5.4.6. The right panel is a zoomed version of the box highlighted in the left panel. Note the agreement between the composite spectrum used as input in our calculation and the SDSS spectrum of UM 287 (green solid line). To prevent a contribution from resonantly scattered photons, we mask the emission from the line center of Lyα and C iv .

of information, for energies greater than one Rydberg we parametrized the SED of the UM 287 quasar with a series of power-laws as

$$f_\nu \propto \begin{cases} \nu^{\alpha_{\rm EUV}}, & \text{if } h\nu \geq 1\,\text{Ryd} \\ \nu^{\alpha}, & \text{if } 30\,\text{Ryd} \leq h\nu < 2\,\text{keV} \\ \nu^{\alpha_{\rm X}}, & \text{if } 2\,\text{keV} \leq h\nu < 100\,\text{keV} \\ \nu^{\alpha_{\rm HX}}, & \text{if } h\nu \geq 100\,\text{keV}. \end{cases} \tag{5.6}$$

5.4.3.4 Input Parameters to Cloudy

Having established our assumptions on the UM 287 SED, and on the resonant scattering, we now explain how we choose the range of our model parameter grid. We perform our calculations with the Cloudy photoionization code (v10.01), last described by Ferland et al. (2013). Because the emitting clouds are expected to be much smaller than their distance $r \sim R_{\rm vir} = 160\,{\rm kpc}$ from the central ionizing source, we assume a standard plane-parallel geometry for the emitting clouds illuminated by the distant quasar. In order to keep the models as simple as possible, and because we are primarily interested in understanding how photoionization together with the observed line ratios can constrain the physical properties of the gas (i.e. $n_{\rm H}$ and $N_{\rm H}$), without resorting to extreme parameter combinations, we proceed as follows. We focus on reproducing the ${\rm SB}_{{\rm Ly}\alpha} \sim 7 \times 10^{-18}\,{\rm erg\,s^{-1}\,cm^{-2}\,arcsec^{-2}}$ at 160 kpc distance from the UM 287 quasar, which is basically the distance probed by the 'red' slit[11]. In particular, Eqn. (2.13) implies that a certain combination of $N_{\rm H}$ and $n_{\rm H}$ are thus required. Further, given the dependence on metallicity (Z) of the C IV and He II lines, and of the gas temperature which determine the amount of collisional excitation in the Lyα line, we also consider variations in Z. Thus, we run a uniform grid of models with this wide range of parameters:

- $n_{\rm H} = 10^{-2}$ to $10^{2}\,{\rm cm^{-3}}$ (steps of 0.2 dex);
- $N_{\rm H} = 10^{18}$ to 10^{22} (steps of 0.2 dex);
- $Z = 10^{-3}\,{\rm Z_\odot}$ to ${\rm Z_\odot}$ (steps 0.2 dex).

Note that by exploring this large parameter range, some of the models that we consider result in clouds optically thick at the Lyman limit, but as explained in §5.4.3.1, these parameter combinations result in nebulae which are too bright and thus inconsistent with the observed Lyα surface brightness. In what follows, we only consider the models which closely reproduce the observed Lyα surface brightness, i.e. $5.5 \times 10^{-18}\,{\rm erg\,s^{-1}\,cm^{-2}\,arcsec^{-2}} < {\rm SB}_{{\rm Ly}\alpha} < 8.5 \times 10^{-18}\,{\rm erg\,s^{-1}\,cm^{-2}\,arcsec^{-2}}$.

Photoionization models are self-similar in the ionization parameter $U \equiv \frac{\Phi_{LL}}{c n_{\rm H}}$, which is the ratio of the number density of ionizing photons to hydrogen atoms. As the luminosity of the central QSO is known, the variation in the ionization parameter U results from the variation of the volume number density $n_{\rm H}$ for the models in our grid. The range of ionization parameters that we cover is comparable to those in previous analysis of photoionization around AGNs, e.g. in the case of the narrow line regions (NLR; e.g. Groves et al. 2004) and in the case of extended emission line regions (EELR; e.g. Humphrey et al. 2008). Finally, we emphasize that once we fix the source luminosity and define the ionizing spectrum, the line ratios we consider are described by two model parameters, namely the density $n_{\rm H}$ of the gas and its metallicity Z. We will see this explicitly in the next section.

---

[11] Note that we have decided to model a single distance from the UM 287 quasar. The sensitivity of our results to this simple assumption is discussed in Section 5.4.6.

5.4.4 MODELS VS OBSERVATIONS

As we discuss in Section §5.4.2, our LRIS observations provide upper limits on the C IV/Lyα and He II/Lyα ratios, i.e. (C IV/Lyα)$_{3\sigma}$ $\lesssim$ 0.16 and (He II/Lyα)$_{3\sigma}$ $\lesssim$ 0.18. On the other hand, each photoionization model in our grid predicts these line ratios, and Figure 5.13 shows the trajectory of these models in the He II/Lyα vs C IV/Lyα plane. The region allowed given our observational constraints on the line ratios is indicated by the green shaded area. We remind the reader that we select only the models which produce the observed Lyα emission of $\mathrm{SB}_{\mathrm{Ly}\alpha} \sim 7 \times 10^{-18}\,\mathrm{erg\,s^{-1}\,cm^{-2}\,arcsec^{-2}}$, which to lowest order requires a combination of N_{H} and n_{H} as shown by Eqn. (2.13). Since the luminosity of the central source is known, these models can be thought to be parametrized by either n_{H} or the ionization parameter U, as shown by the color coding on the color-bar. In the same plot we show trajectories for different metallicities $Z = 1, 0.1, 0.01, 10^{-3}\,Z_{\odot}$.

We now reconsider the covering factor. We argued in §5.4.3.1 that based on nebula morphology the covering factor needed to be $f_{\mathrm{C}} \gtrsim 0.5$, and that optically thick gas clouds would tend to overproduce the Lyα SB for such high covering factors. Our models provide a confirmation of this behavior. For a covering factor of $f_{\mathrm{C}} = 1.0$ a large number of models are available, whereas if we lower the covering factor to $f_{\mathrm{C}} = 0.3$, we find that only two models in our extensive model grid can satisfy the Lyα SB of the nebula. This results because as we decrease f_{C}, assuming the gas is optically thin, Eqn. (2.13) indicates we must correspondingly increase the product $N_{\mathrm{H}}n_{\mathrm{H}}$ by $1/f_{\mathrm{C}}$ in order to match the observed $\mathrm{SB}_{\mathrm{Ly}\alpha}$. However, note that the neutral fraction also scales with this product $x_{\mathrm{HI}} \propto N_{\mathrm{H}}n_{\mathrm{H}}$ such that for low enough values of f_{C} increasing $N_{\mathrm{H}}n_{\mathrm{H}}$ would result in self-shielding clouds that are optically thick. We already argued in §5.4.3.1 that if the clouds are optically thick the covering factor must be much lower $f_{\mathrm{C}} \simeq 0.02$, which is ruled out by the diffuse morphology of the nebula. Hence our constraint on the covering factor $f_{\mathrm{C}} \gtrsim 0.5$ can also be motivated by the simple fact that gas distributions with lower covering factors would over-produce the $\mathrm{SB}_{\mathrm{Ly}\alpha}$. Henceforth, for simplicity, we assume a covering factor of $f_{\mathrm{C}} = 1.0$ throughout this work, but in §5.4.6 we test the sensitivity of our results to this assumption.

The gray symbols in Figure 5.13 also show a compilation of measurements of the He II/Lyα and C IV/Lyα line ratios from the literature for other giant Lyα nebulae from the compilation already used in Chapter 3. Specifically, we show measurements or upper limits for the two line ratios for seven Lyα blobs (Dey et al. 2005; Prescott et al. 2009, 2013; Arrigoni Battaia et al. 2015b)[12], and Lyα nebulae associated with 53 high redshift radio galaxies (Humphrey et al. 2006; Villar-Martín et al. 2007a). Note that we show measurements from the literature in Figure 5.13 for reference, but these measurements cannot be directly compared to our observations or our models for several reasons. First, the emission arising from the narrow line region of the central obscured AGN is typically included for the HzRGs, contaminating the line ratios for the nebulae. In addition, the central source UV luminosities are unknown for both LABs and HzRGs, and thus they cannot be directly compared to our models, which assume a central source luminosity. See §3.3 for a detailed discussion on this dataset and its caveats.

---

[12] From the sample targeted in Chapter 3. We decide to plot only the upper limits of LAB1 and LAB2, which set the tighter constraints for that sample.

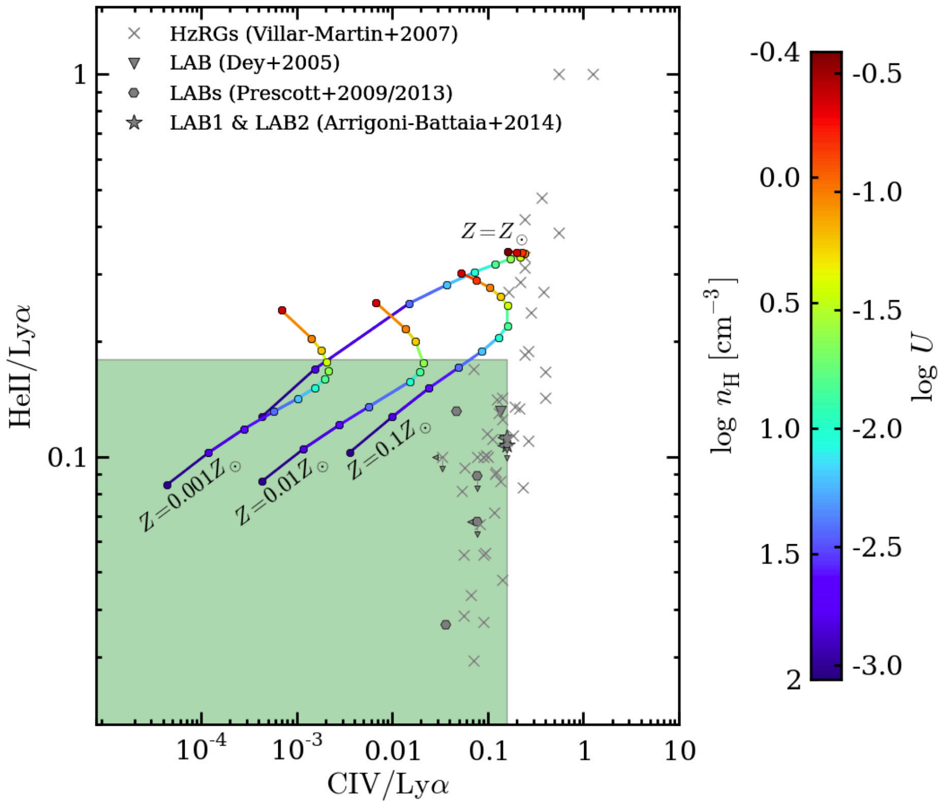

Figure 5.13: HeII/Lyα versus CIV/Lyα log-log plot. Our upper limits on the HeII/Lyα and CIV/Lyα ratios are compared with the Cloudy photoionization models that reproduce the observed $SB_{Ly\alpha} \sim 7 \times 10^{-18}$ erg s^{-1} cm^{-2} arcsec^{-2}. For clarity, we plot only the models with $Z = 0.001, 0.01, 0.1$, and $1\,Z_\odot$. The models are color coded following the ionization parameter U, and thus the volume density n_H (see color bar on the right). The green shaded area represents the region defined by the upper limits of the UM 287 nebula. Note that these upper limits favor models with $n_H \gtrsim 3$ cm^{-3}, $N_H \lesssim 10^{20}$ cm^{-2}, and $\log U \lesssim -1.5$. This is even more clear in Figure 5.14.

The trajectory of our optically thin models through the He II/Lyα and C IV/Lyα diagram can be understood as follows. We first focus on the curve for $Z = Z_\odot$ and follow it from low to high U (i.e. from high to low volume density n_H). First consider the trend of the He II/Lyα ratio. He II is a recombination line and thus, once the density is fixed, its emission depends basically on the fraction of Helium that is doubly ionized. For this reason, the He II/Lyα ratio is increasing from $\log U \sim -3$ and 'saturates', reaching a peak at a value of ~ 0.34 which is set by atomic physics and in particular by the ratio of the recombination coefficients of Lyα and He II . Indeed, if we neglect the contribution of collisional excitation to the Lyα line emission, which is a reasonable assumption near solar metallicity, then both the He II and Lyα are produced primarily by recombination and the recombination emissivity can be written as

$$j_{\rm line} = f_{\rm V}^{\rm elem} \frac{h\nu_{\rm line}}{4\pi} n_{\rm e} n_{\rm ion} \alpha^{\rm eff}_{\rm line}(T), \tag{5.7}$$

where $n_{\rm ion}$ is the volume density of He^{++} and H^{+} for the case of He II and Lyα, respectively. Here $\alpha^{\rm eff}_{\rm line}(T)$ is the temperature dependent recombination coefficient for He II or Lyα, and the factor $f_{\rm V}^{\rm elem} = 3f_{\rm C}N_{\rm elem}/(4Rn_{\rm elem})$ takes into account that the emitting clouds fill only a fraction of the volume (see Eqn.(2.3)). Thus, once the Helium is completely doubly ionized, i.e. $n_{\rm p} \sim n_{\rm H}$ and $n_{\rm He^{++}} \sim (Y/2X)n_{\rm H}$, the ratio between the two lines is given by the relation

$$\frac{j_{\rm He\ II}}{j_{\rm Ly\alpha}} = 0.34 \left(\frac{\alpha^{\rm eff}_{\rm He\ II}(20,000K)}{1.15 \times 10^{-12}\,{\rm cm^3\,s^{-1}}} \right) \left(\frac{\alpha^{\rm eff}_{\rm Ly\alpha}(20,000K)}{2.51 \times 10^{-13}\,{\rm cm^3\,s^{-1}}} \right)^{-1}, \tag{5.8}$$

Note that Eqn. (5.8) depends slightly on temperature, with a decrease of the ratio at higher temperatures. Before reaching this maximum line ratio, He II/Lyα is lower because Helium is not completely ionized, and is roughly given by He II/Lyα $\sim x_{\rm He^{++}} \times (j_{\rm He\ II}/j_{\rm Ly\alpha})_{\rm max}$, where $x_{\rm He^{++}}$ is the fraction of doubly ionized Helium. As stated above, this simple argument does not take into account collisional excitation of Lyα. In particular, at lower metallicities when metal line coolants are lacking, the temperature of the nebula is increased, and collisionally excited Lyα, which is extremely sensitive to temperature, becomes an important coolant, boosting the Lyα emission over the pure recombination value. Thus metallicity variations result in a change of the level of the asymptotic HeII/Lya ratio as seen in Figure 5.13.

Our photoionization models indicate that the C IV emission line is an important coolant and is powered primarily by collisional excitation. The efficiency of C IV as a coolant depends on the amount of Carbon in the C^{+3} ionic state. For this reason, the C IV/Lyα ratio is increasing from log$U \sim -3$, reaches a peak due to a maximum in the C^{+3} fraction, and lowers again at higher U where Carbon is excited to yet higher ionization states, e.g. C V. For example, for the $Z = 0.1\ Z_{\odot}$ models, the C IV/Lyα ratio peaks at log $U = -1.4$ and then decreases at higher U. Given that C IV is a coolant, the strength of its emission depends on the metallicity of the gas. Indeed, for metallicities lower than solar, C IV becomes a sub-dominant coolant with respect to collisionally excited Lyα (and for very low metallicity, e.g. $Z = 10^{-3}Z_{\odot}$, also to He Lyα), and its emission becomes metallicity dependent as can be seen in Figure 5.13.

At lower metallicities the Lyα line becomes an important coolant. For the $Z = 0.001Z_{\odot}$ grid, the collisional contribution to Lyα has an average value of $\sim$ 40%, while it decreases to $\sim$ 37%, $\sim$ 25%, $\sim$ 1% for the $Z = 0.01, 0.1, 1\ Z_{\odot}$ cases, respectively. Given that the strength of the collisionally excited Lyα emission increases with density along each model trajectory, this slightly dilutes the aforementioned trends in the He II and C IV line emission. Specifically, the density dependence of collisionally excited Lyα emission moves the line ratios to lower values for $\log U \gtrsim -1.5$, which would otherwise asymptote at the expected He II/Lyα ratio in Eqn. (5.8). Thus the effect of collisionally excited Lyα emission tend to mask the 'saturation' of the He II/Lyα ratio due to recombination effects alone, and results in a continuous increase of He II/Lyα with U.

Overall, Figure 5.13 illustrates that our simple photoionization models can accommodate the constraints implied by our observed upper limits on the He II/Lyα and C IV/Lyα ratios of UM 287. In particular, our non-detections are satisfied (green shaded region) for models with high volume densities n_{H} and low metallicities Z. These constraints can be more easily visualized in Figure 5.14, where we show the allowed regions in the n_{H}-Z plane implied by our limits on the He II/Lyα (panel 'a') and C IV/Lyα ratios (panel 'b'). Specifically, in these panels the solid black line indicate the upper limits in the case of the UM 287 nebula, i.e. He II/Lyα < 0.18 (or log(He II/Lyα) < -0.74), and C IV/Lyα $= 0.16$ (or log(C IV/Lyα)< -0.79), while the arrows indicate the region of the parameter space that is allowed. It is evident that our limits on the extended emission in the He II/Lyα ratio give us stronger constraints than those from the C IV/Lyα ratio. The He II/Lyα ratio provides a constraint on the volume density which is metallicity dependent, however even if we assume a $\log_{10} Z \simeq -2 - 3$, which are the lowest possible values comparable to the background metallicity of the IGM (e.g. Schaye et al. 2003), we obtain a conservative lower limit on the volume density of $n_{\mathrm{H}} \gtrsim 3\ \mathrm{cm}^{-3}$.

Given this constraint on n_{H}, and the fact that we know the Lyα emission level, which in turns approximately scales as $n_{\mathrm{H}} N_{\mathrm{H}}$ (see Eqn. (2.13)), we can use our lower limit on n_{H} to place an upper limit on N_{H} or equivalently on the total cool gas mass because it scales as $f_{\mathrm{C}}\, N_{\mathrm{H}}$ once the radius is fixed (see Eqn. (5.4)). Panel 'c' of Figure 5.14 shows that our limit on the He II/Lyα ratio combined with the total $\mathrm{SB}_{\mathrm{Ly}\alpha}$ implies the emitting clouds have column densities $N_{\mathrm{H}} \lesssim 10^{20}\ \mathrm{cm}^{-2}$. Thus, if we assume that the physical properties of the slab modeled at 160 kpc are representative of the whole nebula, we can compute a rough estimate for the total cool gas mass. With this strong assumption, that $n_{\mathrm{H}} \gtrsim 3\ \mathrm{cm}^{-3}$ is valid over the entire area of the nebula, i.e. 911 arcsec^2 (from the 2σ isophote of the Lyα map; Figure 5.2), we then deduce that $N_{\mathrm{H}} \lesssim 10^{20}\ \mathrm{cm}^{-2}$ over this same area, and hence the total cool gas mass is $M_{\mathrm{c}} \lesssim 6.4 \times 10^{10}\ \mathrm{M}_{\odot}$.

Further, by combining the lower limit on volume density n_{H} and upper limit on column density N_{H}, we can also obtain an upper limit on the sizes of the emitting clouds defined as $R \equiv N_{\mathrm{H}}/n_{\mathrm{H}}$. Panel 'd' in Figure 5.14 shows that this upper limit is constrained to be $R \lesssim 20$ pc. Assuming a unit covering factor $f_{\mathrm{C}} = 1.0$, this constraint on cloud sizes implies $\gtrsim 53,500$ clouds per square arcsec on the sky, and each cloud should have a cool gas mass $M_{\mathrm{c}} \lesssim 1.3 \times 10^{3}\ \mathrm{M}_{\odot}$. Assuming

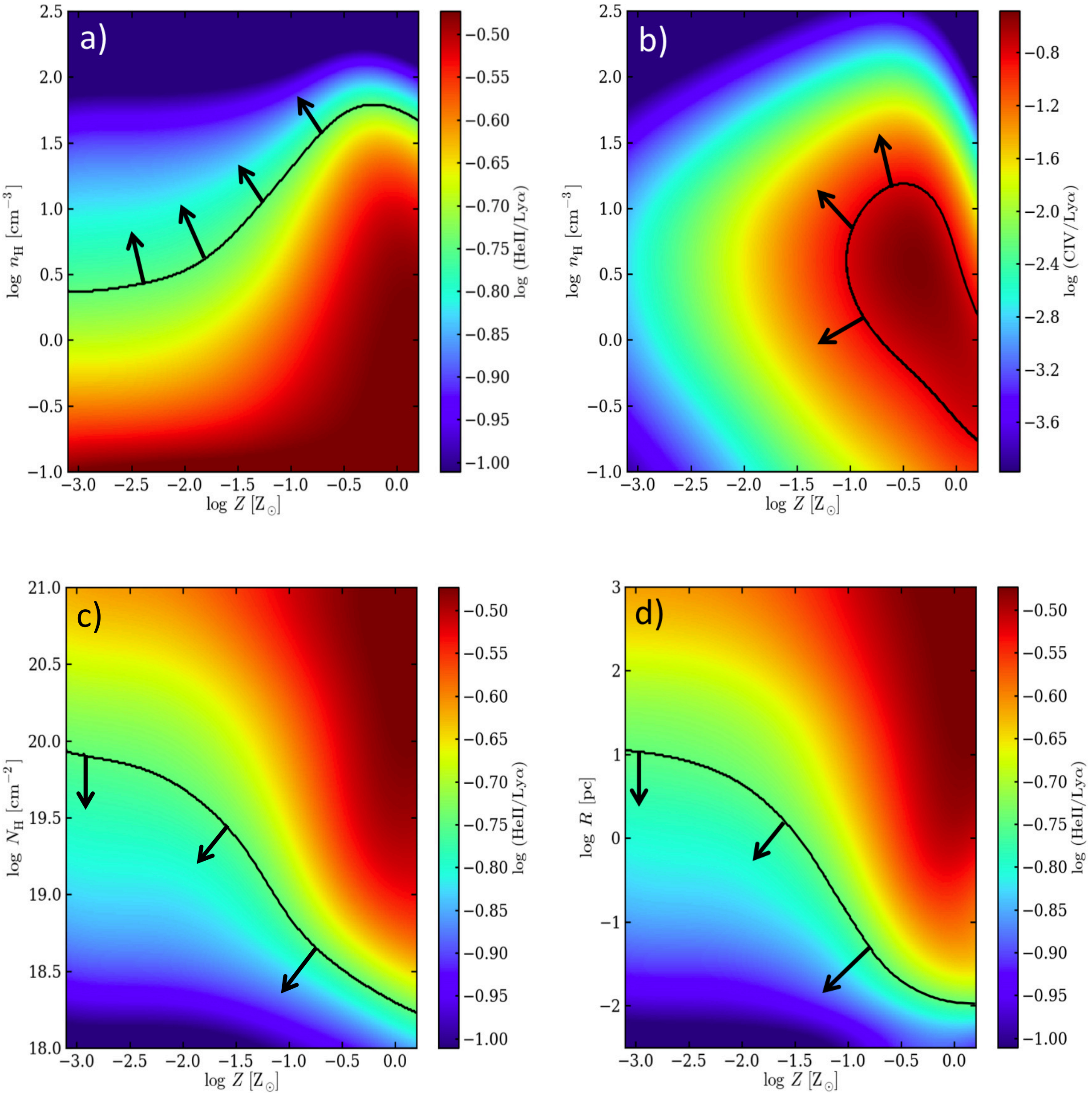

Figure 5.14: Constraints on the physical parameters of the gas clouds from our photoionization models that reproduce the observed $\mathrm{SB_{Ly\alpha}} \sim 7 \times 10^{-18}$ erg s^{-1} cm^{-2} arcsec^{-2} in the case of an input spectrum with $\alpha_{\mathrm{EUV}} = -1.7$. Given the known luminosity of the central source, the assumed SED, and the fixed $\mathrm{SB_{Ly\alpha}}$, our models can be thought to be parametrized by only two parameters, namely n_H and Z. **Panel 'a':** map of the He II/Lyα ratio in the n_H-Z plane. The black solid line indicate our 3σ upper limit He II/Lyα < 0.18 (i.e. log(He II/Lyα)< −0.74). **Panel 'b':** map of the C IV/Lyα ratio in the n_H-Z plane. The black solid line indicate our 3σ upper limit C IV/Lyα < 0.16 (i.e. log(He II/Lyα)< −0.79). Note that the constraints from the He II/Lyα ratio are stronger. **Panel 'c':** map of the He II/Lyα ratio in the N_H-Z plane. The black solid line indicate our 3σ upper limit. Models with $N_H \lesssim 10^{20}$ cm^{-2} are selected. **Panel 'd':** map of the He II/Lyα ratio in the R-Z plane. The black solid line indicate our 3σ upper limit. Note that really small cloud sizes are favored, i.e. $R \lesssim 20$ pc.

these clouds have the same properties throughout the whole nebula, we find that $\gtrsim 4.9 \times 10^7$ clouds are needed to cover the extent of the Lyα emission (~ 911 arcsec^2) [13].

The foregoing discussion indicates that we are able to break the degeneracy between the volume density of the gas $n_{\rm H}$ and the total cool gas mass presented in §5.1 (Cantalupo et al. 2014). As a reminder, this degeneracy arises because the Lyα surface brightness scales as $\rm SB_{Ly\alpha} \propto n_H N_H$, whereas the total cool gas mass is given by $M_{\rm c} \propto N_{\rm H}$. Thus observations of the Lyα alone cannot independently determine the cool gas mass.

By introducing the constraint on the volume density $n_{\rm H} \gtrsim 3$ cm^{-3} using the He II/Lyα ratio, our analysis (i) breaks the degeneracy between density $n_{\rm H}$ (or equivalently C) and total column density $N_{\rm H}$ (or equivalently $M_{\rm c}$), (ii) allows us to then constrain the total cool gas mass $M_{\rm c} \lesssim 6.4 \times 10^{10}$ M$_\odot$ without making any assumptions about the quasar host halo mass, and (iii) demands the existence of a population of extremely compact ($R \lesssim 20$ pc) dense clouds in the CGM/IGM. The ISM-like densities and extremely small sizes of these clouds clearly indicate that they would be unresolved by current cosmological hydrodynamical simulations, given their resolution on galactic scales (Fumagalli et al. 2014; Faucher-Giguere et al. 2014; Crighton et al. 2015; Nelson et al. 2015). Indeed, our measurements would imply a clumping factor $C \gtrsim 200$ for the simulation in §5.3.2, in agreement with the value required in order to reproduce the observed Lyα from the simulated halo.

5.4.4.1 CONSTRAINTS FROM ABSORPTION LINES

A source lying in the background of the UM 287 nebula that pierces the gas at an impact parameter of $\simeq 160$ kpc may also exhibit absorption from high-ion UV transitions like C IV and N V, which can be constrained from absorption spectroscopy. In Figure 5.15 we show a map for the column density of the C IV and N V ionic states ($N_{\rm CIV}$, $N_{\rm NV}$) for our model grid that reproduces the observed $\rm SB_{Ly\alpha} \sim 7 \times 10^{-18}$ erg s^{-1} cm^{-2} arcsec^{-2}. Given our non-detection of He II emission, our upper limits on the He II/Lyα ratios (indicated by the black solid line in both panels), imply $N_{\rm CIV} \lesssim 10^{13.8}$ cm^{-2} and $N_{\rm NV} \lesssim 10^{13.0}$ cm^{-2}, respectively. The quasar UM 287 resides at the center of the nebula, and our narrow band image indicates it is surrounded by Lyα emitting gas. It is thus natural to assume that the UM 287 quasar pierces the nebular gas over a range of radial distances[14]. Thus a non-detection of absorption in these transitions places further constraints on the physical state of the absorbing gas in the nebula.

---

[13] We quote a lower limit on the number of clouds per arcsec^2 because we calculate this value without taking into account the possible overlap of clouds along the line of sight, and also because we use the maximum radius allowed by our constraints. In other words, we simply estimate the number of clouds with radius $R = 20$ pc needed to cover the area of a square arcsec on the sky at the systemic redshift of the UM 287 quasar.

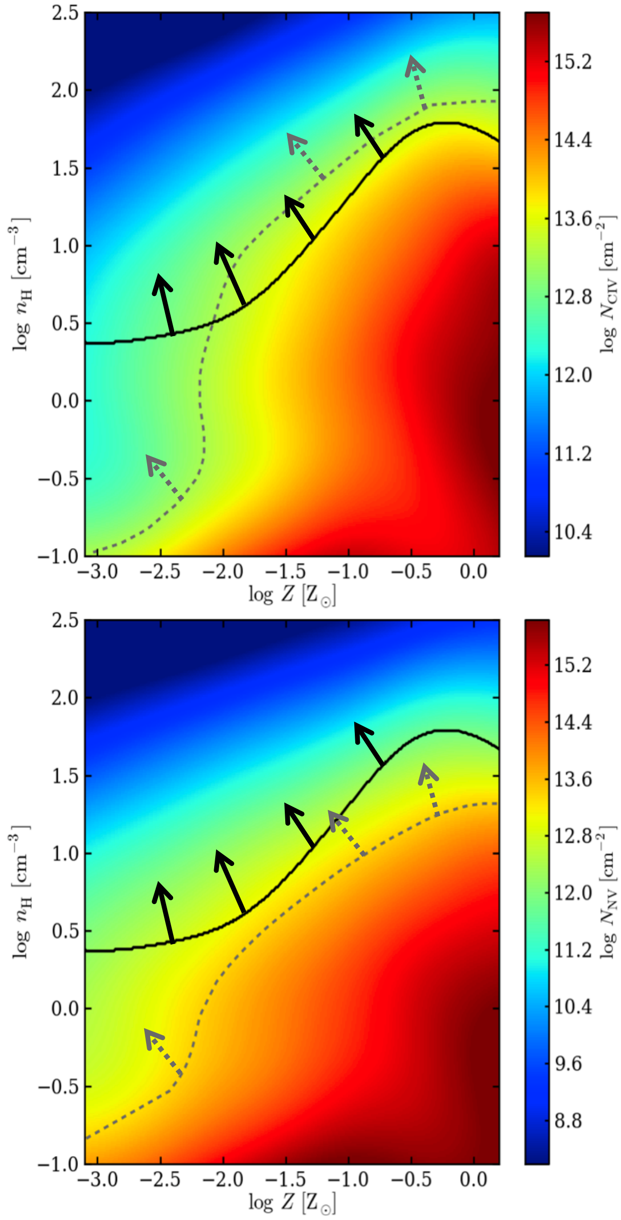

Figure 5.15: Upper Panel: Map of the C IV column density $N_{\rm CIV}$ in the $n_{\rm H}$-Z plane built from our photoionization models that reproduce the observed $\mathrm{SB}_{\mathrm{Ly}\alpha} \sim 7 \times 10^{-18}$ erg s^{-1} cm^{-2} arcsec^{-2} in the case of an input spectrum with $\alpha_{\rm EUV} = -1.7$. The black solid line indicate our 3σ upper limit in the He II/Lyα ratio, while the gray dashed line indicate our limit of $N_{\rm CIV} < 10^{13.2}$ cm^{-2} implied by the absence of absorption at the resolution of the SDSS spectrum of UM 287. **Bottom Panel:** Map of the N V column density $N_{\rm NV}$ in the $n_{\rm H}$-Z plane built from our photoionization models that reproduce the observed $\mathrm{SB}_{\mathrm{Ly}\alpha} \sim 7 \times 10^{-18}$ erg s^{-1} cm^{-2} arcsec^{-2} in the case of an input spectrum with $\alpha_{\rm EUV} = -1.7$. The black solid line indicate our 3σ upper limit in the He II/Lyα ratio, while the gray dashed line indicate our limit of $N_{\rm NV} < 10^{13.4}$ cm^{-2} implied by the absence of absorption at the resolution of the SDSS spectrum of UM 287. The spectroscopic constraints for both species imply that the gas along the sightline, if present, is in a similar state as the observed nebula, being illuminated by the bright quasar as well.

To this end, we examined the high signal-to-noise $\mathrm{S/N} \simeq 70$ pix^{-1} SDSS spectrum of the UM 287 quasar, which has a resolution of $R \simeq 2000$. We find no evidence for any metal-line absorption within a ~ 2000 km s^{-1} window of the quasar systemic redshift coincident with the velocity of the Lyα emitting nebula (see Figure 5.9 and 5.10), implying $N_{\rm CIV} < 10^{13.2}$ cm^{-2} ($\mathrm{EW}_{\rm C\,IV} < 15$ mÅ), and $N_{\rm NV} < 10^{13.4}$ cm^{-2}. These limits constrain the amount of gas in these ionic states intercepted by the quasar at all distances, but in particular at $\simeq$ 160 kpc, where we conducted our detailed modeling of the emission. As such, directly analogous to our constraints from the emission line ratios, we can similarly determine the constraints in the $n_{\rm H}$-Z plane from the non-detections of C IV and N V absorption, which are shown as the gray dashed lines in Figure 5.15. As expected these metal absorption constraints depend sensitively on the enrichment of the gas, but the region of the $n_{\rm H}$-Z plane required by our non-detections are consistent with that required by our He II/Lyα emission constraint. Specifically, for log $Z > -2.3$, the absence of absorption provides a comparable lower-limit on the density as the non-detection of emission, whereas at lower metallicities the absorption constraint allows lower volume densities $n_{\rm H} > 0.1$ cm^{-3} (Figure 5.15), which are already ruled out by He II/Lyα . To conclude, in the context of our simple model, both high-ion metal-line absorption and He II and C IV emission paint a consistent picture of the physical state of the gas.

---

[14] This would not be the case if the emitting gas is all behind the quasar. Given that the quasar shines towards us and contemporary on the gas, this configuration seems unlikely.

For completeness, we also searched for metal-line absorption along the companion quasar 'QSO b' sightline in our Keck/LRIS spectrum (resolution $R \simeq 1000$ and $S/N \simeq 60$ pix^{-1}). We do detect strong, saturated C IV absorption with $N_{\rm CIV} > 10^{14.4}$ cm^{-2} and $z = 2.2601$. This implies, however, a velocity offset of ≈ -1700 km s^{-1} with respect to the systemic redshift of the UM 287 quasar, and thus from the extended Lyα emission detected in the slit spectrum of Figure 5.9. Given this large kinematic displacement from the nebular Lyα emission, we argue that this absorption is probably not associated with the UM 287 nebulae, and is likely to be a narrow-associated absorption line system associated with the companion quasar. This is further supported by the strong detection of the rarely observed N V doublet. The large negative velocity offset -1370 km s^{-1} between the absorption and our best estimate for the redshift of QSOb $z = 2.275$ (from the Si IV emission line) suggests that this is outflowing gas, but given the large error $\sim$ 800km s^{-1} on the latter, and the unknown distance of this absorbing gas along the line-of-sight, we do not speculate further on its nature.

Finally, note that at the time of writing, there is no existing echelle spectrum of UM 287 available, although given that this quasar is hyper-luminous $r \simeq 17$, a high signal-to-noise ratio high resolution spectrum could be obtained in a modest integration. Such a spectrum would allow us to obtain much more sensitive constraints on the high-ion states C IV and N V , corresponding to $N_{\rm CIV} < 10^{12}$ cm^{-2} and $N_{\rm NV} < 10^{12.5}$ cm^{-2}, respectively, and additionally search for O VI absorption down to $N_{\rm OVI} < 10^{13}$ cm^{-2}. If for example C IV were still not detected at these low column densities, this would raise our current constraint on $n_{\rm H}$ by 0.5 dex to $n_{\rm H} \gtrsim 10$ cm^{-3} as shown in Figure 5.15. Furthermore, the detection of metal-line absorption (at a velocity consistent with the nebular Lyα emission) would determine the metallicity of the gas in the nebula, and Figure 5.15 suggests we would be sensitive down to metallicities as low as $Z \simeq -3$, i.e. as low as the background metallicity of the IGM (e.g. Schaye et al. 2003).

5.4.4.2 Comparison to Absorption Line Studies

It is interesting to compare the high volume densities ($n_{\rm H} > 3$ cm^{-3}) implied by our analysis to independent absorption line measurements of gas densities in the CGM of typical quasars. For example, as mentioned in §1.2.2, Prochaska & Hennawi (2009) used the strength of the absorption in the collisionally excited C ii* fine-structure line to obtain an estimate of $n_{\rm H} \simeq 1$ cm^{-3} at an impact parameter of $R_\perp = 108$ kpc from a foreground quasar, comparable to our lower limit obtained from the He ii/Lyα ratio. However, photoionization modeling of a large sample of absorbers in the quasar CGM seem to indicate that the typical gas densities are much lower $n_{\rm H} \sim 0.01 \ll 1$ cm^{-3} (Lau et al. 2015), although with large uncertainties due to the unknown radiation field (see §6.4). If the typical quasar CGM has much lower values of $n_{\rm H} \sim 0.01 \ll 1$ cm^{-3} and column densities of $N_{\rm H} \sim 10^{20}$ cm^{-2} (Lau et al. 2015), this would explain why quasars only rarely exhibit bright Lyα nebulae as in UM 287. Indeed, Eqn. (2.13) would then imply ${\rm SB}_{{\rm Ly}\alpha} = 5.4 \times 10^{-20}$ erg s^{-1} cm^{-2} arcsec^{-2} in the optically thin regime, which is far below the sensitivity of any previous searches for extended emission around quasars (e.g. Hu & Cowie 1987; Heckman et al. 1991b; Christensen et al. 2006), although these low SB levels may be reachable via stacking (Steidel et al. 2011; and see Chapter 6). In this interpretation, quasars exhibiting bright SB $\sim 10^{-17}$ erg s^{-1} cm^{-2} arcsec^{-2} giant Lyα nebulae represent the high end tail of the volume density distribution in the quasar CGM, a conclusion supported by the analysis of another giant nebula with properties comparable to UM 287 (Hennawi et al. 2015) discovered in the Quasars Probing Quasars survey (Hennawi & Prochaska 2013). In this system joint modeling of the Lyα nebulae and absorption lines in a background sightline piercing the nebular gas indicate that cool gas is distributed in clouds with $R \sim 40$ pc, with densities $n_{\rm H} \simeq 2$ cm^{-3}, very similar to our findings for UM 287.

Absorption line studies of gas around normal galaxies also provides evidence for small-scale structure in their circumgalactic media. Specifically, Crighton et al. (2015) conducted detailed photoionization modeling of absorbing gas in the CGM of a Lyα emitter at $z \simeq 2.5$, and deduced very small cloud sizes $< 100 - 500$ pc, although with much lower gas densities ($n_H \simeq 10^{-3} - 10^{-2}$ cm^3) than we find around UM 287. In addition, there are multiple examples of absorption line systems at $z \sim 2 - 3$ in the literature for which small sizes $R \sim 10 - 100$ pc have been deduced (Rauch et al. 1999; Simcoe et al. 2006; Schaye et al. 2007), although the absorbers may be larger at $z \sim 0.2$ (Werk et al. 2014). Also, compact structures with $r \sim 50$ pc have been directly resolved in high-velocity clouds in the CGM of the Milky Way (Ben Bekhti et al. 2009). Given their expected sizes and masses, such small structures are currently unresolved in simulations (see discussion in § 5.3 of Crighton et al. 2015).

5.4.5 MODEL SPECTRA VS CURRENT OBSERVATIONAL LIMITS

In order to assess the feasibility of detecting other emission lines besides Lyα from the UM 287 nebula, and other similar extended Lyα nebulae, e.g. around other quasars, HzRGS, or LABs, we construct model spectra using the output continuum and line emission data from Cloudy. In Figure 5.16 we show the predicted median spectrum for the nebula at 160 kpc from UM 287, resulting from our modeling. Specifically, the solid black curve represents the median of all the models in our parameter grid which simultaneously satisfy the conditions 5.5×10^{-18} erg s^{-1} cm^{-2} arcsec^{-2} $< \mathrm{SB}_{\mathrm{Ly}\alpha} < 8.5\times10^{-18}$ erg s^{-1} cm^{-2} arcsec^{-2}, such that they produce the right Lyα emission level, as well as the emission line constraints He II/Lyα < 0.18 and C IV/Lyα < 0.16 implied by our spectroscopic limits. This grid also includes models with a harder (softer) $\alpha_{\mathrm{EUV}} = -1.1$ ($\alpha_{\mathrm{EUV}} = -2.3$) quasar ionizing continuum as tested in §5.4.6, in addition to our fiducial value of $\alpha_{\mathrm{EUV}} = -1.7$. The gray shaded area indicates the maximum and the minimum possible values for the selected models at each wavelength.

For comparison we show our Keck/LRIS 3σ sensitivity limits from §5.4.1 calculated by averaging over a 1 arcsec^2 aperture and over a 3000 km s^{-1} velocity interval (solid red line), together with the 3σ sensitivity limits for 10 hours of integration with the Multi Unit Spectroscopic Explorer (MUSE) (Bacon et al. 2010; solid blue line), and with the K-band Multi Object Spectrograph (KMOS) (Sharples et al. 2006; gold, orange, and dark-red solid lines), on the VLT, computed for the same spatial and spectral aperture. Note that these sensitivity limits can be lowered by assuming a certain amount of spatial averaging, following the relation $\mathrm{SB}_{\mathrm{limit}} = \mathrm{SB}_{1\sigma}/\sqrt{A}$, where A is the area in arcsec^2 over which the data are averaged. Indeed, we employed this approach in §5.4.2, and averaged over an area of 20 arcsec^2 to obtain a more sensitive constraint on the He II/Lyα and C IV/Lyα line ratios, and this lower SB level is indicated by the red dashed line in Figure 5.16. In contrast with a longslit, integral-field units like MUSE and KMOS, as well as the upcoming Keck Cosmic Web Imager (KCWI, Morrissey et al. 2012), provide near continuous spatial sampling over wide areas, and are thus the ideal instruments for trying to detect extended line emission from the CGM. Thus for MUSE and KMOS, we have assumed that we can average over an area as large as 300 arcsec^2, as shown by the colored dashed lines, and indeed this approach has already been used with the Cosmic Web Imager (Martin et al. 2014a) to study lower SB Lyα emission (Martin et al. 2014c).

Given these expected sensitivities, in Figure 5.16 we indicate the principal emission lines that may be detectable (vertical green dashed lines), whose observation would provide additional constraints on the properties of the emitting gas. The large range of metallicities in our grid $Z = 10^{-3}Z_{\odot}$ to $Z_{\odot}$, results in a correspondingly large range of metal emission line strengths, whereas the Hydrogen Balmer lines and He II are much less sensitive to metallicity and thus show very little variation across our model grid.

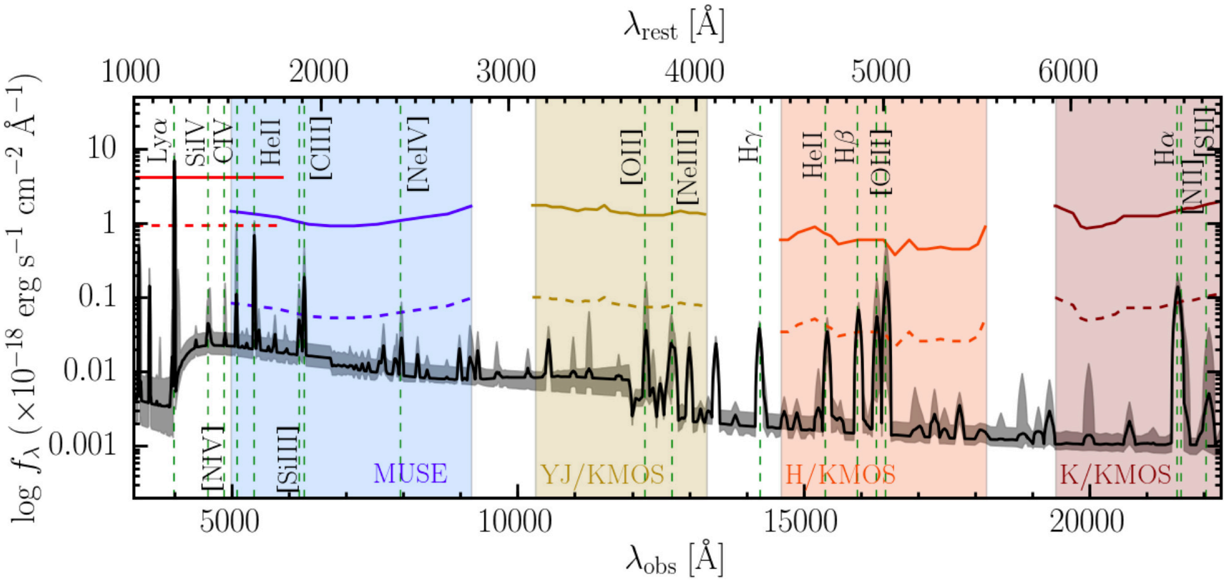

Figure 5.16: Predicted median spectra for the models in our grid that satisfy simultaneously $\mathrm{SB}_{\mathrm{Ly}\alpha} \sim 7\times10^{-18}$ erg s^{-1} cm^{-2} arcsec^{-2} , He ii/Lyα < 0.18, and C iv/Lyα < 0.16. The gray shaded area indicates the maximum and the minimum possible value for the selected models at each wavelength, showing the range of all the possible values, including the variation of the EUV slope, i.e. $\alpha_{\mathrm{EUV}} = -2.3, -1.7$, and -1.1 (see §5.4.6). Our Keck/LRIS 3σ sensitivity limit calculated in 1 arcsec^2 and over 3000 km s^{-1}, is plotted as a solid red line, together with the 3σ sensitivity of MUSE and KMOS (YJ, H, K gratings) for an exposure time of 10 hours (other colored solid lines). The red dashed line indicates our 3σ sensitivity limit average over an aperture of 20 arcsec^2 (see §5.4.2), while all the other dashed lines show the sensitivity averaged over an aperture of 300 arcsec^2, i.e. $SB_{\mathrm{limit}} = SB_{1\sigma}/\sqrt{A}$. The principal emission lines are indicated by the green vertical dashed lines. The lines that may be detectable in the future, given appropriate physical conditions (i.e. n_H, Z) in the targeted nebula are He ii, [C iii], C iv, Si iii, [O ii], [O iii], Hβ, and Hα.

Focusing first on the primordial elements, we see that He ii is the strongest line, and in particular it is stronger than Hα. Indeed, if the Helium is completely doubly ionized then He ii/H$\alpha \sim 3$, and although it decreases to lower values for lower ionization parameters (higher densities), it always remains higher than unity. As we have argued in §5.4.4, a detection of He ii can be used to measure the volume density n_{H} of the emitting gas. Further, by comparing the morphology, size, and kinematics of the non-resonant extended He ii emission to that of Lyα, one can test whether resonant scattering of Lyα plays an important role in the structure of the nebula (Prescott et al. 2015a). Naively, one might have thought that Hα would be ideal for this purpose given that it is the strongest Hydrogen recombination line after Lyα. However, our models indicate that for photoionization by a hard source, the He ii line is always stronger than Hα, and given that He ii is in the optical whereas Hα is in the near-IR, it is also much easier to detect.

Figure 5.16 shows that deep integrations in the near-IR with KMOS will consistently detect the Hydrogen Balmer lines Hα and Hβ. When compared to the Lyα emission, these lines would allows one to determine the extinction due to dust (Osterbrock & Ferland 2006). Further, at the low densities we consider ($n_{\rm H} \ll 10^4$ cm^{-3}), any departure of the ratios Hα/Hβ and Lyα /Hβ from their case B values provide information on the importance of collisional excitation of Lyα, which is exponentially sensitive to the gas temperature (Ferland & Osterbrock 1985). In other words, the amount of collisional excitation is set by the equilibrium temperature of the gas, which is set by the balance of heating and cooling. Photoionization by a hard source will result in a characteristic temperature and hence ratio of Lyα/Hβ set by the ionizing continuum slope, whereas an additional source of heat, as has been postulated in gravitational cooling radiation scenarios for Lyα nebulae (e.g. Rosdahl & Blaizot 2012), would increase the amount of collisionally excited Lyα and hence the ratio of Lyα/Hβ.

Figure 5.16 shows also that one could probably detect metal emission lines depending on the physical conditions in the gas, which are parameterized by $n_{\rm H}$ and Z. In particular, if the gas has metallicity $Z > 0.1 Z_{\odot}$, a deep integration with MUSE would detect C IV, [C III], and, for metallicity close to solar, also Si III λ1883. In the near-IR, we see that a deep integration with KMOS would detect [O III] for $Z > -1$, and [O II] for metallicity close to solar. Note that for similar bright nebulae at different redshifts, it would be possible to detect other lines in extended emission for particular $n_{\rm H}$ and Z combinations, e.g. Si IV λ1394, and N IV λ1480.

According to Figure 5.16, the He II line is the strongest and easiest line to detect, and our analysis in §5.4.4 indicates that a detection constrains the gas properties to lie on a line in the $n_{\rm H}$-Z plane (see panel ‘a’ in Figure 5.14). Following our discussion of C IV (panel ‘b’ of Figure 5.14), the detection of any metal line would define another line in the $n_{\rm H}$-Z plane, and the intersection of these curves would determine the $n_{\rm H}$ and Z of the gas. These conclusions will be somewhat sensitive to the assumed spectral slope in the UV (see §5.4.6), but given the different ionization thresholds to ionized Carbon to C IV (47.9eV), and Oxygen to O III (35.1eV) or O II (13.6eV), it is clear that detections or limits on multiple metal lines from high and low ionization states would also constrain the slope $\alpha_{\rm EUV}$ of the ionizing continuum.

To summarize, our photoionization modeling and analysis provide a compelling motivation to find more bright nebulae by surveying large samples of quasars and HzRGs, and conducting NB emission line surveys of LABs over large areas. Armed with the brightest and largest giant nebulae like UM 287, one can conduct deep observations with IFUs, and combined with suitable spatial averaging, this will uncover a rich emission line spectrum from the CGM and its interface with the IGM, which can be used to constrain the physical properties of the emitting gas, and shed light on physical mechanism powering giant nebulae.

5.4.6 CAVEATS

In section §5.4.4, under the assumption of photoionization by the central QSO, and in the context of a simple model for the gas distribution, we showed how our upper limits on the He II /Lyα and C IV /Lyα ratios, can set constraints on the physical properties of the cool gas observed in emission. However, this simple modeling is just a zeroth-order approximation to a more complicated problem which is beyond the scope of the present work. In what follows, I briefly comment on some of the issues already highlighted in §2.3, in light of the results in the case of UM 287.

Radial Dependence: for simplicity we have evaluated the ionizing flux at a single radial location for input into Cloudy. We have tested the impact of this assumption, by decreasing R from 160 kpc to 100 kpc, and find that our lower limit on the density increases by 0.4 dex. This results from the fact that the He II /Lyα ratio varies with ionization parameter U, and our upper limit on the line ratio sets a particular value of U. By decreasing R, the density $n_{\rm H}$ corresponding to this specific value of U thus increases by a factor R^2. The variation of the ionizing flux with radius, should be taken into account in a more detailed calculation.

Slope of the Ionizing Continuum: we have assumed $\alpha_{\rm EUV} = -1.7$ (Lusso et al. 2015). However, estimates for $\alpha_{\rm EUV}$ in the literature vary widely (Zheng et al. 1997; Scott et al. 2004; Shull et al. 2012), most likely because of uncertainties introduced when correcting for absorption due to the IGM or because of the heterogeneity of the samples considered. Furthermore, the shape of the ionizing continuum near the He II edge of 4 Rydberg is not well constrained.

We have thus tested the robustness of our results to the change of the slope of the EUV as mentioned in §5.4.3.3. In particular, we model the extremes of the range allowed by the recent estimates of Lusso et al. (2015), i.e. $\alpha_{\rm EUV} = -1.7 \pm 0.6$. To fulfill the $\alpha_{\rm OX}$ requirement of Strateva et al. (2005) as explained in Section §5.4.3.3, the value $\alpha_{\rm EUV} = -2.3$ and -1.1 imply at higher energies (30 Ryd $< h\nu <$ 2keV) a slope $\alpha = -0.36$ and -2.93, respectively. In our fiducial input spectrum ($\alpha_{\rm EUV} = -1.7$), the photoionization rate at the Lyman limit is (Eqn. (2.12)) $\Gamma = 6.7 \times 10^{-9}$ s^{-1}, while at 4 Ryd, i.e. at the ionization energy of He II, the photoionization rate is $\Gamma_{\rm 4Ryd} \sim 1.0 \times 10^{-11}$ s^{-1}. By changing the slope in the extreme ultraviolet from $\alpha_{\rm EUV} = -1.7$, to -1.1 and to -2.3, we increase the photoionization rate by ~15% and decrease it by ~13%, respectively. Instead, for the same change, the $\Gamma_{\rm 4Ryd}$ is increased/decreased by a factor of 2.6, respectively. As it is clear from the small changes in Γ, the Hydrogen ionization state is not affected by the change in slope, and the models are always optically thin. Conversely, as expected, the changes in $\Gamma_{\rm 4Ryd}$ affect He II and C IV. The general trend is that a softer slope, e.g. $\alpha_{\rm EUV} = -2.3$, produces fewer He II ionizing photons, and thus at fixed density the He III fraction will be lower, resulting in lower He II recombination emission. This thus leads to a lower He

II/Lyα ratio. Similarly, a softer slope is less effective in ionizing Carbon. In particular, at fixed ionization parameter U, the amount of Carbon in the C^{+3} phase is lower for a softer slope.

In Figure 5.17 we compare our grids of models with different EUV slopes at two different metallicities, i.e. $Z = Z_{\odot}$, and $0.01Z_{\odot}$, in the He II/Lyα versus C IV/Lyα plot. The dependencies outlined above, are better visible in the plot for solar metallicity (upper panel) because the Lyα line is mainly produced by recombinations and its behavior is not influencing the general trends. From this Figure, it is clear that a grid with a softer slope (see grid with $\alpha_{\rm EUV} = -2.3$) can reach lower He II/Lyα ratios because the fraction of doubly ionized Helium is lower at high densities. In the same upper panel of Figure 5.17 it is also evident that the simulation grids for different UV slopes all asymptote to a fixed He II/Lyα ratio when Helium is completely doubly ionized, which occurs at slightly different $n_{\rm H}$ (or equivalently U) for each slope. Note that the value of the asymptotic He II/Lyα ratio varies slightly with slope. Indeed, as mentioned in Section §5.4.4, since this asymptotic value is proportional to the ratio of the recombination coefficients of He II and Lyα , the value depends on temperature (Eqn. (5.8)). Higher temperatures, which arise for a harder slope, lead to a lower asymptotic He II/Lyα ratio.

In the bottom panel of Figure 5.17, we show the same comparison at $Z = 0.01Z_{\odot}$. In this case the trends are masked by the Lyα line, which is powered also by collisions. Indeed, the saturation in the He II/Lyα ratio is not appreciable because, given the dependence on density of the collisional contribution to the Lyα line, the ratio is progressively lowered at higher density. However, it is still appreciable that the C IV/Lyα ratio is moved to lower ratios for higher slopes above $\log U \sim -1.5$. This is mainly due to the fact that Carbon goes to higher ionization state, lowering the fraction of Carbon in the C^{+3} species. Thus, in our case study, where the input spectrum is not well known, the dependence of the amount of C^{+3} on the slope of the EUV makes the C IV line a weak metallicity indicator.

Changes in the slope $\alpha_{\rm EUV}$ only slightly modifies the constraints on $n_{\rm H}$ that we previously obtained. In particular, since the He II/Lyα ratio gives the stronger constraints, in Figure 5.18 we show how a variation in the EUV slope affects the selection of $n_{\rm H}$ (compare Figure 5.17 and 5.18). This Figure highlights in green the parameter space favored by our upper limits (the lines show the location of the upper limit He II/Ly$\alpha = 0.18$). The mild change in the location of the line is explained by the dependencies outlined above. At a fixed low metallicity, where the Lyα line is an important coolant, i.e. $\log Z < -1.5\,Z_{\odot}$, a harder slope moves the lower limit boundary implied by our measurement on the He II/Lyα ratio to lower densities. Indeed, the expected increase of the He II line due to a harder slope is washed out by the increase in the emission in the Lyα line due to collisions. Thus, our constraint on the density that we quote in the main text is weakened from $n_{\rm H} \gtrsim 3$ cm^{-3} to $n_{\rm H} \gtrsim 1$ cm^{-3}. On the other hand, at higher metallicities, a harder UV slope will doubly ionize Helium at higher density, moving the lower limit boundary implied

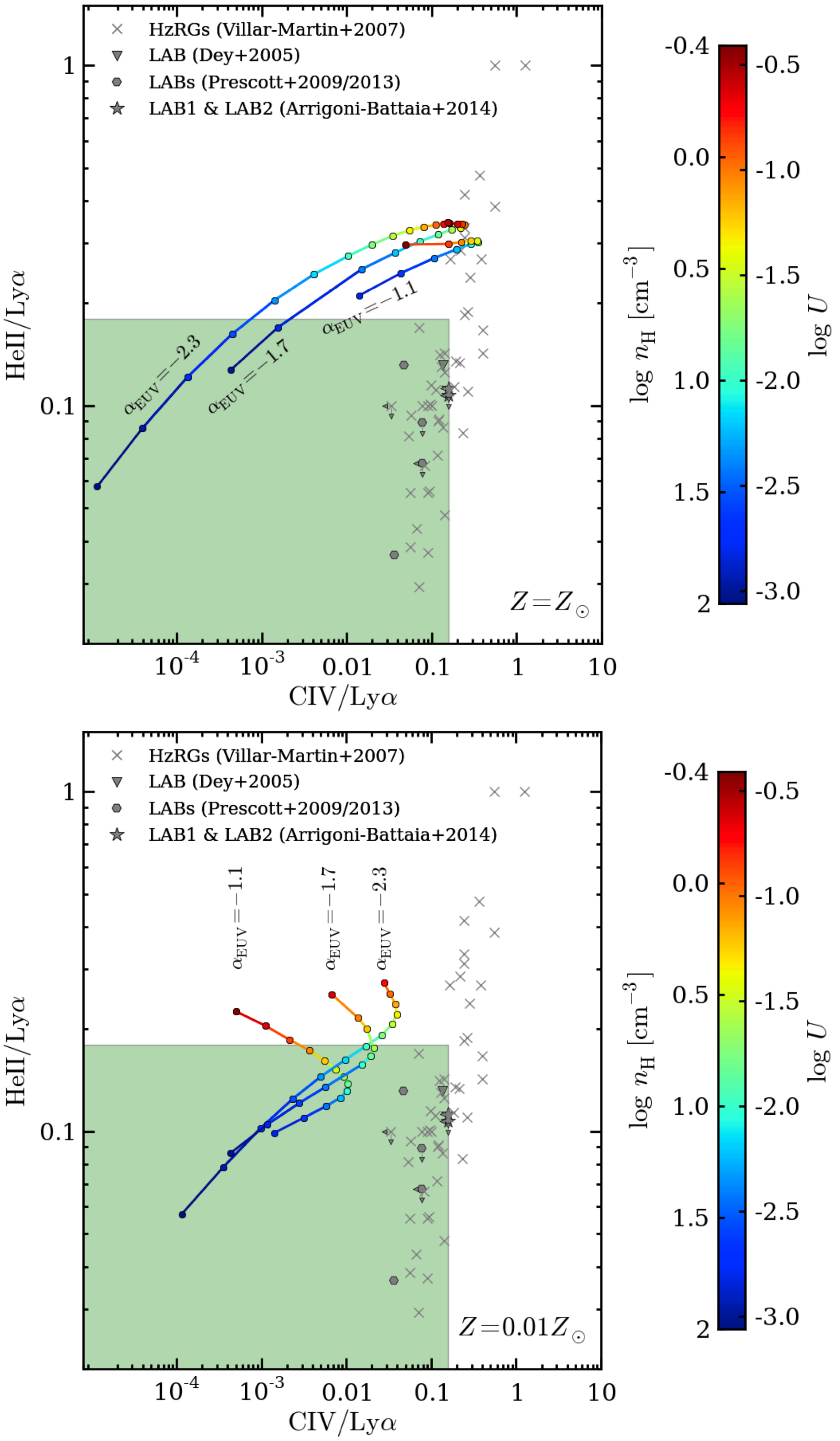

Figure 5.17: He ii/Lyα versus C iv/Lyα log-log plot. Our upper limits on the HeII/Lyα and CIV/Lyα ratios are compared with the Cloudy photoionization models that reproduce the observed $SB_{Ly\alpha} \sim 7 \times 10^{-18}$ erg s^{-1} cm^{-2} arcsec^{-2}. **Upper panel:** comparison of the model grids for different EUV slopes ($\alpha_{EUV} = -1.1, -1.7, -2.3$) at $Z = Z_\odot$. A harder α_{EUV} completely doubly ionize Helium at higher density. **Bottom panel:** same as the upper panel, but at $Z = 0.01\,Z_\odot$. In this case, the Lyα line is also powered by collisions, reshaping the trajectories (see text for explanation on the trends in this Figure). In both panels, the models are color coded following the ionization parameter U, or equivalently the volume density n_H (see color bar on the right). The green shaded area represents the region defined by the upper limits of the UM 287 nebula. See Figure 5.18 for a better visualization of the constraints on the physical parameters.

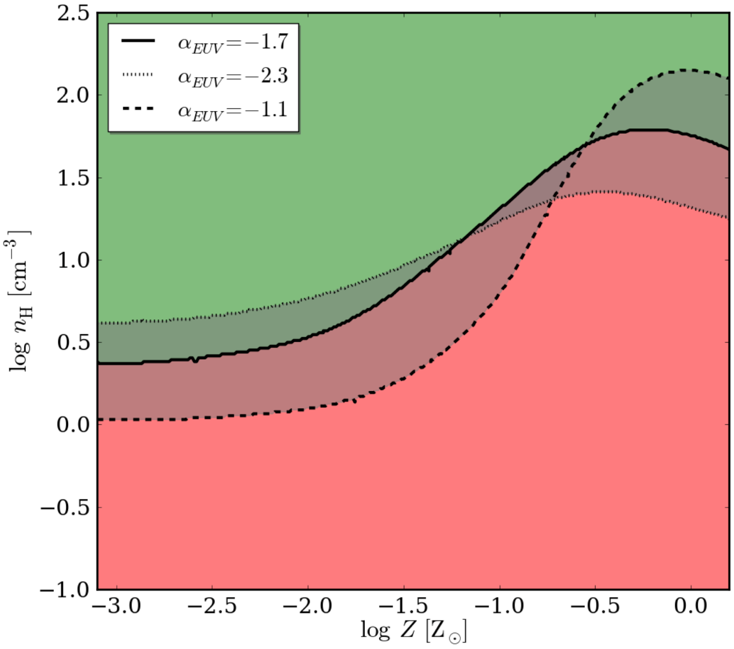

Figure 5.18: Schematic representation on how a variation in $\alpha_{\rm EUV}$ affects the constraints in $n_{\rm H}$ and Z. The green area highlights the region of the parameter space selected by the upper limit He II/Lyα < 0.18 (see panel 'a' of Figure 5.14). The solid, dashed, and dotted lines show the location of this upper limit for $\alpha_{\rm EUV} = -1.7, -1.1$, and -2.3, respectively. It is evident that a change in the ionizing slope do not affect our main conclusions. Namely, if the nebula is photoionized by the UM 287 quasar, there should be a population of dense cool gas clumps with very small sizes ($\lesssim$tens of pc).

by our measurement to higher densities. For example, at solar metallicity, the limit is moved to $\gtrsim 100$ cm^{-3} from $\gtrsim 40$ cm^{-3}.

Thus, in conclusion, our ignorance on the slope of the EUV has a small effect on our density constraints and makes the C IV line a weak metallicity indicator. However, as discussed at the end of §5.4.5, the detection of multiple metal lines with a range of ionization energies would indirectly constrain $\alpha_{\rm EUV}$, and simultaneously constrain the metallicity of the gas.

Covering Factor: Based on the morphology of the emission we argued $f_{\rm C} \gtrsim 0.5$, but assumed the value of $f_{\rm C} = 1.0$ for simplicity. The $f_{\rm C}$ drops out of the line ratios (see Eqn. (2.13) and (5.7)), however our model depends on f_C, since we were selecting only models able to reproduce the observed Lyα SB, which varies linearly with covering factor. We estimate that lowering the covering factor to $f_{\rm C} = 0.4$, only change our lower limit on the density at the 15% level. As discussed in section §5.4.4, lowering $f_{\rm C}$ results in a reduction of the number of models which are able to reproduce the observed Lyα SB, because models with high $n_{\rm H}N_{\rm H}$ valuse become optically thick, and thus over-estimate the Lyα emission. In particular, there are no models which reproduce the observed Lyα SB for low covering factors ($f_C < 0.3$). Thus our conclusions are largely insensitive to the covering factor we assumed.

As said in §2.3, there are also caveats related to the geometry of the system (whose effects should be subdominant) and the assumption of a single population of clouds. In order to properly address all the aforementioned issues, the ideal approach would be to conduct a full radiative transfer calculation on a three dimensional gas distribution, possibly taken from a cosmological hydrodynamical simulation. In §5.3.2, we carried out exactly this kind of calculation treating both ionizing and resonant radiative transfer, however this analysis was restricted only to the Lyα line. Full radiative transfer coupled to detailed photoionization modeling as executed by Cloudy would clearly be too computationally challenging.

5.4.7 Summary and Conclusions

To study the kinematics of the extended Lyα line and to search for extended He ii λ1640 and C iv λ1549 emission, we obtained deep spectroscopy of the UM 287 nebula with the Keck/LRIS spectrograph. Our spectrum of the nebula provides evidence for large motions traced by the Lyα line of FWHM=667 km s^{-1} (resolved by our spectral resolution of FWHM=320 km s^{-1}) which are spatially coherent on scales of ∼150 kpc. There is no evidence for a "double-peaked" line along either of the slits, as might be expected in a scenario where resonant scattering determines the Lyα kinematic structure.

Although our observations achieve an unprecedented sensitivity in the He ii and C iv line ($\mathrm{SB}_{3\sigma} \simeq 10^{-18}$ erg s^{-1} cm^{-2} arcsec^{-2} , average over $1'' \times 20''$and $\Delta v = 3000$ km s^{-1}) for giant Lyα nebulae, we do not detect extended emission in either line for both of our slit orientations. We constrain the He ii/Lyα and C iv/Lyα ratios to be < 0.18 (3σ), and < 0.16 (3σ), respectively.

To interpret these non-detections, we constructed models of the emission line ratios, assuming photoionization by the central quasar and a simple spatial distribution of cool gas in the quasar halo (Chapter 2). We find that:

- if the gas clouds emitting Lyα are optically thick to ionizing radiation, then the nebula would be ∼120× brighter than observed, unless we assume an unrealistically low covering factor, i.e. $f_C \lesssim 0.02$, which is in conflict with the smooth morphology of the nebula. Thus we conclude that the covering factor of cool gas clouds in the nebula is high $f_C \gtrsim 0.5$, and that the gas in the nebula is highly ionized, resulting in gas clouds optically thin ($N_{\mathrm{HI}} < 17.2$) to ionizing radiation.

- The He II line is a recombination line and thus, once the density is fixed, its emission depends primarily on the fraction of Helium that is doubly ionized. On the other hand, the C IV emission line is an important coolant and is powered primarily by collisional excitation, and thus its emission depends on the amount of Carbon in the C^{+3} ionic state. As we know the ionizing luminosity of the central quasar, and the Lyα SB of the nebula, constraints on the He II/Lyα and C IV/Lyα ratios determine where the gas lives in the $n_{\mathrm{H}} - Z$ diagram.

- Photoionization from the central quasar is consistent with the Lyα emission and the He II and C IV upper limits, provided that the gas distribution satisfies the following constraints:

  a) $n_{\mathrm{H}} \gtrsim 3\ \mathrm{cm}^{-3}$,

  b) $N_{\mathrm{H}} \lesssim 10^{20}\ \mathrm{cm}^{-2}$,

  c) $R \lesssim 20$ pc.

  If these properties hold through the entire nebula, it then follows that the total cool gas ($T \sim 10^4$ K) mass is $M_{\mathrm{c}} \lesssim 6.4 \times 10^{10}\ \mathrm{M}_{\odot}$.

Because the Lyα surface brightness scales as $\mathrm{SB}_{\mathrm{Ly}\alpha} \propto n_{\mathrm{H}} N_{\mathrm{H}}$ (Eqn. (2.13)), whereas the total cool gas mass as $M_{\mathrm{c}} \propto N_{\mathrm{H}}$ (Eqn. (2.4)), observations of Lyα emission cannot independently determine the cool gas mass and n_{H} (or the gas clumping factor C), which limited the previous modeling by in §5.3.2. Our non-detection of He II/Lyα combined with photoionization modeling allows us to break this degeneracy, and independently constrain both n_{H} and M_{c}.

Our results point to the presence of a population of compact ($R \lesssim 20$ pc) cool gas clouds in the CGM at ISM-like densities of $n_{\mathrm{H}} \gtrsim 3\,\mathrm{cm}^{-3}$ moving through the quasar halo at high velocities $\simeq 700\,\mathrm{km\,s}^{-1}$. It is well known that even by $z \sim 2$, the gas in the massive $M \sim 10^{12.5}\ \mathrm{M}_{\odot}$ halos hosting quasars is expected to be dominated by a hot shock-heated plasma at the virial temperature $T \sim 10^7$ K (see Chapter 1). Cool clouds moving supersonically through a hot plasma will be disrupted by hydrodynamic instabilities on the cloud-crushing timescale (e.g. Jones et al. 1994; Schaye et al. 2007; Agertz et al. 2007; Crighton et al. 2015; Scannapieco & Brüggen 2015)

$$t_{\mathrm{cc}} \approx 1.3\,\mathrm{Myr}\left(\frac{R}{20\,\mathrm{pc}}\right)\left(\frac{v}{500\,\mathrm{km\,s}^{-1}}\right)^{-1}\left(\frac{n_{\mathrm{cl}}/n_{\mathrm{halo}}}{1000}\right)^{1/2}, \tag{5.9}$$

where we assume that the Lyα line trace the kinematics of the cool clouds, and that the cloud-halo density contrast is of the order of 1000 ($n_{\mathrm{halo}} \sim 10^{-3}\ \mathrm{cm}^{-3}$). If there is hot plasma present in the halo, these clouds are thus very short lived, and can only be transported ~ 0.7 kpc before being disrupted. These very short disruption timescales thus require a mechanism that makes the clumps resistant to hydrodynamic instabilities, such as confinement by magnetic fields (e.g.

McClure-Griffiths et al. 2010; McCourt et al. 2015), otherwise the population of cool dense clouds must be constantly replenished. In the latter scenario, the short lived clouds might be formed in situ, via cooling and fragmentation instabilities. If the hot plasma pressure confines the clouds, this might compresses them to high enough densities (Maller & Bullock 2004; Mo & Miralda-Escude 1996) to explain our results. Emission line nebulae from cool dense gas has also been observed at the centers of present-day cooling flow clusters (Heckman et al. 1989; McDonald et al. 2010), albeit on much smaller scales $\lesssim 50\,\mathrm{kpc}$. The giant Ly$\alpha$ nebula in UM 287 might be a manifestation of the same phenomenon, but with much larger sizes and luminosities, reflecting different physical conditions at high-redshift. Detailed study of the hydrodynamics of cool dense gas clouds, with properties consistent with our constraints, moving at high speeds through hot plasma are clearly required (Scannapieco & Brüggen 2015).

As we showed in §5.4.5, deep observations ($\sim 10\,\mathrm{hr}$) of UM 287 and other giant nebulae with the new integral field units such as MUSE (Bacon et al. 2010), KCWI (Morrissey et al. 2012), and KMOS (Sharples et al. 2006), combined with spatial averaging, will be able to detect extended emission from other lines besides Lyα (see Figure 5.16). In particular, the strongest line will be He ii which should be routinely detectable, and following our analysis, will enable measurements of the volume density $n_{\rm H}$ of the gas. Specifically, a 10 hour MUSE integration would correspond to a sensitivity in He ii/Lyα of ~0.01 (3σ in 300 arcsec^2), which would allow us to probe gas densities as high as $n_{\rm H} = 1000\ \mathrm{cm}^{-3}$. Although we have argued that the UM 287 is powered by photoionization, which is compelling given the presence of a hyper-luminous quasar, a non-detection of He ii in a 10hr MUSE integration would imply such extreme gas densities in the CGM, i.e. $n_{\rm H} > 1000\ \mathrm{cm}^{-3}$, that one might need to reconsider other potential physical mechanisms for powering the Lyα nebula which do not produce He ii (see §1.3.2), such as cold-accretion (e.g., Haiman et al. 2000; Furlanetto et al. 2005; Dijkstra et al. 2006b; Faucher-Giguère et al. 2010; Rosdahl & Blaizot 2012), star-formation (e.g., Cen & Zheng 2013), or superwinds (e.g., Taniguchi & Shioya 2000; Taniguchi et al. 2001; Wilman et al. 2005). Furthermore, comparison of the morphology and kinematics of the nebula in He ii and Lyα can be used to test whether resonant scattering of Lyα photons is important. Although Hα could also be used to test the impact of resonant scattering, it is always fainter than He ii and redshifted into the near-IR, where a detection of extended emission is much more challenging.

In a photoionization scenario, a 10 hr observation of UM 287 or a comparable nebula with MUSE (or KCWI) and KMOS would result in a rich emission line spectrum of the CGM, which, depending on the properties of the gas (i.e. $n_{\rm H}$ and Z), could yield detections of Lyα, N iv, Si iv, Ne iv, C iv, [C iii], Si iii, [O iii], [O ii], Hβ, and Hα. This would enable modeling of the CGM at a comparable level of detail as models of H ii regions and the narrow and broad-line regions of AGN, resulting in comparably detailed constraints on the physical properties of the gas.

> *"You can not expect to see at a first glance. Observing is in some ways an art that must be learned."*
>
> William Herschel

Chapter 6

THE FIRST RADIAL EMISSION PROFILE OF THE QSO CGM

As introduced in Chapter 4, roughly only 10% of the 25 quasars imaged in the FLASHLIGHT survey show a giant Lyα nebula. What is the typical Lyα emission expected on large scales around a QSO? Is this signal easily detectable with current and planned facilities (e.g., MUSE and KCWI)? What are the average properties (e.g., $n_{\rm H}$, $N_{\rm H}$, ionization state) of the gas in the CGM of QSOs?

To try to address these questions from an observational point of view, in this Chapter I present the analysis carried out to characterize the Lyα emission on scales of hundreds of kpc around the 'average QSO' by stacking the narrow-band (NB) data of the 15 QSOs listed in Table 4.1. For this project, we decided to use only the Gemini data (and not all the FLASHLIGHT sample) because they were uniformly reduced, and also because the Keck survey (and data analysis) is still under development at the moment of writing. Note that this analysis was performed as the last project of my PhD work, and thus may need some polishing and further improvements, but the main results should not change significantly.

6.1 IMAGE PREPARATION FOR THE PROFILE EXTRACTION

Figure 6.1 shows an example of the final stacks for the NB (left) and g-band (right). This images show the full field of view (FOV) of our single field observation, i.e. $5.5\,' \times 5.5\,'$, and are shown as χ images, i.e. $\chi = I/\sigma$, where I is the final stack and σ is the square root of the variance image (see §3.1.4 for details on the χ image). Indeed, as described in §4.3, our custom pipeline results in a final stack for each filter (NB and g-band), and in a final variance image (σ^2), which incorporates all the information on the error budget. In the χ images, emission will be manifest as

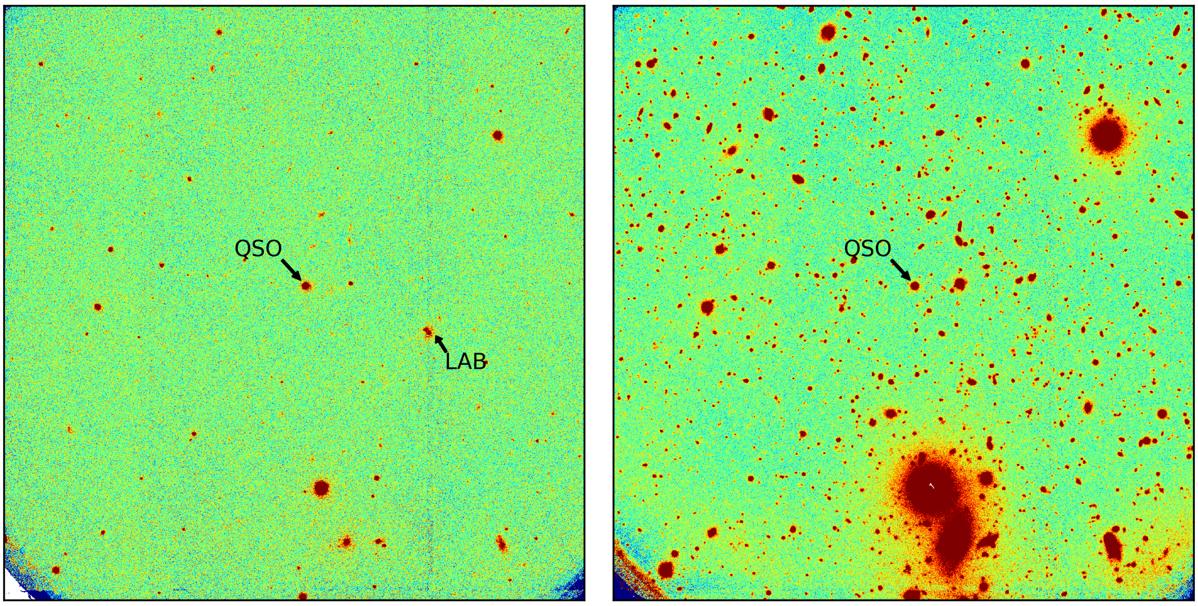

Figure 6.1: NB (left) and g-band (right) χ images for the quasar SDSSJ121503.13+003450.6. The images show the complete field of view of the GMOS-S/Gemini instrument, i.e. $5.5' \times 5.5'$. In these images, the green color indicates values of χ close to zero, while high and low χ values are shown in red and blue, respectively. The position of the QSO and of the LAB discovered (see Fig. 4.2) in this field are indicated. Note the flatness of the images, indicating good flat-fielding/illumination correction and sky subtraction. The lower corners of the images show the presence of the CCD supports. These parts are not used in our analysis.

residual flux, inconsistent with being Gaussian distributed noise (if the noise has been correctly propagated, and thus the σ^2 image is an accurate description of the data).

From Figure 6.1, it is clear that our images are nearly flat in both NB and g-band and lack significant large-scale residuals, indicating that our flat-fielding and background subtraction are good, even if we simply subtract a constant from each individual frame (see §4.3 for details on the sky subtraction). The lower corners of the images show the supports of the CCDs, and are thus noisier in the final stack. These parts of the images are not used in our analysis, but we show them here for the sake of fairness. Note that these χ images correctly show that the noise at the position of the two vertical CCD gaps is slightly higher. This is more evident in the NB stack compared to the g-band image. Indeed, given the typical number of only 6 dithered NB images of 1200s, the gap is closed, but with smaller statistics than in the rest of the image.

As we are interested in the Lyα emission of the gas distribution around the QSO, we should compute a continuum subtracted image as performed in §3.1.3. However, this operation would inevitably increase the error budget (e.g. PSF matching, diffuse light, large galaxies in the g-band, and the use of two images instead of only one), decreasing significantly our ability to detect

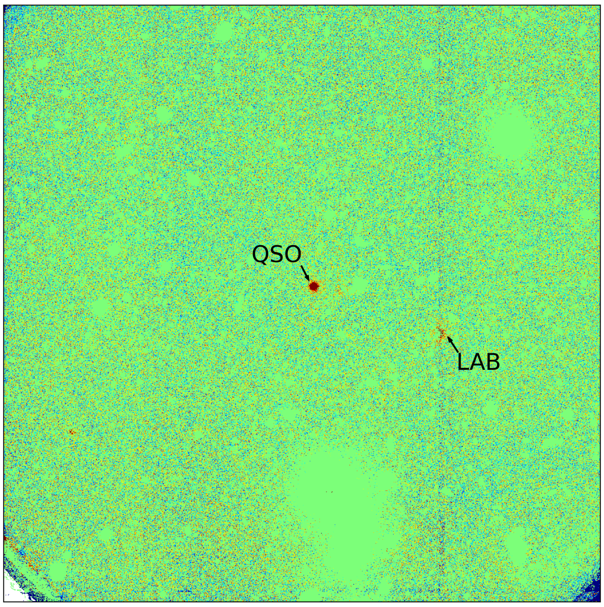

Figure 6.2: NB χ image after masking all the sources as explained in the text. This image is showing the field around the quasar SDSSJ121503.13+003450.6, as in Fig. 6.1, for comparison. Note in particular that the diffuse emission of the LAB is only masked where compact sources are identified, i.e. the LAB is still visible.

the expected weak Lyα signal. Further, we do not expect to detect extended diffuse continuum emission in the halo of a QSO to a level comparable to its Lyα emission.

For these reasons, we decided to avoid the continuum-subtraction step, and instead construct masks for all the sources in the g-band. To build these masks, we run `SExtractor` on the g-band images to identify all the sources down to a very low detection threshold (`DETECT_THRESH`=1.0), and allowing the detection of very compact objects (`DETECT_MINAREA`=5 pixels). We then use the 'segmentation'[1] image produced by `SExtractor` to create the final mask for each NB stack. Given that `SExtractor` unambiguously assigns an identification number to each source in the field, we can 'switch off' the mask for the sources we are interested in, i.e. the QSO or the stars used for the PSF comparison in our analysis.

Further, to be sure that we do not mistakenly detect Lyα signal from compact objects in proximity of the QSOs, we produce an analogous mask using the NB image. However, this mask targets only compact sources and neglects diffuse emission, i.e. `DETECT_MINAREA`=5 pixels and `DETECT_MAXAREA`=15 pixels. To generate the masks, we do not convolve the images with a filter in neither of the `SExtractor` runs. We then generate a final mask by combining the two masks.

---

[1] The 'segmentation' image is already a mask of the image, in which each source is represented by its total isophotal area with flux equal to the identification number in the `SExtractor` catalogue.

Figure 6.2 shows the χ NB image of SDSSJ121503.13+003450.6 after masking all the sources, but the QSO, using the final mask. It is clear, that our method does not mask extended emission in the NB images. Indeed, although there are compact sources within its NB image, the LAB is still clearly visible (compare Fig. 6.1 with Fig. 6.2). Having in hand these final masks, the images are now ready to be used for the following analysis.

6.2 Testing our Narrow-Band Images

We used the final masks built in the previous section to generate images of the NB field showing only the QSO (as in Fig. 6.2), individual stars, and completely masked images. The completely masked images are used to determine a 'zero' profile using random locations, while the stars are needed to determine the point-spread-function (PSF) of our observations.

6.2.1 The 'Zero' Level

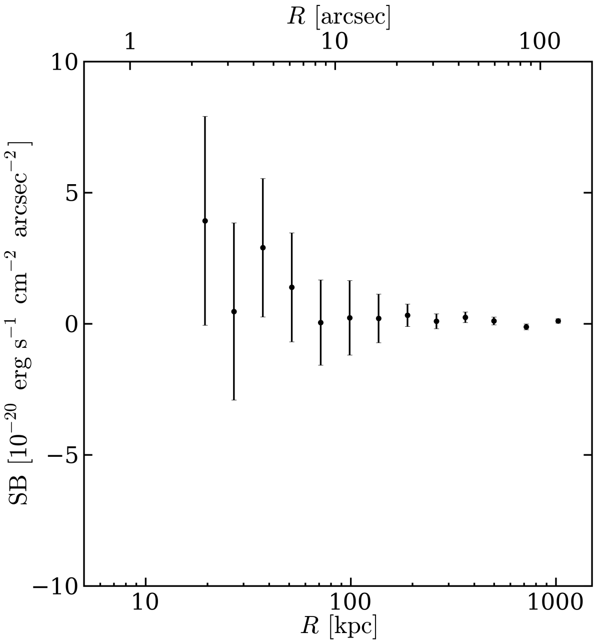

Figure 6.3: Average radial surface brightness profile of the 'zero' level in our images, i.e. of ~ 2000 random locations in the 15 NB fields after masking all the sources. The profile is consistent with zero at all radii. Given the large extent of the last bins, the points at large radii are not completely independent, i.e. some of the 2000 random locations inevitably overlap at large radii, given the FOV of 5.5 ′×5.5 ′.

To assess that our masked images are overall consistent with zero, we compute an average radial surface brightness profile[2] of ~ 2000 random locations in the 15 NB completely masked images. Figure 6.3 shows the resulting average profile, which is consistent with zero at all radii, within our uncertainties. Note that the pixels used to compute the profile at large distances are inevitably not completely independent, given the FOV of 5.5 ′×5.5 ′. However, this is not important for the stacking of the QSOs as we will use completely independent pixels.

---

[2] In this Chapter, the profiles are always evaluated within circular apertures centered at the location of interest. The radius at which the profiles are computed is chosen to increase in logarithmic steps.

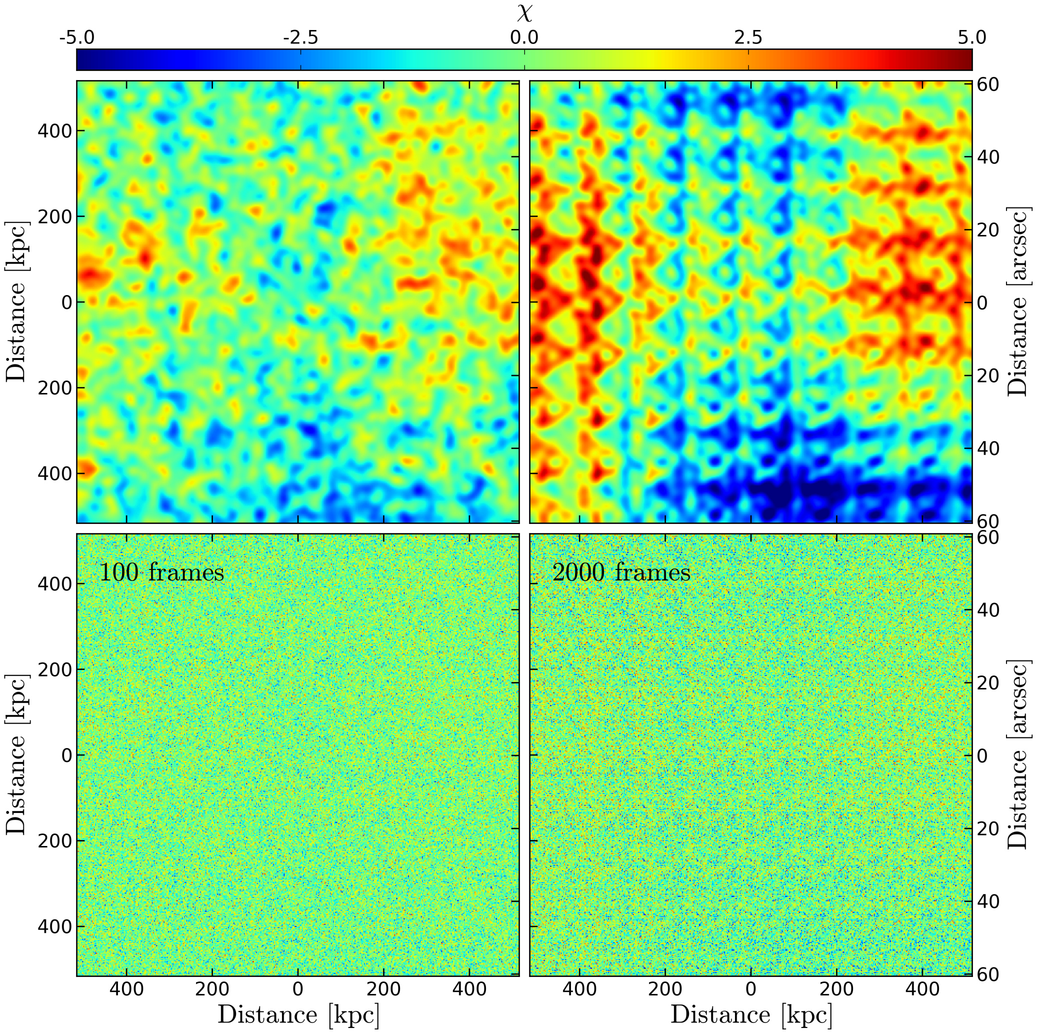

Figure 6.4: Average combined images of 100 (left) and 2000 (right) random locations in the 15 NB fields after masking all the sources. The stacks are shown as χ images in the lower panels, and as $\chi_{\rm smth}$ images in the top panels (here we use a Gaussian kernel with size of 10 pixels; see §3.1.4). Note the pattern visible in the right images due to CCDs imperfections visible at this high sensitivity. Our masks successfully work: no residual flux from compact objects can be seen in these average stacks, which are consistent with zero (in agreement with Fig. 6.3).

Figure 6.3 also illustrates the extremely high sensitivity that one can in principle reach by combining a large number of images. However, one has to be careful because very high sensitivity means that the small imperfections in the CCD will be visible in a 2D combined image. This can be seen in Figure 6.4, where we show how the stack of 60 ″ × 60 ″ random locations varies by increasing the number of frames used. In particular, the bottom panels are χ images, while the upper panel are $\chi_{\rm smth}$ images estimated using a Gaussian kernel with size of 10 pixels (see §3.1.4 for details on the estimate of a $\chi_{\rm smth}$ image).

6.2.2 CONSTRAINING THE PSF OF THE NB IMAGES

To quantify the extended emission in the Lyα line around the quasars in our fields, we have to carefully estimate the PSF of our NB images. We need to compute the PSF with high accuracy, in order to detect even small deviations from its shape in the average profile of the QSOs. For this purpose, we match the SDSS star catalogue with the sources in our 15 NB fields and select all the high S/N stars, resulting in a sample of 115 usable stars. For each of these stars, we have created the NB masked image as explained in §6.1, and calculated its radial profile. The profiles of the 115 stars are then average combined to obtain the PSF of the NB images.

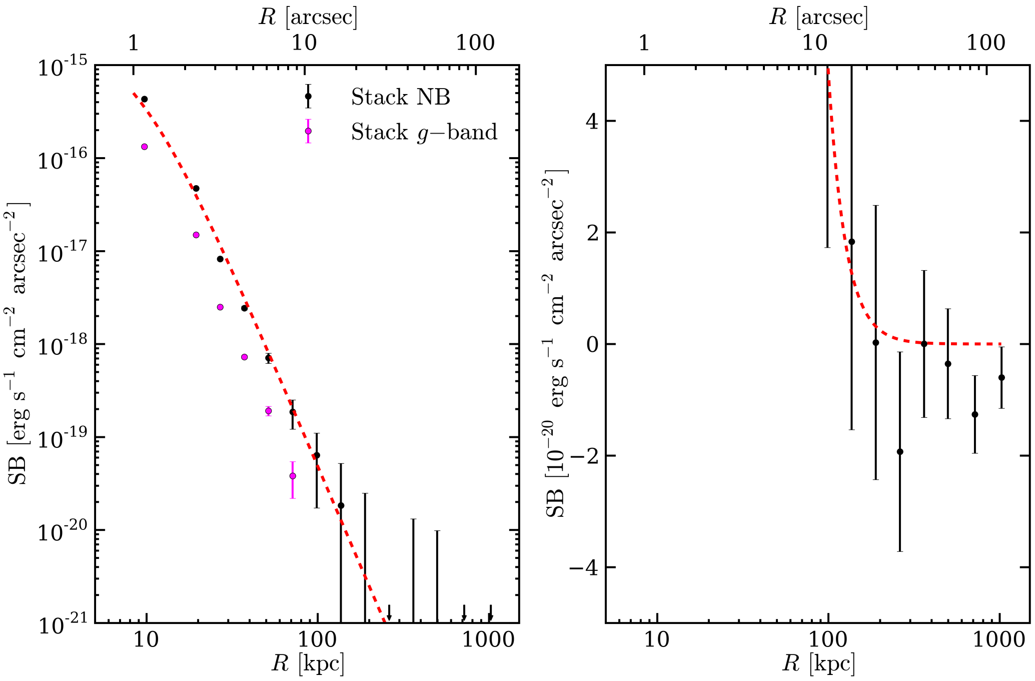

Figure 6.5: Average combined radial profile for 115 stars in our NB images. This PSF is well fitted by a Moffat profile with FWHM= $1.2''$, and $\beta = 2.15$ (red dashed line). **Left:** log-log plot to capture the whole range of the PSF. The PSF of the NB images (black) is in good agreement with the PSF of the g-band (magenta). The black arrows indicate the position of the negative points (see right panel). **Right:** lin-log plot showing the small fluctuations ($\sim 10^{-20} - 10^{-21}$ erg s^{-1} cm^{-2} arcsec^{-2}) around zero of the last bins, and to highlight how the errors decrease as a result of averaging over larger areas.

Figure 6.5 shows the average combined radial profile for the 115 high S/N stars in our images. The profile is consistent with a Moffat function, as expected for seeing limited observations, where the PSF is determined by the wiggling of the stars on the CCD (Trujillo et al. 2001). The normalized Moffat profile is defined as

$$\mathrm{PSF}(r) = \frac{\beta - 1}{\pi\alpha^2}\left[1 + \left(\frac{r}{\alpha}\right)^2\right]^{-\beta}, \tag{6.1}$$

where the full width at half maximum is given by FWHM= $2\alpha\sqrt{(2^{1/\beta} - 1)}$, and the total flux is normalized to 1. We fitted the average profile of the stars with this function and obtained best fit parameter values of FWHM=1.2″and $\beta = 2.15$. The FWHM value we obtained is perfectly consistent with the independent measurement of the median seeing in our observations (see §4.2) estimated by selecting all the stars in the images, by applying the `psfmeasure` task within the IRAF software. The β parameter, in absence of imperfections in telescopes optics, should have a value of ~ 4.765, as expected from turbulence theory (e.g., Saglia et al. 1993; Trujillo et al. 2001). However, it is known that PSFs typically measured in real images have larger "wings", or equivalently, smaller values of β. This is due to the fact that the real seeing also depends on the performance of the telescope optics, and not only on the atmospheric conditions (Trujillo et al. 2001). Our value is in agreement with this picture, however there is no tabulated PSF for the GMOS-S instrument (German Gimeno[3] private communication).

To make our PSF estimate more robust, we perform the same calculation on masked g-band images. We select 15 high S/N not saturated stars, one per field to include in our calculation all possible seeing variations between different stacks. We then calculate the average radial profile, as for the stars in the NB images. The left panel of Figure 6.5 shows (in magenta) this average radial profile. The shape of the Moffat profile of the NB and g-band images are in remarkable agreement. Note that in the case of the g-band PSF calculation, we stop at smaller radii, due to confusion arising mainly from diffuse light from bright objects or haloes that our masks do not completely cover.

Finally, it is important to note that, as expected, the average star profile is consistent with zero at large radii, within our uncertainties (see right panel of Fig. 6.5). Having characterized the PSF of our observations, we can now ascertain whether our sample of QSOs exhibit a signal from the surrounding diffuse gas distribution.

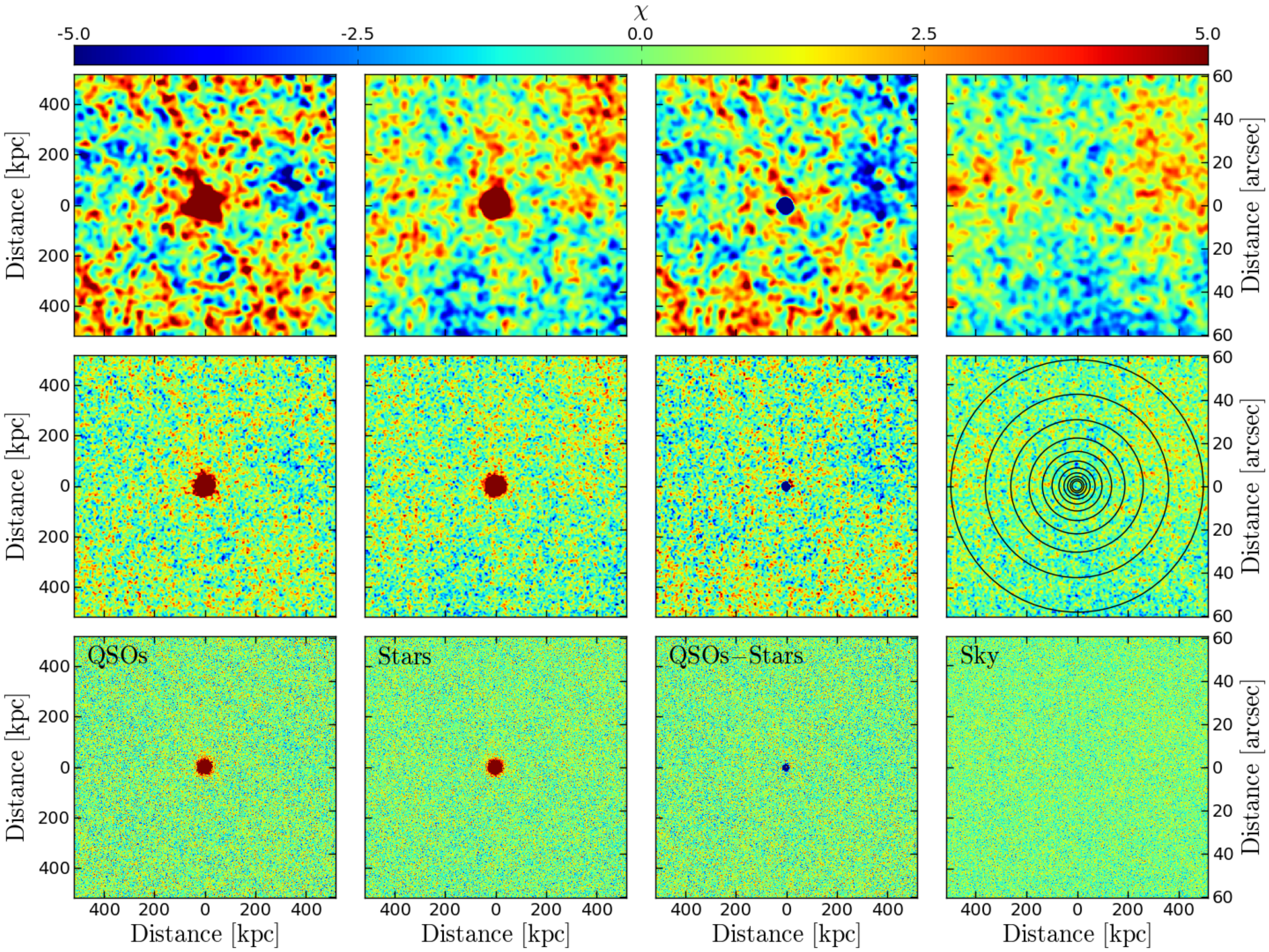

Figure 6.6: Comparison of the average combined images. **First row:** χ images of the stack of the QSOs (first column), $\sim$ 80 stars (second column), difference image between the QSOs and the normalized star image (third column), and the ‘sky’, i.e. the ‘zero’ level (fourth column). **Second row:** $\chi_{\rm smth}$ images, obtained by convolving with a Gaussian of FWHM= 3 pixels ($\sim 0.9''$), as explained in §3.1.4. For reference, we overplot on the sky image the radii at which we calculate the radial profiles in the foregoing analysis (note that are missing the two bins at larger radii). **Third row:** as the second row, but convolved with a wider Gaussian, i.e. FWHM= 10 pixels ($\sim 3''$). It is evident that the QSOs’ stacked emission is not symmetric as the STAR PSF, and the residual of the PSF subtraction is not consistent with being sky.

6.3 RESULTS

We have first computed an average 2D stack of the 15 QSOs after masking all the sources, as explained in §6.1, and compared it with i) an average 2D stack of all the ∼ 80 stars that lie at least 1′ away from the edges of the FOV[4], and ii) the average 2D stack of 100 random 'sky' positions, already shown in Figure 6.4. These stacks are shown in Figure 6.6.

The first row of Figure 6.6 shows the χ images of the final stack of the QSOs (first column), of the stars (second column), and of the random locations (fourth column). The third column of Fig. 6.6 shows the χ image of the difference between the stack of the QSOs and stars. This difference is calculated by scaling the peak of the final stack of the stars to the peak of the quasars. The residual image shows negative values within a roughly circular region with radius of ∼ 7 pixels, corresponding to ∼ 2″ (or equivalently ∼ 17 kpc). This discrepancy on such small scales suggests that a correct 2D PSF modeling on very small scales should take into account centering errors on the PSF evaluation, especially because we have a pixel scale of 0.29″ pixel^{-1}, and a slightly different seeing for each field. Further, one should also take into account the presence of the QSO's host galaxy, as shown by e.g. Mechtley et al. (2012), and Mechtley (2014). The correct 2D subtraction on ∼kpc scales is not the focus of the current work, but will be tested in the future.

On the other hand, at larger radii the QSOs' image seems to be quite different from the more symmetric PSF of the stars (this is evident only in the $\chi_{\rm smth}$ images). Indeed, the residual image tentatively shows extended emission not being consistent with sky noise fluctuations. To firmly quantify this emission, we estimated the average radial profile of the 15 QSOs independently from the 2D stack, as done in the case of the stars in §6.2.2.

Figure 6.7 shows the average combined radial profile of the QSOs, together with the average combined profile of the stars. For comparison purposes, we slightly shift to smaller radii the stars' profile together with the Moffat fit. The right panel of Fig. 6.7 shows that the QSOs' profile is also consistent with zero at large radii, while the left panel clearly indicates that the QSOs' profile deviates from a pure Moffat function at large radii ($\gtrsim$ 60 kpc), and at a low surface brightness level of SB∼ 10^{-19} erg s^{-1} cm^{-2} arcsec^{-2} .

This is more evident if we normalize the stars' profile to the peak of the QSOs' profile. We compare both profiles after the scaling in the left panel of Figure 6.8. Once we normalize the stars' profile, we can subtract the contribution from the unresolved broad line regions of the QSOs, i.e. the PSF of the stars, from the average combined profile of the QSOs. This profile thus represents the average Lyα emission arising from the distribution of the cool gas (T ∼ 10^4 K)

---

[3] German Gimeno is the current Instrument Scientists for GMOS-S.

[4] We decided to use a 1′ × 1′ FOV, and not larger, in order not to lose most stars, and to thus avoid further degradation of the S/N in their final 2D stack.

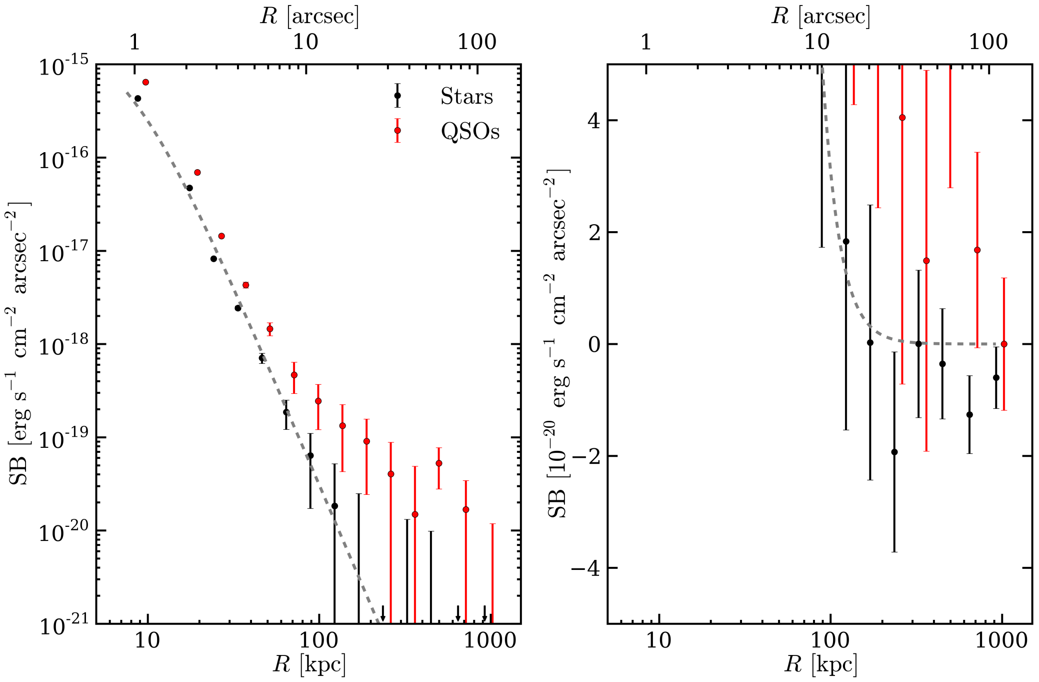

Figure 6.7: Average combined radial profile of 15 QSOs compared to the star PSF. **Left:** log-log plot to show the whole range of the profiles. The QSOs' profile shows a deviation from the stars' PSF at SB$\sim 10^{-19}$ erg s^{-1} cm^{-2} arcsec^{-2}. **Right:** lin-log plot showing that the QSOs' profile is also consistent with zero at large radii. In both panels, the stars' profile, together with the Moffat fit, is slightly shifted to smaller radii for clarity (e.g. to avoid the superposition of the errorbars).

around a typical bright QSO. However, we stress again that we do not subtract the continuum emission from the NB images and thus, on small scales, i.e. the scale of the quasar's host (tens of kpc), the signal we see might be due to contamination from the host galaxy.

We will test whether this is the case in the future. In particular, we will construct the average profile of the QSOs' continuum from the g-band, and assess whether there are residuals from the average PSF of the broad-band image. Any significant residual found on the host galaxy's scale, should then be subtracted from our Lyα profile, after scaling it properly to match the width of the NB filter (see e.g., §3.1.3). However, note that the contribution from the host galaxy should be very small. Mechtley (2014) shows that for $z \sim 2$ QSOs, the host galaxy is three magnitudes fainter than the QSO in the H-band (corresponding roughly to a rest-frame V-band). Further, in our case, the host galaxy's emission would be highly dependent on its dust content, geometry, and morphology. Indeed, given the fact that our observations are in the rest-frame UV, where the galaxy's emission should be attenuated by its dust component, we are confident that if any contribution from the host galaxy is present, this should be minor.

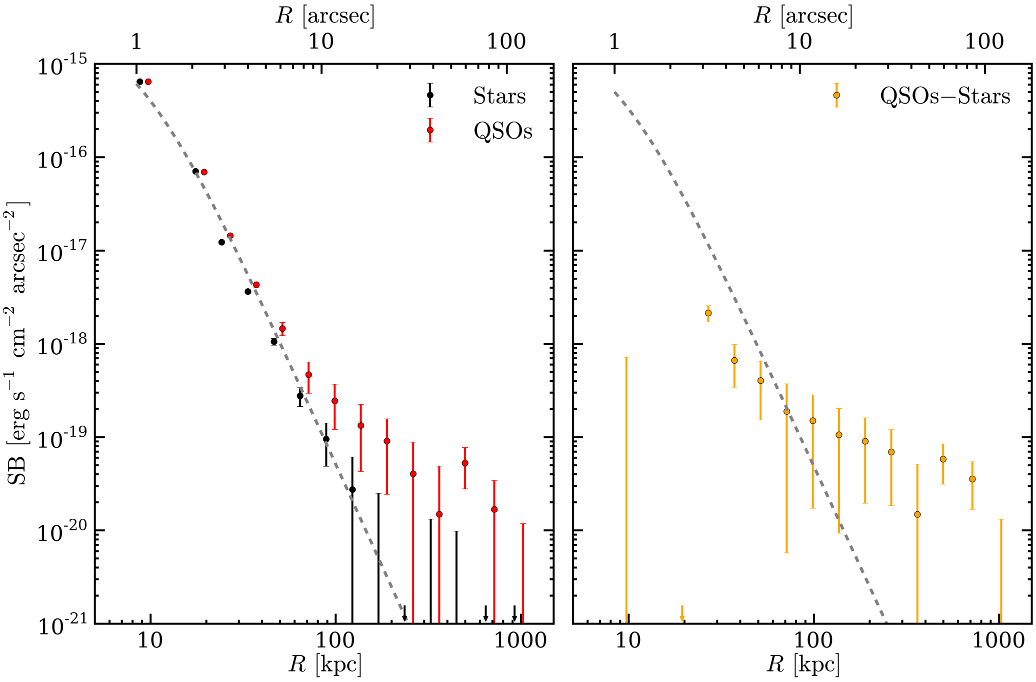

Figure 6.8: Left: Average combined radial profile of 15 QSOs compared to the normalized stars' profile. In this log-log plot, the QSOs' profile clearly shows a deviation from the stars' PSF at about the level of SB$\sim 10^{-19}$ erg s^{-1} cm^{-2} arcsec^{-2}. The profile of the stars, together with the Moffat fit, is slightly shifted to smaller radii for clarity (e.g. to avoid the superposition of the errorbars). **Right:** difference of the average combined QSO profile and the normalized stars profile. This may be interpreted as the average Lyα emission profile of the gas distribution in a typical QSO. In both panels, the small arrows at the bottom of each plot indicate the positions of negative values (see e.g., Fig. 6.5).

Elvis et al. (2012) compare 16 different galaxy templates (Polletta et al. 2007) to the median radio-quiet quasar's SED, showing that any reasonable host would contribute at $\sim 1000 - 2000$Å from $\sim 25\%$ for starburst galaxies down to $< 0.02\%$ in the case of ellipticals (see their Figure 17). Jahnke et al. (2004) show that it is quite difficult to detect the host galaxy at 2000Å, even at HST resolution. In particular, 60% of their sample has non-detected hosts, resulting in less than 5% contribution to the nuclear flux. On the other hand, the brightest host detected contributes $\sim 50\%$ to the total flux (see their Figure 8). Obviously, the host galaxy's contribution to the flux, and thus its detection, also depends on the specific accretion rate of the central AGN, with higher chance to detect the host galaxy for lower accretion objects (but these would not be called quasars).

To further complicate the interpretation, it has been shown that a high fraction of QSO hosts shows signs of recent strong interactions. Specifically, using HST imaging, Mechtley 2014 found that 10/16 $z \sim 2$ QSOs have disturbed host galaxies. It is unclear whether we would be able to detect this signature in our seeing limited observations, i.e. the signal, if present, would be different in each QSO profile on small scales (central tens of kpc). As we are interested in quantifying the signal on much larger scales, we leave this aspect for future analysis.

The right panel of Fig. 6.8 displays the profile of the difference between QSOs and normalized stars' profile, which spans very low levels of surface brightness $\mathrm{SB}_{\mathrm{Ly}\alpha} \sim 10^{-19}$–$10^{-20}$ erg s^{-1} cm^{-2} arcsec^{-2}. However, we have to test its reliability. First, we check if this signal is dependent on the sources used for the QSOs' stacking, as follows. We compute 15 average combined profiles of 14 QSOs, each time removing a different QSO. Then, to obtain the CGM profiles, we subtract from each of them the normalized stars' profile. In this way, it would be clear if a bright QSO in our sample dominates the stack.

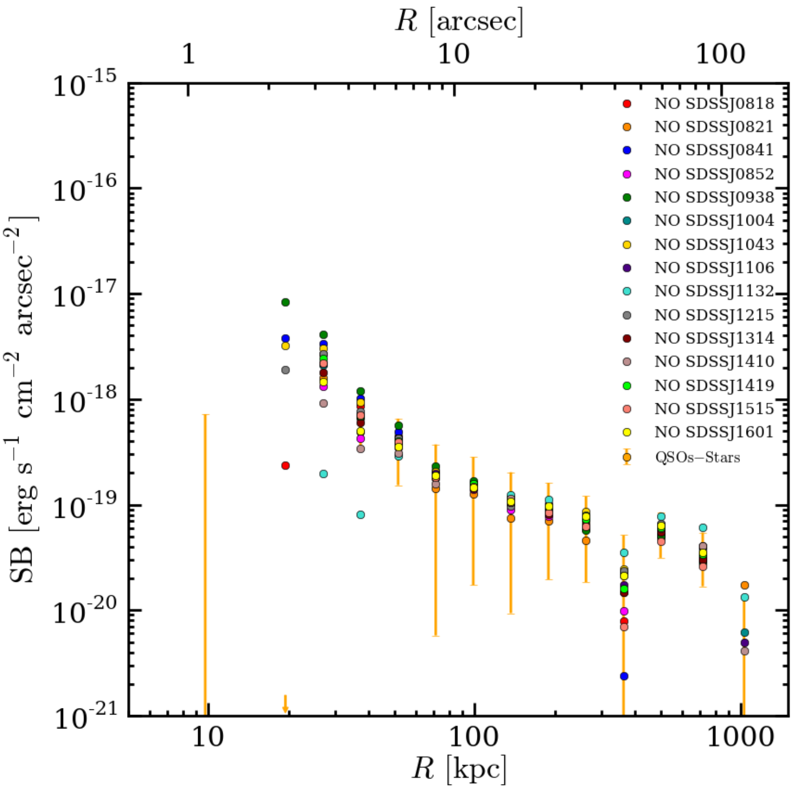

Figure 6.9: Dependence of the Lyα profile on each individual QSO. We estimate the difference between the QSOs' profile and the normalized stars' profile 15 times, each time by removing a different QSO from the QSOs' profile calculation. It is clear, that none of the QSOs of the sample is dominating the Lyα profile. Larger variations occur at smaller radii. This is probably due to slightly different seeing variations or host galaxy contamination (see Section).

Figure 6.9 shows this test. It is clear that the profile is not changing significantly between different calculations. We are then confident that none of the QSOs in our sample dominates the average profile. However, being close to our detection limits[5], we verify the significance of our results in the next Section. In particular, we have to verify that our error estimates hold at large radii. Specifically, we implicitly assume in our analysis that the noise is perfectly following the Poisson statistics, i.e. that the expected error on the SB should drop with the square root of the area probed $\sigma_{\mathrm{SB}}^{\mathrm{Area}} = \sigma_{\mathrm{SB}}^{1\mathrm{arcsec}^2} / \sqrt{\mathrm{Area}}$.

---

[5] All the points on scale of ∼ 100 kpc are $\gtrsim 1\sigma$ detections, and thus close to be just upper limits.

6.3.1 QUANTIFYING THE SIGNIFICANCE OF OUR RESULTS

To firmly assess the significance of our results, we perform a bootstrap analysis. We have built 1000 samples of 15 stars, by randomly selecting objects from the 115 stars that were used to determine the PSF of the NB images (see §6.2.2). For each sample of stars we have then computed the average combined radial profile, and subtracted from it the normalized average profile of the 115 stars. In this way, we are left with 1000 realizations of our same experiment, i.e. QSOs' profile − stars' profile. These profiles should be consistent with zero at each radius, and the χ values should be consistent with a Gaussian distribution of unit variance. If this is the case, and our previously measured Lyα profile shows deviations from these Gaussian distributions, this would then confirm that we have tentative detections with the current binning, but with higher significance within larger bins. In particular, if we find Gaussian distributions with variances greater than 1, it could give us information on how much we underestimate the noise, and at which radius the Poisson statistics are not valid anymore. In other words, the bootstrap analysis will tell us if our measurements lie within the distribution of the 1000 realizations, or if they greatly differ.

In Figure 6.10 we show the distribution of the χ values for these 1000 realizations at each bin, starting from the $\sim$ 50 kpc radius, and compare them to our results. It is clear that the histograms are Gaussians, well centered in zero (blue vertical lines). However the variances increase at large radii, indicating that the error budget is deviating from Poisson statistics. Indeed, for $R \lesssim 200$ kpc, we only slightly underestimate the noise (by 15%), while at large radii we incur in larger errors. This may be due to the fact that we hit the systematics shown in Fig. 6.4, and thus our errors at these large radii, i.e. $\gtrsim 400$ kpc, are dominated by that noise.

The red vertical lines in Figure 6.10 indicate the measurements obtained in the previous section for comparison (right panel Fig. 6.8). With the current binning, our profile is thus just a tentative detection of the Lyα emission from the CGM. This can be better visualized in Figure 6.11, where we highlight the area within the 16th and 84th percentile of the 1000 realizations in comparison to the QSOs' average combined profile (left panel), and with the difference profile (right panel). It is now clearer that our Lyα profile is of low significance in the current binning.

It is important to note that in agreement with the previous histograms (Fig. 6.10), the 16th percentile of the 1000 realizations is negative. This can be seen in Figure 6.12, where we compare the Lyα profile to the area within the 16th percentile and 84th percentile in a log-lin plot centered at zero SB.

If we now use larger bins for the data at the radii where the Poisson statistics hold, our result would be more compelling. In particular, we decide to use the data for 50 kpc $< R <$ 500 kpc, and apply a similar bootstrap analysis. The left panel of Figure 6.13 shows the χ histogram of

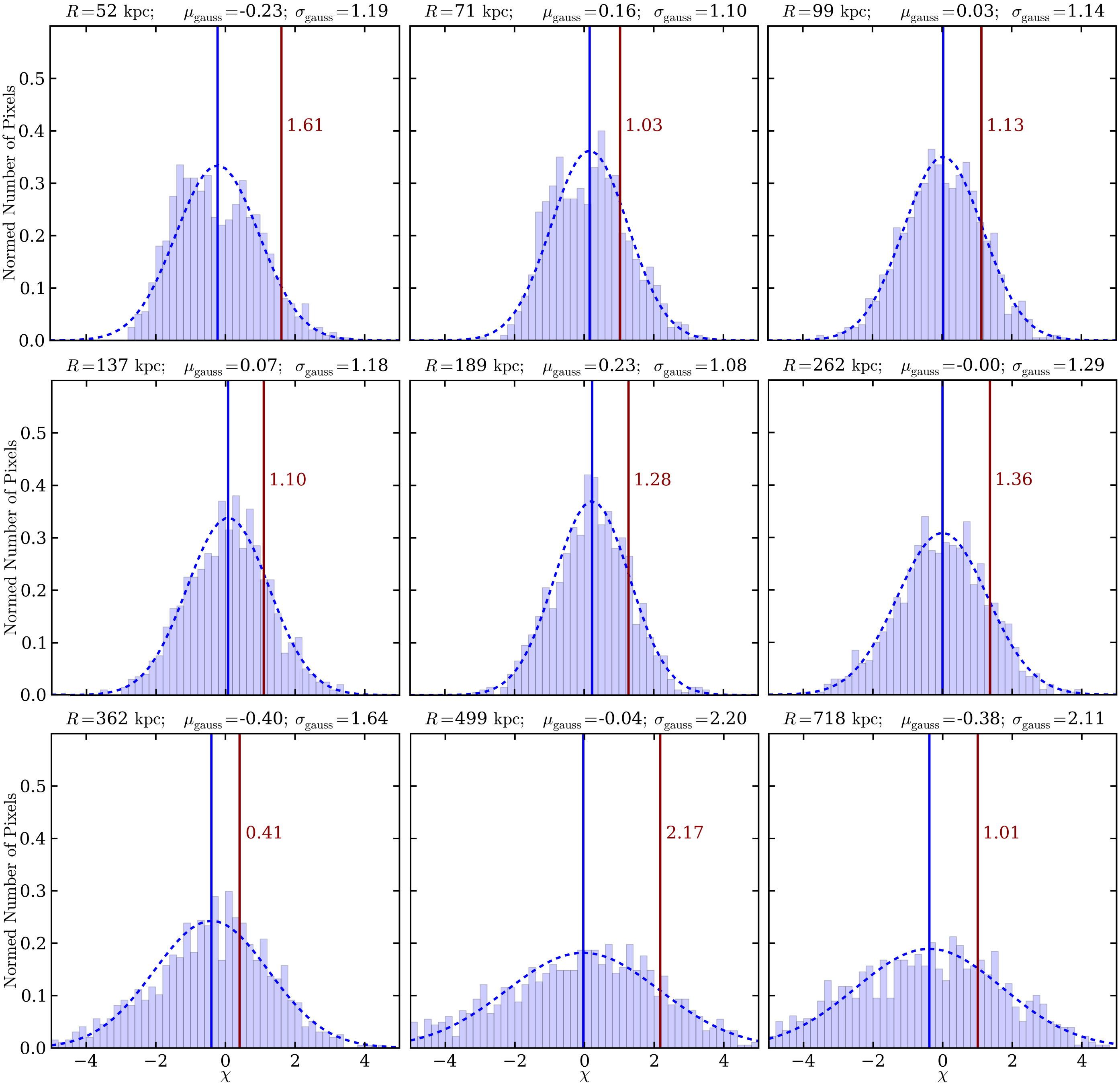

Figure 6.10: χ histograms of the 1000 realizations of our same experiment (see Section for details) using random samples of 15 stars each. We show the histograms for each bin starting from $\sim$ 50 kpc. The histograms are consistent with Gaussian distribution centered in zero (see the central $\mu_{\rm gauss}$ values) and with nearly unit variance (see the $\sigma_{\rm gauss}$ values) till $\sim$ 300 kpc. The bins at larger radii seem to deviate from the simple Poisson statistics. The blue vertical lines indicate the central value of each histogram ($\mu_{\rm gauss}$), while the vertical brown lines indicate the χ for our measurements in the right panel of Fig. 6.8.

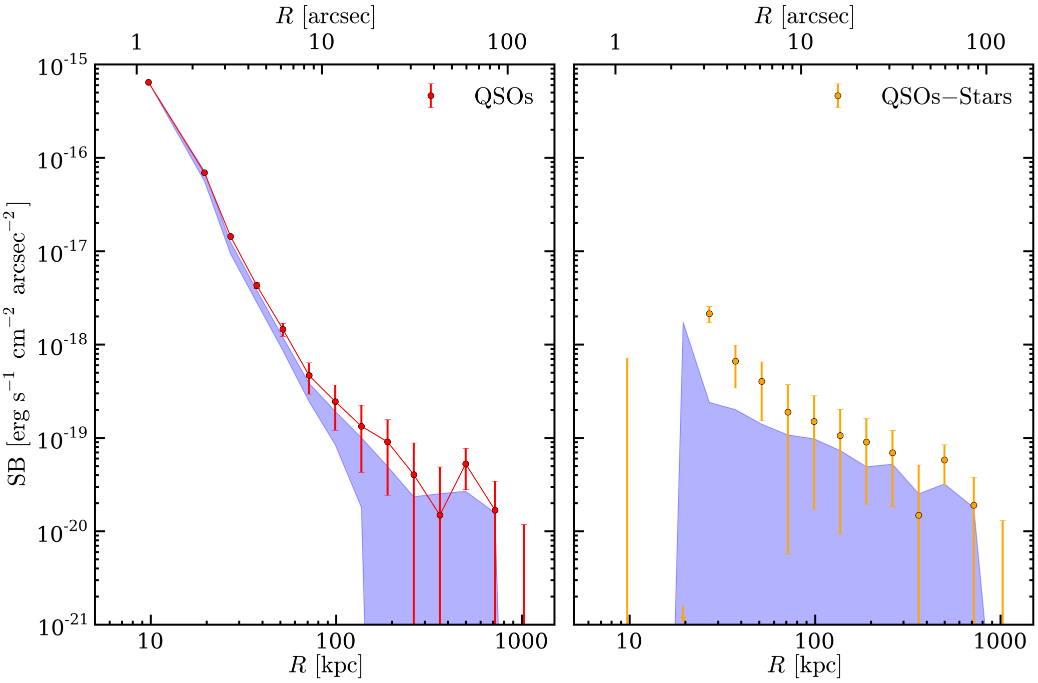

Figure 6.11: Left: the average combined radial profile of the 15 QSOs (red) is compared to the confidence area within the 16th and the 84th percentiles from the bootstrap analysis (blue shaded area). **Right:** the difference between the QSOs' profile and the average profile of the 115 stars (yellow) is compared with the confidence area within the 16th and the 84th percentiles from the bootstrap analysis (blue shaded area). Using the current radial bins, there is only a hint for Lyα signal, as already clear from Fig. 6.10.

the 1000 realizations in comparison to our measurement (red vertical line). As expected from the previous analysis, the distribution is clearly Gaussian and centered at zero, and we somewhat underestimate the error. Specifically, given that we find $\sigma_{\text{gauss}} = 1.30$, our error underestimation is of the order of 30%. However, bearing this in mind, we can still use Poisson statistics for this large bin. It becomes clear now, that our measurement shows a larger offset from the distribution ($\sim 3\sigma$), as compared to what we previously found.

This detection corresponds to $\text{SB}_{\text{Ly}\alpha} = (5.5 \pm 1.8) \times 10^{-20}$ erg s^{-1} cm^{-2} arcsec^{-2} within an annular region extending from 50 kpc to 500 kpc around the QSO. In the right panel of Figure 6.13, we show the comparison between this measurement and the average value of the 1000 realizations in the bin 50 kpc $< R <$ 500 kpc, together with the confidence area defined by the 16th and the 84th percentile. This plot once again shows the reliability of our result. In the next Section we will discuss the implications of our finding in comparison to our current understanding of the gas distribution around QSOs, both from observations and from simulations.

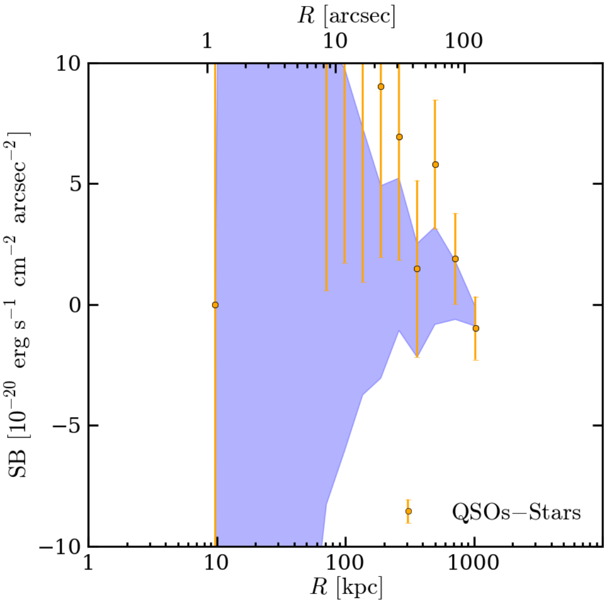

Figure 6.12: Bootstrap analysis around the 'zero' flux level. The 1000 realizations obtained by average combining random sample of 15 stars, and subtracting the 115 stars' profile, fluctuate both positive and negative, as already suggested by Fig. 6.10.

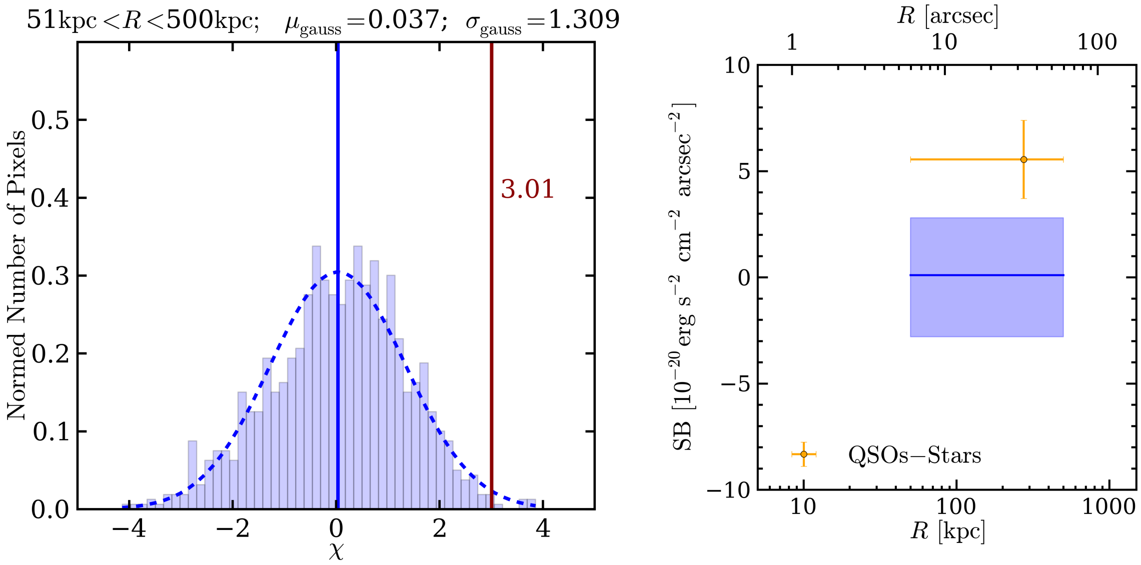

Figure 6.13: **Left:** χ histogram of the 1000 realizations of our same experiment using random samples of 15 stars each (see Section for details) in a bin extending from 50 kpc to 500 kpc. The red vertical line indicates the χ value for our measurement in the same bin. **Right:** Our ~ 3σ detection of the Lyα emission, i.e. $\mathrm{SB}_{\mathrm{Ly}\alpha} = (5.5 \pm 1.8) \times 10^{-20}$ erg s^{-1} cm^{-2} arcsec^{-2} , in the 50 kpc $< R <$ 500 kpc bin is compared to the confidence area within the 16th and the 84th percentiles from the bootstrap analysis for the same bin (blue shaded area). The blue horizontal line indicates the mean value of the bootstrap analysis.

6.4 Discussion

As discussed in detail in §1.1, and shown in Chapter 2 and Chapter 5, one needs to be particular cautious when dealing with observations of the Lyα emission. Here, we interpret our detection following two different approaches. First, we explain the observed $\text{SB}_{\text{Ly}\alpha}$ in light of the simple model for cool halo gas explained in Chapter 2 (Hennawi & Prochaska 2013), and assuming recent observational constraints on the cool gas distribution around $z \sim 2$ QSOs. Secondly, we discuss how our observed value could be interpreted by a typical simulation when applying the calibrated relation Eqn. (5.2) derived in Chapter 5. We remind the Reader that this relation is obtained by comparing the observed Lyα emission from the Slug nebula to a cosmological simulation post-processed with ionization and Lyα radiative transfer (see Chapter 5; Cantalupo et al. 2014).

First of all, it is important to note that if we assume that the QSOs are shining on the gas, it would be inevitably highly ionized and thus optically thin. Indeed, the average magnitude of our sample is i-mag = 18.64, corresponding to a specific luminosity at the Lyman limit $\log L_{\nu_{\text{LL}}} = 30.9$. This value of $L_{\nu_{\text{LL}}}$ is obtained as in §5.4.3.1 by integrating the Lusso et al. (2015) composite quasar spectrum against the SDSS filter curve, and choosing the normalization which gives the correct magnitude. The QSOs in our sample are on average less bright than the UM287 quasar (i-mag=17.28, Chapter 5), which clearly ionize the surrounding gas. However, Hennawi et al. (2015) show that the $z \sim 2$ quasar SDSSJ084158.47+392121.0 (i-mag=19.35), less bright than our average quasar, is able to keep the gas ionized on scales of hundreds of kpc. Specifically, SDSSJ084158.47+392121.0 is also surrounded by a bright ($L_{\text{Ly}\alpha} = 2.1 \times 10^{44}$ erg s^{-1}) Lyα nebulosity as the UM287 quasar. This Lyα nebula extends for $\sim$ 300 kpc, and is currently explained as fluorescent emission powered by the ionizing radiation of the QSO (Hennawi et al. 2015). For these reasons, in the following we assume the scenario in which our measurement is related to optically thin gas, being illuminated by the ionizing radiation of the QSO.

The assumption of an optically thin scenario is also corroborated independently by our stacking procedure. Indeed, we have simply average combined the profiles of the QSOs in our sample, without normalizing them to their luminosity. The fact that we find a signal, and this do not depend on the brighter QSOs in our sample (see Fig. 6.9), is then against a scenario in which the signal from the Lyα emission on large scales depends on the luminosity of the central QSO, as in the optically thick regime (see Eqn. 2.16).

After establishing that the optically thin regime is a good hypothesis, we can derive the physical properties of the emitting gas by assuming recent observational constraints on the distribution of the cool gas ($T \sim 10^4$ K) around a typical QSO. Indeed, the highly ionized scenario implies that $\text{SB}_{\text{Ly}\alpha} \propto f_{\text{C}} N_{\text{H}} n_{\text{H}}$ (see Eqn. (2.13)), and thus our measurement constrains the product of the physical parameters that describe the gas distribution. To break the degeneracy between the covering factor $f_{\rm C}$, column density $N_{\rm H}$, and volume density $n_{\rm H}$, we need independent observations.

Regarding $f_{\rm C}$, it has been shown that the smooth morphology of the emission in giant Lyα nebulae implies a covering factor of $f_{\rm C} \gtrsim 0.5$ (see §3.4.1, and §5.4.3.1). Thus, in what follows, we will always assume a covering factor of $f_{\rm C} = 0.5$. Note that this value is also well motivated by the distribution of optically thick absorbers, which show a high covering factor $f_{\rm C} \simeq 0.6$ on $R \lesssim 200$ kpc in the quasar's CGM (Prochaska et al. 2013b).

Further, the total hydrogen column density $N_{\rm H}$ is usually constrained through photoionization modeling of absorption systems along the sightlines of background QSOs that pierce through the halo of a foreground QSO, i.e. using QSO pairs not physically related (Lau et al. 2015 and references therein). Since the absorption is at the same z of the foreground QSO, it is assumed to arise from the gas distribution surrounding the QSO. Using this method, Hennawi et al. (2015) estimate the hydrogen column density to be $\log N_{\rm H} = 20.4 \pm 0.4$ at an impact parameter of $\sim$ 180 kpc from the quasar SDSSJ084158.47+392121.0 (the same hosting the giant Lyα nebula mentioned above). More generally, we can rely on the study by Lau et al. (2015). They perform a photoionization modeling analysis of a statistical sample of absorbers in the CGM of typical $z \sim 2$ QSOs, finding a median $\log N_{\rm H} = 20.5$ within 200 kpc from the quasars. Being the most reliable and recent estimate for $N_{\rm H}$ in the literature, we will assume this value throughout our analysis, even though it has been shown that there is substantial scatter in the distribution of $N_{\rm H}$ values (Lau et al. 2015).

Thus, plugging the values $z = 2.253$ (the redshift targeted by our NB filter, see §4.2), $f_{\rm C} = 0.5$, and $\log N_{\rm H} = 20.5$ in Eqn. (2.13), i.e. the equation for the Lyα surface brightness in the optically thin scenario, we can solve it to find the typical volume density $n_{\rm H}$ expected on scales of $\sim$ 275 kpc, knowing that ${\rm SB}_{{\rm Ly}\alpha} = (5.5 \pm 1.8) \times 10^{-20}$ erg s^{-1} cm^{-2} arcsec^{-2} from our measurement. We obtain

$$n_{\rm H} = 0.6 \times 10^{-2} \left(\frac{{\rm SB}^{\rm thin}_{{\rm Ly}\alpha}}{5.5 \times 10^{-20}\,{\rm erg\,s^{-1}\,cm^{-2}\,arcsec^{-2}}} \right) \left(\frac{1+z}{3.253} \right)^{4} \left(\frac{f_{\rm C}}{0.5} \right)^{-1} \left(\frac{N_{\rm H}}{10^{20.5}\,{\rm cm^{-2}}} \right)^{-1} {\rm cm^{-3}}. \tag{6.2}$$

We can compare this value to what is found by Lau et al. (2015). Indeed, as mentioned in the foregoing discussion, Lau et al. (2015) performed a photoionization modeling of the optically thick absorbers within 200 kpc from the QSO studied. However, we remind the reader that photoionization models are self-similar in the ionization parameter ($U \equiv \Phi_{LL}/cn_{\rm H} \propto L_{\nu_{\rm LL}}/n_{\rm H}$), and thus a different combination of $L_{\nu_{\rm LL}}$ and $n_{\rm H}$, resulting in the same U value, could explain the data just as well. $n_{\rm H}$ is thus constrained by assuming a source of ionizing photons, once the photoionization parameter U has been determined by the photoionization analysis.

Their U values correspond to an average $\log n_{\rm H} = -2.9$, when absorptions are assumed to be due to gas which does *not* receive the ionizing radiation from the QSO, and thus the gas is only subject to the ultraviolet background (e.g., Haardt & Madau 2012). This value is lower than what we found using our simple approach together with the measured Lyα emission, i.e. $\log n_{\rm H} = -2.2$, implying that an additional source of ionizing radiation is needed to explain our density measurement[6]. Indeed, Lau et al. (2015) show that they obtain higher $n_{\rm H}$ values, with the average being $\log n_{\rm H} = 0.26$, if they assume illumination from a typical QSO. Note however, that their study models optically thick absorption systems, while we are dealing with gas in emission and thus the situation could be quite different. Further, our $n_{\rm H}$ value is a zeroth order result. Given the assumptions made in its calculation, its value could be quite different. In particular, the typical error on $\log N_H$ is ~ 0.5 and the measurement is characterize by large scatter. Further, given that we have assumed $f_{\rm C} = 0.5$, our $n_{\rm H}$ value should be seen as an upper limit.

Further, we can compare our empirically motivated $n_{\rm H}$ value with simulations. We are not aware of an average density profile for the cool gas in massive ($\rm M_{DM} \sim 10^{12.5}$ $\rm M_\odot$) halos in the literature, and we leave for future work its determination. For this reason, here we proceed as follows. We have shown in Chapter 5 (Cantalupo et al. 2014) that one can calibrate relations between $\rm SB_{Ly\alpha}$ and the total hydrogen column density in cosmological simulations post-processed with radiative transfer. With the relation in the case of highly ionized gas, i.e. Eqn. (5.2), we can then determine the total hydrogen column density expected in simulations. If we plug $\rm SB_{Ly\alpha} = 5.5 \times 10^{-20}$ erg s^{-1} cm^{-2} arcsec^{-2} in Eqn. (5.2), we get $\log N_{\rm H} = 19.74$. By using this value in Eqn. (6.2), we find $n_{\rm H} = 0.04$ cm^{-3} (or equivalently $\log n_{\rm H} = -1.4$). Following the results of Lau et al. (2015), this value could only be explained by a QSO shining on the gas.

Note however, that in simulations one can introduce a clumping factor C to account for the small scales not resolved by the simulation setup, as previously mentioned extensively in Chapter 5. Indeed, we have shown in Chapter 5 that simulations are not able to reproduce the bright and extended Lyα emission that we observed around UM287, without using high C values. Here, instead, it seems that also the simulations are able to give a consistent result with simple photoionization models. This means that the simulations have enough cool gas to account for these low levels of $\rm SB_{Ly\alpha}$. Specifically, in §5.1 we have shown that, for a typical QSO's halo of $10^{12.5}$ $\rm M_\odot$, simulations predict $M_{\rm cool} \approx 10^{10.5}$ $\rm M_\odot$ of cool gas ($T < 5 \times 10^4$ K). I we assume that our observed $\rm SB_{Ly\alpha}$ holds within the halo, we find $M_{\rm cool} \approx 10^{10.37}$ $\rm M_\odot$, using Eqn. (5.4) (with $\log N_{\rm H} = 19.74$ and $R = 160$ kpc). Thus, probably because the size of the emitting clouds implied by our measurements are larger, and thus resolved, i.e. $R_{\rm cloud} \equiv N_{\rm H}/n_{\rm H} \sim 0.5 - 20$ kpc, simulations are able to track their physics. This point clearly needs further study.

---

[6] If we assume that our sample and Lau et al. (2015) sample represent the same QSO population, and that their U values hold also in our case.

Finally, we comment on the possibility of routinely detecting the CGM of QSOs in emission. Our analysis shows that the expected Lyα surface brightness expected around QSOs on scales of $\sim$ 200 kpc is very low, $\mathrm{SB}_{\mathrm{Ly}\alpha} = 5.5 \times 10^{-20}$ erg s^{-1} cm^{-2} arcsec^{-2}. Currently, these levels can only be achieved via stacking, even when using new generation instruments, such as MUSE and KCWI. To further complicate the situation, MUSE is able to target the Lyα emission only above $z \sim 3$, given the wavelength range covered. Thus, the cosmological surface brightness dimming implies that one should integrate longer and stack more sources, in order to achieve the same depth as at $z \sim 2$. Specifically, to achieve the same depth of our stack of 15 QSOs, one would need to observe ~ 30 $z \sim 3$ QSOs with MUSE, with a 1σ surface brightness limit in 1 arcsec^2 of $\mathrm{SB}_{\mathrm{lim}} = 2 \times 10^{-18}$ erg s^{-1} cm^{-2} arcsec^{-2} for each field[7]. On the other hand, KCWI would be more competitive. Given its bluer coverage range, it would be possible to image the Lyα line for $z \sim 2$ QSOs, enabling a much easier characterization of the CGM in emission, i.e. less SB dimming.

However, as the brightest line expected from a fluorescence scenario, i.e. Lyα , is already hard to detect, we are left with little hope for characterizing the CGM by means of other emission lines. Nevertheless, the study of bright emission line nebulae, such as the Slug nebula, could probably fill this gap, and teach us the properties of the CGM and IGM. Large statistical surveys targeting the Lyα line around QSOs are fundamental to uncover the brightest Lyα nebulae, which can then be used to test our current interpretation.

6.5 SUMMARY AND CONCLUSIONS

Using the NB data taken with the GMOS-S/Gemini instrument, which are part of the FLASHLIGHT survey (Chapter 4), we have performed a stacking analysis to characterize the Lyα emission around a typical bright QSO. We find that:

- the average combined radial profile of the 15 QSOs in our sample shows a tentative deviation from the Moffat PSF of our NB images, starting at $\sim$ 60 kpc at around $\mathrm{SB}_{\mathrm{Ly}\alpha} \sim 10^{-19}$ erg s^{-1} cm^{-2} arcsec^{-2}. This can be translated to a low significance first radial profile of the Lyα emission of the CGM.

- after a careful test using a bootstrap analysis (see §6.3.1), we ascertain that we have a $\sim 3\sigma$ Lyα line detection within an annular bin spanning 50 kpc $< R <$ 500 kpc from the QSOs. The Lyα emission in this bin, centered at R = 275 kpc, is estimated to be $\mathrm{SB}_{\mathrm{Ly}\alpha} = (5.5 \pm 1.8) \times 10^{-20}$ erg s^{-1} cm^{-2} arcsec^{-2}.

---

[7] This is achievable with MUSE in about 2.5 hours of observations.

- the observed $\mathrm{SB}_{\mathrm{Ly}\alpha}$ on scales of hundreds of kpc implies gas densities $n_{\mathrm{H}} \sim 10^{-2}\ \mathrm{cm}^{-3}$. This value is consistent with the gas being illuminated by a QSO (Lau et al. 2015).

Surface brightness levels $\sim 10^{-20}\ \mathrm{erg\,s^{-1}\,cm^{-2}\,arcsec^{-2}}$ are not easily achievable with current and planned facilities, i.e. MUSE and KCWI. Our results thus seem to indicate that emission from the typical CGM and IGM is far from being routinely observed. The build up of large statistical QSO surveys should be a priority to verify this scenario, and to uncover the brightest nebulae for which we would be able to detect also other emission lines beside the Lyα line.

> *"Arriving at one goal is the starting point to another."*
>
> John Dewey, *Democracy and Education*

Chapter 7

SUMMARY AND FUTURE PERSPECTIVE

7.1 THE SCIENTIFIC FRAMEWORK

In the modern astrophysical lexicon, the intergalactic medium (IGM) is the diffuse medium tracing the large-scale structure in the Universe, while the so-called circumgalactic medium (CGM) is the material on smaller scales within galactic halos, for which non-linear processes and the complex interplay between all mechanisms that lead to galaxy formation take place.

It has been shown that, at early epochs ($z \gtrsim 1.5$), $> 80\%$ of the baryons (Meiksin 2009; Prochaska & Tumlinson 2009, and references therein) resided in these gaseous phases, stressing the importance of understanding the physical properties of these components. Indeed, although current cosmological simulations are mostly consistent with the observed galaxies' properties (e.g, Vogelsberger et al. 2014; Schaye et al. 2015), they still have problems in correctly predict the amount of stars, especially at the high massive end of the halo mass distribution (e.g., Genel et al. 2014; Khandai et al. 2015). Indeed, simulations currently try to solve this problem by 'tuning', with several different prescriptions, highly non linear processes, such as gas cooling, star formation, radiative transfer, stellar and active galactic nucleus (AGN) feedback (e.g., Di Matteo et al. 2005; Kannan et al. 2014a; Steinborn et al. 2015). However, instead, these issues could also be related to the lack of data for the CGM and IGM, and thus to our still limited understanding of the physical conditions within the gas on such large scales (comparable or larger than the virial radius of a dark matter halo). To provide new constraints for cosmological simulations, it is then fundamental to explore in detail the physics of the CGM and IGM.

In the past, these gas phases have been preferentially studied by analyzing absorption features along background sightlines (e.g., Croft et al. 2002; Bergeron et al. 2004; Hennawi et al. 2006; Rudie et al. 2012; Farina et al. 2013; Lee et al. 2014), focusing on the halos of star forming galaxies at $z \sim 2$ and QSOs ($z \sim 2-3$). In the former case, the main results have suggested that typical star-forming galaxies exhibit a modest $\sim 20\%$ covering factor of optically thick neutral hydrogen (Rudie et al. 2012), and enrichment levels ranging from extremely metal-poor (Crighton et al. 2013) to nearly solar (Crighton et al. 2014). While in the latter, the Quasar Probing Quasar survey (Hennawi et al. 2006; Hennawi & Prochaska 2007; Prochaska & Hennawi 2009; Hennawi & Prochaska 2013; Prochaska et al. 2013a,b, 2014; Lau et al. 2015) revealed a massive ($\gtrsim 10^{10}$ M$_\odot$) reservoir of cool gas ($T \simeq 10^4$ K) in the CGM of massive halos (see also Bowen et al. 2006; Farina et al. 2013), which appears to be in conflict with the predictions of hydrodynamical zoom-in simulations of galaxy formation (e.g., Fumagalli et al. 2014). This again points out that current cosmological simulations fail to reproduce the amount of cool gas in massive dark matter halos (which is linked to the amount of star formation). However, as the absorption studies are limited by the rarity of suitably bright background sources near galaxies, and to the one-dimensional information that they provide, they need to be complemented by the direct observation of the medium in emission.

In particular, it has been shown that UV background radiation could be reprocessed by these media and be detectable as fluorescent Lyα emission (Hogan & Weymann 1987; Binette et al. 1993; Gould & Weinberg 1996; Cantalupo et al. 2005). However, current facilities are still not capable of revealing such low radiation levels, e.g. an expected surface brightness (SB) of the order of $\mathrm{SB}_{\mathrm{Ly}\alpha} \sim 10^{-20}$ erg s^{-1} cm^{-2} arcsec^{-2} (see e.g. Rauch et al. 2008). Nonetheless, this signal can be boosted to observable levels by the intense ionizing flux of a nearby quasar which, like a flashlight, illuminates the gas in its surroundings (Rees 1988; Haiman & Rees 2001; Alam & Miralda-Escudé 2002; Cantalupo et al. 2012), shedding light on its physical nature.

Detecting this fluorescence signal has been a subject of significant interest, and several studies which specifically searched for emission from the IGM in the proximity to a quasar (e.g., Fynbo et al. 1999; Francis & Bland-Hawthorn 2004; Cantalupo et al. 2007; Rauch et al. 2008; Hennawi & Prochaska 2013) have so far a not straightforward interpretation, with the exception of the compact Lyα emitters identified by Cantalupo et al. (2012). To date, these objects are the best candidates for fluorescent emission powered by a proximate quasar, having rest-frame equivalent widths exceeding the maximum value expected from star-formation, $EW_0^{\mathrm{Ly}\alpha} > 240$Å (e.g., Charlot & Fall 1993).

Besides illuminating nearby clouds in the IGM, a quasar, or any other AGN, may irradiate gas in its own host galaxy or CGM. At the moment, in the literature, there is not an uniform effort in trying to detect and characterize this signal, and three main branches can be spotted.

1) QSOs: Many searches for emission from the QSOs' CGM have been undertaken, reporting detections on scale of $10-50$ kpc around $z \sim 2-4$ QSOs (e.g, Hu & Cowie 1987; Heckman et al. 1991a,b; Christensen et al. 2006; North et al. 2012), but detailed comparison is hampered by the different methodologies of these studies. Before this Thesis, the largest Lyα nebula reported around a radio-quiet QSO showed a diameter of ~ 100 kpc (Bergeron et al. 1999).

2) High Redshif Radio Galaxies: Extended Lyα nebulae have also been frequently observed around high-redshift ($z \geq 2$) radio galaxies (HzRGs; e.g., McCarthy 1993; van Ojik et al. 1997; Nesvadba et al. 2006; Villar-Martín et al. 2007a; Reuland et al. 2007), in which the AGN is obscured from our perspective (see e.g. Miley & De Breuck 2008a), in accord with unified models of AGN (e.g., Antonucci 1993; Urry & Padovani 1995; Elvis 2000). With an average Lyα luminosity of $L_{\mathrm{Ly}\alpha} \sim 10^{44.5}$ erg s^{-1} and a diameter $\gtrsim$ 100 kpc, these nebulae tend to be brighter and larger than those around QSOs, although current surveys are very inhomogeneous.

3) Lyα Blobs: Large (50–100 kpc) luminous ($L_{\mathrm{Ly}\alpha} \sim 10^{43-44}$ erg s^{-1}) Lyα nebulae at $z \sim 2-6$, which exhibit properties similar to Lyα nebulae around QSOs and HzRGs, but without obvious evidence for the presence of an AGN (e.g., Keel et al. 1999; Steidel et al. 2000; Francis et al. 2001; Matsuda et al. 2004, 2011; Dey et al. 2005; Saito et al. 2006; Smith & Jarvis 2007; Ouchi et al. 2009; Prescott et al. 2009, 2012; Yang et al. 2009, 2010). Despite intense interest and multi-wavelength studies, the physical mechanism powering the Lyα emission in the LABs is still poorly understood. The proposed scenarios include photo-ionization by AGNs (Geach et al. 2009), shock-heated gas by galactic superwinds (Taniguchi & Shioya 2000), cooling radiation from cold-mode accretion (Fardal et al. 2001; Haiman et al. 2000; Dijkstra & Loeb 2009a; Goerdt et al. 2010; Faucher-Giguère et al. 2010), and resonant scattering of Lyα from star-forming galaxies (Steidel et al. 2011; Hayes et al. 2011). Our ignorance of the physical process powering the emission in LABs likely results from the current lack of other emission-line diagnostics besides the strong Lyα line (e.g., Matsuda et al. 2006).

We think that these three categories should be regarded as expression of the same phenomenon, i.e. CGM (or interface with the IGM) gas in emission, and thus accordingly studied.

7.2 THIS WORK

In this Thesis I outlined our work to search for and characterize the emission from the CGM and IGM at the peak of the star formation and AGN activity ($z \sim 2-3$; e.g., Schmidt et al. 1995; Hopkins & Beacom 2006). In particular, I focus on the Lyα line and other expected bright UV lines, in order to better constrain the physical properties of this gas.

Firstly, in Chapter 3 we tried to fill the observational and theoretical gap for the LABs, by conducting a deep search for the He II λ1640 and C IV λ1549 line emissions. These two lines are powerful diagnostics of the physical conditions of the emitting gas (namely the volume density, the metallicity, and the ionization level), and could be used to disentangle the different mechanisms in play. We took the deepest narrow-band images ever taken targeting these two emission lines for a sample of 13 LABs at $z \sim 3$, reaching the surface brightness limits of $\mathrm{SB_{limit}} = 2.1 \times 10^{-18}$ erg s^{-1} cm^{-2} arcsec^{-2} and 3.4×10^{-18} erg s^{-1} cm^{-2} arcsec^{-2} (5σ in 1 arcsec^2), for He II and C IV, respectively. Not detecting extended emission, we were only able to place constraints on emission line ratios. The strongest of which were obtained for the brightest LABs in our field (LAB1 and LAB2), namely He II/Ly$\alpha < 0.11$ (5σ) and C IV/Ly$\alpha < 0.16$ (5σ). We compared these stringent constraints with our photoionization and shock modeling. The photoionization models, assuming the presence of an obscured AGN (see Chapter 2), are able to produce line ratios smaller than our upper limits with physically plausible parameters, implying that much lower SBs have to be reached in order to start to rule out photoionization. On the other hand, our simple shock modeling is able to reproduce our observations only if a ionized precursor is considered. Indeed, a ‘shock-only’ model would predict too high shock velocities in comparison to the weak outflow kinematics found by observations (few hundreds of km s^{-1}; Prescott et al. 2009; Yang et al. 2011, 2014b). Deeper observations in the He II and C IV lines, and polarimetric observations seems to be the best approach in order to make more definitive statements about the mechanism powering the LABs, and study the physical properties of the gas within them.

I then focused on the gas phases around quasars. In Chapter 4 I outlined the survey FLASHLIGHT (**F**luorescent **L**yman-**A**lpha **S**urvey of cosmic **H**ydrogen i**L**lum**I**nated by h**IGH**-redshif**T** quasars), which we conducted using the 10m Keck telescope and the 8.1m Gemini-South telescope, in the past three years (2012-2015). This campaign is based on the aforementioned idea of using a QSO as a searchlight. Indeed, given the strong ionizing radiation emitted by a QSO, we should be able to detect the reprocessed emission from its surrounding gas distribution. FLASHLIGHT, targeting the Lyα line around 25 $z \sim 2$ QSOs, is the deepest line imaging study ever undertaken around quasars. This survey led to the discovery of the largest ($\sim$ 500 kpc) Lyα nebula known at high redshift: the UM 287 nebula (or ‘Slug nebula’). This nebula is currently interpreted as powered by fluorescent emission, and as the first direct detection of the IGM in emission. Having only this detected giant Lyα in our survey, our statistics tells us that about 4% ($3-9$%, 1σ confidence level for the Poisson distribution) of the radio-quiet quasars should show such nebulosity.

In Chapter 5 I presented the observations that led to the discovery of UM 287, and I explained the tension between the luminous large scale of this Lyα nebula and our current understanding of the astrophysics of gas in massive dark matter halos. In particular, we first found that current cosmological simulations, post-processed with ionizing and Lyα radiative transfer, are not able to reproduce this large scale emission (see §5.1; Cantalupo et al. 2014). This can be seen in two different perspectives. First, simulations predict a ten times smaller amount of cool gas

($T < 5 \times 10^4$ K) then inferred from the nebula's Lyα emission, with only 15% of the halo gas in a cool phase able to emit Lyα, in agreement with the theoretical expectation that in massive dark matter halos the gas is shock-heated to the virial temperature ($\sim 10^7$ K) and slowly cool down. However, it is in conflict with the large reservoir of cool gas observed in emission around UM 287. Secondly, this discrepancy can be seen as due to the current inability of cosmological simulations to resolved small scales (few parsecs). Indeed, to reach agreement between current simulations and our observations, we need to introduce a clumping factor $C = \langle n_{\rm H}^2 \rangle / \langle n_{\rm H} \rangle^2$ which takes into account the unresolved scales. As shown in §5.1, high values of C, up to ~ 1000 would then be needed to match the simulations to the Lyα emission of the UM 287 nebula.

In an effort to better characterize the physical properties of the gas within the UM 287 nebula, we searched for other emission lines. In analogy with the work on the LABs, we obtained deep spectroscopic data on the He II and C IV line emissions from this nebula (§5.4). Even though we reached unprecedented sensitivity ($\mathrm{SB}_{3\sigma} \simeq 10^{-18}$ erg s^{-1} cm^{-2} arcsec^{-2} , average over $1'' \times 20''$and $\Delta v = 3000$ km s^{-1}) for giant Lyα nebulae, we failed to detect emission in either line, and constrained the He II/Lyα and C IV/Lyα ratios to be < 0.18 (3σ), and < 0.16 (3σ), respectively. We interpreted these non-detections in light of our photoionization modeling, which assumes photoionization by the central quasar and a simple spatial distribution of cool gas in the host halo (Chapter 2). First, these models rule out a completely optically thick nebula, which would be much brighter than observed, without assuming very low, unrealistic, covering factors ($f_{\rm C} \lesssim 0.02$). Secondly, our models show that in the optically thin case ($N_{\rm HI} \ll 10^{17.2}$ cm^{-2}), once the luminosity of the central ionizing source is known (as in the case of a QSO) and the $\mathrm{SB}_{\mathrm{Ly}\alpha}$ is fixed, the He II/Lyα and C IV/Lyα ratios determine where the gas lives in the $n_{\rm H} - Z$ diagram. Our photoionization models are consistent with the Lyα emission and the He II and C IV upper limits, provided that the gas distribution is composed of a population of clouds with volume density $n_{\rm H} \gtrsim 3$ cm^{-3}, column density $N_{\rm H} \lesssim 10^{20}$ cm^{-2}, and thus a typical radius of $R \lesssim 20$ pc. If these properties hold through the entire nebula, it then follows that the total cool gas ($T \sim 10^4$ K) mass is $M_{\rm c} \lesssim 6.4 \times 10^{10}$ M$_{\odot}$. Thus, our analysis suggests the presence of a population of compact cool, and dense gas clouds in the CGM of quasars. However, it has to be verified if such clumps are able to survive[1] while moving through the hot medium expected to permeate such massive dark matter halos.

Note that the constraints on additional emission lines, in particular on the recombination He II line, are fundamental to break the degeneracy between the cool gas mass and $n_{\rm H}$ (or the gas clumping factor C), which limited our previous modeling based only on the Lyα line mentioned above (§5.1). Indeed, because the Lyα surface brightness scales as $\mathrm{SB}_{\mathrm{Ly}\alpha} \propto n_{\rm H} N_{\rm H}$, whereas the total cool gas mass as $M_{\rm c} \propto N_{\rm H}$, observations of Ly$\alpha$ emission cannot independently determine the cool gas mass and $n_{\rm H}$.

---

[1] Or what are the mechanisms responsible for the formation of these clumps

In §5.4.5 we predicted that deep observations (∼ 10 hr) of UM 287 and other bright giant nebulae with the new integral field units such as MUSE (Bacon et al. 2010), KCWI (Morrissey et al. 2012), and KMOS (Sharples et al. 2006), combined with spatial averaging, will be able to detect extended emission from other lines besides Lyα. Specifically, our photoionization modeling suggests that such observations would result in a rich emission line spectrum of the CGM, which, depending on the properties of the gas (i.e. $n_{\rm H}$ and Z), could yield detections of Lyα, He II, N IV, Si IV, Ne IV, C IV, [C III], Si III, [O III], [O II], Hβ, and Hα. This would enable modeling of the CGM at a comparable level of detail as models of H II regions and the narrow and broad-line regions of AGN, resulting in comparably detailed constraints on the physical properties of the gas.

Finally, in Chapter 6, I exploited all the narrow-band data of the FLASHLIGHT survey taken with Gemini-South, in order to constrain, for the first time, the Lyα emission on scales of hundreds of kpc around a typical bright QSO. We build an average combined radial profile of the 15 QSOs in our sample, and compare it to the stars' profile, shown to obey a Moffat function. We found a tentative deviation of the QSOs' profile from the stars' profile starting at ∼ 60 kpc and at $\mathrm{SB_{Ly\alpha}} \sim 10^{-19}$ erg s^{-1} cm^{-2} arcsec^{-2}. Using a bootstrap analysis, we ascertain that we have a $\sim 3\sigma$ Lyα line detection within an annular bin spanning 50 kpc $< R <$ 500 kpc from the QSOs, corresponding to $\mathrm{SB_{Ly\alpha}} = (5.5 \pm 1.8) \times 10^{-20}$ erg s^{-1} cm^{-2} arcsec^{-2}. This can be interpreted as the first detection of CGM gas around the typical bright QSO. Combined with absorption line measurements on the total CGM gas mass (Lau et al. 2015), this provides the first measurement of the gas density ($n_{\rm H}$ = 0.006 cm^{-3}) in the quasar CGM. Being the first result of its kind, it needs confirmation from future observations, and comparison to simulations. In particular, we showed that current cosmological simulations seem to be able to reproduce these low level of Lyα emission, i.e. there is enough cool gas in the simulated halos to account for this Lyα emission.

7.3 FUTURE WORK

The work conducted so far has opened several important questions and raised few enigmas to our understanding of the physical state of gas in massive dark matter halos. The most relevant is the tension with current cosmological simulations, raised by the discovery of the UM 287 nebula, i.e. there is a lack of cool gas in simulated massive dark matter halos. It is still unclear if the UM 287 nebula is a rare case due to particular environment conditions. However, our current statistics, together with independent works, say that ∼ 10% of quasars should show such giant Lyα nebulae. The solution to this problem should be sought by jointly promoting simulations and observations.

Regarding simulations, we have to understand if the problem is linked just to a resolution issue, or if some physics is not currently implemented (or correctly treated) in the current typical simulation setup (e.g., magnetic field, metal mixing). As resolution is limited by our current computational facilities, we should first focus on understanding the physics in detail. In particular, although our simple photoionization modeling seems to point us in the good direction, it is affected by numerous assumptions. The ideal approach would be to conduct a full radiative transfer calculation on a three dimensional gas distribution, possibly taken from a cosmological hydrodynamical simulation. Obviously, this would be too computationally challenging, if executed to a 'Cloudy level'. However it would be interesting to introduce the solutions of 1-D Cloudy slab models, e.g. something similar to our models, into a realistic gas distribution drawn from a cosmological simulation. This would be relatively straightforward for the case of optically thin nebulae (e.g. van de Voort & Schaye 2013). Once the photoionization physics would be fully captured by the simulations, we will then be able to also test the effects of the magnetic field. Indeed, it has been shown that a way to make small clumps resistant to hydrodynamic instabilities, is the confinement by magnetic fields (e.g. McClure-Griffiths et al. 2010; McCourt et al. 2015). However, to my knowledge, there is no firm characterization of the magnetic field on the large scales of interest to us.

Regarding observations, our photoionization modeling in the case of the UM 287 nebula, and the results of FLASHLIGHT, strongly exhort to conduct larger surveys to provide a better coverage of the overall population of quasar (both radio-quiet and radio-loud), HzRGs, and LABs. In particular, the results in Chapter 6 of a very low $\mathrm{SB}_{\mathrm{Ly}\alpha}$ level ($\sim 10^{-20}$ erg s^{-1} cm^{-2} arcsec^{-2}) from the typical bright QSO, revealed that we would need to observe large samples of quasars to arrive to a firm characterization of the CGM gas. Further, the same large sample will allow us to uncover the largest and brightest Lyα nebulae, such as UM 287. These sources would then be the perfect candidates for deep observations with IFUs, resulting in a rich emission line spectrum from the CGM and its interface with the IGM, which can be used to constrain the physical properties of the emitting gas, and through a comparison to detail modeling, shed light on physical mechanism powering giant nebulae.

7.3.1 OBSERVATIONAL GAME CHANGERS

I conducted most of the work in this Thesis using the narrow-band technique. Although this method has been proven to be successful and reliable, it has some disadvantages, given the very faint signal we aim for. Indeed, as already explained, in order to reduce the sky background, we inevitably had to design extremely narrow custom filter (FWHM$\sim$ 30Å), which turned out to be quite expensive (> 5000 Euros). This forced us to obtain very accurate redshifts for our targeted QSOs, and thus unavoidably cut the bright available QSOs to small numbers.

The advent of new sensitive integral field unit spectrograph with dramatically enhanced sensitivity, such as MUSE and KCWI, is a game changer for our research. Using these instruments, we can simply target the brightest QSOs on the sky with no restrictions on redshift range or redshift accuracy[2]. Indeed, we have already started a survey targeting $z \sim 3$ QSOs, using MUSE. The data are collected in service mode to allow a better scheduling of our observations, and to be able to exploit also bad seeing conditions. We have designed this campaign with roughly the same approach as the 'fast survey' conducted with Gemini-South, and explained in Chapter 6. Specifically, this survey is characterized by short exposures of total ~ 45 minutes per field, resulting in a depth of $\mathrm{SB}_{\mathrm{Ly}\alpha} \sim 2 \times 10^{-18}$ erg s^{-1} cm^{-2} arcsec^{-2} (1σ in 1 arcsec^2). The preliminary results are promising:

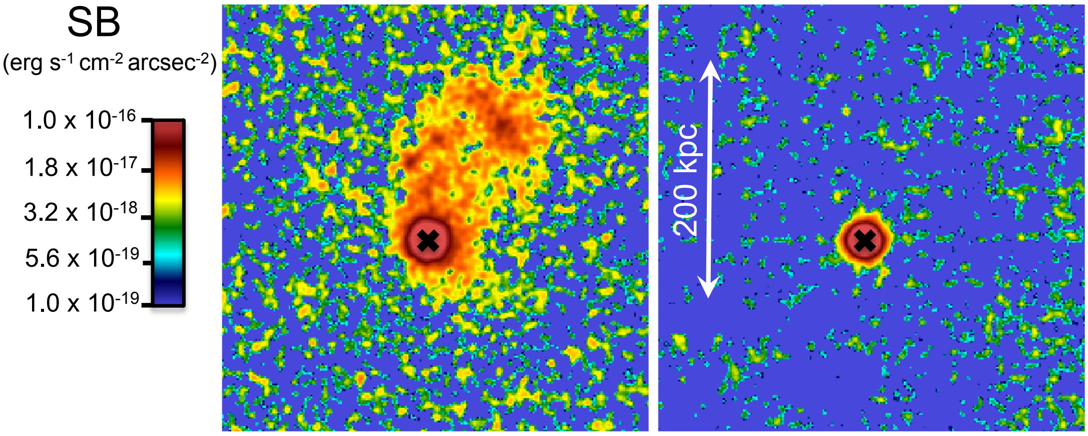

Figure 7.1: A newly discovered giant Lyα nebula around a radio-quiet $z \sim 3$ quasar using MUSE. **Left :** continuum subtracted Lyα surface brightness map corresponding to a 18 Å aperture within the MUSE data-cube around the systemic redshift of the QSO. **Right :** continuum image extracted within a 18Å aperture of the MUSE data-cube redward of the Lyα (centered at 5360Å). The images have been smoothed by a $0.6''$ Gaussian, and the color map indicates the SB which is on the same scale as in Fig. 5.2 (UM 287 nebula), for comparison. The black crosses show the position of the QSO. The extended emission spans a projected angular size of about ~200 kpc, and is fairly bright in all its extent.

Discovery of a New Giant Lyα Nebula (Arrigoni Battaia et al. 2016) Early this year (February 2015) we discovered a giant Lyα nebula around a targeted radio-quiet $z \sim 3$ QSO. The Lyα emission spans roughly ~ 200 kpc in its maximum extent at our current sensitivity, which is already on scales that are larger than the virial radius of the dark matter haloes associated with $z \sim 2-3$ QSOs ($R_{\mathrm{vir}} \sim 160$ kpc). In Figure 7.1 we compare a Lyα and a continuum map for this newly discovered object. Both images were extracted in a 18 Å aperture of the MUSE data-cube: the Lyα map (left panel) is centered at the expected redshifted wavelength of the Lyα line of this source, while the continuum map (right panel) is centered redward of the Lyα line in a region of the spectrum devoid of emission lines (5360 Å). The detection of this nebula confirm the efficacy of our strategy.

---

[2] However, note that, as stressed in §6.4, MUSE is able to observe the Lyα line only for $z \gtrsim 3$. KCWI will be able to observe the Lyα line also at lower redshift ($z \sim 2$).

Fraction of Large Nebulae So far, we have observed 13 sources. Given that we securely detect only one giant Lyα nebula, the current statistics are in agreement with what has been found previously for the frequency of large-scale Lyα emission around QSOs, i.e. $\sim 10\%$ (see §4.4). This result would be much stronger once we have a much higher number of targeted objects.

At the same time, as done in Chapter 6, our ongoing survey would enable us to compute a stacked composite CGM spectrum of quasars which do not exhibit bright nebulae, constraining the gas properties around typical quasars. Further, since MUSE covers the wavelengths of the redshifted He II and C IV at these redshifts, we will be able to put stringent constraints also on these lines, and thus constrain the physical condition of the CGM of QSOs. This should be easier, in theory, with the upcoming KCWI, which would be able to observe the Lyα line of sources at $z \sim 2$, avoiding the larger surface brightness dimming to which $z \sim 3$ targets are subject. Our current data and analysis will be a benchmark for these future CGM observations, helping in defining the best strategy to uncover the physics of this diffuse gas phase. The study of the CGM and IGM in emission, is at its beginning and will definitely be focus of intense research in the next years.

BIBLIOGRAPHY

Adelberger, K. L., Steidel, C. C., Pettini, M., Shapley, A. E., Reddy, N. A., & Erb, D. K. 2005, ApJ, 619, 697

Adelberger, K. L., Steidel, C. C., Shapley, A. E., & Pettini, M. 2003, ApJ, 584, 45

Agertz, O., et al. 2007, MNRAS, 380, 963

Alam, S. M. K., & Miralda-Escudé, J. 2002, ApJ, 568, 576

Allen, M. G., Dopita, M. A., & Tsvetanov, Z. I. 1998, ApJ, 493, 571

Allen, M. G., Groves, B. A., Dopita, M. A., Sutherland, R. S., & Kewley, L. J. 2008, ApJS, 178, 20

Antonucci, R. 1993, ARA&A, 31, 473

Antonucci, R. R. J., & Miller, J. S. 1985, ApJ, 297, 621

Arrigoni Battaia, F. et al. 2016, in prep.

Arrigoni Battaia, F., Hennawi, J. F., Cantalupo, S., & Prochaska, J. X. 2014, Proc. IAU Symp. #304: Multiwavelength AGN Surveys and Studies, Cambridge Univ. Press, 253

Arrigoni Battaia, F., Hennawi, J. F., Prochaska, J. X., & Cantalupo, S. 2015a, ArXiv e-prints

Arrigoni Battaia, F., Yang, Y., Hennawi, J. F., Prochaska, J. X., Matsuda, Y., Yamada, T., & Hayashino, T. 2015b, ApJ, 804, 26

Bacon, R., et al. 2004, in Society of Photo-Optical Instrumentation Engineers (SPIE) Conference Series, Vol. 5492, Ground-based Instrumentation for Astronomy, ed. A. F. M. Moorwood & M. Iye, 1145–1149

Bacon, R., et al. 2010, in Society of Photo-Optical Instrumentation Engineers (SPIE) Conference Series, Vol. 7735, Society of Photo-Optical Instrumentation Engineers (SPIE) Conference Series

Bahcall, J. N., & Salpeter, E. E. 1965, ApJ, 142, 1677

Barnes, J. E., & Hernquist, L. 1992, ARA&A, 30, 705

Barrio, F. E., et al. 2008, MNRAS, 389, 792

Baskin, A., Laor, A., & Stern, J. 2014, MNRAS, 438, 604

Basu-Zych, A., & Scharf, C. 2004, ApJ, 615, L85

Becker, R. H., White, R. L., & Helfand, D. J. 1994, in Astronomical Society of the Pacific Conference Series, Vol. 61, Astronomical Data Analysis Software and Systems III, ed. D. R. Crabtree, R. J. Hanisch, & J. Barnes, 165

Ben Bekhti, N., Richter, P., Winkel, B., Kenn, F., & Westmeier, T. 2009, A&A, 503, 483

Bennert, N., Jungwiert, B., Komossa, S., Haas, M., & Chini, R. 2006, A&A, 456, 953

Bergeron, J., Petitjean, P., Cristiani, S., Arnouts, S., Bresolin, F., & Fasano, G. 1999, A&A, 343, L40

Bergeron, J., et al. 2004, The Messenger, 118, 40

Bertin, E. 2006, in Astronomical Society of the Pacific Conference Series, Vol. 351, Astronomical Data Analysis Software and Systems XV, ed. C. Gabriel, C. Arviset, D. Ponz, & S. Enrique, 112

Bertin, E., & Arnouts, S. 1996, A&AS, 117, 393

Bertin, E., Mellier, Y., Radovich, M., Missonnier, G., Didelon, P., & Morin, B. 2002, in Astronomical Society of the Pacific Conference Series, Vol. 281, Astronomical Data Analysis Software and Systems XI, ed. D. A. Bohlender, D. Durand, & T. H. Handley, 228

Bianchi, S., Maiolino, R., & Risaliti, G. 2012, Advances in Astronomy, 2012, 17

Binette, L., Dopita, M. A., & Tuohy, I. R. 1985, ApJ, 297, 476

Binette, L., Kurk, J. D., Villar-Martín, M., & Röttgering, H. J. A. 2000, A&A, 356, 23

Binette, L., Wang, J. C. L., Zuo, L., & Magris, C. G. 1993, AJ, 105, 797

Binette, L., Wilson, A. S., & Storchi-Bergmann, T. 1996, A&A, 312, 365

Binney, J. 1977, ApJ, 215, 483

Binney, J., & Tremaine, S. 2008, Galactic Dynamics: Second Edition (Princeton University Press)

Boesgaard, A. M., & Steigman, G. 1985, ARA&A, 23, 319

Bond, J. R., Kofman, L., & Pogosyan, D. 1996, Nature, 380, 603

Bouché, N., Murphy, M. T., Kacprzak, G. G., Péroux, C., Contini, T., Martin, C. L., & Dessauges-Zavadsky, M. 2013, Science, 341, 50

Bowen, D. V., et al. 2006, ApJ, 645, L105

Bremer, M. N., Fabian, A. C., Sargent, W. L. W., Steidel, C. C., Boksenberg, A., & Johnstone, R. M. 1992, MNRAS, 258, 23P

Bunker, A., Smith, J., Spinrad, H., Stern, D., & Warren, S. 2003, Ap&SS, 284, 357

Cantalupo, S. 2010, MNRAS, 403, L16

Cantalupo, S., Arrigoni-Battaia, F., Prochaska, J. X., Hennawi, J. F., & Madau, P. 2014, Nature, 506, 63

Cantalupo, S., Lilly, S. J., & Haehnelt, M. G. 2012, MNRAS, 425, 1992

Cantalupo, S., Lilly, S. J., & Porciani, C. 2007, ApJ, 657, 135

Cantalupo, S., & Porciani, C. 2011, MNRAS, 411, 1678

Cantalupo, S., Porciani, C., Lilly, S. J., & Miniati, F. 2005, ApJ, 628, 61

Cen, R., Miralda-Escudé, J., Ostriker, J. P., & Rauch, M. 1994, ApJ, 437, L9

Cen, R., & Zheng, Z. 2013, ApJ, 775, 112

Chamberlain, J. W. 1953, ApJ, 117, 387

Chambers, K. C., Miley, G. K., van Breugel, W. J. M., Bremer, M. A. R., Huang, J.-S., & Trentham, N. A. 1996, ApJS, 106, 247

Charlot, S., & Fall, S. M. 1993, ApJ, 415, 580

Christensen, L., Jahnke, K., Wisotzki, L., & Sánchez, S. F. 2006, A&A, 459, 717

Ciardullo, R., et al. 2012, ApJ, 744, 110

Cielo, S., Antonuccio-Delogu, V., Macciò, A. V., Romeo, A. D., & Silk, J. 2014, MNRAS, 439, 2903

Clark, P. C., Glover, S. C. O., Klessen, R. S., & Bromm, V. 2011, ApJ, 727, 110

Courbin, F., North, P., Eigenbrod, A., & Chelouche, D. 2008, A&A, 488, 91

Cowie, L. L., & Hu, E. M. 1998, AJ, 115, 1319

Crighton, N. H. M., Hennawi, J. F., & Prochaska, J. X. 2013, ApJ, 776, L18

Crighton, N. H. M., Hennawi, J. F., Simcoe, R. A., Cooksey, K. L., Murphy, M. T., Fumagalli, M., Prochaska, J. X., & Shanks, T. 2014, ArXiv e-prints

—. 2015, MNRAS, 446, 18

Crighton, N. H. M., et al. 2011, MNRAS, 414, 28

Croft, R. A. C., Weinberg, D. H., Bolte, M., Burles, S., Hernquist, L., Katz, N., Kirkman, D., & Tytler, D. 2002, ApJ, 581, 20

Czerny, B., & Elvis, M. 1987, ApJ, 321, 305

da Ângela, J., et al. 2008, MNRAS, 383, 565

Davis, M., & Wilkinson, D. T. 1974, ApJ, 192, 251

De Breuck, C., Röttgering, H., Miley, G., van Breugel, W., & Best, P. 2000, A&A, 362, 519

De Breuck, C., van Breugel, W., Minniti, D., Miley, G., Röttgering, H., Stanford, S. A., & Carilli, C. 1999, A&A, 352, L51

De Breuck, C., et al. 2001, AJ, 121, 1241

Dekel, A., & Silk, J. 1986, ApJ, 303, 39

Dekel, A., et al. 2009, Nature, 457, 451

Dey, A., Spinrad, H., & Dickinson, M. 1995, ApJ, 440, 515

Dey, A., Spinrad, H., Stern, D., Graham, J. R., & Chaffee, F. H. 1998, ApJ, 498, L93

Dey, A., et al. 2005, ApJ, 629, 654

Di Matteo, T., Springel, V., & Hernquist, L. 2005, Nature, 433, 604

Dietrich, M., Hamann, F., Shields, J. C., Constantin, A., Vestergaard, M., Chaffee, F., Foltz, C. B., & Junkkarinen, V. T. 2002, ApJ, 581, 912

Dijkstra, M., Haiman, Z., & Spaans, M. 2006a, ApJ, 649, 14

—. 2006b, ApJ, 649, 37

Dijkstra, M., & Loeb, A. 2008, MNRAS, 386, 492

—. 2009a, MNRAS, 400, 1109

—. 2009b, MNRAS, 400, 1109

Djorgovski, S., Spinrad, H., McCarthy, P., & Strauss, M. A. 1985, ApJ, 299, L1

Djorgovski, S. G., Pahre, M. A., Bechtold, J., & Elston, R. 1996, Nature, 382, 234

Dodelson, S. 2003, Modern Cosmology, ed. A. Press (Academic Press)

Dopita, M. A., Groves, B. A., Sutherland, R. S., Binette, L., & Cecil, G. 2002, ApJ, 572, 753

Draine, B. T. 2011, Physics of the Interstellar and Intergalactic Medium

Eales, S. A., Rawlings, S., Dickinson, M., Spinrad, H., Hill, G. J., & Lacy, M. 1993, ApJ, 409, 578

Elvis, M. 2000, ApJ, 545, 63

Elvis, M., et al. 2012, ApJ, 759, 6

Erb, D. K. 2008, ApJ, 674, 151

Erb, D. K., Pettini, M., Shapley, A. E., Steidel, C. C., Law, D. R., & Reddy, N. A. 2010, ApJ, 719, 1168

Evans, I. N., Ford, H. C., Kinney, A. L., Antonucci, R. R. J., Armus, L., & Caganoff, S. 1991, ApJ, 369, L27

Fabian, A. C. 1999, MNRAS, 308, L39

Fall, S. M., & Efstathiou, G. 1980, MNRAS, 193, 189

Fanidakis, N., Macciò, A. V., Baugh, C. M., Lacey, C. G., & Frenk, C. S. 2013, MNRAS, 436, 315

Fardal, M. A., Katz, N., Gardner, J. P., Hernquist, L., Weinberg, D. H., & Davé, R. 2001, ApJ, 562, 605

Farina, E. P., Falomo, R., Decarli, R., Treves, A., & Kotilainen, J. K. 2013, MNRAS, 429, 1267

Faucher-Giguere, C.-A., Hopkins, P. F., Keres, D., Muratov, A. L., Quataert, E., & Murray, N. 2014, ArXiv e-prints

Faucher-Giguère, C.-A., Kereš, D., Dijkstra, M., Hernquist, L., & Zaldarriaga, M. 2010, ApJ, 725, 633

Faucher-Giguère, C.-A., Lidz, A., Zaldarriaga, M., & Hernquist, L. 2009, ApJ, 703, 1416

Ferland, G. J. 2003, ARA&A, 41, 517

Ferland, G. J., & Osterbrock, D. E. 1985, ApJ, 289, 105

Ferland, G. J., Williams, R. E., Lambert, D. L., Slovak, M., Gondhalekar, P. M., Truran, J. W., & Shields, G. A. 1984, ApJ, 281, 194

Ferland, G. J., et al. 2013, RMXAA, 49, 137

Ferrarese, L., & Merritt, D. 2000, ApJ, 539, L9

Finkelstein, S. L., Rhoads, J. E., Malhotra, S., Grogin, N., & Wang, J. 2008, ApJ, 678, 655

Finkelstein, S. L., Rhoads, J. E., Malhotra, S., Pirzkal, N., & Wang, J. 2007, ApJ, 660, 1023

Font-Ribera, A., et al. 2014, JCAP, 5, 27

Francis, P. J., & Bland-Hawthorn, J. 2004, MNRAS, 353, 301

Francis, P. J., et al. 1996, ApJ, 457, 490

—. 2001, ApJ, 554, 1001

Fu, H., & Stockton, A. 2007, ApJ, 666, 794

Fukugita, M., Hogan, C. J., & Peebles, P. J. E. 1998, ApJ, 503, 518

Fumagalli, M., Hennawi, J. F., Prochaska, J. X., Kasen, D., Dekel, A., Ceverino, D., & Primack, J. 2014, ApJ, 780, 74

Fumagalli, M., O'Meara, J. M., Prochaska, J. X., Rafelski, M., & Kanekar, N. 2015, MNRAS, 446, 3178

Furlanetto, S. R., Schaye, J., Springel, V., & Hernquist, L. 2005, ApJ, 622, 7

Fynbo, J. U., Møller, P., & Warren, S. J. 1999, MNRAS, 305, 849

Fynbo, J. U., Thomsen, B., & Möller, P. 2000, A&A, 353, 457

Geach, J. E., Smail, I., Chapman, S. C., Alexander, D. M., Blain, A. W., Stott, J. P., & Ivison, R. J. 2007, ApJ, 655, L9

Geach, J. E., et al. 2009, ApJ, 700, 1

Genel, S., et al. 2014, MNRAS, 445, 175

Gnedin, N. Y., & Hollon, N. 2012, ApJS, 202, 13

Gnedin, N. Y., & Kravtsov, A. V. 2010, ApJ, 714, 287

Goerdt, T., Dekel, A., Sternberg, A., Ceverino, D., Teyssier, R., & Primack, J. R. 2010, MNRAS, 407, 613

Goto, T., Utsumi, Y., Furusawa, H., Miyazaki, S., & Komiyama, Y. 2009, MNRAS, 400, 843

Goto, T., Utsumi, Y., Walsh, J. R., Hattori, T., Miyazaki, S., & Yamauchi, C. 2012, MNRAS, 421, L77

Gould, A., & Weinberg, D. H. 1996, ApJ, 468, 462

Greene, J. E., Zakamska, N. L., Ho, L. C., & Barth, A. J. 2011, ApJ, 732, 9

Groves, B. A., Dopita, M. A., & Sutherland, R. S. 2004, ApJS, 153, 75

Guaita, L., et al. 2010, ApJ, 714, 255

Gültekin, K., et al. 2009, ApJ, 698, 198

Haardt, F., & Madau, P. 2012, ApJ, 746, 125

Haiman, Z., & Rees, M. J. 2001, ApJ, 556, 87

Haiman, Z., Spaans, M., & Quataert, E. 2000, ApJ, 537, L5

Hainline, K. N., Hickox, R. C., Greene, J. E., Myers, A. D., Zakamska, N. L., Liu, G., & Liu, X. 2014, ApJ, 787, 65

Hansen, M., & Oh, S. P. 2006, MNRAS, 367, 979

Hao, H., et al. 2014, ArXiv e-prints

Hayashino, T., et al. 2004, AJ, 128, 2073

Hayes, M., Scarlata, C., & Siana, B. 2011, Nature, 476, 304

Heckman, T. M., Armus, L., & Miley, G. K. 1990, ApJS, 74, 833

Heckman, T. M., Baum, S. A., van Breugel, W. J. M., & McCarthy, P. 1989, ApJ, 338, 48

Heckman, T. M., Lehnert, M. D., Miley, G. K., & van Breugel, W. 1991a, ApJ, 381, 373

Heckman, T. M., Miley, G. K., Lehnert, M. D., & van Breugel, W. 1991b, ApJ, 370, 78

Hennawi, J., Prochaska, J., Cantalupo, S., & Arrigoni Battaia, F. 2015, Science, 348, 779

Hennawi, J. F., & Prochaska, J. X. 2007, ApJ, 655, 735

—. 2013, ApJ, 766, 58

Hennawi, J. F., Prochaska, J. X., Kollmeier, J., & Zheng, Z. 2009, ApJ, 693, L49

Hennawi, J. F., et al. 2006, ApJ, 651, 61

Hogan, C. J., & Weymann, R. J. 1987, MNRAS, 225, 1P

Hook, I. M., Jørgensen, I., Allington-Smith, J. R., Davies, R. L., Metcalfe, N., Murowinski, R. G., & Crampton, D. 2004, PASP, 116, 425

Hopkins, A. M., & Beacom, J. F. 2006, ApJ, 651, 142

Hopkins, P. F., Richards, G. T., & Hernquist, L. 2007, ApJ, 654, 731

Hu, E., & McMahon, R. G. 1996, Nature, 382, 281

Hu, E. M., & Cowie, L. L. 1987, ApJ, 317, L7

Hu, E. M., Cowie, L. L., & McMahon, R. G. 1998, ApJ, 502, L99

Humphrey, A., Binette, L., Villar-Martín, M., Aretxaga, I., & Papaderos, P. 2013, MNRAS, 428, 563

Humphrey, A., Villar-Martín, M., Fosbury, R., Binette, L., Vernet, J., De Breuck, C., & di Serego Alighieri, S. 2007, MNRAS, 375, 705

Humphrey, A., Villar-Martín, M., Fosbury, R., Vernet, J., & di Serego Alighieri, S. 2006, MNRAS, 369, 1103

Humphrey, A., Villar-Martín, M., Vernet, J., Fosbury, R., di Serego Alighieri, S., & Binette, L. 2008, MNRAS, 383, 11

Husemann, B., Wisotzki, L., Sánchez, S. F., & Jahnke, K. 2013, A&A, 549, A43

Ivezić, Ž., et al. 2002, AJ, 124, 2364

Izotov, Y. I., Chaffee, F. H., Foltz, C. B., Green, R. F., Guseva, N. G., & Thuan, T. X. 1999, ApJ, 527, 757

Jaffe, W., et al. 2004, Nature, 429, 47

Jahnke, K., et al. 2004, ApJ, 614, 568

Jones, T. W., Kang, H., & Tregillis, I. L. 1994, ApJ, 432, 194

Kannan, R., Stinson, G. S., Macciò, A. V., Brook, C., Weinmann, S. M., Wadsley, J., & Couchman, H. M. P. 2014a, MNRAS, 437, 3529

Kannan, R., et al. 2014b, MNRAS, 437, 2882

Kashikawa, N., et al. 2012, ApJ, 761, 85

Kawata, D., & Rauch, M. 2007, ApJ, 663, 38

Keel, W. C., Cohen, S. H., Windhorst, R. A., & Waddington, I. 1999, AJ, 118, 2547

Kellermann, K. I., Sramek, R., Schmidt, M., Shaffer, D. B., & Green, R. 1989, AJ, 98, 1195

Kereš, D., Katz, N., Weinberg, D. H., & Davé, R. 2005, MNRAS, 363, 2

Khandai, N., Di Matteo, T., Croft, R., Wilkins, S., Feng, Y., Tucker, E., DeGraf, C., & Liu, M.-S. 2015, MNRAS, 450, 1349

King, A. 2003, ApJ, 596, L27

Klessen, R. S., Burkert, A., & Bate, M. R. 1998, ApJ, 501, L205

Klypin, A. A., Trujillo-Gomez, S., & Primack, J. 2011, ApJ, 740, 102

Knopp, G. P., & Chambers, K. C. 1997, ApJS, 109, 367

Kollmeier, J. A., Zheng, Z., Davé, R., Gould, A., Katz, N., Miralda-Escudé, J., & Weinberg, D. H. 2010, ApJ, 708, 1048

Kraemer, S. B., Ho, L. C., Crenshaw, D. M., Shields, J. C., & Filippenko, A. V. 1999, ApJ, 520, 564

Krawczynski, H., & Treister, E. 2013, Frontiers of Physics, 8, 609

Kreimeyer, K., & Veilleux, S. 2013, ApJ, 772, L11

Krogager, J.-K., Fynbo, J. P. U., Møller, P., Ledoux, C., Noterdaeme, P., Christensen, L., Milvang-Jensen, B., & Sparre, M. 2012, MNRAS, 424, L1

Krumholz, M. R., & Dekel, A. 2012, ApJ, 753, 16

Kudritzki, R.-P., et al. 2000, ApJ, 536, 19

Kurk, J. D., Pentericci, L., Röttgering, H. J. A., & Miley, G. K. 2002, in Revista Mexicana de Astronomia y Astrofisica, vol. 27, Vol. 13, Revista Mexicana de Astronomia y Astrofisica

Conference Series, ed. W. J. Henney, W. Steffen, L. Binette, & A. Raga, 191–195

Kurk, J. D., et al. 2000, A&A, 358, L1

Landolt, A. U. 1992, AJ, 104, 340

Larson, R. B. 1974, MNRAS, 169, 229

—. 1978, MNRAS, 184, 69

Lau, M., Prochaska, J., & Hennawi, J. 2015, submitted to ApJ

Lee, K.-G., et al. 2014, ApJ, 795, L12

—. 2015, ApJ, 799, 196

Lehner, N., et al. 2013, ApJ, 770, 138

Lehnert, M. D., & Becker, R. H. 1998, A&A, 332, 514

Lowenthal, J. D., Hogan, C. J., Green, R. F., Caulet, A., Woodgate, B. E., Brown, L., & Foltz, C. B. 1991, ApJ, 377, L73

Lowenthal, J. D., Hogan, C. J., Leach, R. W., Schmidt, G. D., & Foltz, C. B. 1990, ApJ, 357, 3

Lukić, Z., Stark, C. W., Nugent, P., White, M., Meiksin, A. A., & Almgren, A. 2015, MNRAS, 446, 3697

Lusso, E., Worseck, G., Hennawi, J. F., Prochaska, J. X., Vignali, C., Stern, J., & O'Meara, J. M. 2015, ArXiv e-prints

Lynds, R. 1971, ApJ, 164, L73

Madau, P., & Dickinson, M. 2014, ARA&A, 52, 415

Magorrian, J., et al. 1998, AJ, 115, 2285

Malhotra, S., & Rhoads, J. E. 2002, ApJ, 565, L71

Malkan, M. A., & Sargent, W. L. W. 1982, ApJ, 254, 22

Maller, A. H., & Bullock, J. S. 2004, MNRAS, 355, 694

Martin, C. L., Shapley, A. E., Coil, A. L., Kornei, K. A., Bundy, K., Weiner, B. J., Noeske, K. G., & Schiminovich, D. 2012, ApJ, 760, 127

Martin, D. C., Chang, D., Matuszewski, M., Morrissey, P., Rahman, S., Moore, A., & Steidel, C. C. 2014a, ApJ, 786, 106

—. 2014b, ApJ, 786, 106

Martin, D. C., Chang, D., Matuszewski, M., Morrissey, P., Rahman, S., Moore, A., Steidel, C. C., & Matsuda, Y. 2014c, ApJ, 786, 107

Matsuda, Y., Iono, D., Ohta, K., Yamada, T., Kawabe, R., Hayashino, T., Peck, A. B., & Petitpas, G. R. 2007, ApJ, 667, 667

Matsuda, Y., Yamada, T., Hayashino, T., Yamauchi, R., & Nakamura, Y. 2006, ApJ, 640, L123

Matsuda, Y., et al. 2004, AJ, 128, 569

—. 2005, ApJ, 634, L125

—. 2009, MNRAS, 400, L66

—. 2011, MNRAS, 410, L13

Matsuoka, K., Nagao, T., Maiolino, R., Marconi, A., & Taniguchi, Y. 2009, A&A, 503, 721

Matuszewski, M., Chang, D., Crabill, R. M., Martin, D. C., Moore, A. M., Morrissey, P., & Rahman, S. 2010, in Society of Photo-Optical Instrumentation Engineers (SPIE) Conference Series, Vol. 7735, Society of Photo-Optical Instrumentation Engineers (SPIE) Conference Series, 0

Maxfield, L., Spinrad, H., Stern, D., Dey, A., & Dickinson, M. 2002, AJ, 123, 2321

McCarthy, P. J. 1993, ARA&A, 31, 639

McCarthy, P. J., Spinrad, H., Dickinson, M., van Breugel, W., Liebert, J., Djorgovski, S., & Eisenhardt, P. 1990, ApJ, 365, 487

McCarthy, P. J., Spinrad, H., & van Breugel, W. 1995, ApJS, 99, 27

McClure-Griffiths, N. M., Madsen, G. J., Gaensler, B. M., McConnell, D., & Schnitzeler, D. H. F. M. 2010, ApJ, 725, 275

McCourt, M., O'Leary, R. M., Madigan, A.-M., & Quataert, E. 2015, MNRAS, 449, 2

McDonald, M., Veilleux, S., Rupke, D. S. N., & Mushotzky, R. 2010, ApJ, 721, 1262

McIntosh, D. H., Rieke, M. J., Rix, H.-W., Foltz, C. B., & Weymann, R. J. 1999, ApJ, 514, 40

McLinden, E. M., Malhotra, S., Rhoads, J. E., Hibon, P., Weijmans, A.-M., & Tilvi, V. 2013, ApJ, 767, 48

Mechtley, M. 2014, PhD thesis, Arizona State University ¡EMAIL¿matt.mechtley@asu.edu¡/EMAIL¿

Mechtley, M., et al. 2012, ApJ, 756, L38

Meiksin, A. A. 2009, Reviews of Modern Physics, 81, 1405

Menzel, D. H. 1937, ApJ, 85, 330

Miley, G., & De Breuck, C. 2008a, A&A Rev., 15, 67

—. 2008b, A&A Rev., 15, 67

Miyazaki, S., et al. 2002, PASJ, 54, 833

Mo, H., van den Bosch, F., & White, S. 2010, Galaxy Formation and Evolution

Mo, H. J., Mao, S., & White, S. D. M. 1998, MNRAS, 295, 319

Mo, H. J., & Miralda-Escude, J. 1996, ApJ, 469, 589

Moller, P., & Warren, S. J. 1993, A&A, 270, 43

Moorwood, A., Cuby, J.-G., & Lidman, C. 1998, The Messenger, 91, 9

Mori, M., & Umemura, M. 2006, New Astronomy Review, 50, 199

Morrissey, P., et al. 2012, in Society of Photo-Optical Instrumentation Engineers (SPIE) Conference Series, Vol. 8446, Society of Photo-Optical Instrumentation Engineers (SPIE) Conference Series, 13

Nagao, T., Maiolino, R., & Marconi, A. 2006, A&A, 459, 85

Nelson, D., Genel, S., Pillepich, A., Vogelsberger, M., Springel, V., & Hernquist, L. 2015, ArXiv e-prints

Nesvadba, N. P. H., Lehnert, M. D., Eisenhauer, F., Gilbert, A., Tecza, M., & Abuter, R. 2006, ApJ, 650, 693

Neufeld, D. A. 1990, ApJ, 350, 216

—. 1991, ApJ, 370, L85

Nilsson, K. K., Fynbo, J. P. U., Møller, P., Sommer-Larsen, J., & Ledoux, C. 2006, A&A, 452, L23

North, P. L., Courbin, F., Eigenbrod, A., & Chelouche, D. 2012, A&A, 542, A91

Noterdaeme, P., et al. 2012, A&A, 540, A63

Ocvirk, P., Pichon, C., & Teyssier, R. 2008, MNRAS, 390, 1326

Ohyama, Y., et al. 2003, ApJ, 591, L9

Oke, J. B. 1974, ApJS, 27, 21

Oke, J. B., et al. 1995, PASP, 107, 375

Osterbrock, D. E., & Ferland, G. J. 2006, Astrophysics of Gaseous Nebulae and Active Galactic Nuclei (2nd ed.: Sausalito, CA: Univ. Science Books)

Ouchi, M., et al. 2009, ApJ, 696, 1164

Overzier, R. A., Nesvadba, N. P. H., Dijkstra, M., Hatch, N. A., Lehnert, M. D., Villar-Martín, M., Wilman, R. J., & Zirm, A. W. 2013, ApJ, 771, 89

Padmanabhan, T. 2006, in American Institute of Physics Conference Series, Vol. 843, Graduate School in Astronomy: X, ed. S. Daflon, J. Alcaniz, E. Telles, & R. de la Reza, 111–166

Page, D. N., & Thorne, K. S. 1974, ApJ, 191, 499

Palunas, P., Teplitz, H. I., Francis, P. J., Williger, G. M., & Woodgate, B. E. 2004, ApJ, 602, 545

Pâris, I., et al. 2014, A&A, 563, A54

Partridge, R. B. 1974, ApJ, 192, 241

Partridge, R. B., & Peebles, P. J. E. 1967a, ApJ, 147, 868

—. 1967b, ApJ, 148, 377

Penzo, C., Macciò, A. V., Casarini, L., Stinson, G. S., & Wadsley, J. 2014, MNRAS, 442, 176

Péroux, C., Bouché, N., Kulkarni, V. P., & York, D. G. 2013, MNRAS, 436, 2650

Peterson, B. M. 1993, PASP, 105, 247

Planck Collaboration et al. 2015, ArXiv e-prints

Pogge, R. W. 1988, ApJ, 328, 519

Polletta, M., Weedman, D., Hönig, S., Lonsdale, C. J., Smith, H. E., & Houck, J. 2008, ApJ, 675, 960

Polletta, M., et al. 2007, ApJ, 663, 81

Prescott, M. K. M., Dey, A., & Jannuzi, B. T. 2009, ApJ, 702, 554

—. 2012, ApJ, 748, 125

—. 2013, ApJ, 762, 38

Prescott, M. K. M., Martin, C. L., & Dey, A. 2015a, ApJ, 799, 62

Prescott, M. K. M., Momcheva, I., Brammer, G. B., Fynbo, J. P. U., & Møller, P. 2015b, ArXiv e-prints

Prescott, M. K. M., Smith, P. S., Schmidt, G. D., & Dey, A. 2011, ApJ, 730, L25

Prochaska, J. X., & Hennawi, J. F. 2009, ApJ, 690, 1558

Prochaska, J. X., Hennawi, J. F., & Simcoe, R. A. 2013a, ApJ, 762, L19

Prochaska, J. X., & Tumlinson, J. 2009, Baryons: What,When and Where?, 419

Prochaska, J. X., Wingyee Lau, M., & Hennawi, J. F. 2014, ApJ, 796, 140

Prochaska, J. X., & Wolfe, A. M. 2009, ApJ, 696, 1543

Prochaska, J. X., et al. 2013b, ApJ, 776, 136

Rakic, O., Schaye, J., Steidel, C. C., & Rudie, G. C. 2012, ApJ, 751, 94

Rauch, M., Becker, G. D., Haehnelt, M. G., Gauthier, J.-R., Ravindranath, S., & Sargent, W. L. W. 2011, MNRAS, 418, 1115

Rauch, M., Sargent, W. L. W., & Barlow, T. A. 1999, ApJ, 515, 500

Rauch, M., et al. 2008, ApJ, 681, 856

Rees, M. J. 1984, ARA&A, 22, 471

—. 1988, MNRAS, 231, 91P

Rees, M. J., & Ostriker, J. P. 1977, MNRAS, 179, 541

Reuland, M., et al. 2003, ApJ, 592, 755

—. 2007, AJ, 133, 2607

Richards, G. T., et al. 2006, ApJS, 166, 470

Risaliti, G., & Elvis, M. 2004, in Astrophysics and Space Science Library, Vol. 308, Supermassive Black Holes in the Distant Universe, ed. A. J. Barger, 187

Roche, N., Humphrey, A., & Binette, L. 2014, MNRAS, 443, 3795

Roettgering, H. J. A., van Ojik, R., Miley, G. K., Chambers, K. C., van Breugel, W. J. M., & de Koff, S. 1997, A&A, 326, 505

Rorai, A., Hennawi, J. F., & White, M. 2013, ApJ, 775, 81

Rosdahl, J., & Blaizot, J. 2012, MNRAS, 423, 344

Rubin, K. H. R., Prochaska, J. X., Koo, D. C., Phillips, A. C., Martin, C. L., & Winstrom, L. O. 2014, ApJ, 794, 156

Rudie, G. C., et al. 2012, ApJ, 750, 67

Saglia, R. P., Bertschinger, E., Baggley, G., Burstein, D., Colless, M., Davies, R. L., McMahan, Jr., R. K., & Wegner, G. 1993, MNRAS, 264, 961

Saito, T., Shimasaku, K., Okamura, S., Ouchi, M., Akiyama, M., & Yoshida, M. 2006, ApJ, 648, 54

Sánchez, S. F., & Humphrey, A. 2009, A&A, 495, 471

Sargent, W. L. W. 1980, Phys. Scr, 21, 753

Scannapieco, E., & Brüggen, M. 2015, ArXiv e-prints

Schaye, J., Aguirre, A., Kim, T.-S., Theuns, T., Rauch, M., & Sargent, W. L. W. 2003, ApJ, 596, 768

Schaye, J., Carswell, R. F., & Kim, T.-S. 2007, MNRAS, 379, 1169

Schaye, J., Theuns, T., Rauch, M., Efstathiou, G., & Sargent, W. L. W. 2000, MNRAS, 318, 817

Schaye, J., et al. 2015, MNRAS, 446, 521

Schmidt, M., Schneider, D. P., & Gunn, J. E. 1995, AJ, 110, 68

Schneider, D. P., Gunn, J. E., Turner, E. L., Lawrence, C. R., Hewitt, J. N., Schmidt, M., & Burke, B. F. 1986, AJ, 91, 991

Scott, J. E., Kriss, G. A., Brotherton, M., Green, R. F., Hutchings, J., Shull, J. M., & Zheng, W. 2004, ApJ, 615, 135

Shakura, N. I., & Sunyaev, R. A. 1973, A&A, 24, 337

Shapley, A. E., Steidel, C. C., Pettini, M., & Adelberger, K. L. 2003, ApJ, 588, 65

Sharples, R., et al. 2006, New Astronomy Review, 50, 370

Shen, Y., et al. 2007, AJ, 133, 2222

Shields, G. A. 1978, Nature, 272, 706

Shull, J. M., Stevans, M., & Danforth, C. W. 2012, ApJ, 752, 162

Silk, J., & Rees, M. J. 1998, A&A, 331, L1

Simcoe, R. A., Sargent, W. L. W., Rauch, M., & Becker, G. 2006, ApJ, 637, 648

Smith, D. J. B., & Jarvis, M. J. 2007, MNRAS, 378, L49

Smith, D. J. B., Jarvis, M. J., Simpson, C., & Martínez-Sansigre, A. 2009, MNRAS, 393, 309

Solomon, P. M., & Vanden Bout, P. A. 2005, ARA&A, 43, 677

Somerville, R. S., Hopkins, P. F., Cox, T. J., Robertson, B. E., & Hernquist, L. 2008, MNRAS, 391, 481

Spinrad, H., Filippenko, A. V., Wyckoff, S., Stocke, J. T., Wagner, R. M., & Lawrie, D. G. 1985, ApJ, 299, L7

Steidel, C. C., Adelberger, K. L., Shapley, A. E., Pettini, M., Dickinson, M., & Giavalisco, M. 2000, ApJ, 532, 170

Steidel, C. C., Bogosavljević, M., Shapley, A. E., Kollmeier, J. A., Reddy, N. A., Erb, D. K., & Pettini, M. 2011, ApJ, 736, 160

Steidel, C. C., Erb, D. K., Shapley, A. E., Pettini, M., Reddy, N., Bogosavljević, M., Rudie, G. C., & Rakic, O. 2010, ApJ, 717, 289

Steidel, C. C., & Hamilton, D. 1993, AJ, 105, 2017

Steidel, C. C., Sargent, W. L. W., & Dickinson, M. 1991, AJ, 101, 1187

Steinborn, L. K., Dolag, K., Hirschmann, M., Prieto, M. A., & Remus, R.-S. 2015, MNRAS, 448, 1504

Stenflo, J. O. 1980, A&A, 84, 68

Stern, D., & Spinrad, H. 1999, PASP, 111, 1475

Stern, J., Laor, A., & Baskin, A. 2014, MNRAS, 438, 901

Stockton, A., Fu, H., & Canalizo, G. 2006, New Astronomy Review, 50, 694

Stockton, A., MacKenty, J. W., Hu, E. M., & Kim, T.-S. 2002, ApJ, 572, 735

Strateva, I. V., Brandt, W. N., Schneider, D. P., Vanden Berk, D. G., & Vignali, C. 2005, AJ, 130, 387

Swinbank, A. M., et al. 2010, Nature, 464, 733

—. 2015, MNRAS, 449, 1298

Tadhunter, C., & Tsvetanov, Z. 1989, Nature, 341, 422

Taniguchi, Y., & Shioya, Y. 2000, ApJ, 532, L13

Taniguchi, Y., Shioya, Y., & Kakazu, Y. 2001, ApJ, 562, L15

Teyssier, R. 2002, A&A, 385, 337

Thommes, E., Meisenheimer, K., Fockenbrock, R., Hippelein, H., Roeser, H.-J., & Beckwith, S. 1998, MNRAS, 293, L6

Trainor, R., & Steidel, C. C. 2013, ApJ, 775, L3

Trainor, R. F., & Steidel, C. C. 2012, ApJ, 752, 39

Trujillo, I., Aguerri, J. A. L., Cepa, J., & Gutiérrez, C. M. 2001, MNRAS, 328, 977

Turner, M. L., Schaye, J., Steidel, C. C., Rudie, G. C., & Strom, A. L. 2014, MNRAS, 445, 794

Urry, C. M., & Padovani, P. 1995, PASP, 107, 803

van Breugel, W., De Breuck, C., Stanford, S. A., Stern, D., Röttgering, H., & Miley, G. 1999, ApJ, 518, L61

van de Voort, F., & Schaye, J. 2013, MNRAS, 430, 2688

van de Voort, F., Schaye, J., Booth, C. M., Haas, M. R., & Dalla Vecchia, C. 2011, MNRAS, 414, 2458 van Dokkum, P. G. 2001, PASP, 113, 1420

van Ojik, R., Roettgering, H. J. A., Carilli, C. L., Miley, G. K., Bremer, M. N., & Macchetto, F. 1996, A&A, 313, 25

van Ojik, R., Roettgering, H. J. A., Miley, G. K., & Hunstead, R. W. 1997, A&A, 317, 358

van Ojik, R., Rottgering, H. J. A., Miley, G. K., Bremer, M. N., Macchetto, F., & Chambers, K. C. 1994, A&A, 289, 54

Vanden Berk, D. E., et al. 2001, AJ, 122, 549

Veilleux, S., Cecil, G., & Bland-Hawthorn, J. 2005, ARA&A, 43, 769

Venemans, B. P., et al. 2007, A&A, 461, 823

Verhamme, A., Schaerer, D., & Maselli, A. 2006, A&A, 460, 397

Vernet, J., Fosbury, R. A. E., Villar-Martín, M., Cohen, M. H., Cimatti, A., di Serego Alighieri, S., & Goodrich, R. W. 2001, A&A, 366, 7

Villar-Martín, M., Humphrey, A., De Breuck, C., Fosbury, R., Binette, L., & Vernet, J. 2007a, MNRAS, 375, 1299

Villar-Martín, M., Sánchez, S. F., Humphrey, A., Dijkstra, M., di Serego Alighieri, S., De Breuck, C., & González Delgado, R. 2007b, MNRAS, 378, 416

Villar-Martín, M., Vernet, J., di Serego Alighieri, S., Fosbury, R., Humphrey, A., & Pentericci, L. 2003a, MNRAS, 346, 273

Villar-Martín, M., Vernet, J., di Serego Alighieri, S., Fosbury, R., Humphrey, A., Pentericci, L., & Cohen, M. 2003b, New Astronomy Review, 47, 291

Villar-Martín, M., Vernet, J., di Serego Alighieri, S., Fosbury, R., Pentericci, L., Cohen, M., Goodrich, R., & Humphrey, A. 2002, MNRAS, 336, 436

Villar-Martín, M., et al. 2006, MNRAS, 366, L1

Vogelsberger, M., et al. 2014, MNRAS, 444, 1518

Voit, G. M., Balogh, M. L., Bower, R. G., Lacey, C. G., & Bryan, G. L. 2003, ApJ, 593, 272

Vreeswijk, P. M., et al. 2004, A&A, 419, 927

Weidinger, M., Møller, P., & Fynbo, J. P. U. 2004, Nature, 430, 999

Weidinger, M., Møller, P., Fynbo, J. P. U., & Thomsen, B. 2005, A&A, 436, 825

Weinberg, D. H., Davé, R., Katz, N., & Kollmeier, J. A. 2003, in American Institute of Physics Conference Series, Vol. 666, The Emergence of Cosmic Structure, ed. S. H. Holt & C. S. Reynolds, 157–169

Werk, J. K., et al. 2014, ApJ, 792, 8

White, M., Pope, A., Carlson, J., Heitmann, K., Habib, S., Fasel, P., Daniel, D., & Lukic, Z. 2010, ApJ, 713, 383

White, M., et al. 2012, MNRAS, 424, 933

White, S. D. M., & Frenk, C. S. 1991, ApJ, 379, 52

White, S. D. M., & Rees, M. J. 1978, MNRAS, 183, 341

Willott, C. J., Chet, S., Bergeron, J., & Hutchings, J. B. 2011, AJ, 142, 186

Wilman, R. J., Gerssen, J., Bower, R. G., Morris, S. L., Bacon, R., de Zeeuw, P. T., & Davies, R. L. 2005, Nature, 436, 227

Wilman, R. J., Jarvis, M. J., Röttgering, H. J. A., & Binette, L. 2004, MNRAS, 351, 1109

Wolfe, A. M., Gawiser, E., & Prochaska, J. X. 2005, ARA&A, 43, 861

Wolfe, A. M., Turnshek, D. A., Smith, H. E., & Cohen, R. D. 1986, ApJS, 61, 249

Yang, Y., Walter, F., Decarli, R., Bertoldi, F., Weiss, A., Dey, A., Prescott, M. K. M., & Badescu, T. 2014a, ArXiv e-prints

Yang, Y., Zabludoff, A., Eisenstein, D., & Davé, R. 2010, ApJ, 719, 1654

Yang, Y., Zabludoff, A., Jahnke, K., & Davé, R. 2014b, ArXiv e-prints

Yang, Y., Zabludoff, A., Jahnke, K., Eisenstein, D., Davé, R., Shectman, S. A., & Kelson, D. D. 2011, ApJ, 735, 87

Yang, Y., Zabludoff, A., Tremonti, C., Eisenstein, D., & Davé, R. 2009, ApJ, 693, 1579

Yang, Y., Zabludoff, A. I., Davé, R., Eisenstein, D. J., Pinto, P. A., Katz, N., Weinberg, D. H., & Barton, E. J. 2006, ApJ, 640, 539

Zheng, W., Kriss, G. A., Telfer, R. C., Grimes, J. P., & Davidsen, A. F. 1997, ApJ, 475, 469

Zheng, Z., Cen, R., Weinberg, D., Trac, H., & Miralda-Escudé, J. 2011, ApJ, 739, 62

Zirm, A. W., et al. 2005, ApJ, 630, 68

ACKNOWLEDGEMENTS

I would like to strongly thank my supervisor, Joseph F. Hennawi, for offering me the possibility of working on a cutting-edge topic together with an extremely expert team, and a dynamic environment. His meticulous advices, critic guidance and endless opportunities made this work possible. Despite his numerous students, he has always found time to help me improving my work, always suggesting new directions to make my general formation as broader as possible.

I greatly thank Yujin Yang for sharing his knowledge on the LAB phenomenon and having guided me at the beginning of my PhD, when my english and high-z knowledge was very poor.

This work would not have been possible without the criticism and significant contribution of Sebastiano Cantalupo and J. Xavier Prochaska. Each of them have spent time explaining and clarifying. Their work, suggestions and comments have strengthened this thesis.

I really appreciate the dynamic and stimulating working environment of the ENIGMA group. I sincerely thank all the past and current members for the useful discussions, help and suggestions (especially while bravely attending our interminable group meetings).

I am thankful to Joseph F. Hennawi and Ralf S. Klessen for agreeing to referee my thesis and also to Christian Fendt and Bernd Jähne for being part of my thesis committee.

An enthusiastic thank you to Christian Fendt, the coordinator of the IMPRS program. His work and help are fundamental for students. I really enjoyed to be part of an IMPRS generation.

I would like to deeply thank my bachelor and master supervisor, Giuseppe Gavazzi (il Peppo). If it had not been for you, I probably would not even studied astronomy. Thank you for showing me your love for observations and your infinite, explosive passion for life.

The friends I have made in Heidelberg have kept me sane and kept me going. An immense heart-felt thank you to all of you. Your company, laughs, crazy ideas, dances (also lap-dances),

encouragement, help and jokes, made Heidelberg my second and lovely home. You absolutely enlarged my horizons. I will definitely miss all of you.

A gigantic thank you to my friends in Italy, who have been far from me in these years for most of the time, but did not stop to follow passionately (and with a bit of envy) my adventures around the world. It is always a great pleasure to go back to Italy, meet with all of you and share our experiences. The time spent with you has been always too short in these years.

Finally, I hug my family. I thank my brothers, Nichi, Ale and Raffi, to always patiently wait my return to Italy and, despite the distance, to not stop caring about me. A tremendous thank you to my parents, Nina and Augusto, who threw me into this world with a good trajectory and kept correcting it. Thank you, Papi, to be always present, to be a firm rock on which I can always jump whenever I have the need. Definitely an hero.